

**KARADENİZ TECHNICAL UNIVERSITY  
THE GRADUATE SCHOOL OF NATURAL AND APPLIED SCIENCES**





**KARADENİZ TECHNICAL UNIVERSITY**  
**THE GRADUATE SCHOOL OF NATURAL AND APPLIED SCIENCES**

**ORCID :** - - -

**This thesis is accepted to give the degree of**

**By**  
**The Graduate School of Natural and Applied Sciences at**  
**Karadeniz Technical University**

**The Date of Submission** : / /

**The Date of Examination** : / /

**Thesis Supervisor** :  
**ORCID** : - - -

**Trabzon**

## FOREWORD

This PhD thesis entitled “Metaheuristic Pansharpening Based on Symbiotic Organisms Search Optimization” has been submitted to the Karadeniz Technical University, The Graduate School of Natural and Applied Sciences, Geomatics Engineering Graduate Program.

I would like to express my deepest gratitude to my supervisor Prof. Dr. Oğuz GÜNGÖR whom I have always been happy and honoured to work with. His guidance and understanding have always made me feel comfortable. I feel so privileged to have found the chance to work with him. Being his student will always be the most precious title I will have.

I am also deeply grateful to my PhD thesis committee members Asst. Prof. Dr. Esra TUNÇ GÖRMÜŞ and Asst. Prof. Dr. Mehmet ÖZTÜRK for their interest and support throughout my PhD. My very special thanks also go to the other members of my PhD thesis committee Prof. Dr. Dursun Zafer ŞEKER and Assoc. Prof. Dr. Halil AKINCI for their contributions to my thesis.

My sincerest thanks also go to Prof. Dr. Jie Shan from Purdue University for his helpful contributions on the journal paper derived from my PhD thesis. I also thank the Scientific and Technological Research Council of Turkey (TUBITAK) (project no: 111Y296) for providing the satellite imagery used in this thesis.

I also extend my gratitude to Asst. Prof. Dr. Sultan Sevinç KURT KONAKOĞLU, Asst. Prof. Dr. Berkant KONAKOĞLU and Res. Asst. Ziya USTA for their friendship. I am also grateful to Muhammet GÜMRÜKÇÜOĞLU for his constant guidance.

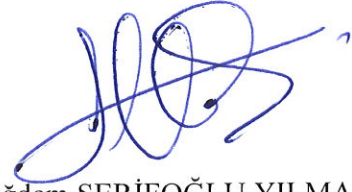
I would also like to express my sincerest thanks and appreciation to my lovely friend Gizem TORUN AVŞAR, who has always been there by my side since my childhood. I wish to thank my parents and sisters for their constant support and love. I have always felt honoured to be a member of this beautiful family. Finally, my very special thanks go to my husband Asst. Prof. Dr. Volkan YILMAZ for his help, patience and understanding during my PhD. Knowing he is always there for me makes me feel special.

Çiğdem ŞERİFOĞLU YILMAZ

Trabzon 2020

## STATEMENT OF ETHICS

I declare that, this PhD thesis, I have submitted with the title “Metaheuristic Pansharpening Based on Symbiotic Organisms Search Optimization” has been completed under the guidance of my supervisor Prof. Dr. Oğuz GÜNGÖR. All the data used in this thesis are obtained by simulation and experimental works done as parts of this work in our research labs. All referred information used in this thesis has been indicated in the text and cited in reference list. I have obeyed all research and ethical rules during my research and I accept all responsibility if proven otherwise. 02/07/2020.



Çiğdem ŞERİFOĞLU YILMAZ

## TABLE OF CONTENTS

	<u>Page No.</u>
FOREWORD.....	III
STATEMENT OF ETHICS .....	IV
TABLE OF CONTENTS .....	V
SUMMARY .....	VII
ÖZET .....	IX
LIST OF FIGURES .....	XI
LIST OF TABLES .....	XIV
LIST OF ABBREVIATIONS .....	XV
1. INTRODUCTION.....	1
1.1. Image Fusion.....	1
1.1.1. Pansharpening .....	3
1.2. Motivation.....	10
1.2.1. Research Questions .....	10
1.2.2. Objectives of the Thesis.....	10
1.2.3. Method .....	11
1.3. Structure of the Thesis .....	12
1.4. Optimization .....	12
1.4.1. Single-Objective Optimization .....	18
1.4.2. Multi-Objective Optimization.....	20
1.4.3. An Overview of Metaheuristics .....	24
2. PANSHARPENING METHODS .....	28
2.1. Brovey (BRV) .....	28
2.2. Synthetic Variable Ratio (SVR).....	28
2.3. Modified IHS (MIHS).....	29
2.4. Gram-Schmidt (GS).....	30
2.5. Hyperspherical Colour Space (HCS).....	32
2.6. Band Dependent Spatial Detail (BDSD).....	33
2.7. à trous Wavelet Transformation (ATWT) .....	34
2.8. Additive Wavelet Luminance Proportional (AWLP).....	36

2.9.	Local Mean Matching (LMM).....	37
2.10.	High-Pass Filtering (HPF) .....	37
2.11.	Smoothing Filter-Based Intensity Modulation (SFIM).....	39
2.12.	Criteria-Based (CB) Method.....	39
2.13.	Principal Component Analysis (PCA) .....	40
2.14.	Discrete Wavelet Transform (DWT).....	41
2.15.	Intensity-Hue-Saturation – Discrete Wavelet Transform (IHS-DWT).....	42
3.	SOS ALGORITHM .....	44
3.1.	MOSOS Algorithm .....	46
4.	APPLICATION .....	50
4.1.	Test Sites and Data.....	50
4.2.	Proposed SOS-SVR and SOS-IHS-DWT Methods.....	51
4.2.1.	SOS-SVR Method.....	51
4.2.2.	SOS-IHS-DWT Method.....	55
4.3.	Proposed MOSOS-SVR and MOSOS-IHS-DWT Methods .....	57
4.3.1.	MOSOS-SVR Method .....	57
4.3.2.	MOSOS-IHS-DWT Method .....	60
4.4.	Quality Investigation.....	64
5.	RESULTS .....	66
5.1.	Qualitative Evaluation .....	66
5.2.	Quantitative Evaluation .....	115
6.	DISCUSSION .....	128
7.	CONCLUSIONS.....	136
8.	REFERENCES .....	145
	CURRICULUM VITAE	

PhD. Thesis

SUMMARY

METAHEURISTIC PANSHARPENING BASED ON SYMBIOTIC ORGANISMS SEARCH  
OPTIMIZATION

Çiğdem ŞERİFOĞLU YILMAZ

Karadeniz Technical University  
The Graduate School of Natural and Applied Sciences  
Geomatics Engineering Graduate Program  
Supervisor: Prof. Dr. Oğuz GÜNGÖR  
2020, 157 Pages

Due to some technical and non-technical reasons, it may not always be possible to obtain remotely-sensed images of high spatial resolution. Pansharpening offers a robust solution for this problem. Pansharpening aims to transfer the spatial detail content of a high spatial resolution panchromatic (PAN) image into a lower spatial resolution multispectral (MS) image, producing an MS image of the same spatial detail quality as the PAN image. A wide range of pansharpening methods have been proposed so far. Of all, the component substitution (CS)-based pansharpening methods draw attention owing to their simplicity and ability to sharpen images. However, the CS-based methods tend to distort the colour features of the input MS images, due to the inconsistencies between the input PAN image and the intensity component computed from the input MS bands. A wide variety of approaches have been developed to estimate the contributions of the input MS bands on the intensity component to minimize the colour distortion. The previous attempts revealed the fact that improving the colour quality causes spatial distortion to a certain degree, which means that more robust solutions are needed to find the best balance between the spectral and spatial quality offered by the CS-based pansharpening methods. Hence, this thesis, for the first time in the literature, proposed to use the symbiotic organisms search (SOS) algorithm, one of the most powerful metaheuristic optimization algorithms, to estimate a weight for each input MS band in order to optimize the intensity components used by the CS-based synthetic variable ratio (SVR) method and a hybrid method that includes both the intensity-hue-saturation (IHS) and discrete wavelet transform (DWT) methods. This thesis also proposed to use the multi-objective version of the SOS algorithm (MOSOS) to find the best compromise between the spatial and spectral fidelity offered by the SVR and IHS-DWT methods. Using the MOSOS algorithm with these methods also enabled the production of pansharpened images of required spectral or spatial quality. The performance of the proposed SOS-SVR, SOS-IHS-DWT, MOSOS-SVR and MOSOS-IHS-DWT methods were qualitatively and quantitatively compared against some of the very popular

pansharpening methods in four test sites with different characteristics. The results showed that the SOS-SVR and SOS-IHS-DWT methods presented a superior colour preservation and spatial detail transfer performance, compared to the other methods used. It was also concluded that the proposed MOSOS-SVR and MOSOS-IHS-DWT methods succeeded in finding the best balance between the spectral and spatial quality; and in producing images of required spectral and spatial quality. These methods were also found to be very successful in producing images of extreme colour and spatial detail quality. The evaluations also revealed that the proposed methods did not show a very good performance on single-sensor input images, but also on multi-sensor input images. They were also found to be able to handle low-contrast images and input images with a high spatial resolution ratio difference. The SOS algorithm does not use any algorithm-specific parameters that may affect the pansharpening performance, which makes it very appropriate for pansharpening process, avoiding analyst intervention.

**Key Words:** Pansharpening, Image fusion, Metaheuristic optimization, Symbiotic organisms search algorithm, Multi-objective optimization

ÖZET

ORTAK YAŞAM ARAMA ALGORİTMASI TABANLI METASEZGİSEL PAN-  
KESKİNLEŞTİRME

Çiğdem ŞERİFOĞLU YILMAZ

Karadeniz Teknik Üniversitesi  
Fen Bilimleri Enstitüsü  
Harita Mühendisliği Anabilim Dalı  
Danışman: Prof. Dr. Oğuz GÜNGÖR  
2020, 157 Sayfa

Bazı teknik ve teknik olmayan nedenlerden dolayı, yüksek uzamsal çözünürlüklü uzaktan algılanmış görüntüler elde etmek her zaman mümkün olamamaktadır. Pan-keskinleştirme işlemi bu problem için etkin bir çözüm sunmaktadır. Pan-keskinleştirmenin temel amacı yüksek uzamsal çözünürlüklü bir pankromatik görüntüdeki uzamsal detayları uzamsal çözünürlüğü daha düşük olan başka bir çok bantlı görüntüye aktararak pankromatik görüntü ile aynı uzamsal detay kalitesine sahip bir çok bantlı görüntü üretmektir. Birçok pan-keskinleştirme yöntemi geliştirilmiştir. Bu yöntemler içinden bileşen değişimi tabanlı yöntemler basit yapıları ve görüntü keskinleştirme yetenekleri sayesinde öne çıkmaktadır. Ancak, bileşen değişimi tabanlı yöntemler, girdi pankromatik görüntü ile girdi çok bantlı görüntünün bantlarından hesaplanan yoğunluk bileşeni arasında tutarsızlıklara neden oldukları için, girdi çok bantlı görüntünün renk yapısını bozma eğilimindedir. Renk bozulmalarını en aza indirmek için, girdi çok bantlı görüntünün her bir bandının yoğunluk bileşenine katkısını kestirebilen çeşitli yaklaşımlar geliştirilmiştir. Önceki girişimler, renk kalitesinin iyileştirilmesinin belirli bir dereceye kadar uzamsal bozulmaya neden olduğu gerçeğini ortaya koymaktadır, bu da bileşen değişimi tabanlı pan-keskinleştirme yöntemlerinin sunduğu spektral ve uzamsal kalite arasındaki en iyi dengeyi bulmak için daha mantıklı çözümlere ihtiyaç duyulduğu anlamına gelmektedir. Bu nedenle, literatürde ilk defa, bu tez kapsamında girdi çok bantlı görüntünün her bir bandına optimum ağırlığın kestirimi için en güçlü metasezgisel algoritmalarından biri olan ortak yaşam arama (SOS) algoritmasının kullanılması önerilmiştir. Önerilen prosedür ile bileşen değişimi tabanlı synthetic variable ratio (SVR) ve intensity-hue-saturation (IHS) ile ayırık wavelet dönüşümü (DWT) yöntemlerini içinde barındıran hibrit bir yöntem tarafından kullanılan yoğunluk bileşenlerinin optimize edilmesi amaçlanmaktadır. Ayrıca, bu tez kapsamında SOS algoritmasının çok amaçlı versiyonu (MOSOS) kullanılarak SVR ve IHS-DWT yöntemlerinin sunduğu renk ve uzamsal detay kalitesi arasındaki en iyi dengenin sağlanması önerilmiştir. MOSOS algoritmasının bu iki pan-keskinleştirme yöntemi ile birlikte kullanılması

arzu edilen renk ve uzamsal detay kalitesine sahip pan-keskinleştirilmiş görüntüler üretilmesine olanak sağlamıştır. Önerilen SOS-SVR, SOS-IHS-DWT, MOSOS-SVR ve MOSOS-IHS-DWT yöntemlerinin performansları çeşitli özelliklere sahip dört test bölgesinde niteliksel ve niceliksel olarak bazı sık kullanılan pan-keskinleştirme yöntemlerinin performansları ile karşılaştırılmıştır. Önerilen SOS-SVR ve SOS-IHS-DWT yöntemlerinin renk kalitesinin korunumunda ve uzamsal detayların aktarımında kullanılan diğer geleneksel yöntemlere göre daha başarılı oldukları sonucuna varılmıştır. Ayrıca, önerilen MOSOS-SVR ve MOSOS-IHS-DWT yöntemlerinin renk ve uzamsal detay kalitesi arasındaki en iyi dengeyi sağlamayı ve istenilen renk ve uzamsal detay kalitesine sahip görüntüler üretmeyi başardığı görülmektedir. Aynı zamanda bu yöntemlerin oldukça iyi renk ve uzamsal detay kalitesine sahip görüntüler üretebildikleri sonucuna varılmıştır. Performans değerlendirmeleri önerilen bütün yöntemlerin sadece tek bir algılayıcı tarafından üretilen görüntülerde değil, farklı algılayıcılar tarafından üretilen görüntülerde de başarılı olduklarını göstermektedir. Ayrıca önerilen yöntemlerin düşük kontrastlı görüntülerde ve aralarında yüksek bir uzamsal çözünürlük farkı bulunan görüntülerde de başarılı oldukları görülmektedir. SOS algoritmasının pan-keskinleştirme performansına etki edebilecek algoritmaya özgü bir parametre kullanmaması bu algoritmanın kullanıcı müdahalesi olmadan pan-keskinleştirme işleminde kullanılabilmesini sağlamaktadır.

**Anahtar Kelimeler:** Pan-keskinleştirme, Görüntü kaynaştırma, Metasezgisel optimizasyon, Ortak yaşam arama algoritması, Çok amaçlı optimizasyon

## LIST OF FIGURES

	<u>Page No.</u>
Figure 1. Electromagnetic spectrum of different remote sensing systems (Eckerstorfer et al., 2016). .....	1
Figure 2. Pansharpener principle .....	4
Figure 3. An example for image pansharpener .....	4
Figure 4. Pansharpener methods used in this thesis .....	7
Figure 5. Brute force search algorithm (left), hill climbing algorithm (right) (Mirjalili and Dong, 2020).....	14
Figure 6. The hill climbing algorithm starting from a different point (Mirjalili and Dong, 2020). .....	15
Figure 7. The hill climbing algorithm using only exploitation operator (Mirjalili and Dong, 2020). .....	16
Figure 8. The simulated annealing algorithm using the exploitation and exploration operators (Mirjalili and Dong, 2020). .....	17
Figure 9. Search space (left) and solution space (right) .....	19
Figure 10. Pareto optimal solution set (left) and Pareto front (right).....	21
Figure 11. General working principle of population-based metaheuristic algorithms..	26
Figure 12. Generation of a new ecosystem .....	49
Figure 13. Test sites.....	50
Figure 14. UIQI, IW-SSIM, CC, SSIM and SR-SIM values computed for thirty pansharpener images produced for the site 1 .....	54
Figure 15. SERGAS values obtained for thirty pansharpener images produced for the site 1 .....	54
Figure 16. Flowchart for the SOS-SVR and SOS-IHS-DWT methods .....	56
Figure 17. Flowchart for the MOSOS-SVR and MOSOS-IHS-DWT methods.....	63
Figure 18. BRV results for the test sites.....	67
Figure 19. MIHS results for the test sites.....	68
Figure 20. HPF results for the test sites.....	69
Figure 21. BSDS results for the test sites .....	70
Figure 22. PCA results for the test sites .....	71
Figure 23. GS results for the test sites.....	72

Figure 24.	HCS results for the test sites .....	73
Figure 25.	SFIM results for the test sites.....	74
Figure 26.	LMM results for the test sites .....	75
Figure 27.	ATWT results for the test sites .....	76
Figure 28.	AWLP results for the test sites.....	77
Figure 29.	CB results for the test sites.....	78
Figure 30.	DWT results for the test sites.....	79
Figure 31.	IHS-DWT results for the test sites .....	80
Figure 32.	SOS-SVR results for the test sites .....	81
Figure 33.	SOS-IHS-DWT results for the test sites .....	82
Figure 34.	MOSOS-SVR results for the site 1 .....	83
Figure 35.	MOSOS-SVR results for the site 2 .....	84
Figure 36.	MOSOS-SVR results for the site 3 .....	85
Figure 37.	MOSOS-SVR results for the site 4.....	86
Figure 38.	MOSOS-IHS-DWT results for the site 1 .....	87
Figure 39.	MOSOS-IHS-DWT results for the site 2 .....	88
Figure 40.	MOSOS-IHS-DWT results for the site 3 .....	89
Figure 41.	MOSOS-IHS-DWT results for the site 4.....	90
Figure 42.	Zoomed-in BRV results for the test sites.....	91
Figure 43.	Zoomed-in MIHS results for the test sites .....	92
Figure 44.	Zoomed-in HPF results for the test sites.....	93
Figure 45.	Zoomed-in BDSO results for the test sites .....	94
Figure 46.	Zoomed-in PCA results for the test sites .....	95
Figure 47.	Zoomed-in GS results for the test sites .....	96
Figure 48.	Zoomed-in HCS results for the test sites .....	97
Figure 49.	Zoomed-in SFIM results for the test sites.....	98
Figure 50.	Zoomed-in LMM results for the test sites.....	99
Figure 51.	Zoomed-in ATWT results for the test sites.....	100
Figure 52.	Zoomed-in AWLP results for the test sites.....	101
Figure 53.	Zoomed-in CB results for the test sites.....	102
Figure 54.	Zoomed-in DWT results for the test sites .....	103

Figure 55.	Zoomed-in IHS-DWT results for the test sites .....	104
Figure 56.	Zoomed-in SOS-SVR results for the test sites.....	105
Figure 57.	Zoomed-in SOS-IHS-DWT results for the test sites.....	106
Figure 58.	Zoomed-in MOSOS-SVR results for the site 1 .....	107
Figure 59.	Zoomed-in MOSOS-SVR results for the site 2 .....	108
Figure 60.	Zoomed-in MOSOS-SVR results for the site 3 .....	109
Figure 61.	Zoomed-in MOSOS-SVR results for the site 4 .....	110
Figure 62.	Zoomed-in MOSOS-IHS-DWT results for the site 1 .....	111
Figure 63.	Zoomed-in MOSOS-IHS-DWT results for the site 2 .....	112
Figure 64.	Zoomed-in MOSOS-IHS-DWT results for the site 3 .....	113
Figure 65.	Zoomed-in MOSOS-IHS-DWT results for the site 4 .....	114
Figure 66.	Average CCs computed from the user-defined polygons for the site 1.....	120
Figure 67.	Average CCs computed from the user-defined polygons for the site 2.....	121
Figure 68.	Average CCs computed from the user-defined polygons for the site 3.....	122
Figure 69.	Average CCs computed from the user-defined polygons for the site 4.....	123
Figure 70.	Average spectral and spatial quality scores calculated for all test sites.....	143

## LIST OF TABLES

	<u>Page No.</u>
Table 1.	Characteristics of the test sites and input images used ..... 51
Table 2.	Optimum band weights estimated by the SOS-SVR method ..... 53
Table 3.	Optimum band weights estimated by the SOS-IHS-DWT method ..... 57
Table 4.	Optimum band weights estimated by the MOSOS-SVR method..... 59
Table 5.	Optimum band weights estimated by the MOSOS-IHS-DWT method..... 61
Table 6.	Optimum weights estimated by the MOSOS-IHS-DWT method for the approximation components computed from the intensity components and histogram-matched PAN images ..... 62
Table 7.	Mathematical definitions of the spectral quality evaluation metrics ..... 64
Table 8.	Mathematical definitions of the spatial quality evaluation metrics ..... 65
Table 9.	Spectral quality evaluation metric values for the site 1 ..... 115
Table 10.	Spectral quality evaluation metric values for the site 2 ..... 116
Table 11.	Spectral quality evaluation metric values for the site 3 ..... 117
Table 12.	Spectral quality evaluation metric values for the site 4 ..... 118
Table 13.	Spatial quality evaluation metric values for the site 1 ..... 124
Table 14.	Spatial quality evaluation metric values for the site 2 ..... 125
Table 15.	Spatial quality evaluation metric values for the site 3 ..... 126
Table 16.	Spatial quality evaluation metric values for the site 4 ..... 127
Table 17.	Spectral quality scores given for the site 1 ..... 138
Table 18.	Spectral quality scores given for the site 2 ..... 139
Table 19.	Spectral quality scores given for the site 3 ..... 139
Table 20.	Spectral quality scores given for the site 4 ..... 140
Table 21.	Spatial quality scores given for the site 1 ..... 140
Table 22.	Spatial quality scores given for the site 2 ..... 141
Table 23.	Spatial quality scores given for the site 3 ..... 141
Table 24.	Spatial quality scores given for the site 4 ..... 142

## LIST OF ABBREVIATIONS

ABC	Artificial Bee Colony
ACO	Ant Colony Optimization
ALI	Advanced Land Imager
ATWT	à trous Wavelet Transformation
AWL	Additive Wavelet Luminance
AWLP	Additive Wavelet Luminance Proportional
BE	Bee Algorithm
BDS	Band Dependent Spatial Detail
BRV	Brovey
CB	Criteria-Based
CC	Correlation Coefficient
CoDE	Composite Differential Evolution
CS	Component Substitution
DE	Differential Evolution
DWFT	Discrete Wavelet Frame Transform
DWT	Discrete Wavelet Transform
EMS	Electromagnetic Spectrum
EP	Evolutionary Programming
ERGAS	Erreur Relative Globale Adimensionnelle de Synthèse
ES	Evolution Strategy
ETM	Enhanced Thematic Mapper
FA	Firefly Algorithm
FFT	Fast Fourier transform
GA	Genetic Algorithm
GLP	Generalized Laplacian Pyramid
GS	Gram-Schmidt
HCS	Hyperspherical Colour Space
HPF	High-Pass Filtering
HS	Hyperspectral
Ifov	Instantaneous Field of View

IHS	Intensity-Hue-Saturation
IHS-DWT	IHS and DWT Hybrid Method
IW-SSIM	Information Content Weighted SSIM
LiDAR	Light Detection and Ranging
LMM	Local Mean Matching
MIHS	Modified IHS
MOSOS	Multi-objective SOS Algorithm
MOSOS-IHS-DWT	MOSOS-based IHS-DWT Method
MOSOS-SVR	Multi-objective SOS-based SVR Method
MRA	Multiresolution Analysis
MS	Multispectral
MSE	Mean Square Error
MTF	Modulation Transfer Function
MTF-GLP	GLP with MTF Matched Filter
MTF-GLP-HPM	MTF-GLP with High-Pass Modulation
NDVI	Normalized Difference Vegetation Index
NSGA-II	Non-Domination Sorting Genetic Algorithm-II
PAN	Panchromatic
PBA	Particle Bee Algorithm
PCA	Principal Component Analysis
PSO	Particle Swarm Optimization
RMSE	Root Mean Square Error
SAM	Spectral Angular Mapper
SAR	Synthetic Aperture Radar
SB	Statistics-Based
SCC	Spatial Correlation Coefficient
SERGAS	Spatial ERGAS
SFIM	Smoothing Filter-based Intensity Modulation
SID	Spectral Information Divergence
SOS	Symbiotic Organisms Search
SOS-IHS-DWT	SOS-based IHS-DWT Method
SOS-SVR	SOS-based SVR Method
SRMSE	Spatial RMSE

SR-SIM	Spectral Residual Based Similarity
SSIM	Structural Similarity Index
SVR	Synthetic Variable Ratio
TIR	Thermal Infrared
UAS	Unmanned Aerial System
UIQI	Universal Image Quality Index
VIR	Visible and Near Infrared



# 1. INTRODUCTION

## 1.1. Image Fusion

In recent years, the advances in Earth observation satellites have enabled more accurate and comprehensive monitoring of the objects on the surface of the Earth. Imageries acquired with more sophisticated satellites do not only allow for better discrimination of the features on the ground, but also provide more accurate spatial information for various applications.

Sensors are designed to obtain significant information from received signals. The structure of the signals is affected by the materials on the ground, i.e. their shape and structure. Depending on the structure of the surface, electromagnetic energy is reflected, absorbed and emitted in different ways. Remote sensing sensors differ from one another in the way they emit the received waves. The active sensors such as light detection and ranging (LiDAR) and synthetic aperture radar (SAR) etc. emit their own waves, whereas the passive sensors such as visible and near infrared (VIR) or thermal infrared (TIR) emit the radiation and reflections of illuminated surfaces. The sun is the energy sources for the passive sensors (Pohl and van Genderen, 2016). Different sensors record the energy from different portions of the electromagnetic spectrum (EMS).

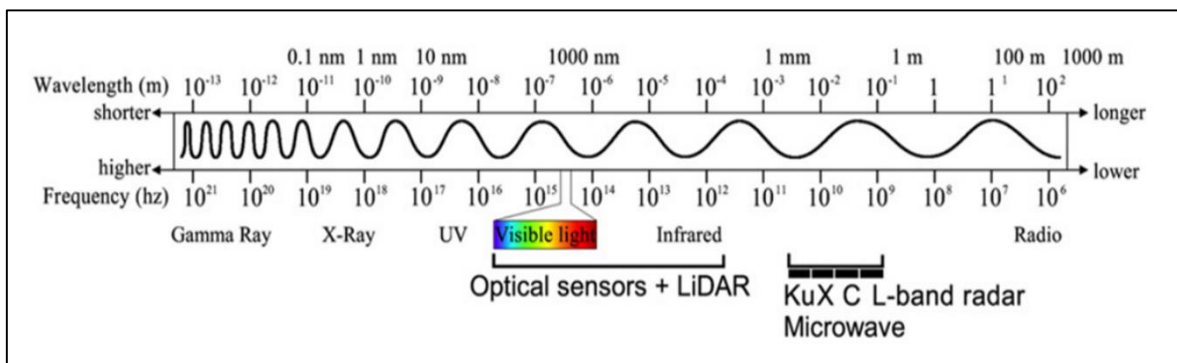


Figure 1. Electromagnetic spectrum of different remote sensing systems (Eckerstorfer et al., 2016).

Figure 1 depicts the portions of the EMS. As seen from the figure, LiDAR sensors record the energy from the visible and near infrared portions of the spectrum, whereas radar sensors are capable of recording the radiation from the microwave region (Eckerstorfer et al., 2016). The sensors sensitive to the visible and near-infrared portions of the EMS benefits from the radiation of the sun that is reflected from the surface of the Earth. The optics of the sensors record the sum of the reflected energy, ground emissions and the path radiance, which are then converted into electrical signals (Pohl and van Genderen, 2016).

The ground resolution and image contrast are the two factors that affect the detectability of the objects with satellite imagery. The spectral resolution of the imageries plays also a significant role in the specification and interpretability of the objects (Pohl and van Genderen, 2016). Spectral resolution refers to the width of the regions of the electromagnetic spectrum that can be recorded by satellite sensors. The narrower spectrum regions, the higher spectral resolution. In other words, images of a large number of spectral bands can be said to have a high spectral resolution. A better discrimination among ground features can be achieved through the use of high spectral resolution images. The spatial resolution of the imageries to be used is also another factor that affects the success in the observation of the ground features. The spatial resolution defines the size of the smallest land cover feature that can be observed by the human eye. Images of higher spatial resolution do not only provide a better visual appearance, but also offer more accurate planimetric measures for various purposes. Another resolution type in remote sensing is the temporal resolution, which refers to how frequent imageries are acquired for a specific terrain.

A wide range of recent engineering applications require the use of high spectral and spatial resolution imageries. However, it may not always be possible to obtain such imageries due to some technical and non-technical limitations. The amount of the energy recorded by the sensors is dependent on both the IFOV (instantaneous field of view) of the sensor and its capability to collect the radiation over a certain spectral bandwidth. There is an inverse proportion between the IFOV of a sensor and the spatial resolution of the acquired image. Since the sensors with larger IFOVs record the radiation from a larger area on the surface of the Earth, larger IFOVs lead to a lower spatial resolution. To avoid this, the radiation is recorded over a broader spectral bandwidth, increasing the amount of the radiation that reaches the sensor. Increasing the sensor's collection capability and reducing the IFOV enable the preservation of the spatial resolution of the imagery (Pradhan, 2005). This is the reason that the panchromatic images have a better spatial resolution than the

multispectral images produced by the same sensor (Gungor, 2008). Such reasons may limit the access to high spectral and spatial resolution images at any time. Hence, the researchers have sought for new alternatives to produce their own high spectral and spatial resolution imageries. Image fusion is a widely-accepted method used to solve this problem.

Image fusion is a common tool utilized to combine information gathered from multi-source imageries. The main objective of image fusion is to combine the disparate and complementary data to improve the useful information content obtained by the source data. This also ensures the increase in the reliability of the interpretation. Image fusion integrates the information obtained from images of different spectral, spatial and temporal resolutions to achieve fused data that is more informative than the input images (Pohl and van Genderen, 2016). To date, image fusion has been applied for numerous purposes such as stereotactic radiotherapy and radiosurgery treatment planning (Kooy et al., 1994), concealed weapon detection (Zhang and Blum, 1997), object detection (Broussard et al., 1999), logo watermarking (Kundur and Hatzinakos, 2004), face recognition (Singh et al., 2004), context enhancement and video surrealism (Raskar et al., 2005), in situ damage localization in plates (Michaels and Michaels, 2007), enhanced visualization (Piella, 2009), sharpening remote sensing images (Ehlers et al. 2010), change detection in SAR images (Gong et al., 2011), feature extraction (Kang et al., 2013), archaeological interpretative mapping (Verhoeven et al., 2016), illumination-invariant palmprint recognition (Lu et al., 2017), land cover classification (Chen et al., 2017), weed detection (Barrero and Perdomo, 2018) and radiological identification of decedents (Gascho et al., 2018)

### **1.1.1. Pansharpening**

Pansharpening is a special case of image fusion, where the spatial features of a high-resolution panchromatic (PAN) image are combined with the spectral features of a lower-resolution multispectral (MS) image with the aim to produce an MS image of high spatial resolution. Figure 2 illustrates the idea behind the pansharpening theory.

Figure 2 describes the pansharpening process of an MS image with a PAN image with four-times better spatial resolution than the MS image. As demonstrated in Figure 2, the pansharpening process enables the generation of MS images with the spatial resolution of the input PAN image. The output image contains approximately the same amount of spatial content as the input PAN image.

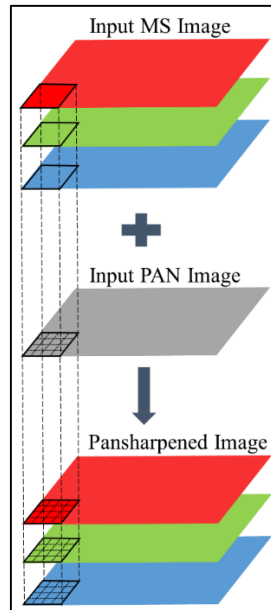


Figure 2. Pansharpening principle

A special case of pansharpening is when two optical images are fused. As known, earlier platforms such as Landsat Enhanced Thematic Mapper (ETM)+ and SPOT 2-5 offered a scale ratio of 2, which means that the spatial resolution of the PAN image provided by these platforms was two times better than that of the MS image offered by these systems. However, more advanced satellites such as WorldView-2/3, IKONOS, QuickBird and GeoEye-1/2 offer a scale ratio of 4. This, of course, enables the analysts to produce higher quality images through pansharpening. Another special case of pansharpening is when a high-resolution optical image is fused with a lower-resolution SAR data or vice versa (Pohl and van Genderen, 2016). This type of pansharpening is not as common as the first one. Figure 3 shows an example for image pansharpening.

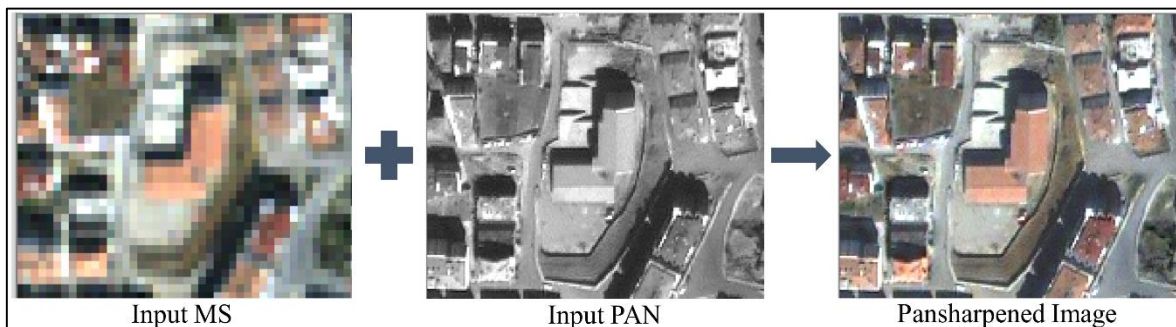


Figure 3. An example for image pansharpening

A successful pansharpening procedure should retain the colour characteristics of the input MS image whilst injecting the spatial structure information. There are several factors that affect the performance of the pansharpening process (Yılmaz, 2012; Serifoglu Yılmaz et al., 2020):

- The spectral range of the input MS and PAN data should match for a better pansharpening performance. This is the main reason that single-sensor input images generally achieve a better colour preservation. For example, pansharpening an IKONOS MS image with an IKONOS PAN image tend to keep the colour characteristics. On the other hand, a large amount of colour distortion is expected when pansharpening a Hyperion hyperspectral (HS) image with an Advanced Land Imager (ALI) PAN image as these data cover different portions of the electromagnetic spectrum. If multi-sensor input images are used for pansharpening, then a histogram matching between the input images prior to pansharpening may resemble the wavelength interval of these images, reducing colour deterioration.
- The atmospheric conditions at the moment when the input images are acquired should be compatible with each other for a better colour preservation. If this is not the case, then necessary atmospheric correction procedures should be employed on the input images. If necessary, input images should be corrected radiometrically to ensure a colour variety of high quality.
- If the acquisition dates of the input MS and PAN data are not close to each other, then inconsistent pansharpening results are likely to be obtained as the details of one image may not be in the other one.
- The input images should be co-registered for a better visual appearance and colour quality. If the input data are not registered to the same projection and coordinate system, then these images may not cover the same area on the surface of the Earth, resulting in misaligned pansharpening results. Even if both images to be fused do not have the same coordinate system, they should be completely overlapping for a better spatial consistency.
- It is worth noting that the size (i.e. number of rows and columns) of the input images should be the same when performing pansharpening. To ensure this, prior to pansharpening, the size of the input MS image is matched to that of the input PAN image, which is called upsampling. Upsampling is conducted with respect to a

resampling method such as nearest neighbour interpolation, bilinear interpolation, bicubic interpolation etc.

- The analyst's pansharpening experience plays also a vital role in the performance of the pansharpening process. The analyst should make the purpose of the pansharpening clear and specify the correct pansharpening technique for the application.

A lot of pansharpening methods have been reported to date, some of which tend to retain the spectral features of the input MS data whilst some tend to produce crisp images (Yilmaz et al., 2020). In general, pansharpening approaches can be categorized into three classes as component substitution (CS)-based, multiresolution analysis (MRA)-based and statistics-based (SB) methods.

The CS-based methods project the input MS data onto another domain, in which it is more likely to separate the spatial features from the colour features in different components. The PAN image is swapped by the component that comprises the spatial structure. An inverse transform into the original domain results in the pansharpened image (Ghassemian, 2016; Serifoglu Yilmaz et al., 2019). The CS-based pansharpening techniques perform well if the input images are highly correlated. If this is not the case, prior to pansharpening, a histogram matching may be conducted between the PAN image and the component retaining the spatial features in order to match the colour contents of these images, avoiding colour deterioration (Ghassemian, 2016). The CS-based methods are easy-to-implement and are famous for their success in sharpening the images. However, they are expected to deteriorate the colour features of the MS data (Serifoglu Yilmaz et al., 2019; Ghahremani et al., 2019). The most famous CS-based pansharpening techniques include the Brovey (BRV) (Hallada and Cox, 1983), Synthetic Variable Ratio (SVR) (Munechika et al., 1993; Zhang, 1999), Intensity-Hue-Saturation (IHS) (Chen et al., 2003; Ling et al., 2007), modified IHS (MIHS) (Siddiqui, 2003), Gram-Schmidt (GS) (Laben and Brower, 2000), Principal Component Analysis (PCA) (González-Audícana et al., 2004; Shahdoosti and Ghassemian, 2016), Hyperspherical Colour Space (HCS) (Padwick et al., 2010) and Band Dependent Spatial Detail (BDSD) (Garzelli et al., 2008).

The MRA-based pansharpening methods employ multiresolution transforms (i.e. wavelet, curvelet etc.) on the input PAN data to extract its spatial structure (Gogineni and Chaturvedi, 2018; Serifoglu Yilmaz et al., 2019), which is then integrated into the input MS image (Xing et al., 2018). Compared to the CS-based techniques, the MRA-based techniques offer images of higher colour fidelity. The biggest disadvantage of the MRA-based

techniques is that they are expected to deteriorate the spatial fidelity of the PAN data (Gogineni and Chaturvedi, 2018; Serifoglu Yilmaz et al., 2019). An accurate co-registration of the input data is necessary to achieve a better spatial fidelity with the MRA-based methods. Otherwise, significant spatial distortion becomes inevitable. The most prevalent MRA-based methods include the Discrete Wavelet Transform (DWT) (Li et al., 2002; Amolins et al., 2007), Additive Wavelet Luminance Proportional (AWLP) (Otazu et al., 2005), à trous Wavelet Transformation (ATWT) (Nunez et al., 1999; Garzelli and Nencini, 2006), Generalized Laplacian Pyramid (GLP) with Modulation Transfer Function (MTF) matched filter (MTF-GLP) (Aiazzi et al., 2006) and MTF-GLP with High-Pass Modulation (MTF-GLP-HPM) (Vivone et al., 2014a; 2014b).

The SB techniques, as the name implies, employ some statistics-based procedures to keep the colour characteristics after pansharpening. It is very challenging for these techniques to find the best balance between the colour and spatial structure fidelity. Compared to many other pansharpening techniques, the SB methods are easy-to-use and do not rely on complicated computations. The Local Mean Matching (LMM) (de Béthune et al., 1997), High-Pass Filtering (HPF) (Schowengerdt, 1980; Witharana et al., 2016), Smoothing Filter-based Intensity Modulation (SFIM) (Liu, 2000) and Criteria-Based (CB) (Gungor, 2008) methods are among the most popular members of the SB pansharpening techniques family. Figure 4 categorizes the pansharpening methods used in this thesis.

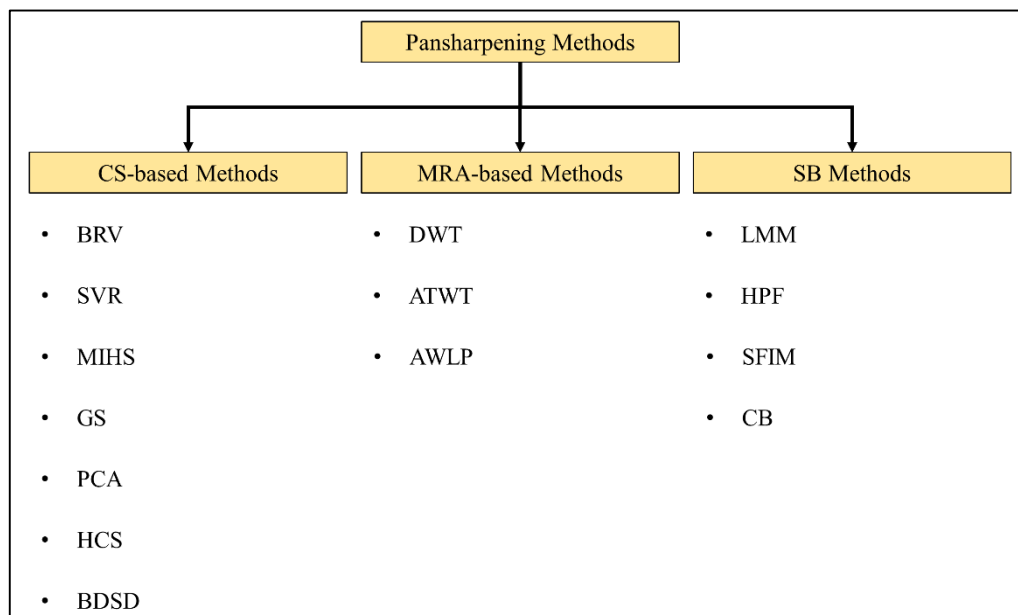


Figure 4. Pansharpening methods used in this thesis

Apart from these, some hybrid pansharpening methods have also been introduced to make use of the advantages of at least two different methods. For example, Nunez et al., (1999) used a pansharpening technique that used the wavelet and IHS transforms. Cao et al., (2003) used a pansharpening technique, which included both the wavelet transform and PCA transform. Another example is that Chibani (2006) combined the BRV and à trous wavelet transform-based methods. Ehlers (2005) and Klonus (2008) used the Ehlers method, where the IHS transform method was combined with the fast Fourier transform (FFT). El-Samie et al., (2012) indicated that the DWT and Discrete Wavelet Frame Transform (DWFT) techniques can be combined with the IHS transform method. In recent years, researchers have also focused on pansharpening through deep learning (Huang et al., 2015; Masi et al., 2016; Palsson et al., 2017; Wei et al., 2017; Dian et al., 2018; Cai et al., 2018; Song et al., 2018), sparse representation (Wang et al., 2014; Vicinanza et al., 2014; Yin, 2015; Chen et al., 2018; Yin, 2019; Fei et al., 2019; Wang et al., 2019) and metaheuristic algorithms (Niazi et al., 2016; Khademi and Ghassemian, 2017; Chen et al., 2019; Serifoglu Yilmaz et al., 2019; 2020; Yilmaz et al., 2019; 2020).

Best pansharpening results are obtained when the contributions of the input images to the pansharpened image are specified accurately, which makes pansharpening a challenging task. It is important to note that all pansharpening methods proposed so far are expected to deteriorate the spectral quality of the MS data or spatial detail quality of the PAN data to some degree. This leads us to the fact there is no perfect pansharpening method (Serifoglu Yilmaz et al., 2020), which has encouraged the analysts to develop enhanced pansharpening methods. In recent years, a limited number of studies utilized the metaheuristic algorithms to identify the contributions of the input images to the pansharpened image.

Xiao et al., (2015) introduced a variational pansharpening method, which aimed to use the composite differential evolution (CoDE) algorithm to optimize an objective function that was formed by combining two pansharpening quality metrics including the root mean square error (RMSE) and a spatial quality evaluation metric that measured the edge information quality of the scene. Niazi et al., (2016) proposed to improve the IHS-based pansharpening method by using the GA. The proposed framework identified the vegetated areas through the normalized difference vegetation index (NDVI). The relationship between the red and near-infrared bands were used to enhance the green band. An intensity component was then generated as a linear combination of the input MS bands. The optimum weights for the MS bands were estimated by the GA. The proposed scheme was found to yield a good colour

and spatial detail quality. Khademi and Ghassemian (2017) utilized a multi-objective metaheuristic method to enhance a CS-based pansharpening framework. The proposed framework employed the non-dominated sorting genetic algorithm II (NSGA-II) to optimize the objective functions inverse of the correlation coefficient (CC) and weighted sum of the Erreur Relative Globale Adimensionnelle de Synthèse (ERGAS). The authors concluded that using a multi-objective metaheuristic approach enabled the achievement of a good balance between the spectral and spatial structure fidelity of the pansharpened images. Azarang and Ghassemian (2017) improved a CS-based pansharpening technique with the help of the PSO algorithm. The proposed method first calculated a weight for each input MS band using the least squares method to generate an intermediary detail map. A linear combination of the image gradients of the input data were then used to refine the detail map. The weights of the gradients were determined by the PSO algorithm. The ERGAS metric was used as the fitness criterion of the PSO. Chen and Zhang (2017) presented an adaptive IHS-based pansharpening method that optimized the pansharpening results using an evolutionary algorithm, whose objective function considered the relationship between the pansharpened image and input images. This relationship was identified assuming that a linear combination of the optimum pansharpened bands could result in the input PAN image and that the input MS image could be obtained by degrading the optimum pansharpened bands. The presented scheme was found to result in pansharpened images of high quality. Chen et al., (2019) introduced a multi-objective IHS-based pansharpening scheme, which relied on using the CoDE algorithm for the optimization of two objective functions that focused on preserving the colour quality and transferring the spatial details. Serifoglu Yilmaz et al., (2019) proposed to improve the performance of the CS-based SVR pansharpening method by using the SOS optimization algorithm. The proposed method used the SOS algorithm to estimate the weights for MS bands to optimize the intensity component used by the SVR technique for a better colour preservation. The fitness criterion of the SOS algorithm was the RMSE. The authors concluded that the proposed method produced images of superior colour and spatial structure fidelity, compared to the other pansharpening methods used. Yilmaz et al., (2019) presented a pansharpening method, which aimed to optimize the SVR pansharpening result with the GA. The RMSE was the fitness criterion of the GA. The results showed that the proposed technique did not only preserve the colour characteristics, but also managed to transfer the spatial structure information with a high success. Yilmaz et al., (2020) utilized the GA to improve the performance of another CS-

based pansharpening method, GS. The presented method optimized the intensity component used by the GS method. The RMSE was the fitness criterion of the GA. The authors concluded that the proposed framework achieved to produce crisp images, preserving the colour characteristics. Serifoglu Yilmaz et al., (2020) proposed a SOS-based scheme to improve the colour preservation capability of a hybrid pansharpening method, which included both the CS-based IHS method and MRA-based techniques DWT and DWFT. The ERGAS metric was employed as the fitness criterion of the SOS algorithm. The proposed scheme was found to be very successful in estimating the optimum band weights that produced the optimum intensity component used by the hybrid pansharpening method. This procedure managed to preserve the colour features of the MS data and inject the spatial structure content of the PAN data.

## **1.2. Motivation**

### **1.2.1. Research Questions**

As mentioned before, this thesis focused on pansharpening methods as three categories, namely the CS-based, MRA-based and SB. Each category has its own advantages and disadvantages. This thesis focused on improving the performances of the CS-based methods, which offer a good spatial detail quality at the expense of significant colour distortion. Hence, the first main research question of this thesis is: ‘What can be done to improve the colour preservation capability of the CS-based pansharpening methods?’

As known, the pansharpening approaches developed so far focus either on keeping the colour features or producing the sharpest image possible at the cost of colour deterioration. This reveals the fact that finding the optimum balance between the colour and spatial detail quality is very challenging. Hence, the second main research question is: ‘What can be done to achieve the optimum balance between the colour and spatial detail quality of the pansharpened images?’

### **1.2.2. Objectives of the Thesis**

The main objectives of this thesis are to;

- Automate the pansharpening process to avoid user intervention, which may result in greater colour or spatial detail distortion than it should be.
- Propose to use the algorithm-specific parameter-free SOS metaheuristic search algorithm to enhance the colour preservation performance of the conventional CS-based SVR pansharpening method without deteriorating the spatial fidelity.
- Propose to improve the spectral quality preservation and spatial structure transfer capability of a hybrid pansharpening method through the use of the SOS algorithm.
- Propose to use the multi-objective SOS (MOSOS) metaheuristic algorithm to find the best compromise between the spatial and colour fidelity of the CS-based SVR pansharpening results and the results of a hybrid pansharpening scheme that includes both an MRA-based method and a CS-based method.
- Qualitatively and quantitatively compare the colour and spatial detail fidelity of the images obtained by the proposed pansharpening frameworks against those of the most popular CS-based, MRA-based and SB pansharpening techniques in the literature.

### **1.2.3. Method**

In recent years, the researchers mainly used the metaheuristic algorithms to improve the performances of the CS-based techniques due to their simplicity and efficiency. However, the used metaheuristic approaches utilize parameters that need to be fine-tuned by the users. Hence, it is not so reasonable to use metaheuristic algorithms that relies on user intervention to optimize the performances of the pansharpening methods that already use parameters needed to be fine-tuned to achieve optimum pansharpening results. On the other hand, the CS-based pansharpening techniques suffer from colour deterioration. This is because there is not a robust protocol for these methods to compute the component comprising the spatial structure of the scene. This, of course, leads to statistical differences between this component and input PAN image, causing colour distortion. Hence, this thesis proposed to use the SOS algorithm to optimize the component that includes the spatial details of the scene. It was also proposed to use the MOSOS algorithm to achieve the optimum balance between the spectral and spatial quality of the CS-based pansharpened images, and images obtained from a hybrid pansharpening approach including a CS-based method and an MRA-based method. The proposed methods, which were encoded in MATLAB

environment, were tested on four test sites acquired by different satellites and a digital camera mounted on an Unmanned Aerial System (UAS).

### **1.3. Structure of the Thesis**

- Section 2 introduces the pansharpening methods used in this thesis to compare against the proposed methods.
- Section 3 presents theoretical background for the SOS algorithm and its multi-objective version, i.e. MOSOS algorithm.
- Section 4 introduces the test sites and the data used in this thesis. In addition, this section introduces the proposed SOS-based SVR (SOS-SVR), SOS-based IHS-DWT (SOS-IHS-DWT), MOSOS-based SVR (MOSOS-SVR) and MOSOS-based IHS-DWT (MOSOS-IHS-DWT) methods. This section also provides the mathematical definitions of the spectral and spatial quality evaluation metrics used to compare the performances of all pansharpening methods used in this thesis.
- Section 5 presents the qualitative and quantitative evaluation results for the images produced by all the pansharpening methods used.
- Section 6 discusses the pansharpening results in detail.
- Section 7 presents the conclusions drawn from this thesis.

### **1.4. Optimization**

The optimization algorithms are powerful search algorithms designed to find the optimal solution among all possible candidate solutions in order to maximize or minimize one or more objectives. Since their first introduction, they have been very popular in the field of artificial intelligence (Mirjalili and Dong, 2020). The optimization is used by numerous disciplines in many applications, from engineering design to financial markets, from our daily activities to holiday planning, from computer science to industrial applications, and so on.

In the past, the designing applications in computational engineering were conducted experimentally (Klockgether and Schwefel, 1970), which means that the models designed in the experimental process were real physical models. For example, a real aircraft or its

prototype had to be placed in very large wind tunnels for its aerodynamic controls (URL-1). However, this procedure was a very slow and costly process (Mirjalili, 2019).

After the development of computers, engineers began to simulate their models on computers, and thus had the chance to analyse the system in many ways. This revolutionary innovation met the need for engineers to create real physical models, reducing the time and cost needed. Thanks to computer simulations, which allowed the engineers to better observe and analyse, problems could be better understood and appropriate design parameters that are specific to the models could be obtained. However, despite all these developments, the parameters developed for the models and directly affecting the design were still entered manually (Mirjalili, 2019).

Afterwards, people started to determine the optimum design parameters of the current problem with the help of the computational or optimization algorithms they developed on the computers. In this way, computers were able to determine the required parameter values with limited human intervention (Mirjalili, 2019). The fact that this need was met successfully in this way played an important role in the spread of different optimization algorithms.

Optimization algorithms can be classified in many ways. One of the most common classifications accepted in the literature is to classify the methods into two groups as deterministic and stochastic. The deterministic methods rely on calculus and can be gradient search methods or second-order methods (Du and Swamy, 2016). These methods have yielded successful results in solving many problems. The most deterministic methods are uninformed methods, which concern only with the instructions of the problem (i.e. problem definition), not with the quality of the solutions obtained. Therefore, they have no information about their distance to the goal. The uninformed methods are exact algorithms that guarantee to find the best solution. Every step of such algorithms is equally good. However, as the size of the problem increases, their computing abilities decrease and they slow down. The breadth-first search, depth-first search and brute-force search methods are among the most popular examples of the uninformed methods, which are also known as blind search methods (Mirjalili and Dong, 2020).

Unlike the deterministic methods, the stochastic methods make use of various random rules to reach a reasonable solution (Yang, 2011). The stochastic algorithms do not need any derivation and are also not gradient-based. Most of these methods are informed methods. Unlike the uninformed methods, the informed search methods utilize an additional

information that indicates the approximate distance to the objective. Such algorithms are often called heuristic search algorithms (Kanal and Kumar, 2012). The heuristic algorithms are able to consciously explore different parts of the search space, making educated decisions, which enables them to take better or worse steps each time, unlike the uninformed methods (Mirjalili et al., 2020). Instead of searching the entire search space, these algorithms allow for a conscious search, greatly reducing the computational load and giving faster results, no matter the size of the problem. This, of course, has made them quite popular. However, the heuristic search algorithms do not guarantee the best results. Instead, they give a reasonable result that is closest to the best in a short time. The greedy search (Resende and Ribeiro, 2003) and hill climbing (Yuret and De La Maza, 1993) algorithms are some of the most popular examples for the heuristic algorithms.

The literature also reports hybrid algorithms, that is, they can show both deterministic and stochastic features. For example, the hill climbing algorithm, previously classified as a stochastic method, will give the same result each time if it is started from the same starting point. However, if there is randomness at the starting point, then the final result may change. However, since there is a random component in hybrid methods, these methods are often classified as stochastic algorithms in the optimization literature (Yang, 2011).

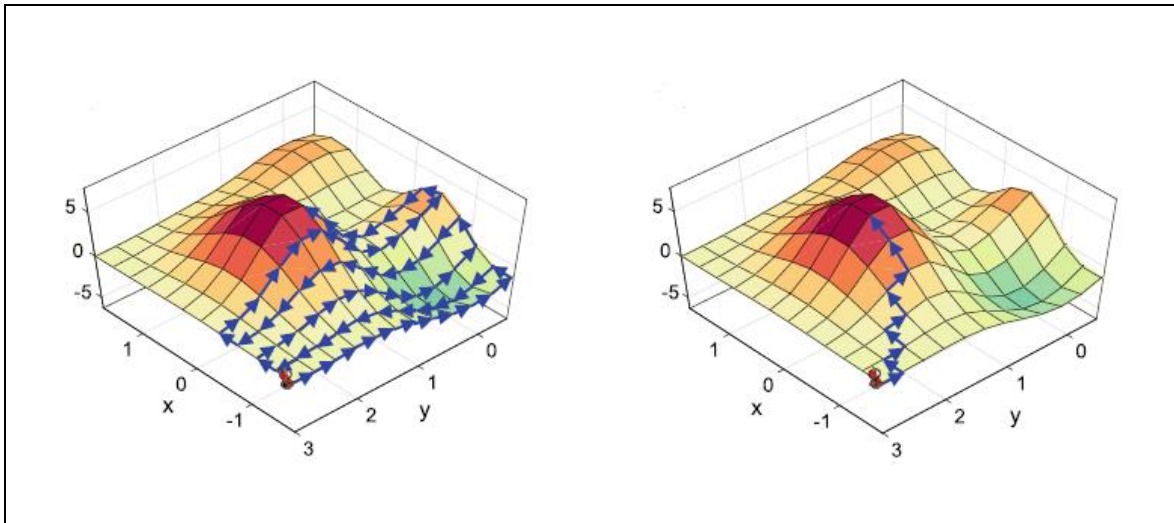


Figure 5. Brute force search algorithm (left), hill climbing algorithm (right) (Mirjalili and Dong, 2020).

Figure 5 explains the informed and uninformed search algorithms by an example. The problem illustrated in this figure is to find the highest point using a wheeled robot in the

region given. The given region is divided into grids with 144 points, as shown in the figure. The arrows in the figure show the route followed by the wheel robot while searching for the highest point. Although the uninformed brute force method finds the highest point (see Figure 5(left)), in order to determine whether this point is the targeted point, it has to go all the way to the ending point and compare each point with the highest point it has found so far (Mirjalili and Dong, 2020). Thus, the method ensures to find the best solution in any region, but this will bring a lot of computational burden.

Figure 5(right) shows an example for the informed (i.e. heuristic) hill climbing algorithm. In this case, the wheeled robot evaluates all its neighbours before taking a step, and then selects the highest point. In this way, the best solution can be achieved in only nine steps. However, the success here largely depends on the correct selection of the starting point. For example, when the same method is applied by starting from a different point as shown in Figure 6, the peak reached by the wheeled robot is not the highest peak of the region (Mirjalili and Dong, 2020). This shows that, although it is quite faster than the brute force algorithm, the performance of the heuristic hill climbing algorithm changes with the differentiation of the starting point.

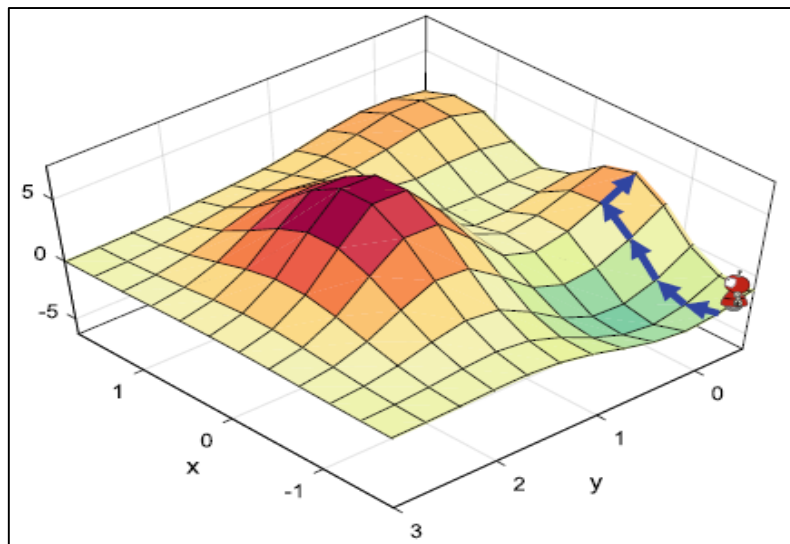


Figure 6. The hill climbing algorithm starting from a different point (Mirjalili and Dong, 2020).

To sum up, the heuristic algorithms can perform well within a reasonable time frame. This is because the algorithm is able to choose the most reasonable option before taking a

step. Also, the ability to make educated decisions in this way significantly reduces the size of the search space. However, these methods cannot be considered reliable in finding the best possible result (Mirjalili and Dong, 2020). In addition, the heuristic algorithms are problem-specific, and therefore need problem-specific information. For example, the best first search algorithm selects the most ‘promising’ location among all the locations available in the search space with respect to a certain rule (Burns et al., 2010). The beam search algorithm, which is an advanced version of the best first search algorithm, determines the best location through a search tree created specifically for the problem (Dechter and Pearl, 1985; Gavrilas, 2010).

The problem-dependent heuristic algorithms have motivated the researchers to develop metaheuristic algorithms that are easily applied to different problems. The metaheuristic algorithms are able to provide the optimum solutions for many difficult optimization problems without being have to be fully adapted. The Greek-based 'meta' prefix in the metaheuristic word points out that, unlike problem-specific heuristic algorithms, these algorithms are high-level heuristic algorithms (Boussaïd et al., 2013). The metaheuristic methods have the capacity to explore the search space more actively and efficiently than the heuristic methods. Another advantage of the metaheuristic algorithms is that they are not slope-based algorithms. Thus, they can give the optimal result without the need for derivative calculations. In this way, problems of large size and complex structure can be successfully solved in a short time (Talbi, 2009).

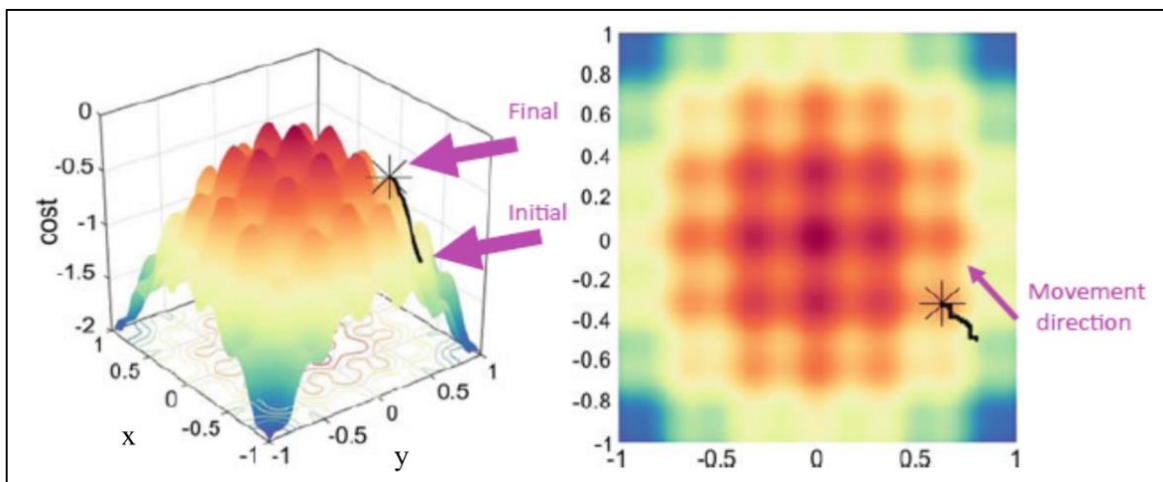


Figure 7. The hill climbing algorithm using only exploitation operator (Mirjalili and Dong, 2020).

The metaheuristic algorithms use two very important operators, exploitation and exploration. The exploitation conducts a local search around the best solutions in the search space whereas, the exploration explores different regions of the search space. These two operators are explained by examples given in Figures 7 and 8 for a better understanding. A simple hill climbing algorithm is given in Figure 7. Here, after starting from a starting point, the algorithm proceeds by selecting the best neighbour every time. Figure 7 shows that, in complex models (i.e. models including the local optima together with global minimum or maximum), the method that conducts only a neighbourhood search (i.e. exploitation) gets stuck at one of the local maxima in the search space. This is because the algorithm chooses only the highest of its closest neighbours at each step. However, in order to reach the highest point, algorithms should sometimes go down the hills moving to another points to discover new hills (Mirjalili and Dong, 2020).

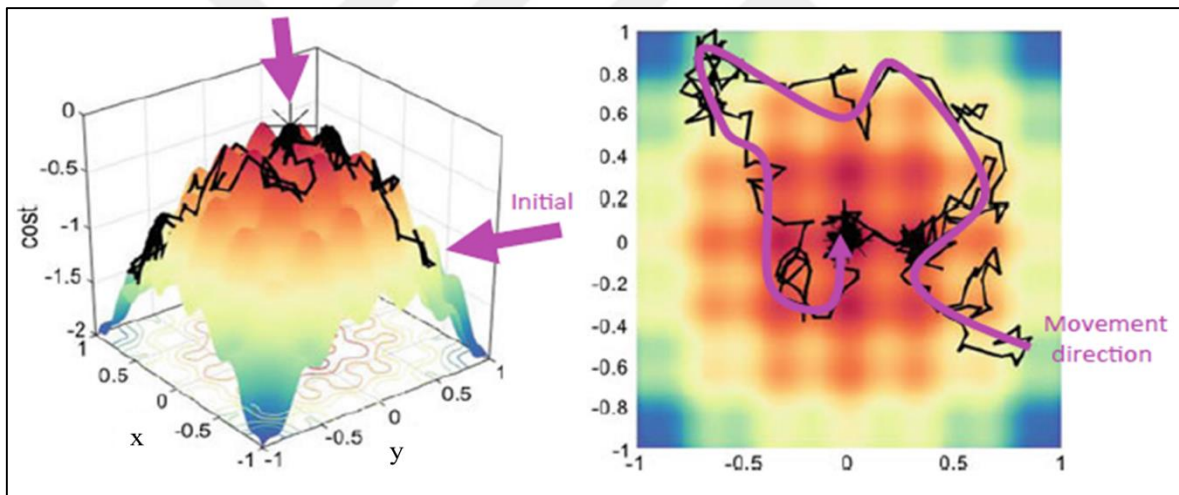


Figure 8. The simulated annealing algorithm using the exploitation and exploration operators (Mirjalili and Dong, 2020).

The compromise between the exploration and exploitation greatly affects the success of the metaheuristic search algorithms. For example, if an algorithm uses only the exploration operator, that is, it searches globally, it will probably find a point at the maximum peak, but this point will not be of the expected quality because the algorithm cannot improve this point by doing small moves. In contrast, an algorithm that uses only the exploitation operator will converge very quickly at one of the local maximum traps. Therefore, an

appropriate balance between these two operators is essential to achieve the global optimum point, regardless of the problem.

Unlike neighbourhood search, the algorithms sometimes take bad steps in search space to avoid the local optimal traps. As an example for this, the metaheuristic simulated annealing (Kirkpatrick et al., 2009) algorithm is given in Figure 8. The simulated annealing method uses a certain possibility to go down from the point where it is located or to make a jump. This allows the method to make extensive searches in the search space, as seen in Figure 8, so that the algorithm avoids the local maximum traps. However, in order to find the maximum possible point, it has to search the neighbourhood. The algorithm tries to do this by reducing the chance of jumping. As can be seen from Figure 8, if the problem is non-linear, then the exploitation and exploration operators must be employed in harmony together (Kirkpatrick et al., 2009; Mirjalili and Dong, 2020).

#### 1.4.1. Single-Objective Optimization

The optimization algorithms aim to achieve the optimum parameter values for the problem so as to maximize or minimize an objective function. In the literature, the objective function is often called fitness or cost function. The single-objective optimization algorithms aim to minimize or maximize a single objective function. In general, a single-objective optimization problem is expressed mathematically to minimize the objective as follows (Yang, 2011):

$$\min_{x \in \mathbb{R}^n} f(x_1, x_2, \dots, x_n) \quad (1.1)$$

$$g_i(x_1, x_2, \dots, x_n) \geq 0, \quad i = 1, 2, \dots, l \quad (1.2)$$

$$h_i(x_1, x_2, \dots, x_n) = 0, \quad i = 1, 2, \dots, p \quad (1.3)$$

$$lb_i \leq x_i \leq ub_i, \quad i = 1, 2, \dots, n \quad (1.4)$$

where,  $f$  denotes the objective function to be minimized,  $x$ , which can take any real value in  $n$  dimensional space, is called the design or decision variable, and  $n$  is the number

of decision variables. The space generated by the decision variables is called the search space, whereas the space containing the values obtained from the objective function is called the solution or objective space. Some optimization problems may have constraints in the search space. These constraints are actually the gaps in the search space that an optimization algorithm should avoid. The region in the search space that contains all possible decision variables that meet the constraints of the problem is called the feasible search region, and the region that corresponds this region in the solution space is called the feasible solution region.

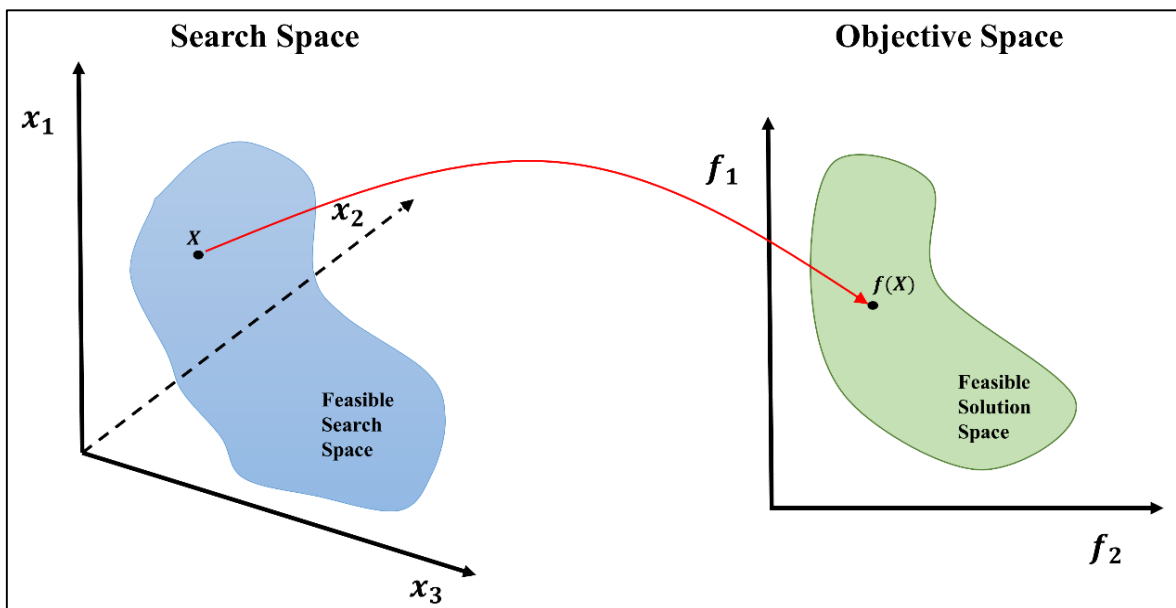


Figure 9. Search space (left) and solution space (right)

In Figure 9, the search space and solution space are shown for a two-objective optimization problem of the three-element decision variable vector, with the appropriate search and solution regions. The Equations 1.2 and 1.3 define the inequality  $g_i$  and equality  $h_i$  constraint functions, respectively. Here,  $l$  denotes the number of inequality constraints and  $p$  indicates the number of equality constraints. If  $l = p = 0$ , then the optimization problem is unconstrained. If  $p \geq 1$ ,  $l = 0$ , then the problem is equality-constrained, and if  $l \geq 1$ ,  $p = 0$ , then the problem is said to be an inequality-constrained optimization problem (Yang, 2011).

### 1.4.2. Multi-Objective Optimization

In the multi-objective optimization problem, there are multiple objective functions that need to be optimized. Compared to the single-objective optimization, multi-objective optimization is much more difficult to apply since optimal values are sought by addressing multiple and often conflicting purposes. The multi-objective optimization problem is mathematically formulated to minimize objectives as follows (Mirjalili and Dong, 2020);

$$\min_{X \in \mathbb{R}^n} f(X) = [f_1(X), f_2(X), \dots, f_m(X)], \quad m \geq 2 \quad (1.5)$$

$$X = (x_1, x_2, \dots, x_n)^T \quad (1.6)$$

where,  $f(X)$  is the objective function vector and  $m$  denotes the total number of objective functions. The Equation 1.6 expresses the decision variable vector  $X$  of  $n$  elements in the feasible solution space. The constraint equations (i.e. Equations 1.2 and 1.3) and limit value equation (i.e. Equation 1.4) used in single-objective optimization also apply to multi-objective optimization.

In single-objective optimization, the results obtained in the solution space can be evaluated with mathematical greatness or smallness operators, while these operators are insufficient in multi-objective optimization. For example, in a multi-objective optimization, when there are two different objective functions for a minimization problem, a decision variable vector may give the minimum value for one objective but not the other. That is, both of the objective functions to be optimized may not yield the optimum value at the same point (with the same decision variable), in which case no single optimum value can be mentioned. Therefore, there is a need for an operator where vectors of decision variables can be compared with each other. This operator is the Pareto optimal dominance (Censor, 1977; Mirjalili and Dong, 2020), which can determine the best decision variable vectors. According to this operator, a decision variable vector dominates another one only if it is as good as the other in all objective function values, and if it is better than the other in at least one objective function value. The Pareto dominance minimization problem can be expressed mathematically as follows (Deb, 2001; Tran et al., 2016);

The decision variable vector  $X_1(x_{1,1}, x_{1,2}, \dots, x_{1,n})^T$  dominates the other decision variable vector  $X_2(x_{2,1}, x_{2,2}, \dots, x_{2,n})^T$  if the following two conditions are met:

1.  $\forall i \in (1, 2, \dots, m): f_i(X_1) \leq f_i(X_2)$ . The decision variable vector  $X_1$  should yield a value as good as  $X_2$  in each objective function.
2.  $\exists i \in (1, 2, \dots, m): f_i(X_1) < f_i(X_2)$ . The decision variable vector  $X_1$  should definitely perform better than  $X_2$  in at least one objective function.

Three possible relationships exist between the decision variables  $X_1$  and  $X_2$ :

- ✓  $X_1$  dominates  $X_2$  ( $X_1 < X_2$ )
- ✓  $X_2$  dominates  $X_1$  ( $X_2 < X_1$ )
- ✓  $X_1$  and  $X_2$  cannot dominate each other.

The set of decision variables that cannot be dominated by any decision variable is called the Pareto optimal solution set. This set consists of vectors of decision variables that provide the best balance between the objective functions. The set consisting of the values in the solution space obtained by evaluating the Pareto optimal solution set in the objective functions is referred to as the Pareto front. These two sets, which are very important in multi-objective optimization, are illustrated in Figure 10.

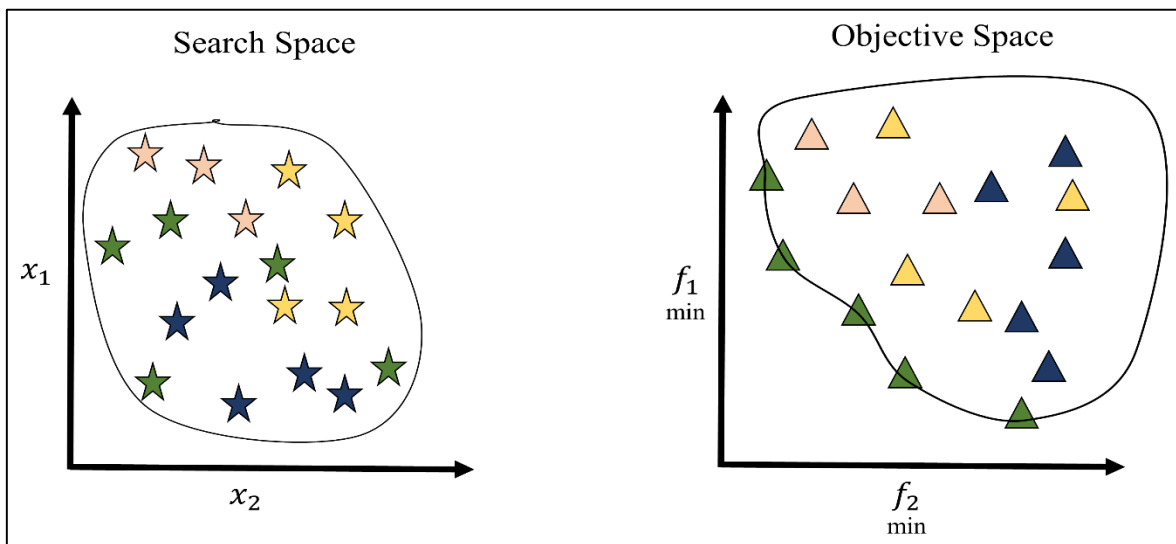


Figure 10. Pareto optimal solution set (left) and Pareto front (right)

In Figure 10, the stars in the search space represent two-element decision variable vectors that are different from each other, whereas the triangles show their response in the

solution space, that is, the objective values when the vectors of this decision variable are put in the functions  $f_1$  and  $f_2$ . The set shown with green triangles in the solution space forms the Pareto front. This set includes the triangles that cannot be dominated by all other triangles in the polygon (i.e. feasible solution region) given in the solution space. In other words, the green triangles dominate all other triangles in the region. The green stars that correspond to the green triangles in the search space on the Pareto front form the Pareto optimal solution set. The green stars in the Pareto optimal solution set are decision variables that cannot be dominated by any other stars in the feasible solution region.

The literature reports different techniques to solve metaheuristic multi-objective optimization problems. These techniques can be classified with respect to when the decision maker uses preference information in the optimization process (i.e. at the beginning, during or after the optimization process) (Evans, 1984; Ruzika and Wiecek, 2005; Atlas, 2008). Accordingly, these methods will be given in three different groups. The first is the situation where the decision maker has prior knowledge before optimization. An example of this class is the weighted sum multi-objective optimization method (Marler and Arora, 2010), which is frequently used in the literature due to its simplicity. In this method, multi-objective optimization problems are converted into fixed-weight linear functions and solved as if they are single-objective optimization problems. The mathematical expression of this procedure for any minimization problem is as follows (Yang, 2014);

$$\min_{X \in \mathcal{R}^n} f(X) = w_1 f_1(X) + w_2 f_2(X) + \dots + w_m f_m(X), \quad m \geq 2 \quad (1.7)$$

$$\sum_{i=1}^m w_i = 1, \quad w_i > 0 \quad (1.8)$$

As can be seen in the Equations 1.7 and 1.8, at the beginning of each objective function, there are weights that must be determined by the decision maker and the sum of these weights should be 1. The constraint equations (i.e. Equations 1.2 and 1.3) and limit value equation (i.e. Equation 1.4) given earlier are also valid for the weighted sum multi-objective optimization method. It is very advantageous that this method is easy to understand and has no computational load. Because, this method finds the solution like single-objective optimization and does not need non-dominated solutions. However, this method has many

disadvantages (Jin et al., 2001; Yang, 2014). Firstly, finding the appropriate weight values affects the solution. Another disadvantage of this method is that it is necessary to run the algorithm by trying different weights many times in order to obtain the Pareto front. In addition, different weights tried can prevent the Pareto front from being formed from homogeneously distributed points (Mirjalili and Dong, 2020).

The second is when the decision maker is involved during the optimization process (Jaszkiewicz and Branke, 2008). In this type of optimization methods, the decision maker chooses the most suitable decision variable by pausing the algorithm at certain intervals and the algorithm continues with the selected decision variable (Meignan et al., 2015). These methods are known as interactive methods since the decision-maker takes an active role in every step of the solution (Lieberman, 1991). Algorithms such as the hierarchical decomposition technique and Steuer technique can be given as examples of interactive methods (Lieberman, 1991; Lofti et al., 1997; Atlas, 2008). One of the advantages of the methods in this class is that the decision maker gives continuous preference throughout the process, hence, the problem is better understood by the decision maker. Also in this case, the problem is gradually improved in line with the preferences of the decision maker. The disadvantage of the method is that the results of the problem depend on how accurate the decision maker's decisions are. In addition, the decision maker is expected to make a great effort throughout the calculation process (Atlas, 2008), which is another disadvantage for this method.

The third class includes the algorithms that use the preferences of the decision maker after the optimization process. These methods aim to optimize all objective functions at the same time. The Equations 1.2, 1.3, 1.4, 1.5 and 1.6 are used for the mathematical expression of the methods in this class. These methods generate the Pareto front through the Pareto optimal dominance operator first, then the decision maker prefers the solutions that are most suitable for the problem. The evolutionary algorithms can be categorized under this class. The biggest advantage of the algorithms in this class is that the solutions are independent from the decision maker. Another advantage is that it can find the Pareto front by running the program only once. Having many solutions on the Pareto front gives the user the chance to make multiple selections. However, too complex algorithms make it difficult for decision makers to understand. A second disadvantage is that many solutions on the Pareto front force the user to decide (Atlas, 2008; Mirjalili and Dong, 2020).

### 1.4.3. An Overview of Metaheuristics

The metaheuristic algorithms are classified with respect to many different criteria in the literature. One of them is the classification with respect to the search agents (Talbi, 2009; Boussaïd et al., 2013), namely the single-point/solution-based (i.e. trajectory methods) and population-based.

In single-point metaheuristic algorithms, a single candidate solution (decision variable) that is randomly identified at the beginning is improved until an optimum result is achieved. The single-point metaheuristic algorithms do not need too much iteration to reach the optimum, which is an important advantage for these algorithms. However, the only solution candidate in these algorithms gets stuck at local optimum traps that prevent reaching the global optimum point, especially in difficult real world problems (Talbi, 2009). The simulated annealing (Hwang, 1988), tabu search (Glover, 1989) and hill climbing (Goldfeld et al., 1966) are examples for these methods.

The population-based metaheuristic algorithms use a random set of candidates to find the global optimum. Contrary to the single-point methods, they have the ability to conduct an extensive search in the search space, which makes them less likely to get stuck in local traps. In these methods, even if a solution candidate in the population has a local optimum value, other solution candidates help it get rid of this trap in subsequent iterations (Mirjalili, 2019). These methods, however, require more iterations, bringing a lot of computational burden.

The nature-inspired population-based metaheuristic algorithms can be roughly categorized into two groups as evolutionary and swarm-based algorithms (Talbi, 2009; Yang, 2010a; Du and Swamy, 2016; Almufti, 2019). The evolutionary algorithms mimic the biological evolution process in nature while solving the optimization problem. The genetic algorithm (GA) (Holland, 1975), evolutionary programming (EP) (Yao and Liu, 1996), evolution strategy (ES) (Mezura-Montes and Coello, 2005), differential evolution (DE) (Das and Suganthan, 2011) and multi-objective version of the GA (i.e. Non-Domination Sorting Genetic Algorithm-II) (Deb et al., 2002) can be given as examples for the evolutionary algorithms. All these evolutionary algorithms use similar principles and operators (Boussaïd et al., 2013). However, one of the most famous evolutionary metaheuristic algorithms is the GA, which mimics Darwin's evolution theory and natural selection in biological systems.

The GA, which relies on the principle of the survival of strong genes, has been the subject of thousands of research articles and hundreds of books due to its success in optimization problems in many different fields (Yang, 2010a). Every metaheuristic algorithm inspired by nature uses specific names in the optimization parameters accordingly. For example, the vector of decision variables given in the Equation 1.6 is called 'chromosome' in GA, whereas each candidate solution in the vector is called 'gene'. The GA conducts exploitation and exploration through the crossover and mutation operators, respectively. The GA needs parameter values such as crossover and mutation rate to find the optimum solution.

The swarm-based algorithms solve optimization problems by imitating the behaviour of real flocks such as birds, fish, bees and ants. In these algorithms, the location vector is defined for each solution candidate in the population and these position vectors are moved with respect to some rules. Each movement step is defined by the direction and speed of the candidate solutions (Mirjalili, 2019). The literature reports numerous swarm-based algorithms. Some of the most widely-used ones include the particle swarm optimization (PSO) (Kennedy and Eberhart, 1995; Alam et al., 2015), ant colony optimization (ACO) (Dorigo and Di Caro, 1999), cuckoo search algorithm (Yang and Deb, 2009; Yang, 2010a), artificial bee colony (ABC) algorithm (Karaboga, 2010) and firefly algorithm (FA) (Yang, 2010b) etc.

Figure 11 shows the general working principles of population-based metaheuristic algorithms. The population-based metaheuristic algorithms often perform similarly. These algorithms usually start with a randomly generated initial population. In the next step, the performance of the objective function is evaluated with the candidate solutions in the population. It is then checked whether the termination criteria are met. The iterations are terminated if the algorithm converges to a certain value. If it is not possible to converge, then the iterations are terminated once the maximum iteration number is reached. The algorithms then use the exploitation and exploration operators to search for the optimum result by conducting a local search around the possible solutions and a global search in different portions of the search space, respectively. The new generations obtained this way are subjected to the same processes throughout the iterations, and the initial population is improved until the termination criteria are met.

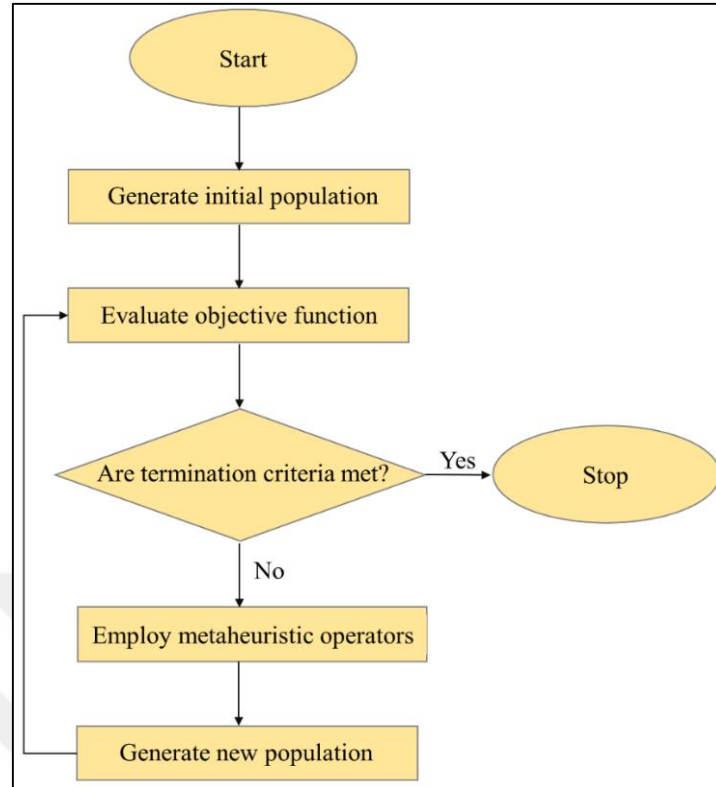


Figure 11. General working principle of population-based metaheuristic algorithms

An extensive literature review revealed that there are many different metaheuristic algorithms inspired by different concepts in nature. In the last decades, researchers have tried to develop powerful optimization algorithms that work well for all problems. However, as the popular 'no free lunch' theorem (Wolpert and Macready, 1997) states, no single optimization algorithm is able to solve all optimization problems. For this reason, many new algorithms are developed every year, either by making some modifications to existing optimization algorithms or by designing a new algorithm from scratch.

One of the most striking population-based metaheuristic algorithms of recent times is the Symbiotic Organisms Search (SOS) algorithm developed by Cheng and Prayogo (2014). The SOS algorithm simulates the symbiotic interaction between organisms in nature. The most important advantage of the SOS algorithm over many other metaheuristic algorithms is that it does not use any user-defined parameters that will affect the performance of the algorithm. The SOS algorithm only needs general information used also by other metaheuristics, such as the number of iterations and the population size. Other metaheuristics such as the GA, DE, PSO, ACO and cuckoo search employ at least one algorithm-specific

parameter other than these two general parameters. Cheng and Prayogo (2014) compared the performance of the SOS algorithm against five different methods including the GA, DE, PSO, Bee Algorithm (BA) (Pham et al., 2006) and a hybrid method Particle Bee Algorithm (PBA) (Cheng and Lien, 2012). 26 different metaheuristic algorithm benchmark functions and 4 different structural design problems were used in the comparison of methods. In the study, the SOS algorithm gave more successful results than the others within all benchmark functions and optimization problems. In addition, it was stated in the study that the SOS algorithm achieved the optimal result with lower iteration numbers, compared to other algorithms (Cheng and Prayogo, 2014). The SOS algorithm was found to be more successful than most metaheuristic algorithms in many different engineering applications (Das et al., 2016; Prayogo et al., 2017; Das and Bhattacharya, 2018; Dosoglu et al., 2018; Xiong et al., 2018; Rathore et al., 2019; Singh et al., 2020). Further information on the SOS algorithm and its working principle will be given in Section 3.

## 2. PANSHARPENING METHODS

The pansharpening methods used in this thesis include the CS-based BRV, SVR, MIHS, GS, PCA, HCS and BDSF; the MRA-based DWT, ATWT and AWLP; and SB methods HPF, LMM, SFIM and CB and a hybrid method called IHS-DWT. This section provides theoretical background for these methods.

### 2.1. Brovey (BRV)

The BRV method, one of the earliest and most successful pansharpening methods used by the remote sensing community, computes each pansharpened band by multiplying each MS band by the input PAN band and dividing the result by an intensity component calculated as the sum of all input MS bands (Hallada and Cox, 1983; Pohl and van Genderen, 2016). This method is implemented as:

$$P_i = \frac{MS_i}{I} \times PAN \quad (2.1)$$

where,  $I$  is the intensity component calculated as  $MS_1 + MS_2 + \dots + MS_n$ ,  $MS_i$  denotes the  $i$ th MS band,  $PAN$  denotes the PAN band and  $P_i$  is the  $i$ th pansharpened band.

### 2.2. Synthetic Variable Ratio (SVR)

The SVR method, enhanced version of the BRV, computes an intensity component as the weighted sum of all input MS bands. Each input MS band is then multiplied by the input PAN image and the result is normalized by dividing it by the intensity component (Munehika et al., 1993; Serifoglu Yilmaz et al., 2019). The equation for the SVR method is the same as that of the BRV (see Equation 2.1). The SVR technique computes the intensity component ( $I$ ) as:

$$I = MS_1 \times w_1 + MS_2 \times w_2 + \dots + MS_n \times w_n \quad (2.2)$$

where,  $w_i$  is the weight for the  $i$ th MS band. The performance of the SVR technique depends highly on the statistical relationship between the intensity component and input PAN image. Hence, feasible band weights should be used for each MS band. The literature reports different approaches to achieve the optimum band weights for the MS bands. Munechika et al., (1993) and Zhang (1999) employed regression analysis to estimate the band weights. Yilmaz et al., (2019) and Serifoglu Yilmaz et al., (2019) utilized the GA and SOS algorithms to estimate the optimum band weights, respectively.

### 2.3. Modified IHS (MIHS)

The MIHS is the modified version of the conventional IHS method, where the 3-band input MS data is transformed into the IHS color space. In this space, hue refers to the pure colors that are defined by specific colors, saturation indicates the amount of the white color in all pure colors and intensity is used as the most effective descriptor of the monochromatic images (El-Samie et al., 2012; Serifoglu Yilmaz et al., 2020). The calculated intensity component is considered to comprise the majority of the spatial structure of the scene. Hence, this component is substituted by the input PAN image. An inverse IHS transform is employed to produce the pansharpened bands. The biggest disadvantage of the standard IHS technique is that it is able to deal with only 3-band MS images. A very common IHS transform is given as (Pohl and van Genderen, 2016):

$$\begin{pmatrix} I \\ v_1 \\ v_2 \end{pmatrix} = \begin{pmatrix} \frac{1}{\sqrt{3}} & \frac{1}{\sqrt{3}} & \frac{1}{\sqrt{3}} \\ \frac{1}{\sqrt{6}} & \frac{1}{\sqrt{6}} & \frac{-2}{\sqrt{6}} \\ \frac{1}{\sqrt{2}} & \frac{1}{\sqrt{2}} & 0 \end{pmatrix} \times \begin{pmatrix} R \\ G \\ B \end{pmatrix} \quad (2.3)$$

$$H = \tan^{-1} \left( \frac{v_2}{v_1} \right) \quad (2.4)$$

$$S = \sqrt{v_1^2 + v_2^2} \quad (2.5)$$

The inverse IHS transform is given as (Pohl and van Genderen, 2016):

$$\begin{pmatrix} R \\ G \\ B \end{pmatrix} = \begin{pmatrix} \frac{1}{\sqrt{3}} & \frac{1}{\sqrt{6}} & \frac{1}{\sqrt{2}} \\ \frac{1}{\sqrt{3}} & \frac{1}{\sqrt{6}} & -\frac{1}{\sqrt{2}} \\ \frac{1}{\sqrt{3}} & -\frac{2}{\sqrt{6}} & 0 \end{pmatrix} \times \begin{pmatrix} I \\ v_1 \\ v_2 \end{pmatrix} \quad (2.6)$$

Siddiqui (2003) proposed a modification to the IHS method (MIHS) to handle images of more than three MS bands. The proposed scheme assesses the spectral overlap between the input MS and PAN data and utilizes these relative wavelengths to weighting the merge. This is why the MIHS technique works best when fusing input images covering similar parts of the electromagnetic spectrum. The MIHS method processes triple band combinations of the input MS images. For example, when fusing the 1-2-3 and 2-3-4 band combinations of the first four bands of the WorldView-2 imagery, the MIHS method stacks the 1-2-3 bands from the first merge and band 4 from the second merge to process all MS bands.

#### 2.4. Gram-Schmidt (GS)

The GS method is a common CS-based pansharpening technique. The first step of this technique is to simulate a low-resolution PAN data as a linear combination of the MS bands. The GS technique vectorises the MS bands and combines the MS band vectors with the low-resolution PAN vector, the low-resolution PAN vector being the first (Laben and Brower, 2000). The GS transform is employed to the combined data. The GS transform produces orthogonal and normalized vectors and employs the projection operator  $\text{Proj}_a$  for the vectors  $a$  and  $b$  as (Pohl and van Genderen, 2016; Yilmaz et al., 2020):

$$\text{Proj}_a(b) = \frac{\langle a|b \rangle}{\langle a|a \rangle} a \quad (2.7)$$

where,  $a|b$  denotes the inner product. The orthogonal vectors are generated by the GS method as:

$$a_1 = b_1 \quad (2.8)$$

$$a_2 = b_2 - \text{Proj}_{a_1}(b_2) \quad (2.9)$$

$$a_3 = b_3 - \text{Proj}_{a_1}(b_3) - \text{Proj}_{a_2}(b_3) \quad (2.10)$$

$$a_m = b_m - \sum_{j=1}^{m-1} \text{Proj}_{a_j}(v_m) \quad (2.11)$$

where,  $m = n + 1$  (i.e. total number of MS and PAN bands) and  $a_1, a_2 \dots a_m$  denote the normalized orthogonal vectors ortho-normalized ( $c_1, c_2 \dots c_m$ ) as:

$$c_1 = \frac{a_1}{\|a_1\|} \quad (2.12)$$

$$c_2 = \frac{a_2}{\|a_2\|} \quad (2.13)$$

$$c_3 = \frac{a_3}{\|a_3\|} \quad (2.14)$$

$$c_m = \frac{a_m}{\|a_m\|} \quad (2.15)$$

Once the forward GS transform is applied, the first GS component is swapped by the histogram-matched PAN image. An inverse GS transform is employed to produce the pansharpened data (Laben and Brower, 2000).

The GS methods reported in the literature vary in the way they simulate the low-resolution PAN data. A common way of generating the low-resolution PAN image is to averaging the MS bands. Using a low-pass filter is another common way to achieve this (Laben and Brower, 2000). Garzelli et al., (2008) proposed to calculate the low-resolution PAN data as the weighted average of the MS bands. The weights were estimated through the minimization of the mean square error (MSE). Maurer (2013) stated that covariance matrices can be utilized to estimate these weights. Pohl and van Genderen (2016) also stated that these

weights can be estimated from the spectral sensitivity curves of the sensor through the use of least-square methods or linear regression.

### 2.5. Hyperspherical Colour Space (HCS)

The HCS technique transforms the MS data from native color space to HCS color space. This transformation produces an intensity component ( $I$ ) and  $n - 1$  ( $n$  is the total number of dimensions) angular components on the hypersphere. The HCS transform from native color space to HCS color space is applied as (Padwick et al., 2010):

$$I = \sqrt{\chi_1^2 + \chi_2^2 + \dots + \chi_n^2} \quad (2.16)$$

$$\varphi_1 = \tan^{-1} \left( \frac{\sqrt{\chi_n^2 + \chi_{n-1}^2 + \dots + \chi_2^2}}{\chi_1} \right) \quad (2.17)$$

$$\varphi_{n-2} = \tan^{-1} \left( \frac{\sqrt{\chi_n^2 + \chi_{n-1}^2}}{\chi_{n-2}} \right) \quad (2.18)$$

$$\varphi_{n-1} = \tan^{-1} \left( \frac{\chi_n}{\chi_{n-1}} \right) \quad (2.19)$$

where,  $\chi_i$  is the  $i$ th component of the native color space and  $\varphi$  is the angular component in the HCS. The inverse transform to the native color space is defined as (Padwick et al., 2010):

$$\chi_1 = I \cos \varphi_1 \quad (2.20)$$

$$\chi_2 = I \sin \varphi_1 \cos \varphi_2 \quad (2.21)$$

$$\chi_{n-1} = I \sin \varphi_1 \sin \varphi_2 \dots \sin \varphi_{n-2} \cos \varphi_{n-1} \quad (2.22)$$

$$\chi_n = I \sin \varphi_1 \sin \varphi_2 \dots \sin \varphi_{n-2} \sin \varphi_{n-1} \quad (2.23)$$

Since all color components are positive, the  $\varphi$  values vary between 0 and  $\pi/2$  (Wu et al., 2015). After transformation into the HCS space, the mean and standard deviation of the square of the PAN image are matched to those of the square of the  $I$  as (Padwick et al., 2010):

$$PAN^2 = \frac{\sigma_0}{\sigma_1} (PAN^2 - \mu_1 + \sigma_1) + \mu_0 - \sigma_0 \quad (2.24)$$

where,  $\mu_1$  and  $\sigma_1$  define the mean and standard deviation of the square of the PAN image (i.e.  $PAN^2$ ); and  $\mu_0$  and  $\sigma_0$  denote the mean and standard deviation of the square of the  $I$  (i.e.  $I^2$ ). An adjusted intensity ( $I_a$ ) is calculated as the square root of the  $PAN^2$  as:

$$I_a = \sqrt{PAN^2} \quad (2.25)$$

As a final step,  $I_a$  is replaced by  $I$  and the pansharpened image is produced by using Equations 2.20-2.23 (Padwick et al., 2010).

## 2.6. Band Dependent Spatial Detail (BDSD)

The BDSD method injects the details image to the input MS image as (Garzelli et al., 2008; Imani, 2018):

$$P = \widehat{MS}_k + g_k \left( PAN - \sum_{l=1}^B \alpha_{k,l} \widehat{MS}_l \right) \quad (2.26)$$

where,  $P$  defines the pansharpened image,  $\widehat{MS}$  defines the upsampled input MS image and  $B$  denotes the total number of MS bands. On the contrary to the CS-based techniques, the BDSD method combines the bands of the MS image (i.e.  $\widehat{MS}_l$ ) together with the band dependent coefficients  $\alpha_{k,l}$ . The minimum variance unbiased estimator is used to estimate

the coefficients  $g_k$  ( $k = 1, \dots, B$ ) and  $\alpha_{k,l}$  ( $k, l = 1, \dots, B$ ) (Imani, 2018). An approximation image  $A_k$  is generated with a linear combination of the MS bands as:

$$A_k = \sum_{l=1}^B \alpha_{k,l} \widehat{MS}_l \quad (2.27)$$

The details image  $D_k$  is obtained by subtracting the  $A_k$  from the PAN image as:

$$D_k = PAN - A_k \quad (2.28)$$

The pansharpened image is produced by adding the  $D_k$  to the  $\widehat{MS}_k$  as (Imani, 2018):

$$P = \widehat{MS}_k + g_k D_k \quad (2.29)$$

## 2.7. à trous Wavelet Transformation (ATWT)

The ATWT is common MRA-based technique that aims to extract the spatial structure of the PAN data and inject it into the input MS data to sharpen it whilst preserving the color properties. The ATWT method first upsamples the input MS bands to the size of the PAN image. The input PAN image ( $I_0^{\text{PAN}}$ ) is then decomposed as (Gungor, 2008):

$$I_{j+1} = \text{convolve}(I_j, H_j) \quad (2.30)$$

$$w_{j+1} = I_j - I_{j+1} \quad (2.31)$$

where,  $w_j$  denotes the wavelet planes containing the details coefficients in horizontal, vertical and diagonal directions.  $H_j$  denotes the convolution mask, where  $j$  is used to define the number of zeros needed to be inserted into the filter coefficients of the original filter  $H_0$  given as (Starck and Murtagh, 1994):

$$H_0 = \frac{1}{256} \begin{bmatrix} 1 & 4 & 6 & 4 & 1 \\ 4 & 16 & 24 & 16 & 4 \\ 6 & 24 & 36 & 24 & 6 \\ 4 & 16 & 24 & 16 & 4 \\ 1 & 4 & 6 & 4 & 1 \end{bmatrix} \quad (2.32)$$

For the first decomposition level (i.e.  $j = 1$ ), no zeros needed to be inserted into the filter  $H_0$ , since  $2^{j-1} - 1 = 0$ . Likewise, for the second decomposition level (i.e.  $j = 2$ ), only 1 zero is needed to be inserted between each element of  $H_0$ , and the new filter ( $H_1$ ) becomes:

$$H_1 = \frac{1}{256} \begin{bmatrix} 1 & 0 & 4 & 0 & 6 & 0 & 4 & 0 & 1 \\ 0 & 0 & 0 & 0 & 0 & 0 & 0 & 0 & 0 \\ 4 & 0 & 16 & 0 & 24 & 0 & 16 & 0 & 4 \\ 0 & 0 & 0 & 0 & 0 & 0 & 0 & 0 & 0 \\ 6 & 0 & 24 & 0 & 36 & 0 & 24 & 0 & 6 \\ 0 & 0 & 0 & 0 & 0 & 0 & 0 & 0 & 0 \\ 4 & 0 & 16 & 0 & 24 & 0 & 16 & 0 & 4 \\ 0 & 0 & 0 & 0 & 0 & 0 & 0 & 0 & 0 \\ 1 & 0 & 4 & 0 & 6 & 0 & 4 & 0 & 1 \end{bmatrix} \quad (2.33)$$

Each decomposition results in wavelet planes ( $w$ ) and an approximation image ( $I$ ) whose resolution is two times coarser than the original image. In each decomposition level, the detail image ( $w_{j+1}$ ) is computed as the difference between  $I_j$  and  $I_{j+1}$ , where  $j$  denotes the decomposition level. The set of  $\{w_j\}$  can be summed with the last approximation image ( $I_j$ ) to reconstruct the first approximation image ( $I_0$ ) as (Nunez et al., 1999):

$$I_0 = I_j + \sum_{j=1}^J w_j \quad (2.34)$$

The decomposition continues until the detail content of the last approximation image ( $I_j$ ) matches to the detail content of the input MS image ( $I_k^{MS}$ ), where  $k$  defines the  $k$ th MS band. All  $w_j$  values are summed to determine the spatial structure difference between the input MS and PAN images as:

$$W = \sum_{j=1}^J w_j \quad (2.35)$$

Each pansharpened band ( $P_k$ ) is computed by adding  $W$  to each MS band ( $I_k^{MS}$ ) as:

$$P_k = I_k^{MS} + W \quad (2.36)$$

The number of decomposition level is defined based on the spatial resolution ratio between the input MS and PAN data (Gungor, 2008). Since each decomposition generates an approximation image of two times coarser resolution, two decompositions should be applied for input images whose spatial resolution ratio is four.

## 2.8. Additive Wavelet Luminance Proportional (AWLP)

The AWLP technique is an extended version of the Additive Wavelet Luminance (AWL) technique (Nunez et al., 1999; Otazu et al., 2005), which is able to process only three MS bands at a time. The AWL technique first transforms the input RGB image into the IHS space. The histogram of the PAN data is then matched to that of the intensity component. The histogram-matched PAN image is decomposed into  $n_w$  wavelet planes through the à trous wavelet transformation described in Section 2.7. The obtained wavelet planes ( $w_k$ ) are added to the intensity component to obtain the spatially-enhanced intensity component ( $I_e$ ):

$$I_e = I + \sum_{k=1}^{n_w} w_k \quad (2.37)$$

The final step of the AWL method is to apply an inverse IHS transform using the enhanced intensity ( $I_e$ ), hue and saturation to produce the pansharpened data. The number of wavelet planes  $n_w$  is determined as (Otazu et al., 2005):

$$n_w = \log_2 \left( \frac{r_{MS}}{r_{PAN}} \right) \quad (2.38)$$

where,  $r_{MS}$  and  $r_{PAN}$  stand for the spatial resolutions of the input MS and PAN data, respectively.

Otazu et al., (2005) extended the AWL pansharpening method for input MS images of arbitrary band numbers. According to this extension, the high-frequency details are injected proportionally to the MS bands. Let  $L$  be the total number of MS bands, the AWLP method is formulated as (Kim et al., 2010):

$$P_i = MS_i + \frac{MS_i}{(1/L) \sum_{i=1}^L MS_i} \sum_{j=1}^n w_{PAN} \quad (2.39)$$

## 2.9. Local Mean Matching (LMM)

The LMM method was proposed to minimize the difference between the pansharpened bands and corresponding MS bands, keeping the spectral features. The LMM method employs normalization functions at a local scale to match the local mean values (de Béthune et al., 1997). The LMM method is given as:

$$P_{i,j} = PAN_{i,j} \cdot \frac{\overline{MS}_{i,j(w,h)}}{\overline{PAN}_{i,j(w,h)}} \quad (2.40)$$

where,  $P_{i,j}$  denotes the pansharpened image and  $PAN_{i,j}$  denotes the input PAN data at pixel coordinates  $(i, j)$ .  $\overline{MS}_{i,j}$  and  $\overline{PAN}_{i,j}$  are the local means computed from the window of size  $(w, h)$  (de Béthune et al., 1997). It is possible to control the amount of the colour information needed to be preserved by adjusting the window size (de Béthune et al., 1998).

## 2.10. High-Pass Filtering (HPF)

The HPF method is one of the most fundamental pansharpening methods, which has been used since the 1980s. The main theory behind this method is to improve the spatial detail quality of the input PAN data with a HPF and integrate these improved details into the input MS data (Schowengerdt 1980; Chavez et al., 1991).

The HPF method first filters the input PAN data with a HPF, whose size is determined based on the pixel resolution ratio ( $R$ ) between the input MS and PAN data.  $R$  is computed as:

$$R = \frac{PR_{MS}}{PR_{PAN}} \quad (2.41)$$

where,  $PR_{MS}$  and  $PR_{PAN}$  denote the pixel resolution of the input MS and PAN data, respectively. The optimal kernel size is equal to  $2R$ . Prior to the addition to the input MS bands, the HPF-enhanced PAN image ( $PAN_e$ ) is weighted to optimize the pansharpening result. The global standard deviation of the MS bands ( $\sigma_{MS_i}$ ) are used to determine the weights  $w_i$ . The standard deviation of the  $i$ th MS band ( $\sigma_{MS_i}$ ) is calculated as (Pohl and van Genderen, 2016):

$$\sigma_{MS_i} = \sqrt{\frac{\sum_{j=1}^k (MS_{ij} - \mu_{MS_i})^2}{k - 1}} \quad (2.42)$$

where,  $j$  defines a specific pixel and  $MS_{ij}$  denotes the gray value of that pixel in the  $i$ th MS band.  $\mu_{MS_i}$  is the mean of the  $i$ th MS band. The weight  $w_i$  is computed as:

$$w_i = \frac{\sigma_{MS_i}}{\sigma_{PAN_e}} f \quad (2.43)$$

where,  $f$  is a modulation factor that enables the users to adjust the crispness of the result. The pansharpened image is calculated as (Pohl and van Genderen, 2016):

$$P = MS + wPAN_e \quad (2.44)$$

### 2.11. Smoothing Filter-Based Intensity Modulation (SFIM)

The SFIM method, introduced by Liu (2000), makes use of the ratio between the input PAN data and its low-pass filtered version to modulate a low-resolution MS data (Pohl and van Genderen, 2016). The SFIM method is implemented as:

$$P_{i,j,k} = \frac{MS_{i,j,k} \times PAN_{i,j}}{M_{i,j}} \quad (2.45)$$

where,  $P_{i,j,k}$  is the pansharpened image at pixel location  $i, j$  in band  $k$ ,  $M$  is a low-resolution PAN image obtained by applying an averaging filter on the PAN data and  $MS_{i,j,k}$  is the input MS image at pixel location  $i, j$  in band  $k$  (Liu, 2000; Pohl and van Genderen, 2016). The size of the filter is equal to the spatial resolution ratio between the input images (Khan et al., 2007).

### 2.12. Criteria-Based (CB) Method

The CB method, proposed by Gungor (2008), generates the pansharpened bands as a linear combination of the input MS and PAN images. This method computes the pansharpened bands as:

$$P_{k(m,n)} = a_{(m,n)} \cdot I_{0(m,n)} + b_{(m,n)} \cdot I_{k(m,n)} \quad (2.46)$$

where,  $k = 1, 2 \dots N$  is the band number, while  $m$  and  $n$  define the row and column number, respectively.  $P_k$  is the pansharpened image,  $I_0$  is the input PAN data and  $I_k$  is the  $k$ th band of the upsampled MS data.  $a$  and  $b$  denote the weighting coefficients that control the contribution of the PAN and MS image to the pansharpening result, respectively.  $a$  and  $b$  coefficients are determined by following three criteria given as (Gungor, 2008):

- The pansharpened image and input PAN data should have the same variance to keep the spatial structures after pansharpening. This criterion is formulized as:

$$\text{Cov}(P_k, P_k) = a_k^2 \sigma_o^2 + 2a_k b_k \sigma_{ok} + b_k \sigma_k^2 = \sigma_o^2 \quad (2.47)$$

where,  $o$  and  $k$  indicate the PAN and MS image, respectively.  $\sigma_o^2$ ,  $\sigma_k^2$  and  $\sigma_{ok}$  denote the variance of the PAN image, variance of the MS image and covariance between the PAN and MS images, respectively (Yilmaz and Gungor, 2016a).

- The mean of the pansharpened image should be equal to that of the input MS image to preserve the color features after pansharpening. This criterion is formulized as:

$$\text{Mean}(P_k) = a_k \mu_o + b_k \mu_k = \mu_k \quad (2.48)$$

where,  $\text{Mean}(P_k)$  denotes the mean of the  $k$ th pansharpened band,  $\mu_o$  denotes the mean of the PAN image and  $\mu_k$  define the mean of the  $k$ th MS band (Yilmaz and Gungor, 2016a).

- The inter-band relationship among the MS bands should be kept after pansharpening. This criterion is formulized as:

$$P_{k(m,n)} = C_{(m,n)} \cdot I_{k(m,n)} \quad (2.49)$$

where,  $C$  is a coefficient used to retain the ratio among the input MS bands. To determine the coefficients  $a$  and  $b$ , the CB method solves the Equations 2.46-2.49 for each pixel location using the least squares technique. The CB method is not applied on the whole image. Instead, it employs local sliding windows to solve the equations. The size of the window is set to the closest odd number that is equal or greater than the spatial resolution ratio between the input MS and PAN images (Gungor, 2008).

### 2.13. Principal Component Analysis (PCA)

The PCA method is a statistical method similar to the GS. As a first step, the PCA method uses a linear transformation to transform the original MS image into an eigenvector space, whose axes are principal components. The correlation between these principal components are removed in this new space (Armenakis et al., 2003).

Mathematically, each pixel vector of an MS image is represented as:

$$x_i = (x_1, x_2, \dots, x_k)^T \quad (2.50)$$

where,  $k$  denotes the total number of MS bands,  $x$  is a gray value and T is the transpose operator. To transform the MS image into eigenvector space, the covariance matrix  $C_x$  is calculated as:

$$C_x = \frac{1}{M} \sum_{i=1}^M (x_i - m)(x_i - m)^T \quad (2.51)$$

$$m = \frac{1}{M} \sum_{i=1}^M x_i \quad (2.52)$$

where,  $m$  is the mean vector of all the vectors in the image. To remove the correlation among the bands, the following transform is applied to obtain the PCA pixel vectors ( $y_i$ ):

$$y_i = A^T \cdot x_i \quad (2.53)$$

where,  $A$  comprises the eigenvectors of the  $C_x$ . The eigenvalues and eigenvectors are then arranged in descending order. As a result of this procedure, the first row of the  $A^T$  becomes the eigenvector that has the greatest eigenvalue (Gonzales and Woods, 2003).

The PCA pansharpener method replaces the input PAN data by the first principal component, considering that this component retains the majority of the spatial details of the scene. After the replacement, the pansharpener image is generated through an inverse PCA transform applied as (Gungor, 2008):

$$x_i = A \cdot y_i \quad (2.54)$$

#### 2.14. Discrete Wavelet Transform (DWT)

The DWT is a frequently-used MRA-based pansharpener technique applied in different ways. The à trous, Mallat's multiresolution and M-Band wavelet transform

approaches are among the most common DWT approaches used for pansharpening purposes (Gungor, 2008). This study used the M-Band wavelet transform based type.

The DWT method first decomposes the PAN image using the DWT. The DWT method applies the following scaling function  $\phi(x, y)$  and wavelet functions ( $\psi^{(0,m)}(x, y)$ ,  $\psi^{(m,0)}(x, y)$  and  $\psi^{(m,n)}(x, y)$ ) on the input PAN image in horizontal, vertical and diagonal directions, respectively (Yang et al., 2006; Gungor, 2008).

$$\phi(x, y) = \phi(x)\phi(y) \quad (2.55)$$

$$\psi^{(0,m)}(x, y) = \phi(x)\psi^m(y) \quad (2.56)$$

$$\psi^{(m,0)}(x, y) = \psi^m(x)\phi(y) \quad (2.57)$$

$$\psi^{(m,n)}(x, y) = \psi^m(x)\psi^n(y) \quad (2.58)$$

where,  $m = 1, 2, \dots, M - 1$  and  $n = 1, 2, \dots, M - 1$ . Each decomposition results in one approximation image and  $M^2 - 1$  detail images. The approximation image includes the color information, whereas the detail images (i.e. wavelet subplanes) include the high frequency details in horizontal, vertical and diagonal directions. It should also be noted that each decomposition generates sub-images of size  $1/M$  (Gungor, 2008).

After the first decomposition, second decomposition is applied by employing the Equations 2.55-2.58) to the approximation component obtained in the first decomposition. The decompositions continue until the resolution of the input MS image is achieved. Once achieved, each MS band is substituted by the approximation image achieved at the coarsest resolution and the pansharpened image is generated by applying an inverse DWT with the wavelet planes obtained in previous decompositions (Serifoglu Yilmaz et al., 2020).

### **2.15. Intensity-Hue-Saturation – Discrete Wavelet Transform (IHS-DWT)**

The IHS-DWT hybrid method aims to combine the color preservation capability of the DWT method and sharpening capability of the IHS method. The IHS-DWT technique first transforms the input MS data into the IHS space. A histogram matching is then applied

between the input PAN data and the intensity component to retain the color information after pansharpening. A DWT is employed on the intensity component and histogram-matched PAN image. The last approximation component achieved for the intensity component is swapped by its average with the last approximation component achieved for the histogram-matched PAN image. An intermediary intensity component is generated by applying an inverse DWT using the final approximation component and high-frequency detail images. An inverse IHS transform is employed using the intermediary intensity component and original hue and saturation components to generate the pansharpened image (El-Samie et al., 2012; Serifoglu Yilmaz et al., 2020).



### 3. SOS ALGORITHM

The SOS algorithm mimics the interactions seen among the organisms in nature. It is a well-known fact that the organisms rely on each other in many ways to survive, which is referred to as 'symbiosis'. The word 'symbiosis' comes from a Greek word that means 'living together'. Symbiotic relationships seen in nature can be roughly divided into two categories. The first is when two organisms need each other to survive, and the second is when two organisms get benefit from each other in a nonessential relationship. The most prominent symbiotic relationships seen include the mutualism, commensalism and parasitism. The mutualism refers to a relationship between two species where both get benefit. The commensalism, on the other hand, refers to a relationship, where only one gets benefit whilst the other one remains unaffected. The parasitism is when one organism gets benefit whilst the other one is harmed. These relationships help the organisms adapt to environmental conditions (Cheng and Prayogo, 2014). The SOS algorithm aims to search for the optimum global solution through the use of a population that is composed of candidate solutions. Each nature-inspired metaheuristic algorithm names its variables and operators based on the phenomenon it relies on. Hence, the populations comprising the candidate solutions are referred to as 'ecosystem' in the SOS algorithm and each candidate solution is referred to as an 'organism'.

The SOS algorithm starts by randomly generating an initial ecosystem. Then, the fitness of each organism is evaluated with its objective function value. Similar to almost all metaheuristic algorithms, the SOS algorithm improves the ecosystem with respect to the fundamentals of the biological interactions between two species. The SOS algorithm employs the aforementioned mutualism, commensalism and parasitism operators to improve the ecosystem in each iteration (Cheng and Prayogo, 2014).

The relationship between an oxpecker (a kind of bird) and zebra can be given as an example for a mutualistic relationship. Oxpeckers eat ticks or other parasites on zebra that live on its skin. In this relationship, the zebra gets rid of the parasites and the oxpeckers get food, which means that both species get benefit. Let  $X_i$  be an organism corresponding to the  $i^{\text{th}}$  organism of the ecosystem. The organism  $X_j$  that will interact with the organism  $X_i$  is selected randomly from ecosystem. Both organisms interact with each other to increase their

chance of survival. The SOS algorithm models the new candidate solutions for  $X_i$  (i.e.  $X_{i\_new}$ ) and  $X_j$  (i.e.  $X_{j\_new}$ ) as (Cheng and Prayogo, 2014);

$$X_{i\_new} = X_i + \text{rand}(0,1) \times (X_{\text{best}} - MV \times BF_1) \quad (3.1)$$

$$X_{j\_new} = X_j + \text{rand}(0,1) \times (X_{\text{best}} - MV \times BF_2) \quad (3.2)$$

$$MV = \frac{X_i + X_j}{2} \quad (3.3)$$

where,  $MV$  denotes the mutual vector and  $\text{rand}(0,1)$  is a vector consisting of random numbers between 0 and 1. On the other hand, the  $BF_1$  and  $BF_2$  defines to what degree each organism gets benefit from the interaction. The  $BF_1$  and  $BF_2$  get random numbers of either 1 or 2, which means partial or full benefit from the interaction, respectively. The organism  $X_i$  and  $X_j$  are updated only if their new fitness values  $X_{i\_new}$  and  $X_{j\_new}$  are better. Since the mutualism phase generates candidate solutions around the best solution, it contributes to the local search capability (i.e. exploitation) of the algorithm.

The relationship between the birds and trees can be given as an example for commensal interaction. The birds live on the hollows of the trees. The tree does not actually get harmed from this relationship and provides a shelter for the bird, which is the benefit that the bird gets from this interaction. As in the mutualism phase, the SOS algorithm randomly selects an organism  $X_j$  to interact with  $X_i$ . In this relationship, the organism  $X_i$  is expected to get benefit from this interaction, whilst the organism  $X_j$  is expected to remain unaffected. The SOS algorithm models the new candidate solution for the organism  $X_i$  as follows (Cheng and Prayogo, 2014);

$$X_{i\_new} = X_i + \text{rand}(-1,1) \times (X_{\text{best}} - X_j) \quad (3.4)$$

where,  $\text{rand}(-1,1)$  denotes a vector comprising random numbers between -1 and 1. The organism  $X_i$  is updated only if its new fitness value  $X_{i\_new}$  is better. The commensalism phase increases the exploitation capability, due to the fact that this phase computes the new candidate solution taking the best organism at the current iteration into consideration.

The relationship between the tick and dogs can be given as an example for a parasitic relationship. In this relationship, the tick is fed from dog's blood, whilst the dog is harmed. Let  $X_i$  be an organism that generates a parasite vector by duplicating itself. Some random modifications are then made of this vector. Afterwards, an organism  $X_j$ , which is expected to be the host to the parasite vector, is randomly selected from the ecosystem. The fitness of these two organisms are calculated. The organism  $X_j$  is killed if the parasite vector results in a fitter solution. If the organism  $X_j$  has a better fitness value, then it is said to have acquired immunity to the parasite and the parasite vector perishes. The parasitism phase enables the achievement of a compromise between the exploitation and exploration capabilities, therefore, plays a vital role in the exploration capability (Cheng and Prayogo, 2014).

The SOS algorithm continues to iterate with new ecosystems generated through the mutualism, commensalism and parasitism operations until the required convergence or a predefined maximum iteration number is reached.

### 3.1. MOSOS Algorithm

The MOSOS algorithm, introduced by Tran et al., (2016), aims to solve multi-objective problems using the SOS algorithm, which shows a fast convergence and great robustness in single-objective optimization problems (Tran et al., 2016). The main steps of the MOSOS algorithm used in this thesis are as follows (Seshadri, 2006):

1. An  $N$ -sized initial ecosystem  $E$  is generated randomly.
2. The ecosystem is sorted based on non-domination, which was originally used in the NSGA-II algorithm (Deb et al., 2002). The non-domination sorting procedure is applied as (Seshadri, 2006):
  - 2.1. For each organism  $o$  in the  $E$ ,
    - ❖  $D_o = \emptyset$ , which includes the organisms that are dominated by  $o$ , is initialized.
    - ❖  $n_o = 0$ , which is the number of the organisms that dominate  $o$ , is initialized.
    - ❖ For each  $s$  organism in the  $E$ ,
      - ✓  $s$  is added to the  $D_o$ , if  $o$  dominates  $s$  (i.e.  $D_o = D_o \cup \{s\}$ ).

✓ The domination counter  $n_o$  is increased by 1, if  $s$  dominates  $o$ . (i.e.  $n_o = n_o + 1$ ).

❖ If  $n_o = 0$ , then none of the organisms can be said to have dominated  $o$  and  $o$  is assigned to the first front  $F_1$  and its rank is set to 1 (i.e.  $o_{\text{rank}} = 1$ ) (i.e.  $F_1 = F_1 \cup \{o\}$ ).

2.2.The procedure applied in the step 2.1 is repeated for all the organisms in the  $E$ .

2.3.The following is done while  $F_i \neq \emptyset$ :

❖ Initialize  $S = \emptyset$ , which stores the organisms for the  $(i + 1)^{\text{th}}$  front.

❖ For each organism  $o$  in the front  $F_i$  and each organism  $s$  in the  $D_o$ ,

✓  $n_o$  is decreased by 1 for each organism  $s$  (i.e.  $n_o = n_o - 1$ ).

✓ If  $n_o = 0$ , then none of the organisms in the subsequent fronts can be said to be able to dominate  $s$ ; and  $o_{\text{rank}} = i + 1$  and  $S = S \cup s$ .

❖ Add 1 to the front counter (i.e.  $F_i = F_{i+1}$ ).

❖ The  $S$  is assigned to the next front ( $F_i = S$ ).

3. Sort the fronts based on the crowding distance. As may be remembered, the non-domination sorting scheme assigns the candidate organisms to the fronts based on their ranks and these organisms are sorted with respect to their rank values. However, more than one organisms may be in the same front. In such cases, the crowding distance is used to sort the organisms in each front. Let  $l$  be the number of organisms, the mathematical definition of the crowding distance operator is as follows (Seshadri, 2006):

3.1.For each front  $F_i$ ,

❖ Let  $j$  be the  $j^{\text{th}}$  organism in the  $l$ -sized front  $F_i$ , initialize a distance vector for each organism. The starting value for this vector is assigned to zero (i.e.  $F_i(d_j) = 0$ ).

❖ For each objective function  $m$ ,

✓ The organisms in the front  $F_i$  are sorted based on the objective function  $m$  (i.e.  $I = \text{sort}(F_i, m)$ ).

✓ The distance values of the organisms that yield the minimum and maximum objective function values are assigned to infinitive (i.e.  $I(d_1) = \infty$  and  $I(d_l) = \infty$ ).

✓ for  $u = 2$  to  $(l - 1)$ ,

$$I(d)_u = I(d)_u + \frac{I(u + 1) \cdot m - I(u - 1) \cdot m}{f_m^{\max} - f_m^{\min}} \quad (3.5)$$

where,  $I(u) \cdot m$  is the  $m$ th objection function value of the  $u$ th organism in the  $I$ .  $f_m^{\max}$  and  $f_m^{\min}$  stand for the maximum and minimum values for the  $m$ th objective function computed for all solutions in the  $I$ .

For each objective, the individual distance values are summed to determine the overall crowding distance value (Deb et al., 2002). The crowding distance operator aims to find the distance between each pair of organisms. Smaller crowding distance values indicate a high density around the solution.

4. The crowded comparison operator ( $\prec_n$ ) is employed to select the optimal organisms from uniformly distributed Pareto optimal front. The selection is conducted based on two factors, including the non-domination rank (i.e.  $o_{\text{rank}}$ ) and crowding distance value (i.e.  $F_i(d_j)$ ).

❖  $o \prec_n s$ , if

✓  $o_{\text{rank}} < s_{\text{rank}}$

✓ or  $o_{\text{rank}} = s_{\text{rank}}$  and  $F_i(d_o) > F_i(d_s)$

More specifically, in this step, the organism with smaller rank is preferred. If the organisms share the same rank value, then the organism with greater crowding distance value is selected.

5. For  $m$  objectives, the mutualism (see Equations 3.1, 3.2 and 3.3), commensalism (see the Equation 3.4) and parasitism operators of the SOS algorithm are employed. The candidate optimum organism is selected based on the Pareto optimal dominance operator given in section 1.4.2. According to this operator, an organism dominates another one only if it is as good as the other in all objective function values, and if it is better than the other in at least one objective function value. If the new solutions obtained from the mutualism, commensalism and parasitism operators dominate the old ones, then these new solutions are replaced by the old ones. The old solutions are also moved to an advanced ecosystem  $AE$ . If the new solutions do not dominate each other or the old ones, then they are moved to the

$AE$ . This is done to ensure an elitist selection in further steps. This step is repeated for all organisms in the ecosystem.

6. The ecosystems  $E$  and  $AE$  are combined, obtaining a combined ecosystem  $CE$  of  $5N$  (i.e.  $CE = E \cup AE$ ). The  $CE$  is then sorted based on the non-domination sorting, crowding distance operator and crowded comparison operator given in the steps 2, 3 and 4, respectively.
7. Since the  $CE$  consists of the previous and current organisms, an elitist selection is conducted. The first front  $F_1$  includes the best non-dominated organisms in the  $CE$ . Hence, the organisms in this front are regarded as the most important ones. If the size of the  $F_1$  is smaller than that of the initial ecosystem  $N$ , then all organisms in the  $F_1$  are assigned to the next generation (i.e. ecosystem). The remaining members of the new ecosystem are selected from subsequent fronts. The selection continues with subsequent fronts until the ecosystem size of  $N$  is achieved. If the size of the last front to be selected exceeds the size  $N$ , the remaining members are selected based on the crowded comparison operator  $<_n$  (see Figure 12).
8. The ecosystem is improved with iterations between the steps 2 and 7 until predefined convergence criteria or a maximum iteration number is reached.

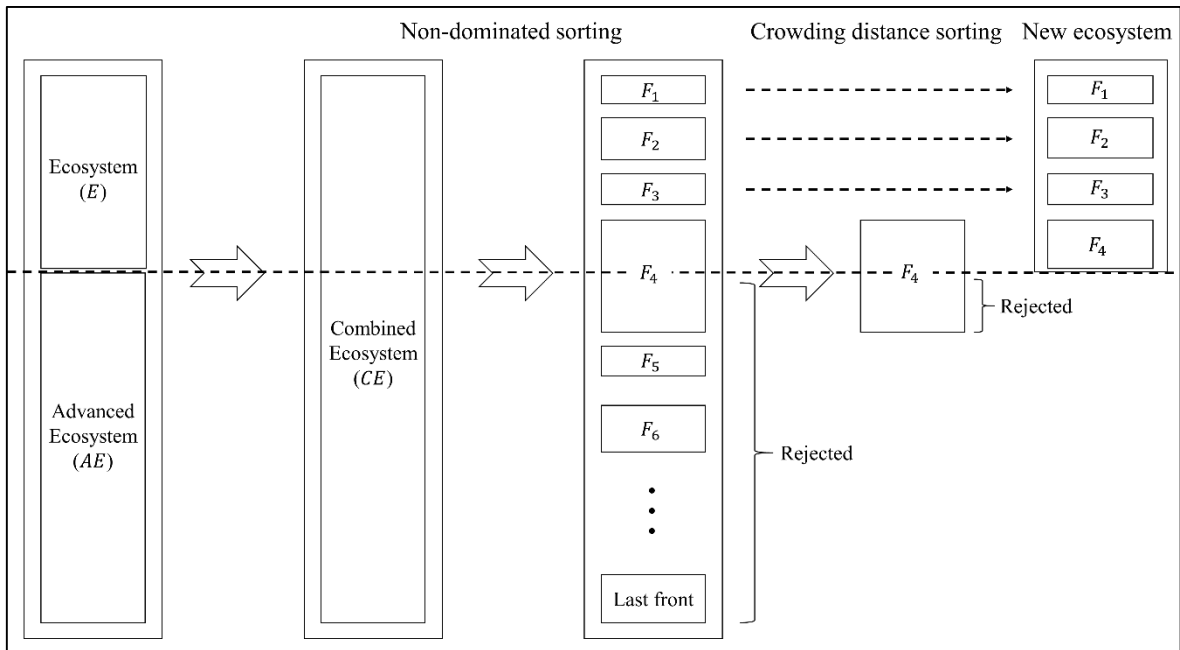


Figure 12. Generation of a new ecosystem

## 4. APPLICATION

### 4.1. Test Sites and Data

The performances of all pansharpening methods used in this thesis were tested on four test sites in Trabzon, Turkey. The site 1, a mixture of urban and rural areas, was captured by the WorldView-2 satellite, which offers a 50-cm PAN image and eight 2-m MS bands. The site 2, an area from the city centre, was captured by the IKONOS satellite, which offers a 1-m PAN image and four 4-m MS bands. The site 3, a rural area, was captured by the WorldView-2 satellite. The input MS data of the site 4 was a WorldView-2 image acquired in 2013. The input PAN image of this site was an orthophoto image, which was produced from 256 aerial images taken in 2013 from a RICOH GR DIGITAL IV digital camera mounted on a Gatewing X100 UAS. The 3-band 20-cm orthophoto was produced by using the Agisoft Photoscan Professional software. The input PAN data of the site 4 was calculated as the average of the bands of the orthophoto. The test sites are shown in Figure 13.

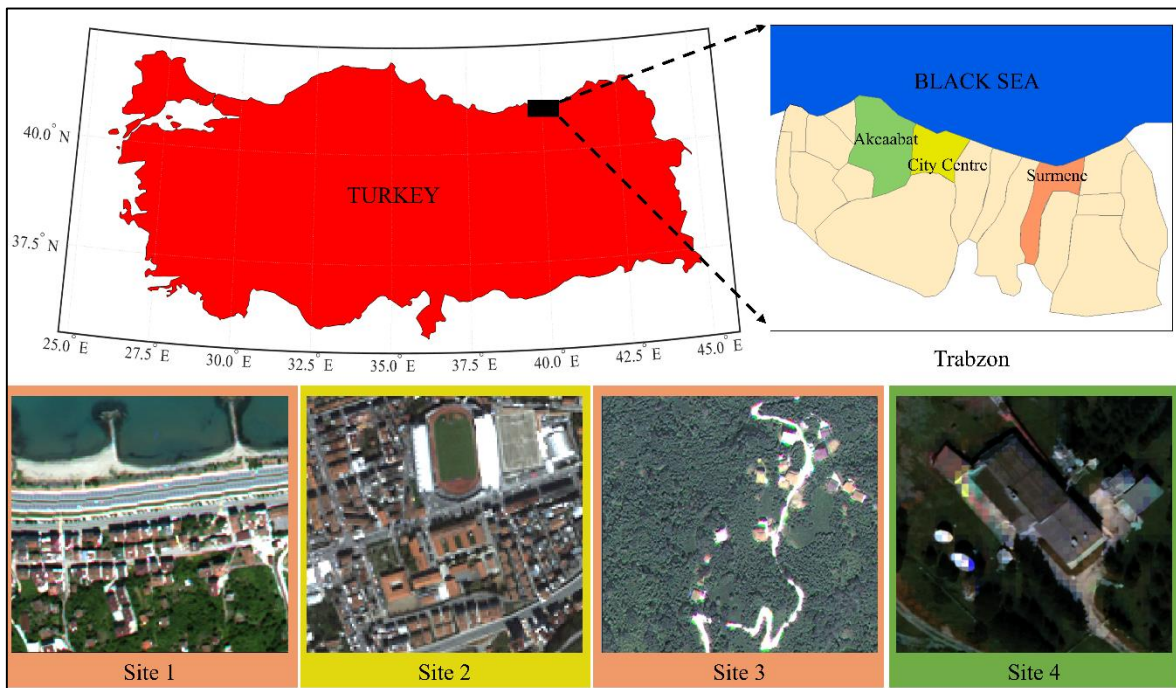


Figure 13. Test sites

The pansharpening was expected to be more challenging in the site 4, whose input MS and PAN images were taken from different sensors. In addition, the spatial resolution of the input PAN image (i.e. 20 cm) of this site was ten times better than the spatial resolution of the input MS data (2 m), which was another factor that made this site more challenging for pansharpening, compared to the other sites. Except for the 8-bit PAN data of the site 4, all images used in this thesis had a radiometric resolution of 11 bits. Table 1 summarizes the characteristics of the input images and test sites.

Table 1. Characteristics of the test sites and input images used

Site	Type	Input MS Image	Input PAN Image
1	Urban/Rural	WorldView-2 MS (2 m, 11 bits)	WorldView-2 PAN (50 cm, 11 bits)
2	Urban	IKONOS MS (4 m, 11 bits)	IKONOS PAN (1 m, 11 bits)
3	Rural	WorldView-2 MS (2 m, 11 bits)	WorldView-2 PAN (50 cm, 11 bits)
4	Urban/Rural	WorldView-2 MS (2 m, 11 bits)	Orthophoto PAN (20 cm, 8 bits)

## 4.2. Proposed SOS-SVR and SOS-IHS-DWT Methods

As may be recalled, the biggest problem with the conventional SVR and IHS-based pansharpening methods is that it is very hard for these methods to produce intensity components that share the same statistical characteristics as the input PAN image, resulting in a considerable amount of colour distortion. This, of course, encouraged the researchers to develop more efficient strategies to optimize the intensity components used by these methods. For example, Munechika et al., (1993) and Zhang (1999) utilized the regression analysis to achieve this. Hence, this thesis, for the first time in the literature, introduced to optimize the intensity components used by the SVR and IHS-DWT methods by estimating a weight for each MS band through the SOS algorithm. The proposed SOS-SVR and SOS-IHS-DWT methods were encoded in MATLAB environment.

### 4.2.1. SOS-SVR Method

The proposed SOS-SVR method was implemented as follows: (1) An initial ecosystem was randomly generated. Each organism of the ecosystem was a vector consisting of random numbers between 0 and 1. Since the input MS image of the sites 1, 2, 3 and 4 had 8, 4, 8 and

8 MS bands, the length of each organism was 8, 4, 8 and 8 for the sites 1, 2, 3 and 4, respectively. A 100-organism ecosystem was found to be sufficient for the sites 1 and 3, whereas an ecosystem size of 300 was found to be sufficient for the sites 2 and 4. (2) Each organism of the ecosystem was evaluated by using its values as the weights given in the Equation 2.2. Each intensity component calculated this way was used in the Equation 2.1 to produce the pansharpened images for the initial ecosystem. The RMSE metric was calculated between each pansharpening result and input MS image to evaluate the fitness of each organism (i.e. candidate solution). (3) It was checked whether a termination criterion or a maximum iteration number was reached. This study considered a termination criterion based on the difference between the global minimum value and fitness value within each iteration. Considering this, the stopping criterion was set to a difference value below  $1E-03$ . Theoretically, it was not possible to achieve this value, hence, a maximum iteration number of 350 was also defined to stop the iterations for all test sites. (4) The mutualism operator was employed using the Equations 3.1, 3.2 and 3.3 to generate new candidate solutions around the best candidate solution in the ecosystem. The mutualism phase, in this way, enabled the conduction of the exploitation operation in the search space. The fitness of each new candidate solution was then evaluated with the objective function in the way explained above. It was then checked whether new fitness values were better than the pre-interaction values. If the new fitness values of the organisms were better, then they were replaced by the old organisms, updating the ecosystem. (5) The commensalism operator was employed using the Equation 3.4 to increase the exploitation capability in the search space. Similar to the mutualism phase, the fitness of a new candidate solution was evaluated by using the objective function. If the new organism was fitter than the old one, the new organism was swapped by the old one. What makes the commensalism operator different than the mutualism is that it further enhances the exploitation capability in a wider range around the best solution, compared to the mutualism operator. (6) The parasitism operator was applied on some randomly selected candidate solutions to conduct a global search (i.e. exploration) in the search space. If the fitness of the generated parasite vectors were better, then the old vectors were killed in the ecosystem and the ecosystem was updating by adding the parasite vectors into it. (7) The iterations continue by applying the steps between (2) - (6) on new generations until the termination criterion or maximum iteration number was achieved. Table 2 shows the optimum band weights achieved by the SOS-SVR method for all test sites.

Table 2. Optimum band weights estimated by the SOS-SVR method

Site	MS Band							
	1	2	3	4	5	6	7	8
1	0.17	0.01	0.01	0.18	0.47	0.00	0.16	0.10
2	0.37	0.11	0.28	0.29				
3	0.10	0.23	0.05	0.26	0.13	0.00	0.11	0.20
4	0.23	0.25	0.12	0.18	0.04	0.06	0.05	0.07

The SOS algorithm searches for the best solutions in randomly generated search spaces. The mutualism, commensalism and parasitism operators used by the SOS algorithm update the ecosystems in a random way. Hence, the SOS algorithm results in different solutions each time it is run. However, a successful metaheuristic algorithm should provide solutions that are consistent with each other. To assess the consistency of the SOS algorithm, Universal Image Quality Index (UIQI) (Wang and Bovik, 2002), Information Content Weighted SSIM (IW-SSIM) (Wang and Li, 2011), CC (Zeng et al., 2010), SSIM (Wang et al., 2004) and Spectral Residual Based Similarity (SR-SIM) (Zhang and Li, 2012) metric values were calculated to assess the colour quality of thirty pansharpened images produced by the SOS-SVR method for the site 1. The calculated metric values are given in Figure 14. The figure shows that the SOS algorithm returned very consistent metric values for all pansharpened images. The standard deviations of the metric values were also computed to see to what degree the metric values were diverged from each other. The standard deviations of 0.0069, 0.0042, 0.0024, 0.0041 and 0.0012 were calculated for the UIQI, IW-SSIM, CC, SSIM and SR-SIM metrics, respectively. On the other hand, to assess the consistency in terms of spatial fidelity, the spatial ERGAS (SERGAS) (Lillo-Saavedra et al., 2005; Gonzalo-Martin and Lillo-Saavedra, 2011) metric was calculated for the same thirty pansharpened images produced by the SOS-SVR method for the site 1. Figure 15 depicts the calculated SERGAS values. As seen in the figure, the SOS algorithm returned SERGAS values ranging between 10.8 and 11.5. A standard deviation of 0.1568 was computed for the SERGAS values, which also demonstrates that the SERGAS values did not vary too much. Since the standard deviations computed from the spectral and spatial quality evaluation metric values were so small, the SOS algorithm can be said to have produced pansharpened images that were very consistent with each other. This reveals that the analysts do not have to run the SOS algorithm so many times to achieve the optimum pansharpening result. It is

worth noting that this conclusion applies only for pansharpener problems. Some other engineering problems may necessitate the execution of the SOS algorithm so many times.

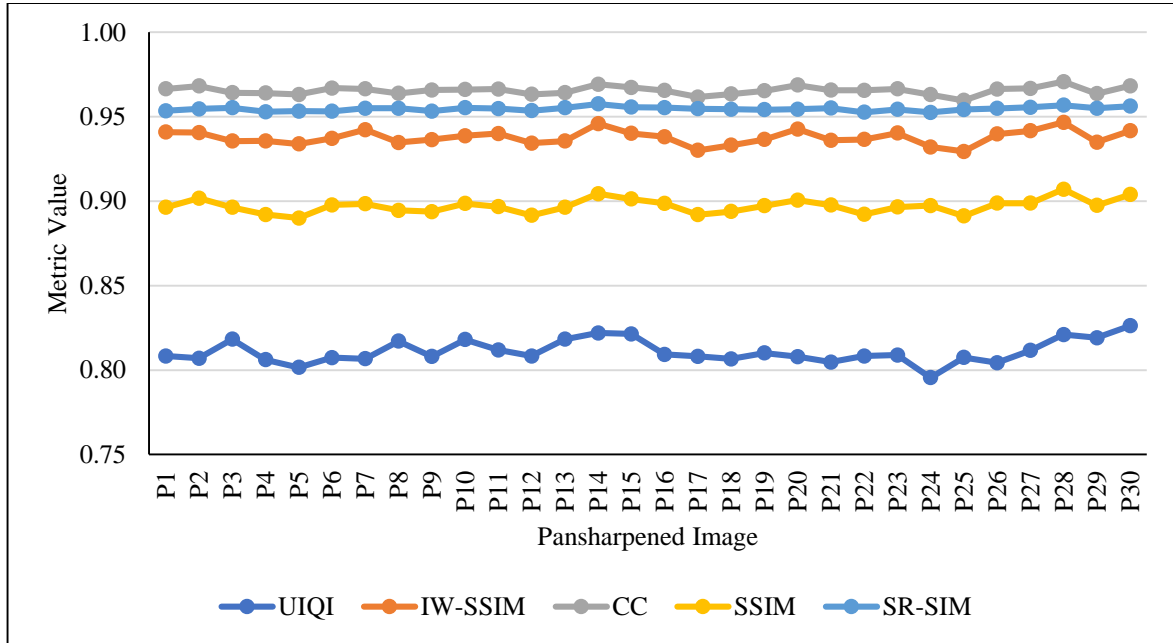


Figure 14. UIQI, IW-SSIM, CC, SSIM and SR-SIM values computed for thirty pansharpener images produced for the site 1

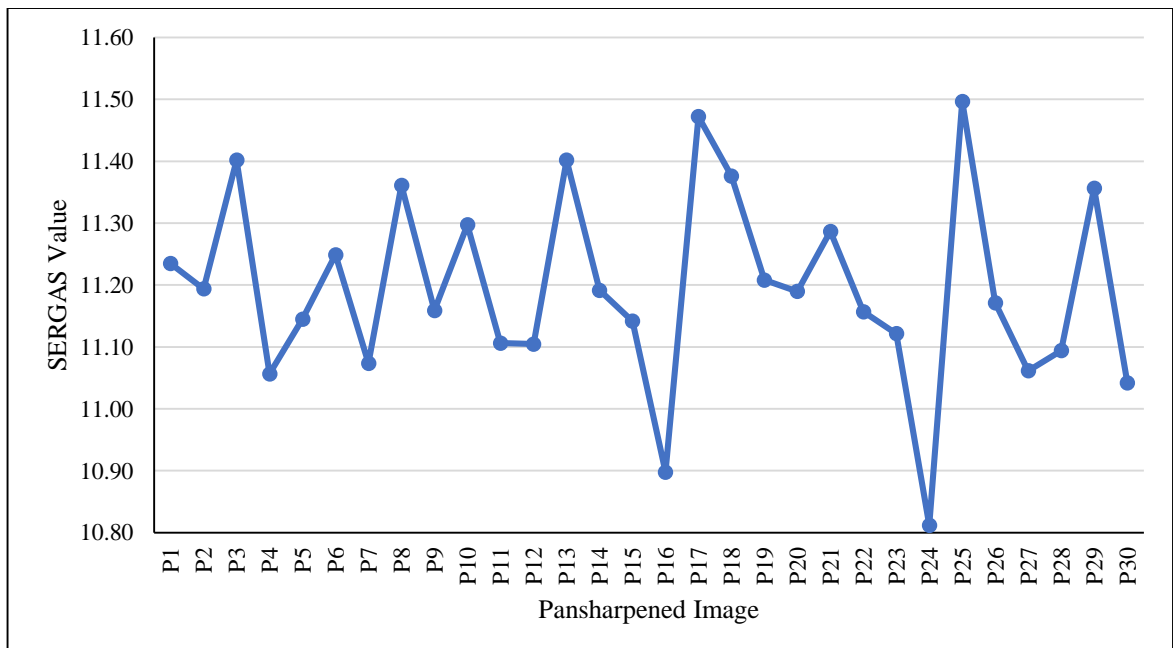


Figure 15. SERGAS values obtained for thirty pansharpener images produced for the site 1

#### 4.2.2. SOS-IHS-DWT method

The proposed SOS-IHS-DWT method employed the same steps applied for the SOS-SVR method. The SOS-IHS-DWT method differed from the SOS-SVR method in the way it calculated the objective function in the step (2). In this step, the proposed SOS-IHS-DWT method calculated the pansharpened bands within trilateral band combinations. For example, since the input MS data of the sites 1, 3 and 4 had a total of eight MS bands, the SOS-IHS-DWT was applied in three stages in these sites, first pansharpening the MS bands 1-2-3 and input PAN image, second pansharpening the MS bands 4-5-6 and input PAN image, and third pansharpening the MS bands 6-7-8 and input PAN image. Since no statistically significant difference was observed in the final pansharpened products produced by the band 6 derived from the stages two and three, the band 6 derived from the second stage was decided to be used for the sites 1, 3 and 4. A similar situation was also true for the site 2. The proposed SOS-IHS-DWT method was applied in two stages in this site, first pansharpening the MS bands 1-2-3 and input PAN image, second pansharpening the MS bands 2-3-4 and input PAN image. In this site, the bands 2 and 3 derived from the first stage were decided to be used for the site 2. The SOS-IHS-DWT method applied the forward and inverse IHS transform by the Equations 2.3, 2.4, 2.5 and 2.6. The main purpose of the SOS-IHS-DWT method was to estimate a weight for each MS band to compute the optimum intensity component. The histogram of the input PAN image was matched to that of the intensity component to retain the spectral information after pansharpening. A DWT is applied on the intensity component and histogram-matched PAN image using the Equations 2.55, 2.56, 2.57 and 2.58. The Equation 2.55 enabled the production of the approximation component within each decomposition, whereas the Equations 2.56, 2.57 and 2.58 allowed for the generation of the components including the high frequency details in horizontal, vertical and diagonal directions within each decomposition. The last approximation component achieved for the intensity component was swapped by its average with the last approximation component achieved for the histogram-matched PAN image. An intermediary intensity component was generated by applying an inverse DWT using the final approximation component and high-frequency detail images. An inverse IHS transform was employed using the intermediary intensity component and original hue and saturation components to generate the pansharpened image. Figure 16 demonstrates the flowchart for the SOS-SVR and SOS-IHS-DWT methods.

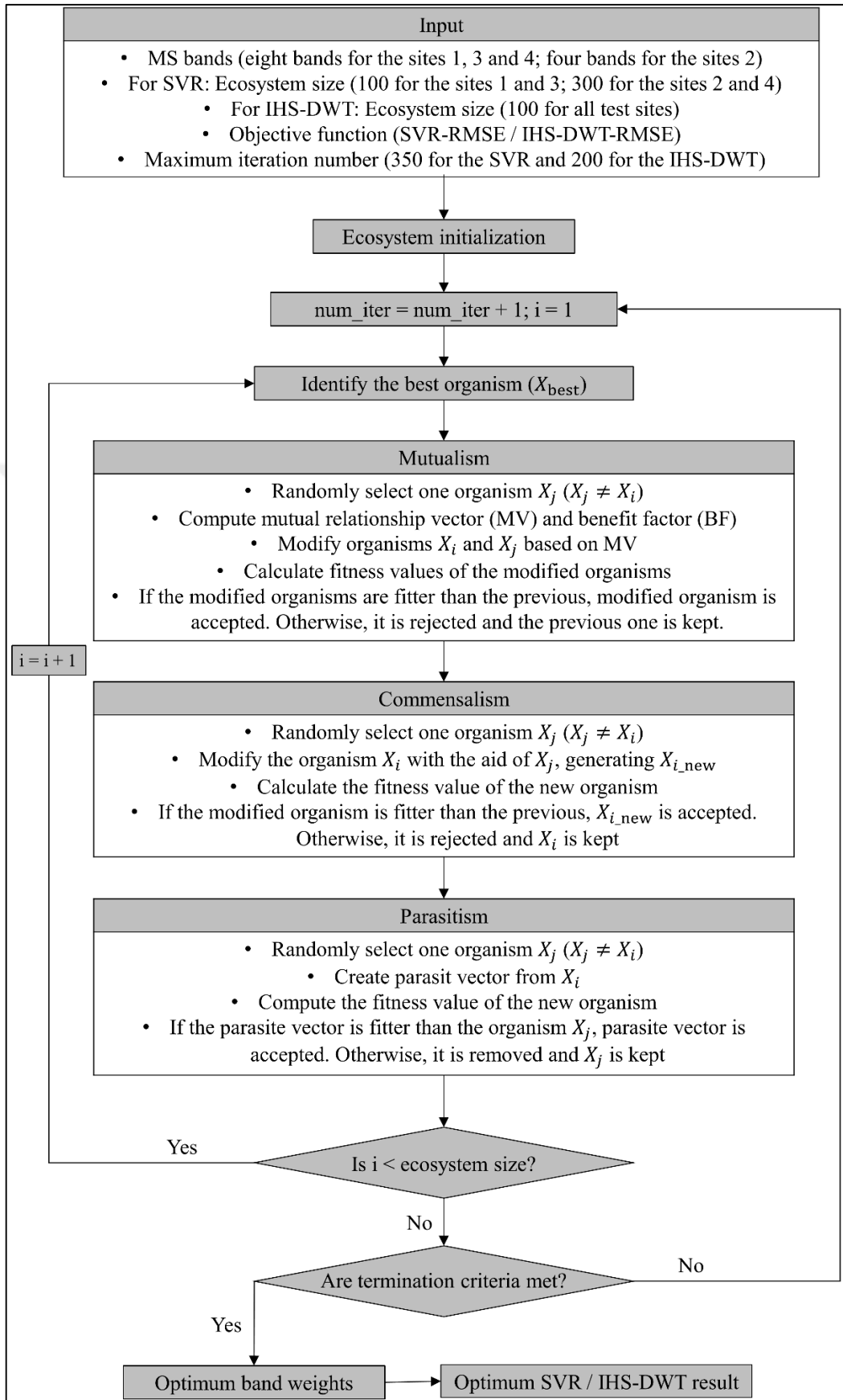


Figure 16. Flowchart for the SOS-SVR and SOS-IHS-DWT methods

Apart from these, the SOS-IHS-DWT method applied the same steps between (2) and (7) given for the SOS-SVR method. Table 3 shows the optimum band weights achieved by the SOS-IHS-DWT method for all test sites.

Table 3. Optimum band weights estimated by the SOS-IHS-DWT method

Site	MS Band							
	1	2	3	4	5	6	7	8
1	0.73	0.77	0.52	0.74	0.74	0.71	0.72	0.65
2	0.43	0.28	0.25	0.58				
3	0.78	0.83	0.58	1.00	1.00	1.00	0.79	0.51
4	0.68	0.69	0.65	0.63	0.86	0.84	0.46	1.00

### 4.3. Proposed MOSOS-SVR and MOSOS-IHS-DWT Methods

The biggest problem with the pansharpening methods is that they focus either on keeping the colour features or on sharpening the images, which makes it very hard to find the best compromise between the colour and spatial detail content of the pansharpened images. This leads us to the fact that the pansharpening can be considered as a multi-objective problem such that one objective is to keep the colour features properly and the other one is to produce the sharpest image possible. This thesis utilized the recently introduced MOSOS algorithm to take the pansharpening into consideration as a two-objective problem. The proposed MOSOS-SVR and MOSOS-IHS-DWT methods were encoded in MATLAB environment.

#### 4.3.1. MOSOS-SVR Method

The MOSOS-SVR method was implemented as follows: (1) An initial ecosystem of 75 randomly generated organisms was generated for all test sites. Each organism consisted of  $b$  random numbers between 0 and 1,  $b$  being the total number of bands for the input MS images, which were 8, 4, 8 and 8 for the sites 1, 2, 3 and 4, respectively. (2) The RMSE and Structural Similarity Index (SSIM) (Wang et al., 2004) were selected as the objective functions to keep the colour content of the MS images and to transfer the spatial information of the PAN images, respectively. (3) Each organism of the ecosystem was the evaluated by

using its values as the weights given in the Equation 2.2. Each intensity component calculated this way was used in the Equation 2.1 to produce the pansharpened images for the initial ecosystem. The RMSE metric was calculated between each pansharpening result and MS data to evaluate the fitness of each organism (i.e. candidate solution) in terms of colour conservation. The SSIM metric was employed between the pansharpening result and input PAN image to assess the fitness of each organism in terms of spatial fidelity. (4) The initial ecosystem was initially sorted based on non-domination and crowding distance operators to obtain the rank and crowding distance value of each organism, respectively. As may be recalled, the non-domination operator divides the ecosystem into Pareto fronts, the first fronts are being the most important ones, which means that they include the non-dominated organisms. On the other hand, the crowding distance operator is used (see the Equation 3.5) to assign a distance value for each organism on each front. The crowded comparison operator ( $\prec_n$ ) then sorts the organisms based on the computed rank and crowding distance values to specify the best organism in the ecosystem. (5) The mutualism operator was employed between the first member of the ecosystem and a randomly selected organism using the Equations 3.1, 3.2 and 3.3 to generate new candidate solutions around the best candidate solution in the ecosystem. In this step, the two new organisms achieved by the mutualism operator are compared against the old organisms with respect to the Pareto optimal dominance operator. If the new organisms dominate the old ones, then these organisms are replaced by the old ones in the ecosystem and the old organisms are transferred into the advanced ecosystem. If the new organisms cannot dominate the old ones, then the ecosystem remains the same and these new organisms are transferred into the advanced ecosystem. (6) The commensalism operator was employed between the first member of the ecosystem and a randomly selected organism using the Equation 3.4 to generate a new organism. If this new organism dominates the old one, then it is swapped by the old one in the ecosystem and the old organism is transferred to the advanced ecosystem. If the old organism dominates the new one, then the ecosystem remains the same and the new organism is transferred into the advanced ecosystem. (7) The parasitism operator was applied between two randomly selected organisms in the ecosystem. The Pareto optimal dominance operator was used to investigate whether or not these organisms dominate the each other. (8) The steps between (4) and (7) were applied iteratively for all organisms in the ecosystem, which resulted in a total of  $4N$  organisms ( $N = 75$ ). (9) The ecosystem and advanced ecosystem were combined to produce a combined ecosystem of size  $5N$ . (10) The combined ecosystem was sorted

based on non-domination. The first front with a rank value of 1 can be said to have the best non-dominated set in the combined ecosystem. Here, if the size of the first front is smaller than that of the initial ecosystem (i.e.  $N$ ), then all the organisms on this front should be selected for the new ecosystem. The remaining organisms are selected from subsequent fronts to achieve a final  $N$ -sized ecosystem. For the last front to be added, if the size of  $N$  is exceeded, then the organisms with greater crowding distance values are selected to ensure the completion of the size of  $N$ . (11) For the new ecosystem, the steps between (3) and (10) were repeated until the predefined maximum iteration number of 100 was reached in all test sites. (12) The obtained optimal Pareto front includes the organisms that are not dominated by any other organisms and provide the best balance between the objective functions.

The MOSOS-SVR method resulted in a total of 75 non-dominated optimal solutions, which were all equally important for the pansharpening problem. These solutions varied between the one that provided the spectrally optimum result and the one that resulted in the spatially optimum result, with the aim to provide options for the users for their application. This thesis focused on only three of them, the one that led to the best colour fidelity, the one that produced the sharpest image and the one that provided a moderate colour and spatial detail fidelity. Table 4 presents the band weights estimated by the MOSOS-SVR method for the test sites.

Table 4. Optimum band weights estimated by the MOSOS-SVR method

Site	Image	MS Band							
		1	2	3	4	5	6	7	8
1	Spectrally optimum	0.00	0.14	0.21	0.16	0.37	0.17	0.08	0.04
	Optimum	0.13	0.08	0.13	0.16	0.21	0.19	0.10	0.04
	Spatially optimum	0.26	0.15	0.04	0.05	0.03	0.18	0.15	0.12
2	Spectrally optimum	0.00	0.23	0.36	0.38				
	Optimum	0.12	0.39	0.23	0.26				
	Spatially optimum	0.37	0.17	0.33	0.16				
3	Spectrally optimum	0.00	0.08	0.36	0.21	0.21	0.09	0.18	0.00
	Optimum	0.06	0.06	0.30	0.18	0.08	0.10	0.16	0.04
	Spatially optimum	0.18	0.01	0.14	0.08	0.04	0.18	0.16	0.11
4	Spectrally optimum	0.00	0.25	0.01	0.16	0.01	0.00	0.01	0.00
	Optimum	0.01	0.32	0.00	0.15	0.01	0.00	0.00	0.00
	Spatially optimum	0.18	0.22	0.01	0.15	0.05	0.07	0.18	0.19

### 4.3.2. MOSOS-IHS-DWT Method

As known, the previously introduced SOS-SVR, SOS-IHS-DWT and MOSOS-SVR methods aimed to find the optimum weights for the input MS bands to achieve the optimum intensity components. In addition to the MS bands, the proposed MOSOS-IHS-DWT method also estimates weights for the last approximation components obtained for the intensity component and histogram-matched PAN image. As may be remembered, the original IHS-DWT method and SOS-IHS-DWT method replace the last approximation component achieved for the intensity component by its average with the last approximation component achieved for the histogram-matched PAN image. To sum up, the MOSOS-IHS-DWT method optimizes a total of five variables, including three MS bands and two approximation components. The main reason for this was to ensure a more robust balance between the colour and spatial detail content.

The MOSOS-IHS-DWT method was applied as follows: (1) An initial ecosystem of size 50 was randomly generated for all test sites. Since the IHS pansharpening procedure used in this thesis was able to fuse three MS bands at a time and there were two approximation components to be optimized, each organism of the ecosystem comprised a total of five members. (2) An IHS transform was applied on three input MS bands using the Equations 2.3, 2.4 and 2.5. Note that the MOSOS-IHS-DWT method performs with trilateral band combinations, just like the IHS-DWT and SOS-IHS-DWT methods. (3) The histogram of the input PAN image was matched to that of the intensity component obtained in the previous step. (4) A DWT was then employed on the intensity component and histogram-matched PAN image (see the Equations 2.55, 2.56, 2.57 and 2.58). The number of DWTs was defined as the half of the spatial resolution ratio between the input images. Hence, the number of DWTs was calculated as 2, 2, 2 and 5 for the test sites 1, 2, 3 and 4, respectively. (5) The last approximation component achieved for the intensity component was swapped by its weighted sum with the last approximation component achieved for the histogram-matched PAN image. (6) An inverse DWT was applied using the final approximation component and high-frequency detail images to generate a new intensity component. (7) An inverse IHS transform was employed (see the Equation 2.6) using the new intensity component, hue component and saturation component to produce three pansharpened bands. (8) The spectral quality of the pansharpened bands were assessed through the RMSE determined between the MS bands and pansharpened bands, whereas the spatial fidelity was

evaluated via the SSIM determined between the PAN image and pansharpened bands. (9) The ecosystem was sorted based on the non-domination sorting and crowding distance operators and the best organism was selected based on the crowded comparison operator ( $\prec_n$ ). (10) The mutualism, commensalism and parasitism operations were applied as in the MOSOS-SVR method to generate new organisms, generating an advanced ecosystem and modifying the existing ecosystem. (11) The steps between (2) and (10) were repeated for all organisms in the ecosystem. (12) The obtained advanced ecosystem and modified ecosystem were combined, leading to a  $5N$ -sized ecosystem. (13) The combined ecosystem was sorted with respect to the non-domination sorting and crowding distance operators. To generate a new ecosystem of an exact size of  $N$ , the organisms were selected starting from the first front. This selection was conducted through the crowded comparison operator ( $\prec_n$ ), which was explained in the step (10) of the MOSOS-SVR method (see Section 4.3.1). (14) The steps between (2) and (13) were repeated until a predefined maximum iteration number of 100 was achieved for all test sites. Figure 17 depicts the flowchart for the MOSOS-SVR and MOSOS-IHS-DWT methods.

Table 5. Optimum band weights estimated by the MOSOS-IHS-DWT method

Site	Image	MS Band							
		1	2	3	4	5	6	7	8
1	<b>Spectrally Optimum</b>	0.59	0.66	0.51	0.62	0.66	0.61	0.67	0.58
	<b>A Spectrally Good</b>	0.36	0.55	0.58	0.20	0.79	0.28	0.98	0.45
	<b>Optimum</b>	0.30	0.67	0.69	0.20	0.79	0.20	0.78	0.21
	<b>A Spatially Good</b>	0.14	0.87	0.97	0.13	0.88	0.06	0.84	0.05
	<b>Spatially Optimum</b>	0.01	0.82	0.99	0.06	0.96	0.01	0.96	0.01
2	<b>Spectrally Optimum</b>	1.00	0.51	0.63	0.62				
	<b>A Spectrally Good</b>	0.61	0.25	0.63	0.52				
	<b>Optimum</b>	0.36	0.11	0.66	0.29				
	<b>A Spatially Good</b>	0.37	0.01	0.79	0.05				
	<b>Spatially Optimum</b>	0.09	0.01	0.78	0.01				
3	<b>Spectrally Optimum</b>	0.72	0.81	0.62	0.74	0.88	0.81	0.56	0.53
	<b>A Spectrally Good</b>	0.56	0.86	0.76	0.20	0.83	0.38	0.83	0.65
	<b>Optimum</b>	0.50	0.91	0.71	0.07	0.84	0.26	0.89	0.77
	<b>A Spatially Good</b>	0.16	0.65	0.77	0.01	0.65	0.11	0.72	0.25
	<b>Spatially Optimum</b>	0.01	1.00	0.81	0.13	0.58	0.03	0.44	0.01
4	<b>Spectrally Optimum</b>	0.92	0.99	0.86	0.86	0.96	0.90	0.71	0.67
	<b>A Spectrally Good</b>	0.76	0.56	0.70	0.74	0.67	0.92	0.84	0.85
	<b>Optimum</b>	0.14	0.30	0.67	0.07	0.20	0.22	0.29	0.16
	<b>A Spatially Good</b>	0.08	0.26	0.57	0.38	0.83	0.12	0.01	0.13
	<b>Spatially Optimum</b>	0.01	0.92	0.13	0.01	1.00	0.01	0.01	0.01

All aforementioned steps were applied on trilateral band combinations. This means that these steps were applied three times for the sites 1, 3 and 4; and two times for the site 2. Hence, three different Pareto fronts were obtained for the sites 1, 3 and 4; and two different

Pareto front was obtained for the site 2. Each of these Pareto fronts included 50 different non-dominated solutions. Optimizing the last approximation components obtained for the intensity component and histogram-matched PAN image in addition to three MS bands increased the variety in the solution space. Hence, five different solutions were decided to be given, including the spectrally optimum one, a spectrally good one, a spectrally and spatially optimum one, a spatially good one and the spatially optimum one. Table 5 demonstrates the band weights estimated by the MOSOS-IHS-DWT method for the test sites and Table 6 shows the optimum weights estimated by the MOSOS-IHS-DWT method for the approximation components computed from the intensity components and histogram-matched PAN images.

Table 6. Optimum weights estimated by the MOSOS-IHS-DWT method for the approximation components computed from the intensity components and histogram-matched PAN images

Site	Image	Bands 1-2-3		Bands 4-5-6		Bands 6-7-8	
		ACHMP	ACI	ACHMP	ACI	ACHMP	ACI
1	Spectrally Optimum	0.01	1.00	0.01	1.00	0.01	1.00
	A Spectrally Good	0.26	0.77	0.53	0.76	0.20	0.83
	Optimum	0.61	0.44	0.80	0.54	0.41	0.64
	A Spatially Good	0.81	0.26	0.99	0.61	0.67	0.34
	Spatially Optimum	1.00	0.02	1.00	0.88	0.84	0.09
Site	Image	Bands 1-2-3		Bands 2-3-4			
		ACHMP	ACI	ACHMP	ACI		
2	Spectrally Optimum	0.02	1.00	0.01	0.99		
	A Spectrally Good	0.28	0.74	0.29	0.71		
	Optimum	0.57	0.47	0.63	0.39		
	A Spatially Good	0.79	0.23	0.89	0.13		
	Spatially Optimum	0.99	0.01	0.98	0.01		
Site	Image	Bands 1-2-3		Bands 4-5-6		Bands 6-7-8	
		ACHMP	ACI	ACHMP	ACI	ACHMP	ACI
3	Spectrally Optimum	0.01	1.00	0.01	1.00	0.01	1.00
	A Spectrally Good	0.35	0.71	0.32	0.95	0.27	0.62
	Optimum	0.44	0.64	0.74	0.97	0.33	0.46
	A Spatially Good	0.87	0.32	1.00	0.98	0.42	0.32
	Spatially Optimum	1.00	0.39	1.00	1.00	0.54	0.03
Site	Image	Bands 1-2-3		Bands 4-5-6		Bands 6-7-8	
		ACHMP	ACI	ACHMP	ACI	ACHMP	ACI
4	Spectrally Optimum	0.01	1.00	0.01	1.00	0.01	1.00
	A Spectrally Good	0.23	0.52	0.14	0.56	0.01	0.54
	Optimum	0.16	0.55	0.19	0.45	0.01	0.61
	A Spatially Good	0.27	0.28	0.22	0.53	0.09	0.34
	Spatially Optimum	0.38	0.01	0.55	0.03	0.18	0.01
ACHMP: Approximation component for histogram-matched PAN image							
ACI: Approximation component for intensity component							

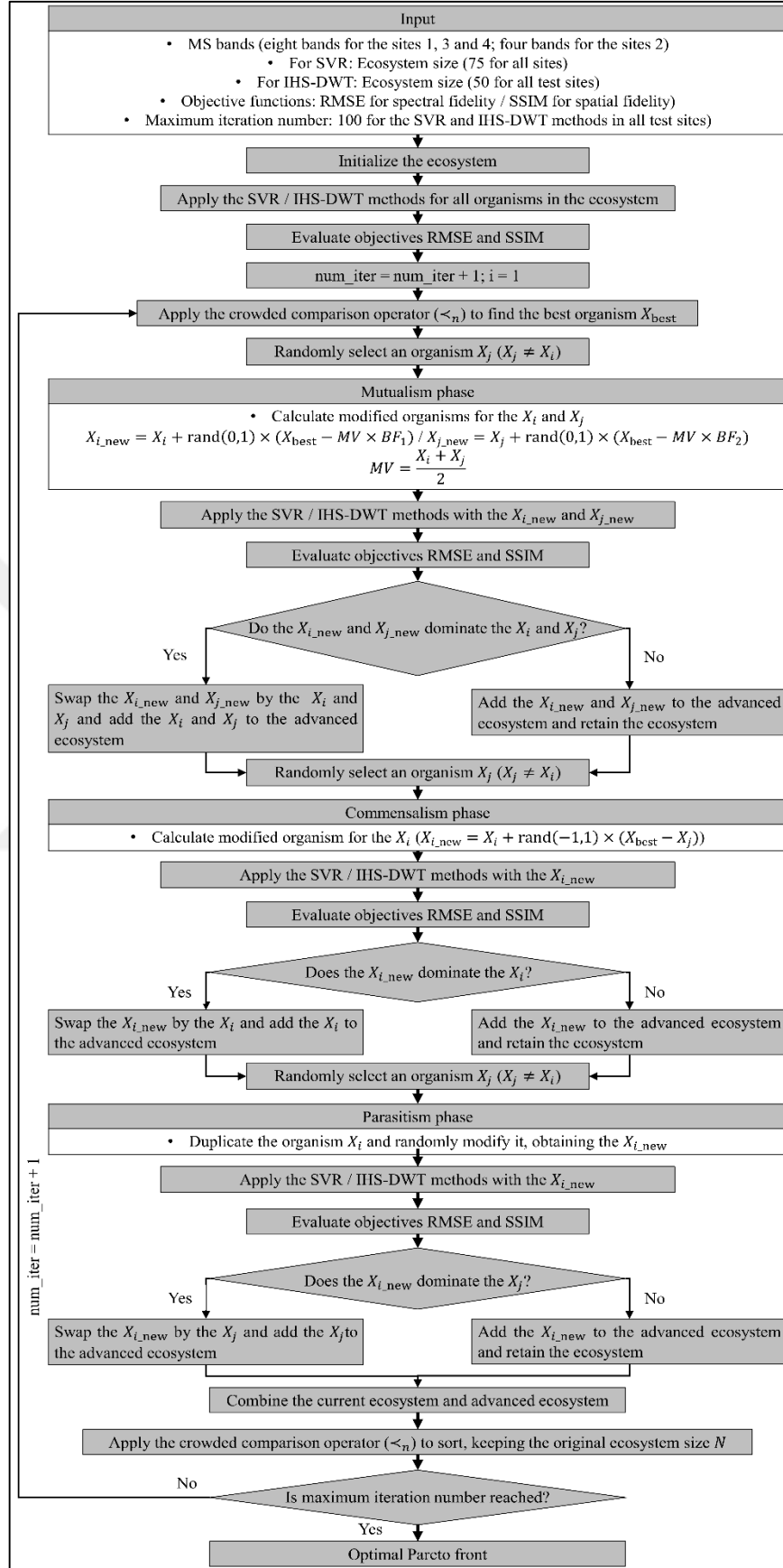


Figure 17. Flowchart for the MOSOS-SVR and MOSOS-IHS-DWT methods

#### 4.4. Quality Investigation

The spectral quality of each pansharpened image was investigated by using the ERGAS (Wald, 2000), SSIM (Wang et al., 2004), Spectral Residual Based Similarity (SR-SIM) (Zhang and Li, 2012), Information Content Weighted SSIM (IW-SSIM) (Wang and Li, 2011), Spectral Angular Mapper (SAM) (Alparone et al., 2006; 2007), Universal Image Quality Index (UIQI) (Wang and Bovik, 2002), Spectral Information Divergence (SID) (Strait et al., 2008) and CC (Zeng et al., 2010) metrics.

Table 7. Mathematical definitions of the spectral quality evaluation metrics

Metric	Formula	Optimum
SR-SIM	$SR - SIM = \frac{\sum_{x \in \Omega} S(x) \cdot R_m(x)}{\sum_{x \in \Omega} R_m(x)}$	1
ERGAS	$ERGAS = 100 \frac{h}{l} \sqrt{\frac{1}{K} \sum_{k=1}^K \left( \frac{RMSE_k}{\mu(MS_k)} \right)^2}$	0
SID	$SID = D(x  y) + D(y  x)$ $D(x  y) = \sum p_i \log \left( \frac{p_i}{q_i} \right) \quad D(y  x) = \sum q_i \log \left( \frac{q_i}{p_i} \right)$ $p_j = \frac{x_j}{\sum_{i=1}^K x_i} \quad q_j = \frac{y_j}{\sum_{i=1}^K y_i}$	0
SAM	$SAM(x, y) \triangleq \arccos \left( \frac{\langle x, y \rangle}{\ x\ _2 \cdot \ y\ _2} \right)$	0
UIQI	$UIQI = \frac{4\mu_x\mu_y\sigma_{xy}}{(\mu_x^2 + \mu_y^2)(\sigma_x^2 + \sigma_y^2)}$	1
SSIM	$SSIM = \frac{(2\mu_x\mu_y + C_1)(2\sigma_{xy} + C_2)}{(\mu_x^2 + \mu_y^2 + C_1)(\sigma_x^2 + \sigma_y^2 + C_2)}$	1
IW-SSIM	$IW - SSIM_j = \frac{\sum_i w_{j,i} c(x_{j,i}, y_{j,i}) s(x_{j,i}, y_{j,i})}{\sum w_{j,i}}$ $IW - SSIM = \prod (IW - SSIM_j)^{B_j}$	1
CC	$CC = \frac{\sum_{m,n} (MS_{mn} - \mu(MS))(P_{mn} - \mu(P))}{\sqrt{(\sum_{m,n} (MS_{mn} - \mu(MS))^2 (\sum_{m,n} (P_{mn} - \mu(P))^2)}}$	1

where,  $PAN$  is the input PAN image,  $MS$  denotes the MS image,  $P$  denotes the pansharpened image,  $pn$  denotes the total number of pixels,  $l$  denotes the spatial resolution of the MS data,  $h$  denotes the spatial resolution of the PAN data,  $K$  denotes the total number of bands,  $M$  denotes the mean radiance,  $\mu$  refers to mean,  $\sigma$  refers to variance,  $y$  is a pixel vector in the PAN data,  $x$  is a pixel vector in the MS data,  $w$  denotes the information content weight,  $\Omega$  refers to the image spatial domain,  $S(x)$  denotes the local similarity and  $R_m(x) = \max(R_1(x), R_2(x))$  is used to weighting the importance of  $S(x)$ .

Wald et al., (1997) proposed three protocols regarding the investigation of the quality of the pansharpened images. The first of these protocols have been adopted in a large number

of studies (Alparone et al., 2008; Yilmaz and Gungor, 2016b; Delleji et al., 2016; Dou, 2018). This protocol states that any pansharpened image degraded to the size of the input MS data should match the input MS data (Wald et al., 1997). Hence, in this thesis, the aforementioned spectral (i.e. colour) quality evaluation metrics were calculated between the MS data and degraded pansharpened images. The mathematical definitions of the used spectral quality evaluation metrics are given in Table 7.

The spatial fidelity of each pansharpening result was assessed through the CC, spatial correlation coefficient (SCC) (Zhou et al., 1998) and spatial ERGAS (SERGAS) (Lillo-Saavedra et al., 2005; Gonzalo-Martin and Lillo-Saavedra, 2011) metrics computed between the pansharpened image and corresponding input PAN data. The SCC metric applies a Laplacian filter on both the pansharpened image and input PAN image and calculates the CC between these two filtered data. On the other hand, unlike the ERGAS metric, the SERGAS metric incorporates the input PAN image into the evaluation, utilizing the spatial RMSE (Gonzalo and Lillo-Saavedra, 2008) computed between the pansharpened bands and corresponding PAN image. Table 8 presents the mathematical definitions of the spatial quality evaluation metrics employed in this thesis.

Table 8. Mathematical definitions of the spatial quality evaluation metrics

Metric	Formula	Optimum
CC	$CC = \frac{\sum_{m,n}(PAN_{mn} - \mu(PAN))(P_{mn} - \mu(P))}{\sqrt{(\sum_{m,n}(PAN_{mn} - \mu(PAN))^2 (\sum_{m,n}(P_{mn} - \mu(P))^2)}}$	1
SCC	$SCC = \frac{\sum_{m,n}(\overline{PAN}_{mn} - \mu(\overline{PAN}))(\overline{P}_{mn} - \mu(\overline{P}))}{\sqrt{(\sum_{m,n}(\overline{PAN}_{mn} - \mu(\overline{PAN}))^2 (\sum_{m,n}(\overline{P}_{mn} - \mu(\overline{P}))^2)}}$	1
SERGAS	$SERGAS = 100 \frac{h}{l} \sqrt{\frac{1}{K} \sum_{k=1}^K \left( \frac{SRMSE_k}{\mu(PAN_k)} \right)^2}$ $SRMSE = \frac{1}{pn} \sqrt{\sum_{f=1}^{pn} (PAN(f) - P(f))^2}$	0

where,  $PAN$  is the input PAN image,  $P$  is the pansharpened image,  $pn$  is the total number of pixels,  $l$  is the spatial resolution of the MS data,  $h$  is the spatial resolution of the PAN data,  $K$  denotes the total number of bands,  $\mu$  refers to mean,  $\overline{PAN}$  is the Laplacian filtered PAN image and  $\overline{P}$  is the Laplacian filtered pansharpened image.

## **5. RESULTS**

This section presents the pansharpener results of the proposed methods. This section also compares the performances of the proposed methods against those of the other pansharpener methods used.

The aim of pansharpener process is to increase the spatial structure content while preserving the colour features of the MS data. Therefore, the spectral and spatial fidelity of the pansharpener images should be evaluated to see to what degree the pansharpener process become successful. Hence, in this section, the colour and spatial detail qualities of the pansharpener images were evaluated qualitatively and quantitatively.

### **5.1. Qualitative Evaluation**

Figures 18-33 show the BRV, MIHS, HPF, BDS, PCA, GS, HCS, SFIM, LMM, ATWT, AWLP, CB, DWT, IHS-DWT, SOS-SVR and SOS-IHS-DWT results of all test sites for colour quality evaluation, respectively. Figures 34, 35, 36 and 37 show the MOSOS-SVR results of the sites 1, 2, 3 and 4 for spectral quality evaluation, respectively. These figures show the spectrally optimum, spatially optimum and optimum MOSOS-SVR results for the test sites. Figures 38, 39, 40 and 41 depict the MOSOS-IHS-DWT results of the sites 1, 2, 3 and 4 for colour quality evaluation, correspondingly. These figures depict the spectrally optimum result, a spectrally good result, optimum result, a spatially good result and spatially optimum result for the test sites. Figures 42-57 demonstrated the zoomed-in BRV, MIHS, HPF, BDS, PCA, GS, HCS, SFIM, LMM, ATWT, AWLP, CB, DWT, IHS-DWT, SOS-SVR and SOS-IHS-DWT results of all test sites for spatial quality evaluation, respectively. Figures 58, 59, 60 and 61 depict the zoomed-in MOSOS-SVR results of the sites 1, 2, 3 and 4 for spatial fidelity evaluation, correspondingly. These figures show the spectrally optimum, spatially optimum and optimum MOSOS-SVR results for the test sites. Figures 62, 63, 64 and 65 show the zoomed-in MOSOS-IHS-DWT results of the sites 1, 2, 3 and 4 for spatial quality evaluation, respectively. These figures depict the spectrally optimum result, a spectrally good result, optimum result, a spatially good result and spatially optimum result for the test sites.

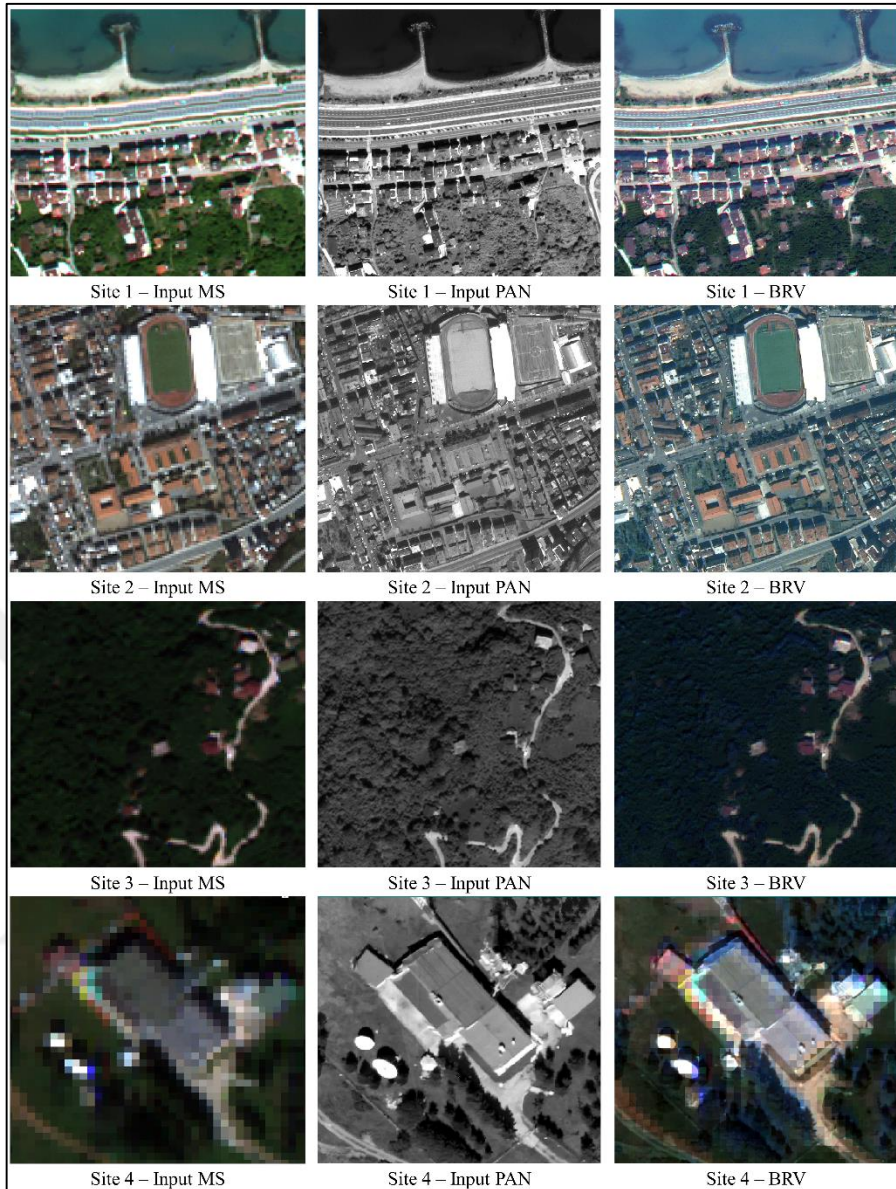


Figure 18. BRV results for the test sites

As seen in Figure 18, the BRV method caused significant colour distortions in all test sites. In the site 1, the BRV method could not manage to preserve the colours of the water, vegetation and building rooftops. In the site 2, the BRV method partially succeeded in keeping the colours of the building rooftops. However, the colours of the vegetation and road features were not preserved in this site. In the site 3, the BRV method caused significant changes in the colours of the vegetation and building rooftops. The BRV method, on the other hand, caused considerable colour distortions in almost all land cover features of the site 4. It should also be noted that the BRV method returned colour distortions on shadowy areas.

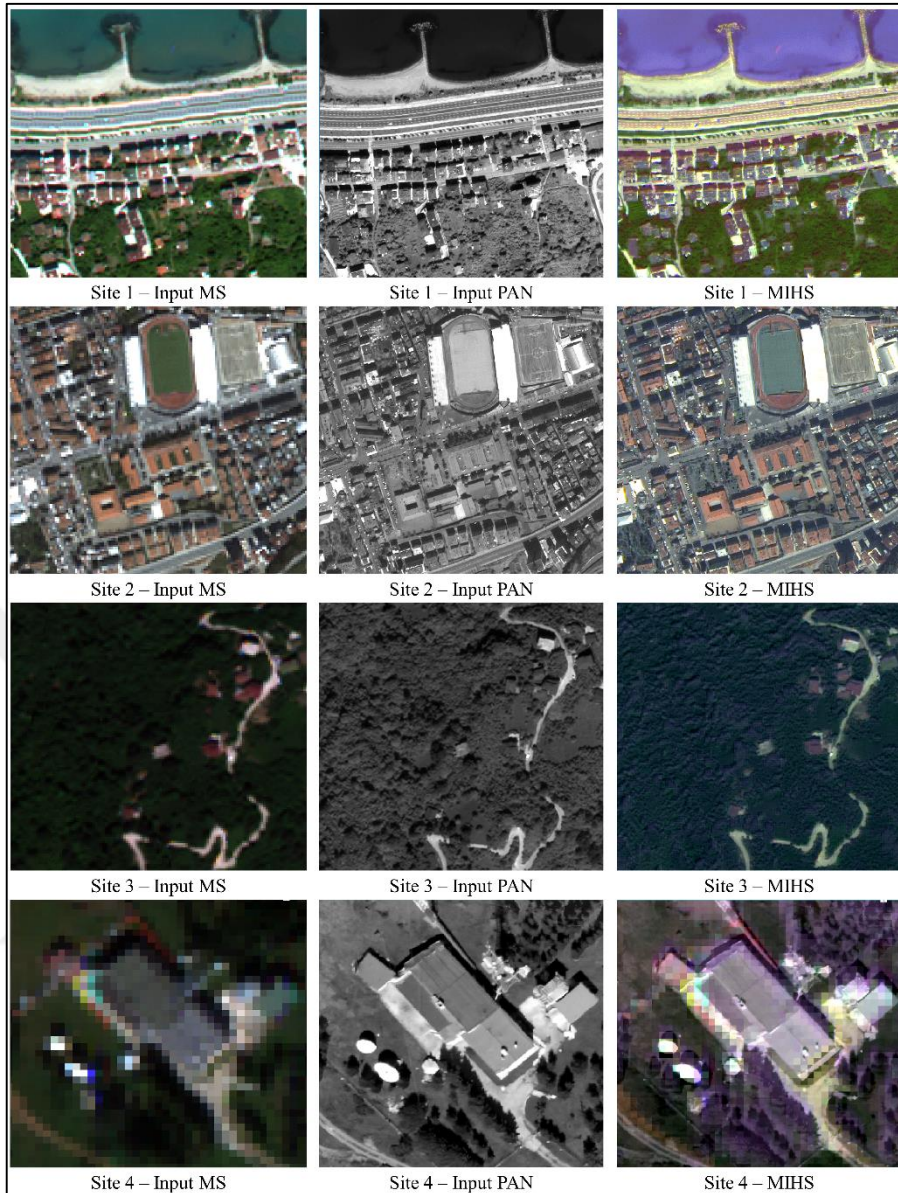


Figure 19. MIHS results for the test sites

Figure 19 depicts that the MIHS method resulted in considerable colour deterioration in all test sites. As seen in the figure, in the site 1, the MIHS method returned very inconsistent colours. In the site 2, the MIHS method led to a more robust colour preservation, as the colours of the land cover features, except for the vegetation, were kept to some degree. Significant colour distortions can also be observed in the site 3, especially on the vegetation and building rooftops. As seen in Figure 19, the MIHS method did not present a good colour preservation performance in the site 4, where drastic colour changes were observed on all land cover features. The MIHS method distorted the colour features of the shadowy areas in this site, similar to the BRV method.

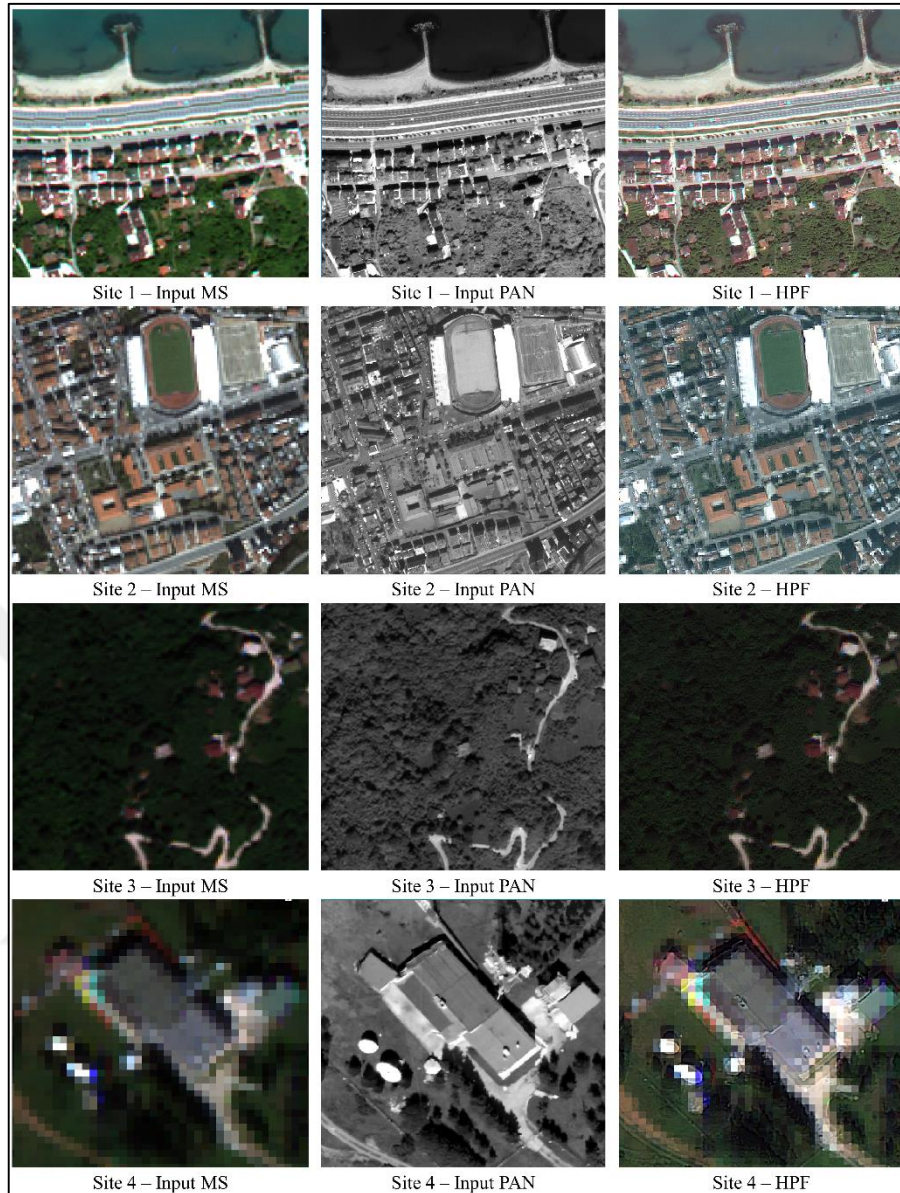


Figure 20. HPF results for the test sites

Figure 20 depicts that the HPF method achieved a satisfying colour preservation in all test sites, especially in the sites 1 and 2. As seen in the figure, in the site 1, the HPF method managed to retain the colours of the vegetation, water, road and building rooftops to a certain degree. In the site 2, the HPF method returned some colour distortions on the vegetated areas and building rooftops. However, the colours of the building rooftops were kept to some degree. Figure 20 demonstrates that, in the site 3, the colour distortions caused by the HPF method were not as significant as those caused by the BRV and MIHS methods. In the site 4, the HPF method retained the colour content of the building rooftops, vegetated areas and shadows to a certain degree, which can be seen in Figure 20.

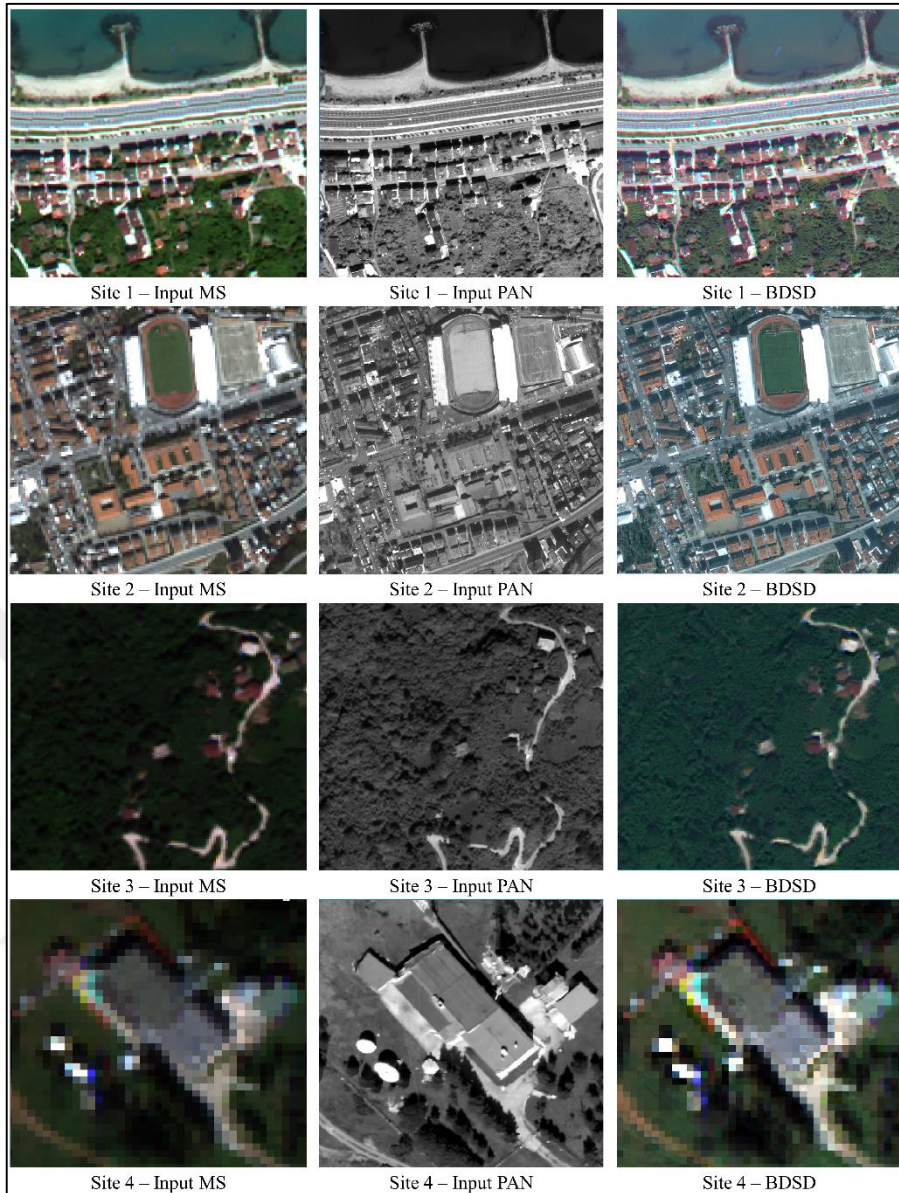


Figure 21. BSDS results for the test sites

As seen in Figure 21, the BSDS method showed a precarious performance in the test sites. The figure shows that the BSDS method partially succeeded in keeping the colour content of the water, building rooftops and vegetated areas in the site 1. As also seen in Figure 21, a satisfying colour balance was achieved by the BSDS method in the site 2. The BSDS method returned a significant colour deterioration on the vegetated areas of the site 3. The colours of the building rooftops and road were retained to some degree in this site. Figure 21 also shows that the BSDS method produced visually consistent colours in the site 4. It can be observed that the vegetated areas were slightly distorted in this site, whereas the colours of the shadows seem to be kept.

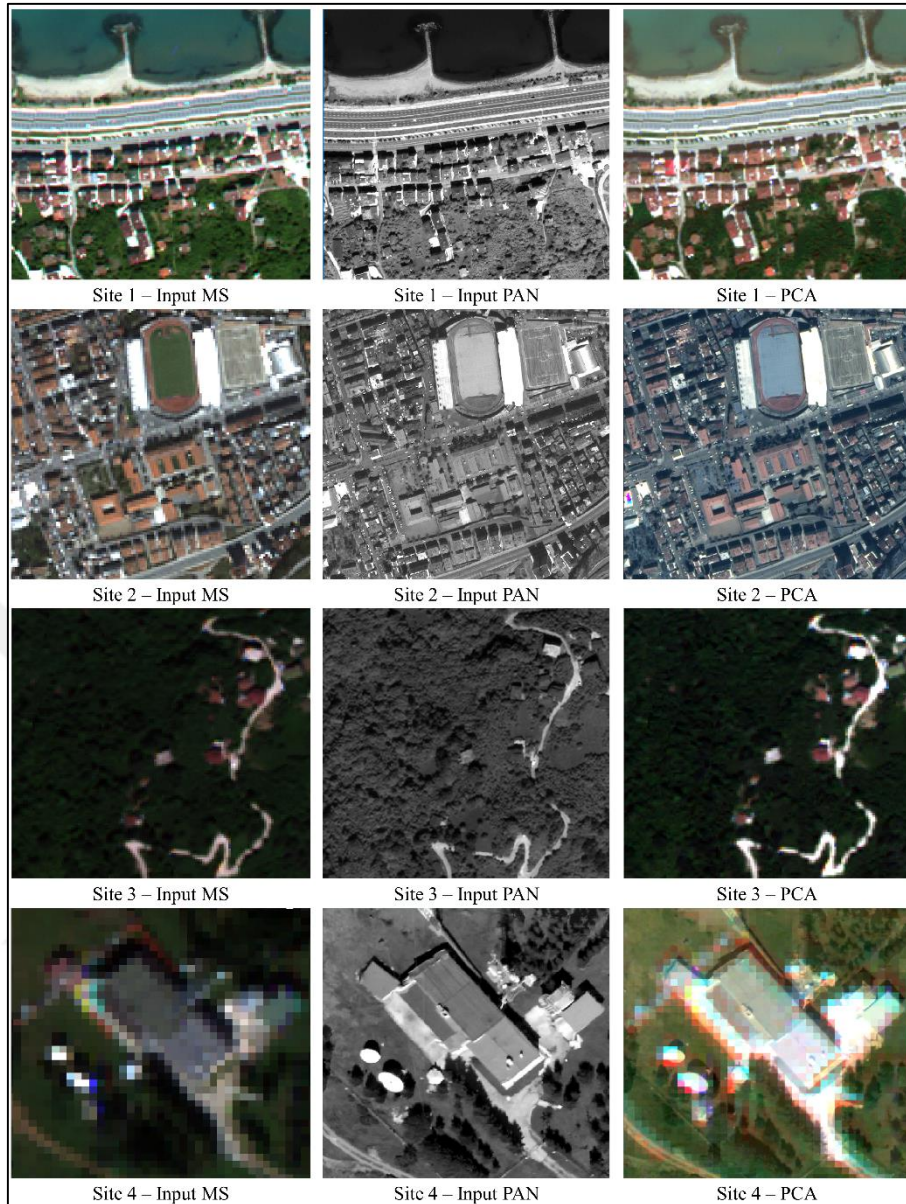


Figure 22. PCA results for the test sites

As seen in Figure 22, the PCA method cannot be considered successful in retaining the colour features of the input MS images. Figure 22 depicts that the PCA method achieved to preserve the colour content of the water, building rooftops and vegetated areas to a certain extent in the site 1. In the site 2, the PCA method distorted the colour of the vegetated areas and building rooftops, which can be seen in Figure 22. The colour characteristics of the roads were partially kept by the PCA method in this site. The PCA method seems to have conserved the colour features in the site 3. As also seen in Figure 22, the PCA method caused significant colour distortions on the land cover features of the site 4.

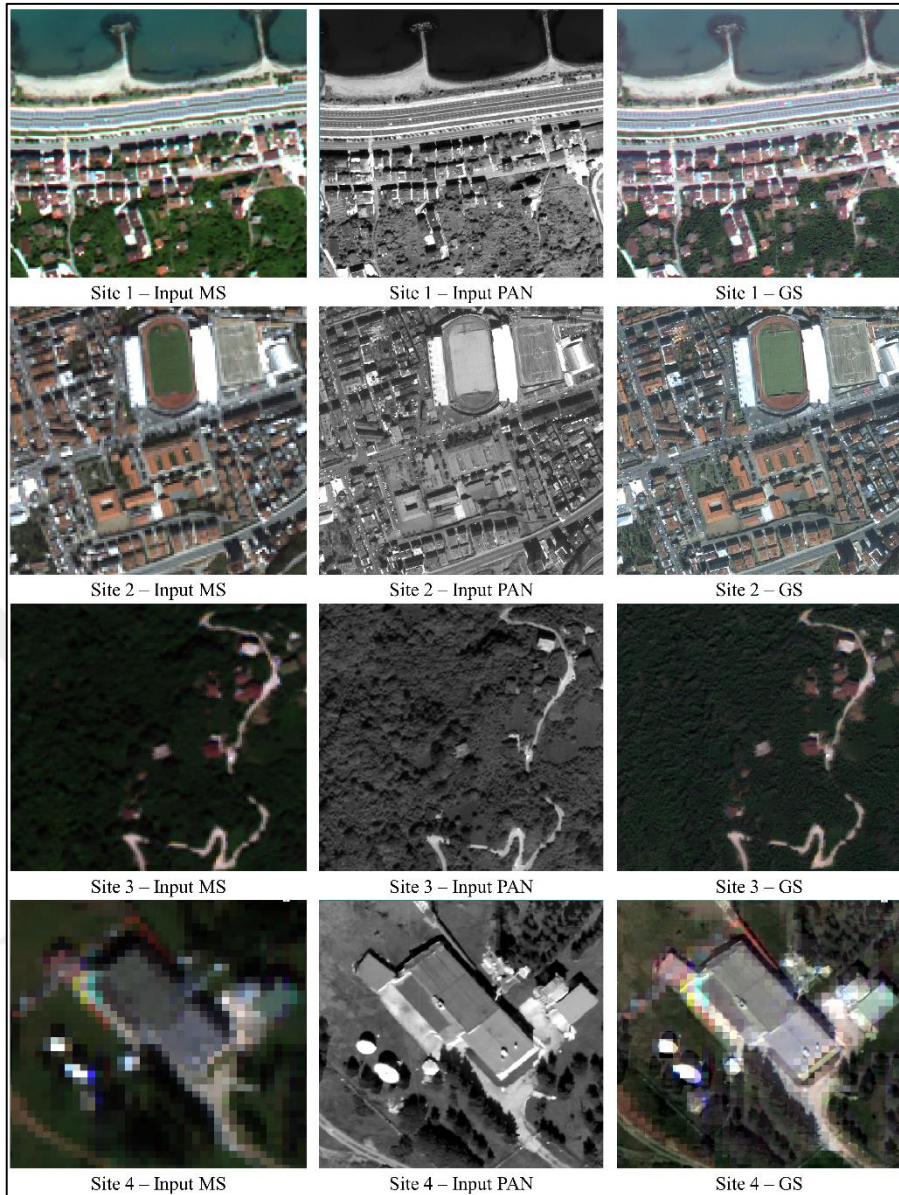


Figure 23. GS results for the test sites

Figure 23 demonstrates that the GS method was partially successful in preserving the colour balance in the test sites. The figure demonstrates that, in the site 1, the GS method caused changes in the colours of the water, building rooftops and vegetated areas. The GS method showed a better colour preservation performance in the site 2, as this method retained the colours of the building rooftops, roads vegetated areas to some extent. Figure 23 also demonstrates that colours of the building rooftops and vegetated areas were preserved by the GS method in the site 3. In the site 4, the GS method moderately conserved the colour characteristics of the building rooftops, road, shadow areas and vegetated areas, which can be seen in Figure 23.

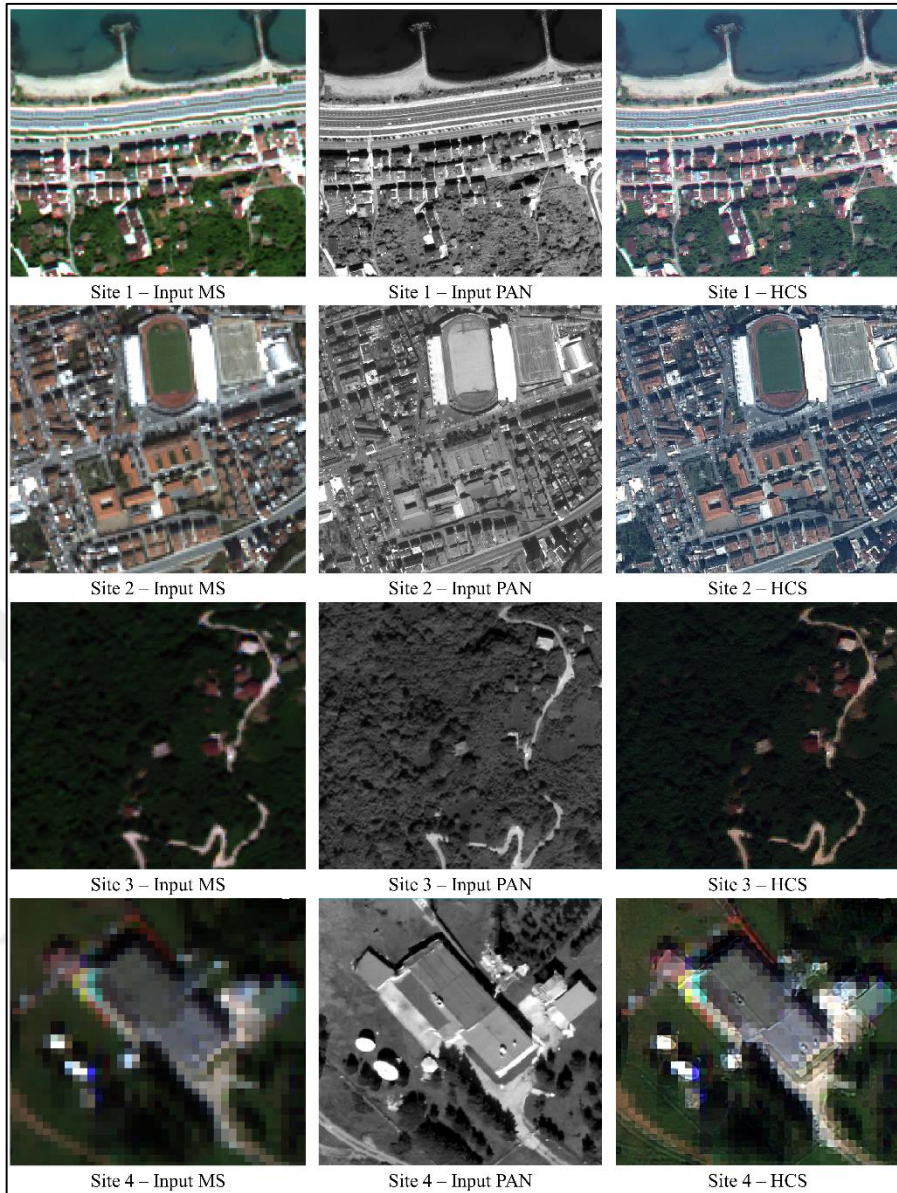


Figure 24. HCS results for the test sites

Figure 24 demonstrates that the HCS method was moderately successful in conserving the colours of the land features in the test sites. The figure depicts that, the HCS method deteriorated the colours of the water and vegetated areas in the site 1, whereas it seems to have preserved the spectral features of the building rooftops to a certain degree. In the site 2, the HCS method returned a considerable amount of colour distortions on the roads and vegetated areas. On the other hand, the vegetated areas in the site 3 were partially kept by the HCS method, which can also be seen in Figure 24. The colours of the building rooftops and roads were distorted by this method in this site. In the site 4, the HCS method kept the colour information of the building rooftops and vegetated areas, as seen in Figure 24.

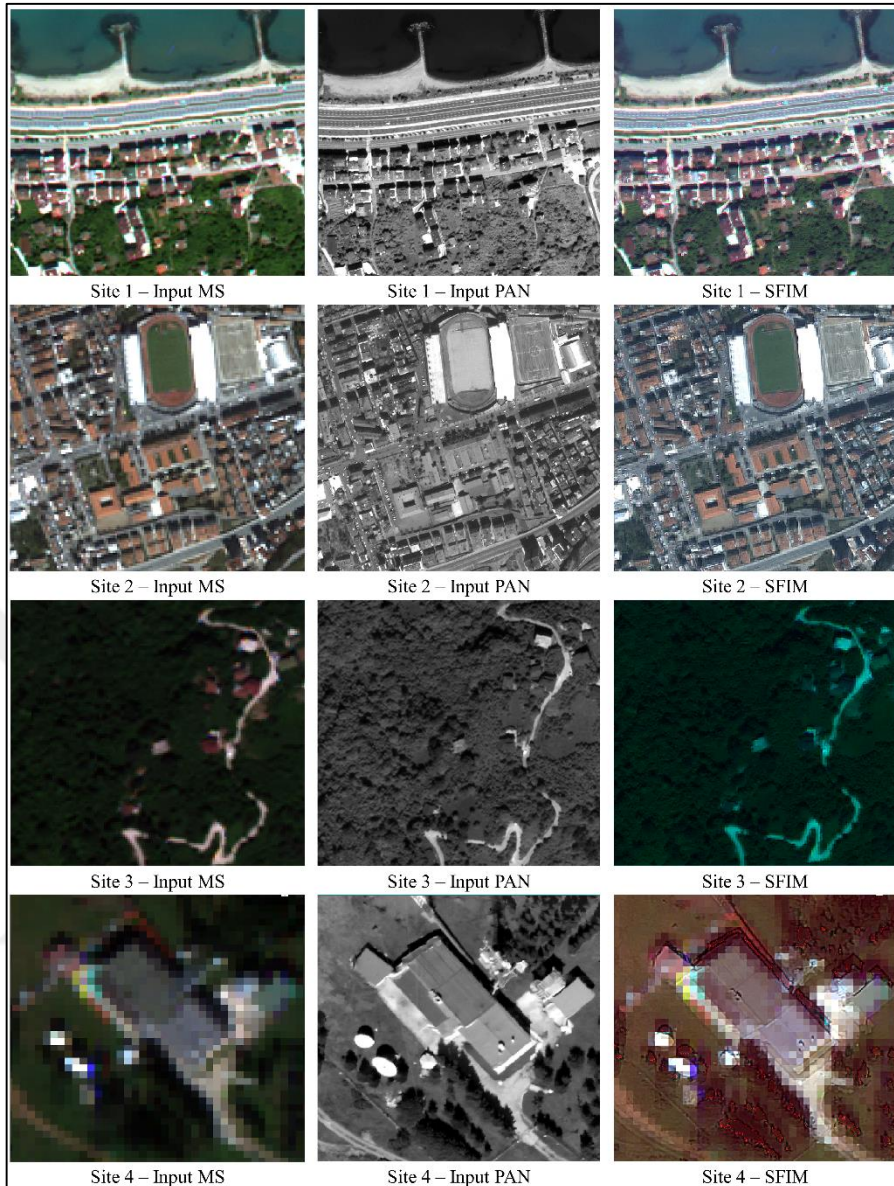


Figure 25. SFIM results for the test sites

As seen in Figure 25, the SFIM method was not so successful in keeping the colour content, as it caused global colour distortion especially in the sites 1, 3 and 4. Figure 25 shows that, in the site 1, the SFIM method caused colour deterioration on the water, building rooftops and vegetated areas. In the site 2, the SFIM method was found to be more successful in retaining the colours of the building rooftops and vegetated areas. On the other hand, in the sites 3 and 4, the SFIM method produced colours that are inconsistent with the input MS images. The colours of all land cover features were totally distorted by the SFIM method in the site 3. In addition, the SFIM method caused some reddish pixel effects on the shadowy areas in the site 4, which can also be seen in Figure 25.

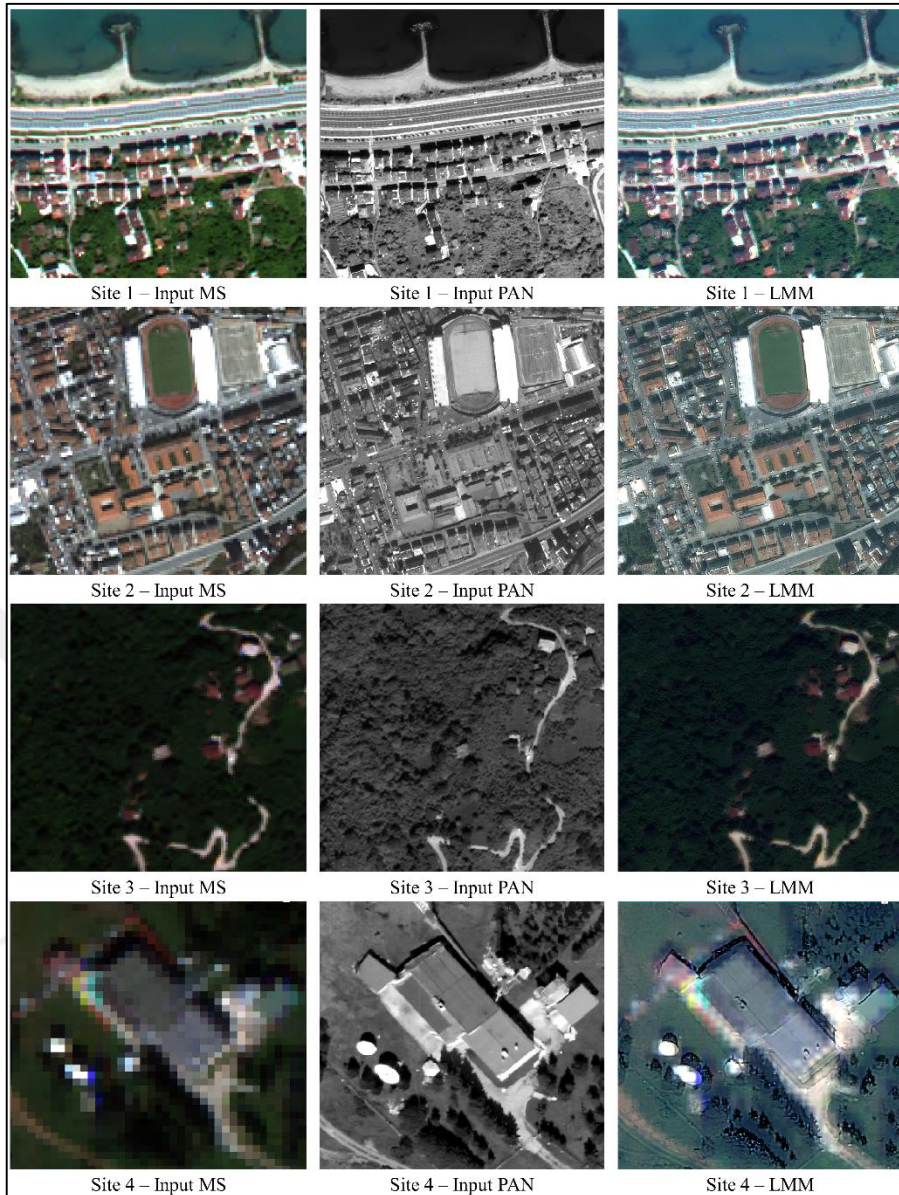


Figure 26. LMM results for the test sites

As seen in Figure 26, the LMM method led to global colour deterioration, especially in the sites 1, 3 and 4. The LMM method caused considerable colour distortion on the water, building rooftops, roads and vegetated areas, which can be seen in Figure 26. The figure also depicts that the LMM method managed to conserve the colour features of the building rooftops and roads to in some measure in the site 2. However, the colour characteristics of the vegetated areas could not be kept well by the LMM method in this site. Although the LMM method fairly retained the colour features of the roads in the site 3, the colours of the vegetated areas were distorted by this method. The LMM method produced the most inconsistent colours in the site 4.

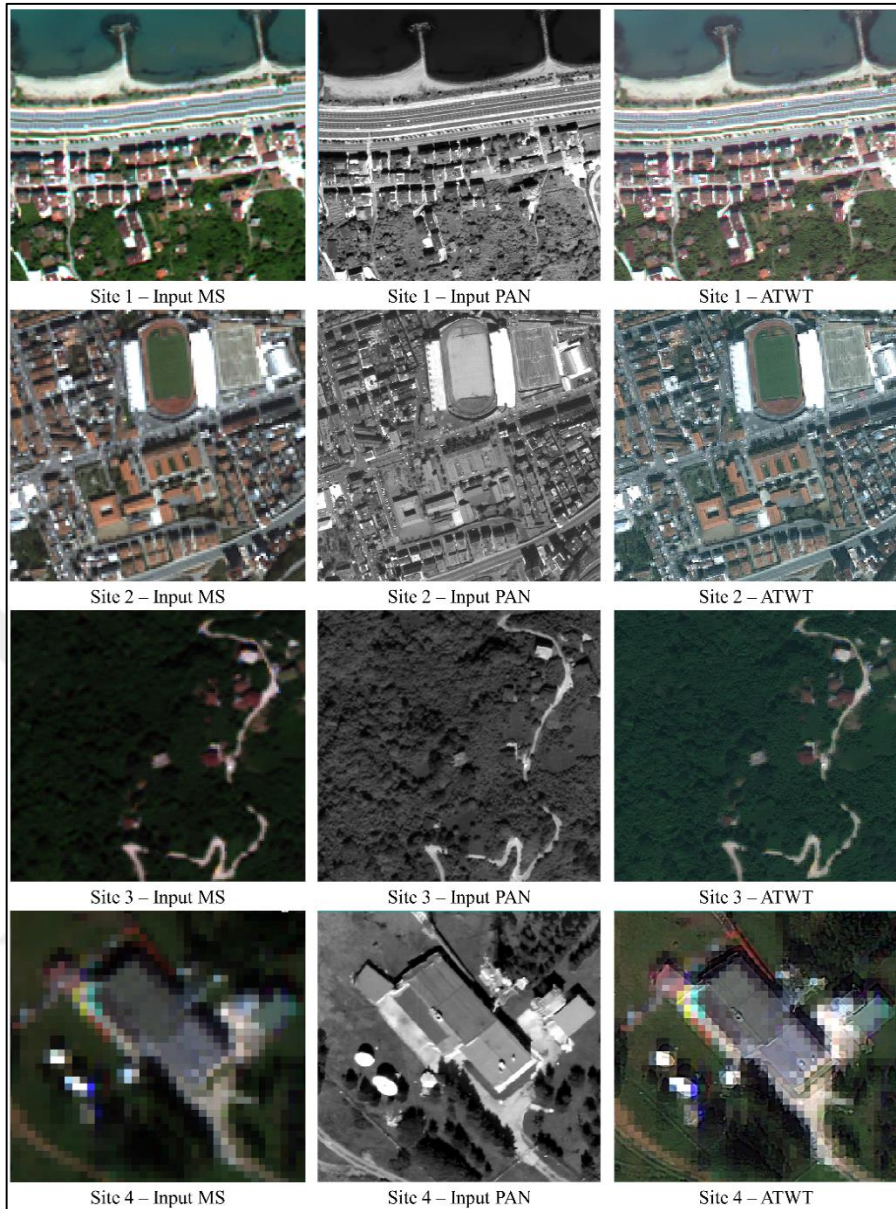


Figure 27. ATWT results for the test sites

Figure 27 demonstrates that the ATWT method presented a satisfying performance in preserving the global colour content of the test sites. The ATWT method kept the colour features of the water, building rooftops and vegetated areas in the site 1. On the other hand, the ATWT method returned some colour deterioration on the building rooftops and vegetated area in the site 2. Figure 27 demonstrates that the colours of the vegetated areas in the site 3 were not properly preserved by the ATWT method. However, the colours of the roads and building rooftops were conserved by the ATWT method in this site. The ATWT method can be said to have preserved the global colour content of the site 4.

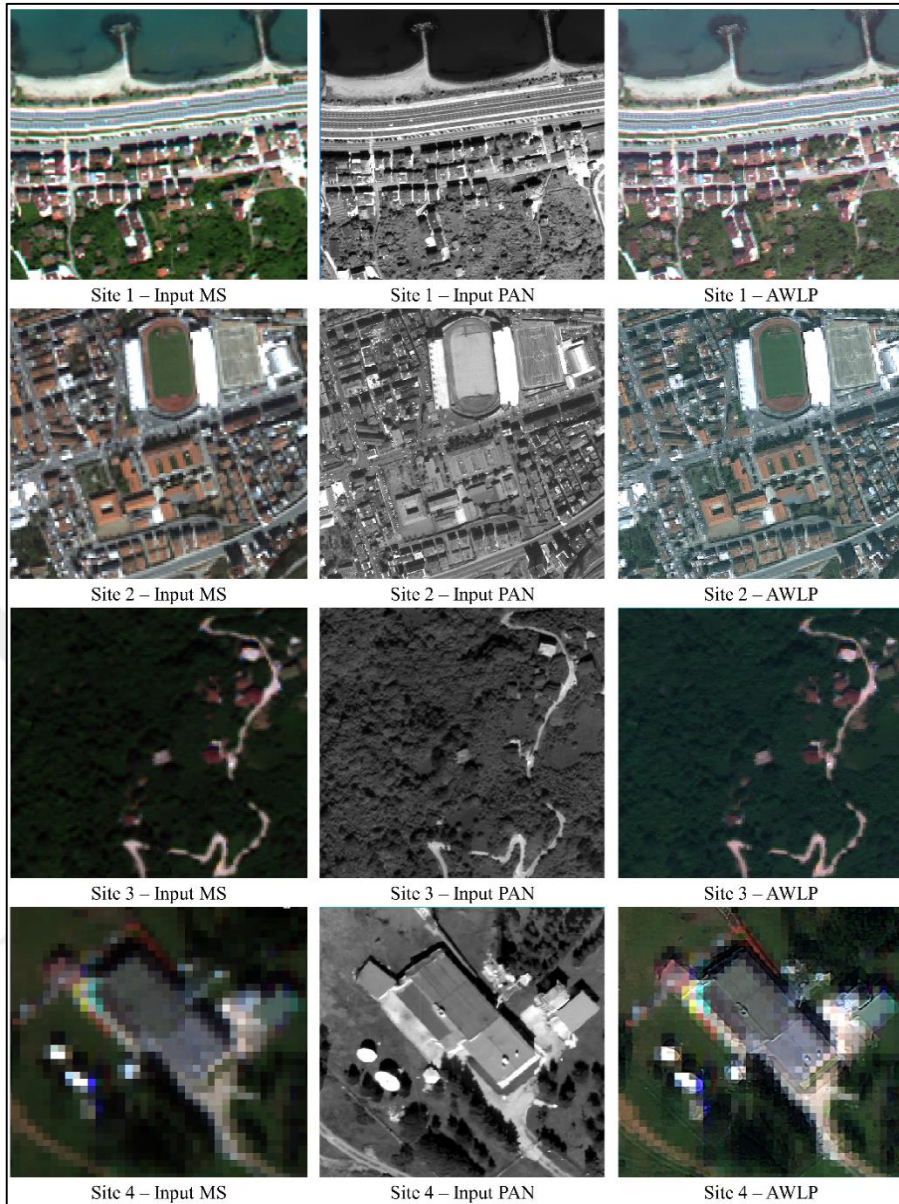


Figure 28. AWLP results for the test sites

Figure 28 shows that the AWLP method presented a similar performance to the ATWT method in the test sites. As seen in the figure, the AWLP method kept the colour characteristics of the water and vegetated areas in the site 1. Figure 28 also depicts that the AWLP method was more successful in retaining the colour features of the roads and building rooftops than in preserving the colours of the vegetated areas in the site 2. In the site 3, the AWLP method yielded inconsistent colours for the vegetated areas, keeping the colour features of the roads and building rooftops with a relatively higher success. As also seen in Figure 28, the AWLP method seems to have kept the global colour content of the site 4.

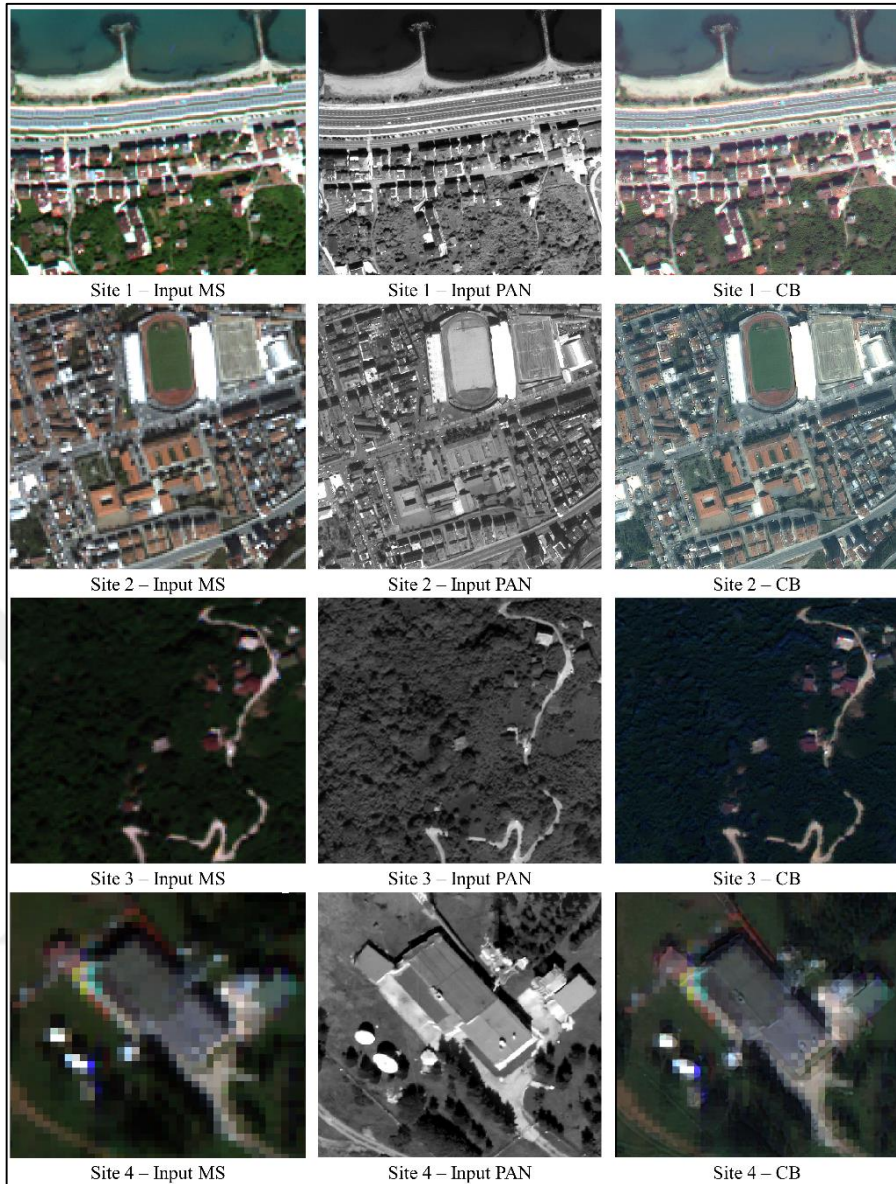


Figure 29. CB results for the test sites

As demonstrated in Figure 29, the CB method seems to have produced satisfying colours in all test sites except for the site 2. The figure depicts that the CB method was moderately successful in conserving the spectral content of the water, roads, building rooftops and vegetated areas in the site 1. It can also be seen in the figure that the CB method preserved the colour features of the roads and building rooftops in the site 1, distorting the colours of the vegetated areas to a certain degree. The CB method caused global colour distortion in the site 3. In addition, the shadowy areas were also distorted by the CB method in this site. As also seen in Figure 29, the CB method can be said to have conserved the global colour content of the site 4.

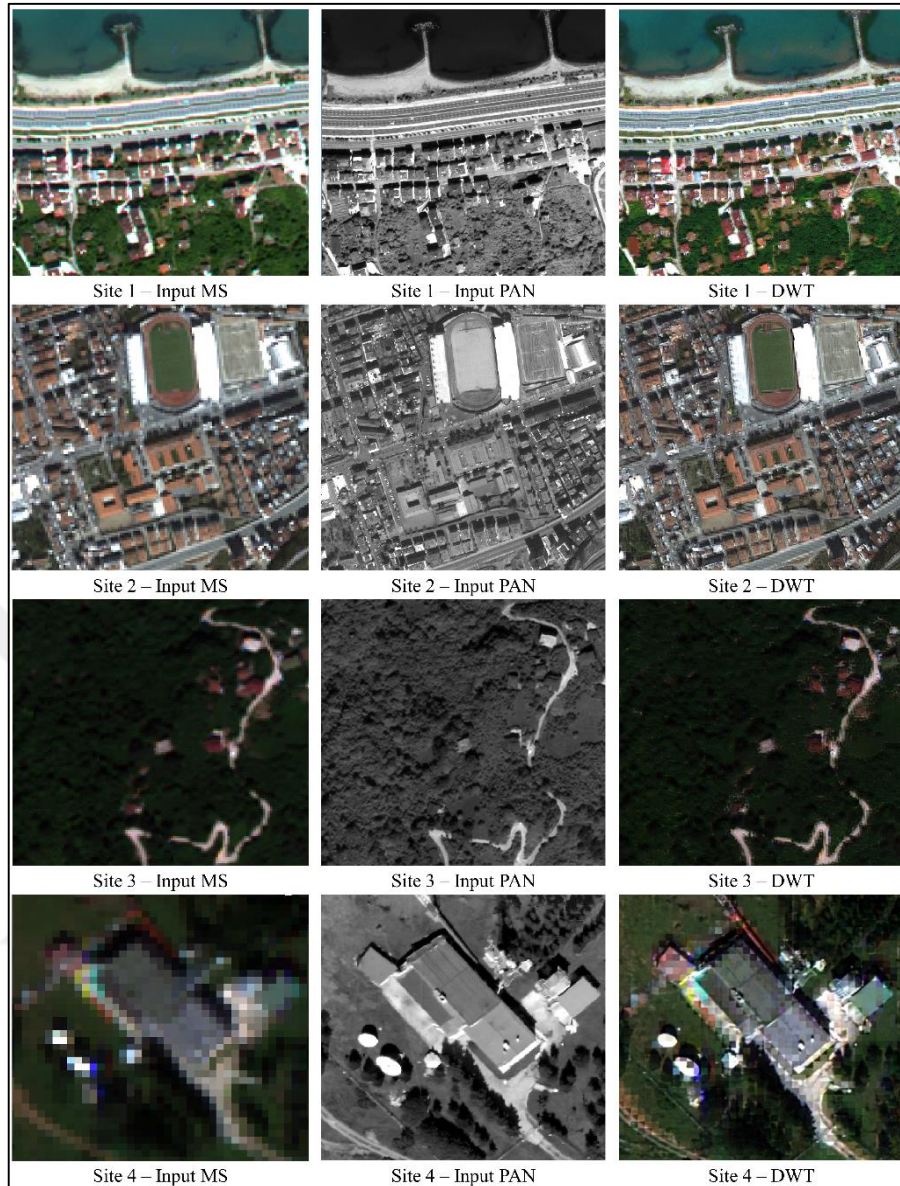


Figure 30. DWT results for the test sites

As seen in Figure 30, the DWT method kept the global colour content in all test sites. The figure shows that the DWT method preserved the colours of the water, roads and vegetated areas with a high success in the site 1, whereas the colour features of the building rooftops were distorted. The DWT method presented a very good colour preservation performance in the site 2, as can be seen in Figure 30. The DWT method also achieved to conserve the colour information of the features in the site 3. Figure 30 also depicts that the DWT method caused slight colour distortions in the roads, building rooftops and vegetated areas in the site 4. In general, the DWT method can be said to have preserved the global colour quality in the site 4.

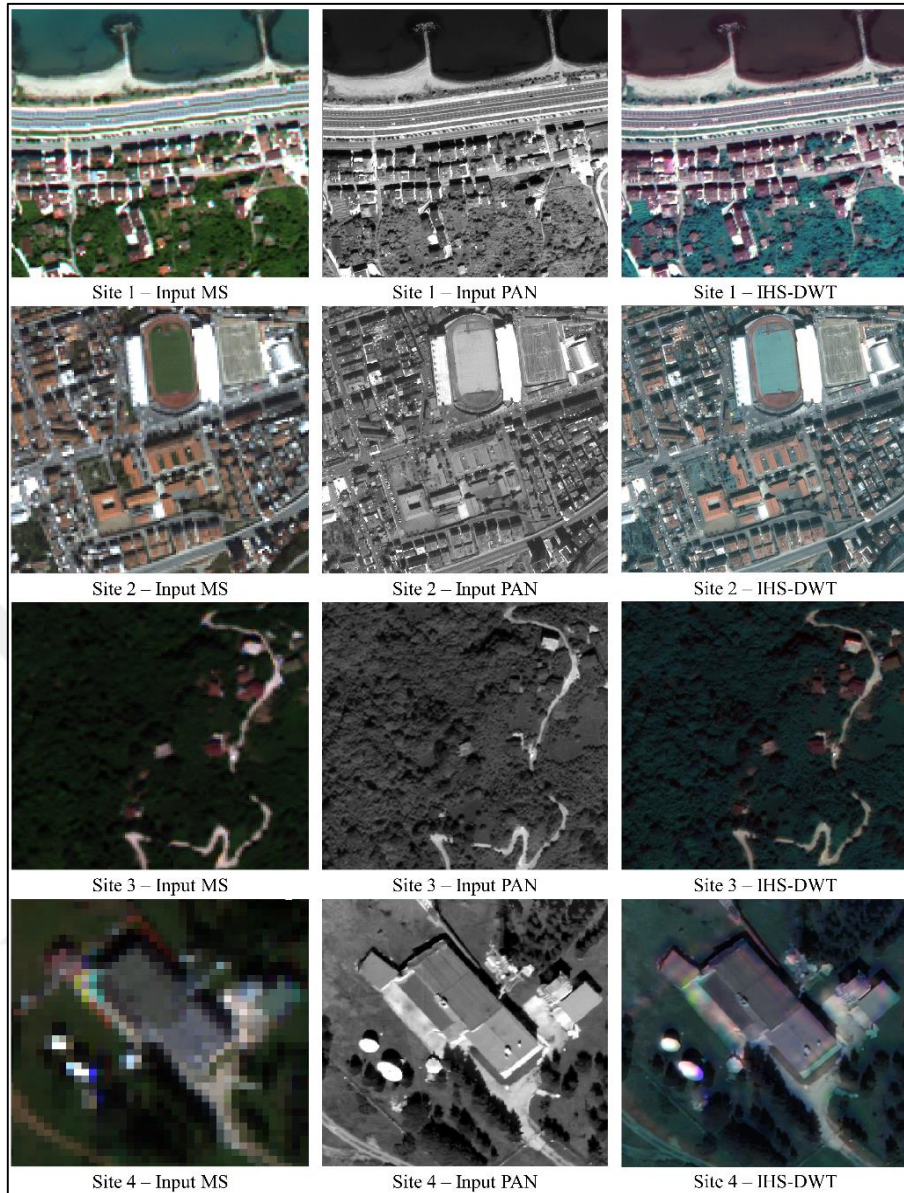


Figure 31. IHS-DWT results for the test sites

As seen in Figure 31, the IHS-DWT method deteriorated the global colour content in all test sites. Figure 31 shows that the IHS-DWT method distorted the colours of the water, road, building rooftops and vegetated areas in the site 1. The IHS-DWT method did not achieve to keep the colour features of the vegetated areas in the site 2, whereas it moderately conserved the colours of the building rooftops and roads in this site. As also seen in Figure 30, the IHS-DWT method distorted a significant amount of the vegetated areas in the site 3. The IHS-DWT method was found to keep the colour characteristics of the roads and building rooftops to some degree in this site. Figure 31 also depicts that the IHS-DWT method deteriorated the colours of the all land cover features in the site 4.

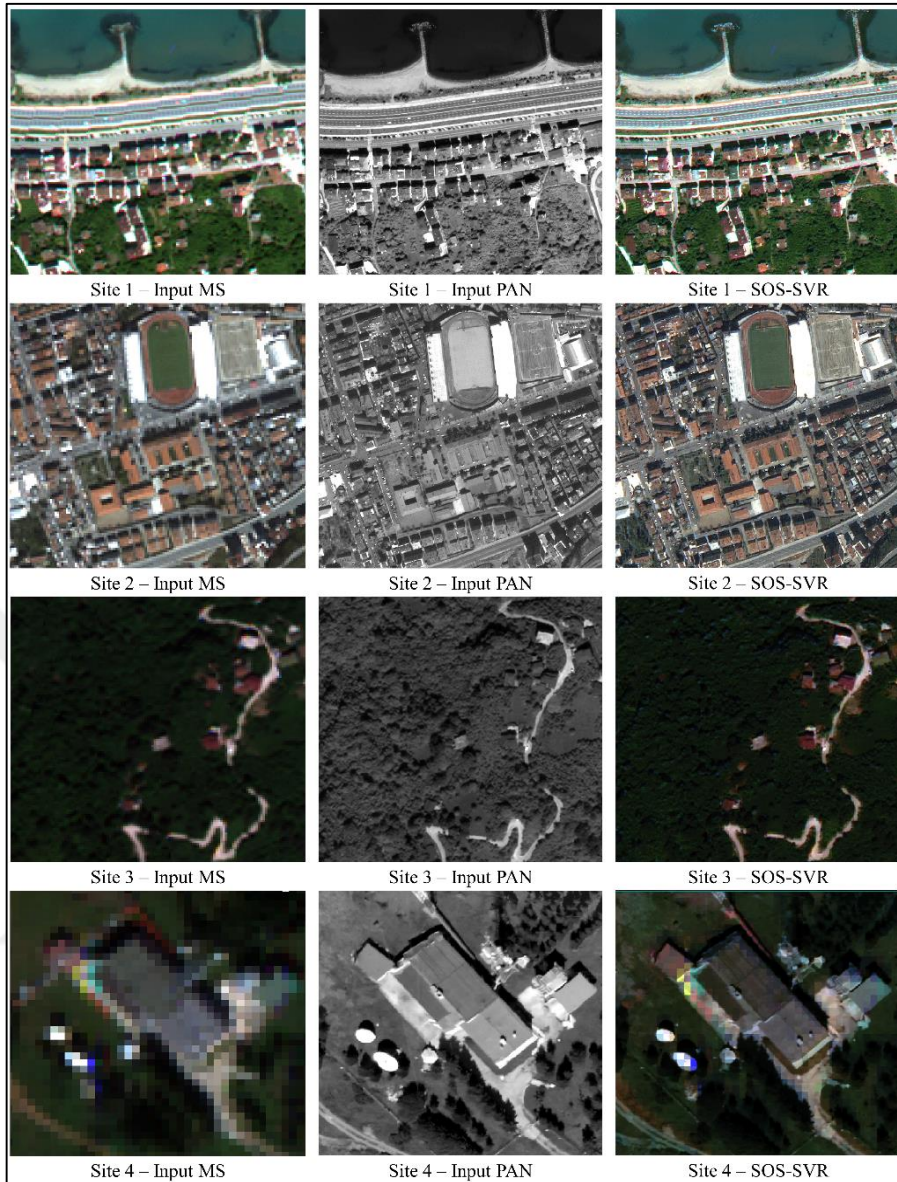


Figure 32. SOS-SVR results for the test sites

Figure 32 shows that the proposed SOS-SVR method presented a superb performance in preserving the colour balance between the pansharpened images and input MS data in all test sites. The SOS-SVR method was also very successful in retaining the colour features of the vegetated areas in the site 2. It should be noted that all the other methods used had significant a difficulty in retaining the colour content of this land cover feature. The SOS-SVR method preserved the spectral characteristics of the vegetated areas of the sites 3 and 4. As may be recalled, many other methods distorted the colour of these land cover features. The SOS-SVR method kept the colour content of the land cover features that the other methods had a difficulty in dealing with.

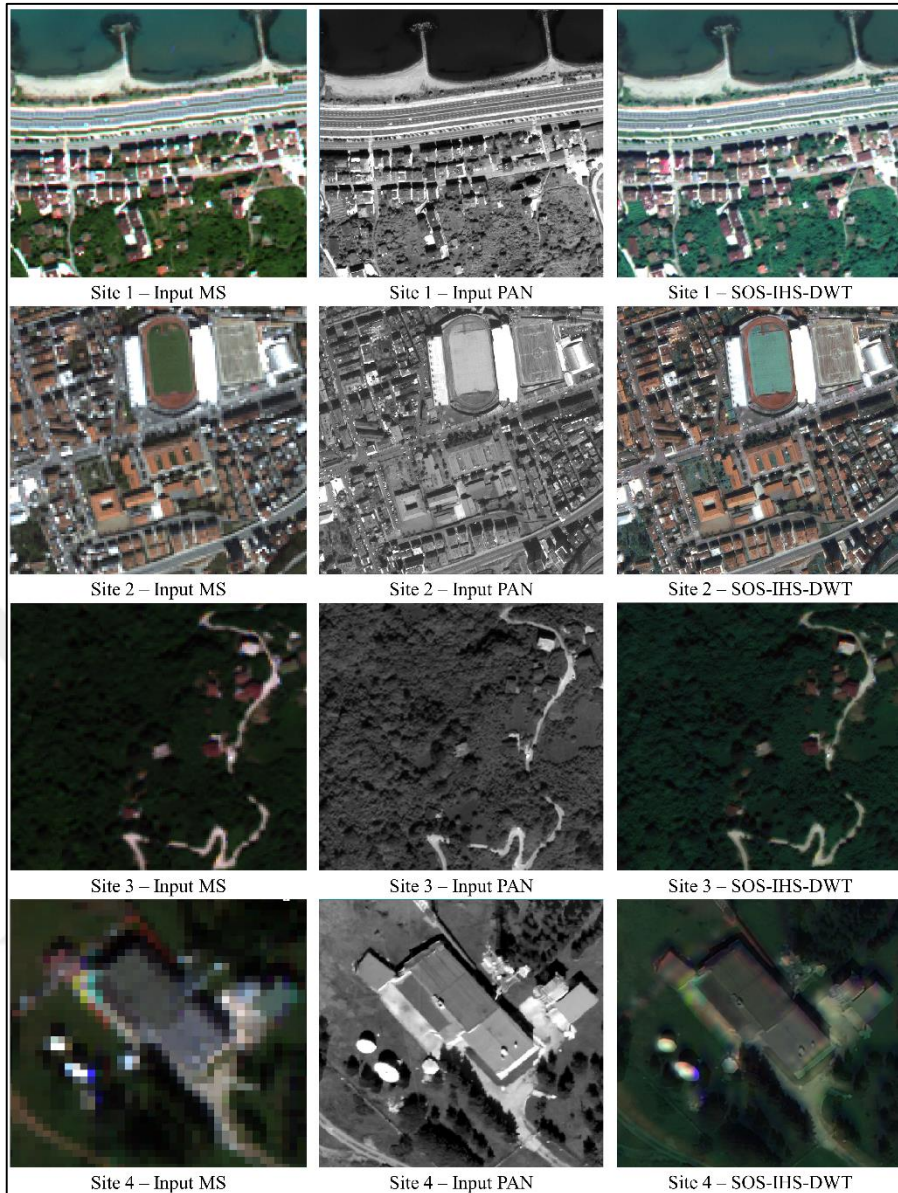


Figure 33. SOS-IHS-DWT results for the test sites

As seen in Figure 33, the SOS-IHS-DWT method retained the colour balance to some measure in all test sites. Figure 33 depicts that the SOS-IHS-DWT method preserved the colour characteristics of the water, roads and building rooftops to some degree in the site 1. However, it distorted the colours of the vegetated areas in this site. In the site 2, the SOS-IHS-DWT method kept the colour features of the roads and building rooftops, which can be observed in Figure 33. The SOS-IHS-DWT method achieved to conserve the global colour content of the sites 3 and 4. As seen in Figure 33, especially the colours of the vegetated areas were preserved by the SOS-IHS-DWT in these sites. The SOS-IHS-DWT method distorted the colours of the roads and building rooftops in the site 4.

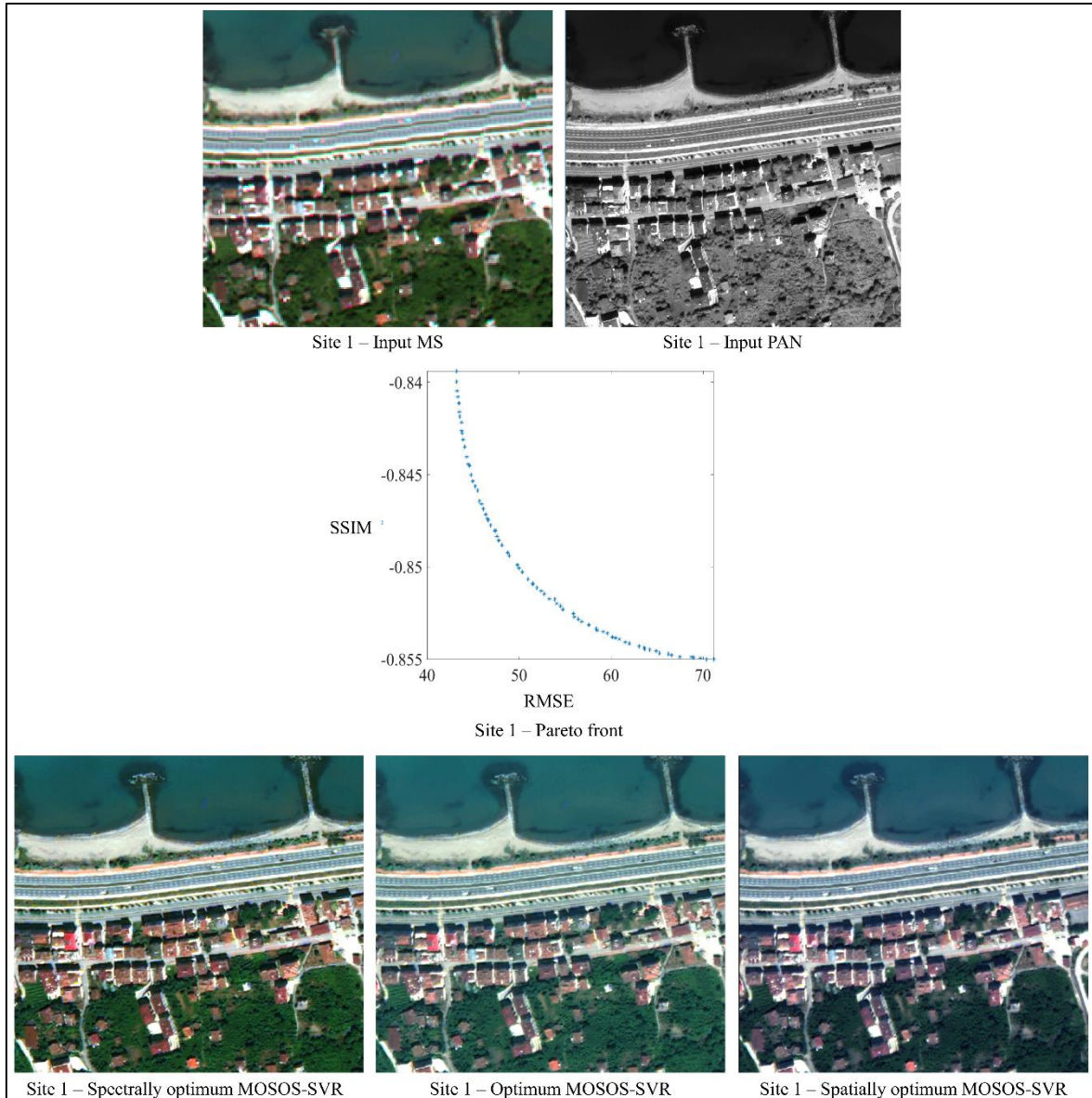


Figure 34. MOSOS-SVR results for the site 1

As seen in Figure 34, the spectrally optimum pansharpened image produced by the MOSOS-SVR method contains the global colour content of the site 1. However, slight colour distortion is still noticeable on the water, building rooftops and vegetated areas in the spectrally optimum MOSOS-SVR result. Figure 34 also depicts that the optimum MOSOS-SVR result has a greater amount of colour deterioration, compared to the spectrally optimum MOSOS-SVR result. On the other hand, the MOSOS-SVR method caused significant colour distortion when producing spatially optimum pansharpened image of the site 1. As can be seen in Figure 34, the colours of the land cover features in the spatially optimum MOSOS-SVR result are much different than those of the input MS data of this site.

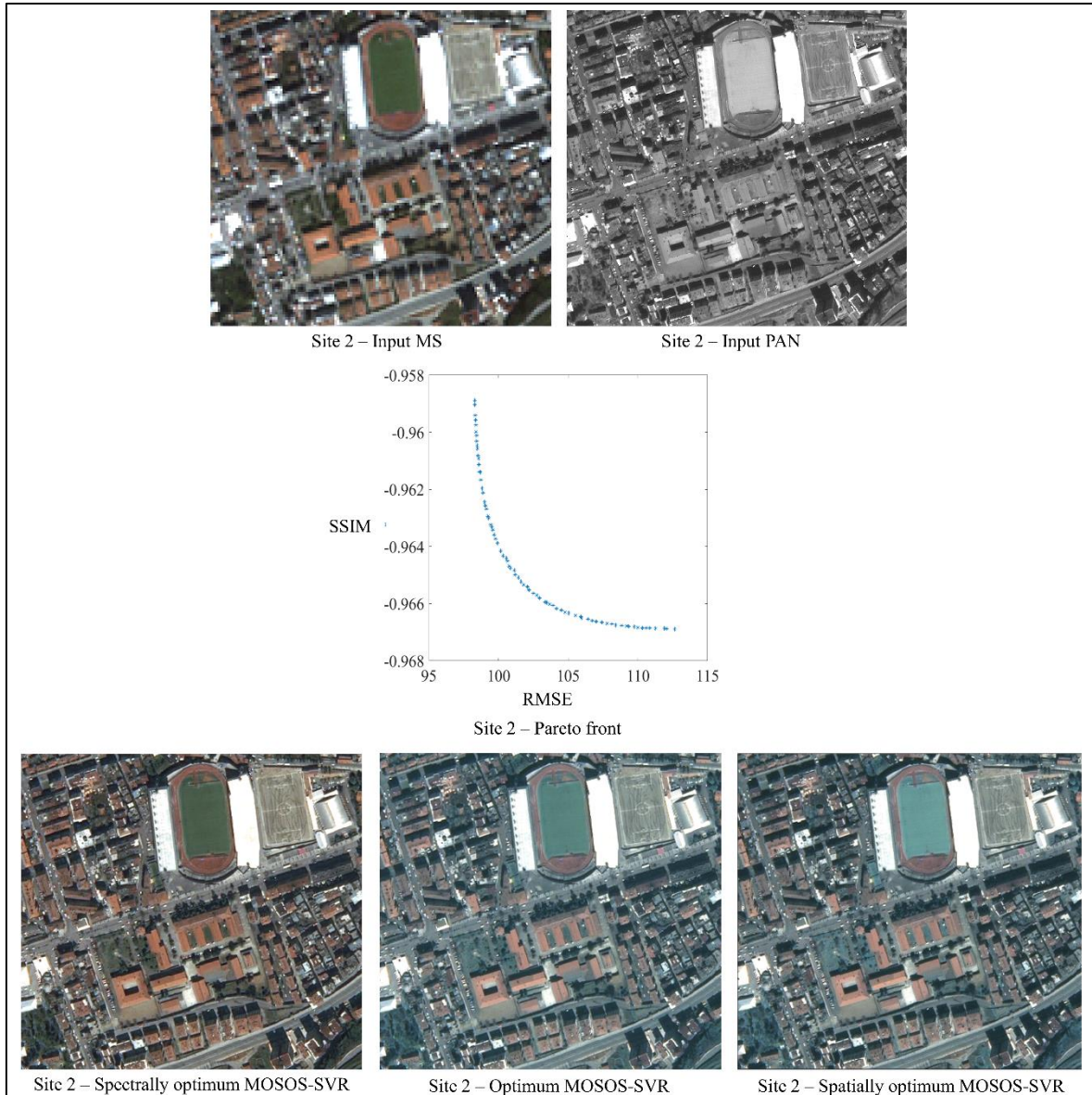


Figure 35. MOSOS-SVR results for the site 2

Figure 35 depicts that, despite the fact that the spectrally optimum MOSOS-SVR result preserved the colours of the input MS data of the site 2, a small amount of colour deterioration can be observed on this result, especially on the vegetated areas. On the other hand, the optimum band weights returned by the MOSOS-SVR method were found to distort the colour content of the site 2, which can be seen on the optimum MOSOS-SVR result given in Figure 35. The band weights achieved to spatially optimize the MOSOS-SVR result caused significant colour distortion in the site 2. As seen in Figure 35, the colours in the spatially optimum MOSOS-SVR result look very similar to those in the optimum MOSOS-SVR result.

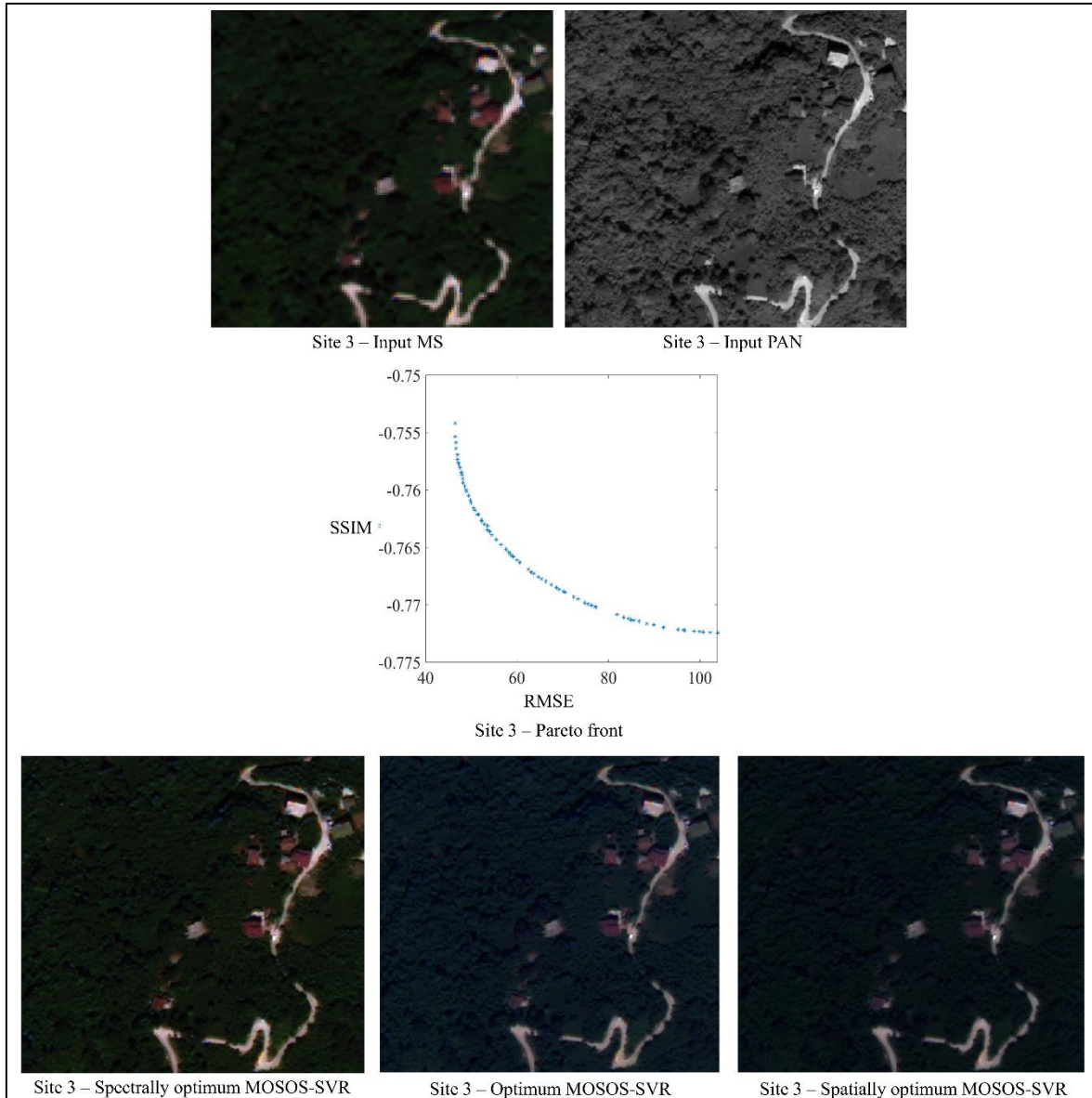


Figure 36. MOSOS-SVR results for the site 3

As seen in Figure 36, the band weights returned by the MOSOS-SVR method to optimize the colour quality in the site 3 achieved to preserve the spectral features with a very high success. As also seen in Figure 36, the band weights estimated by the MOSOS-SVR result to find the best balance between the colour and spatial detail quality in the site 3 resulted in a greater amount of colour distortion, compared to the spectrally optimum MOSOS-SVR result. These band weights especially deteriorated the colours of the vegetated areas in this site. The band weights estimated to produce the sharpest possible image for the site 3 were found to change the colours of the land features.

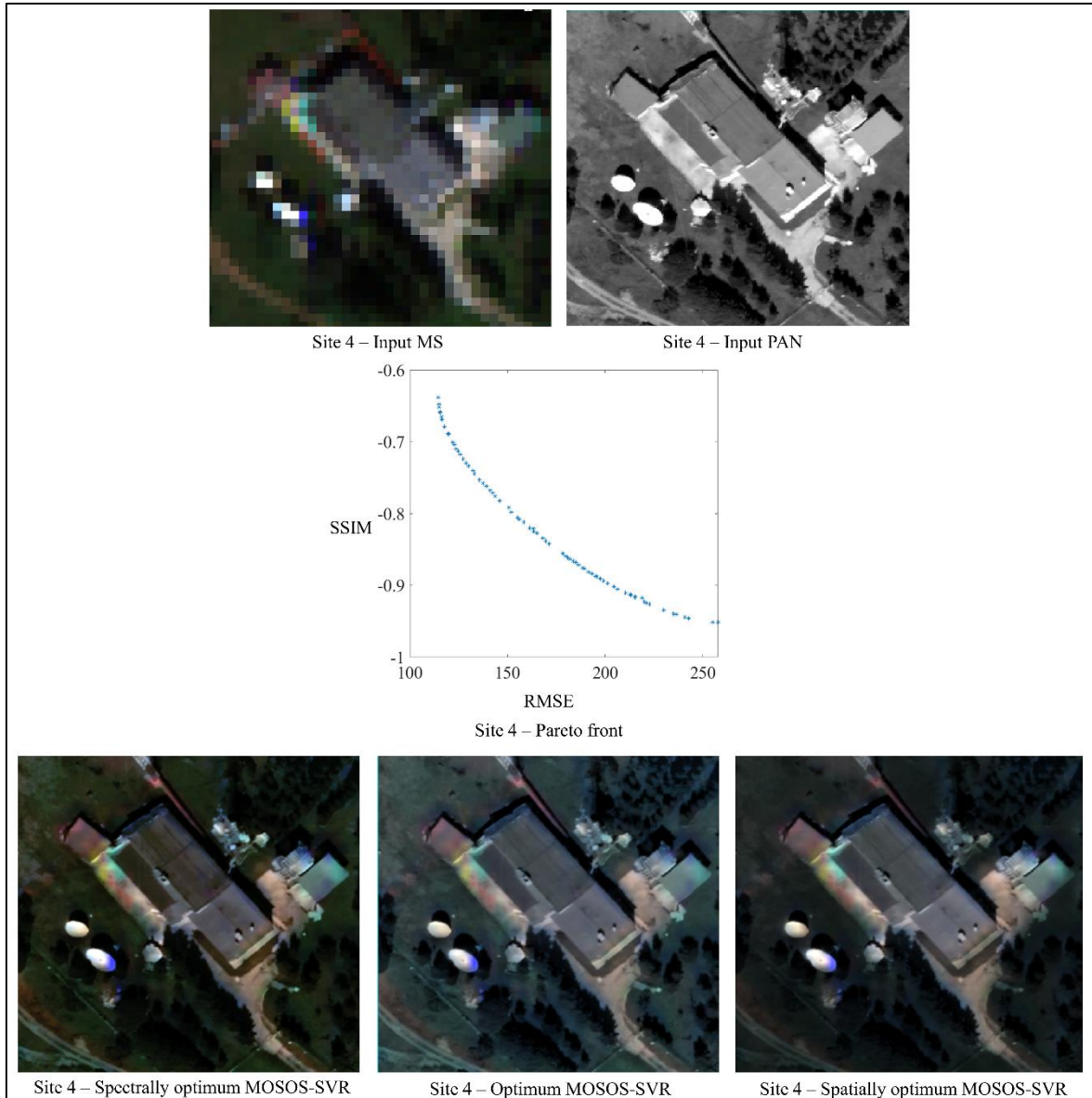


Figure 37. MOSOS-SVR results for the site 4

As demonstrated in Figure 37, the MOSOS-SVR method succeeded in finding the best band weights that conserved the colour features of the site 4. As seen in the figure, the colours in the spectrally optimum MOSOS-SVR result are very similar to those in the input MS image. On the other hand, the band weights estimated to achieve the best balance between the colour and spatial detail quality were found to cause considerable colour distortion in the site 4. As also seen in the figure, the spatially optimum MOSOS-SVR result comprises a greater amount of colour distortion, compared to the spectrally optimum MOSOS-SVR result produced for the site 4.

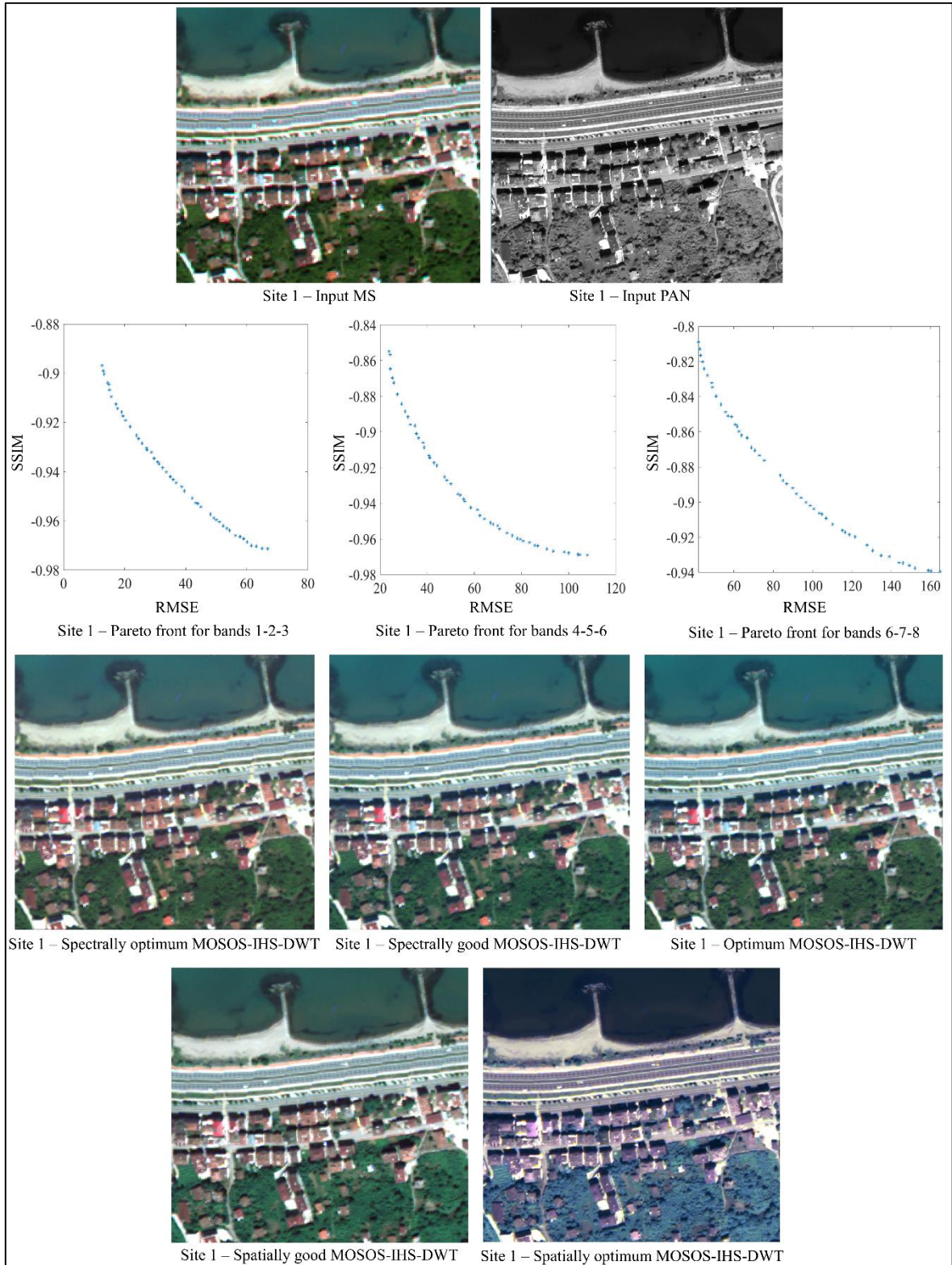


Figure 38. MOSOS-IHS-DWT results for the site 1

As seen in Figure 38, in the site 1, the global colour distortion increases from spectrally optimum MOSOS-IHS-DWT result towards spatially optimum MOSOS-IHS-DWT result.

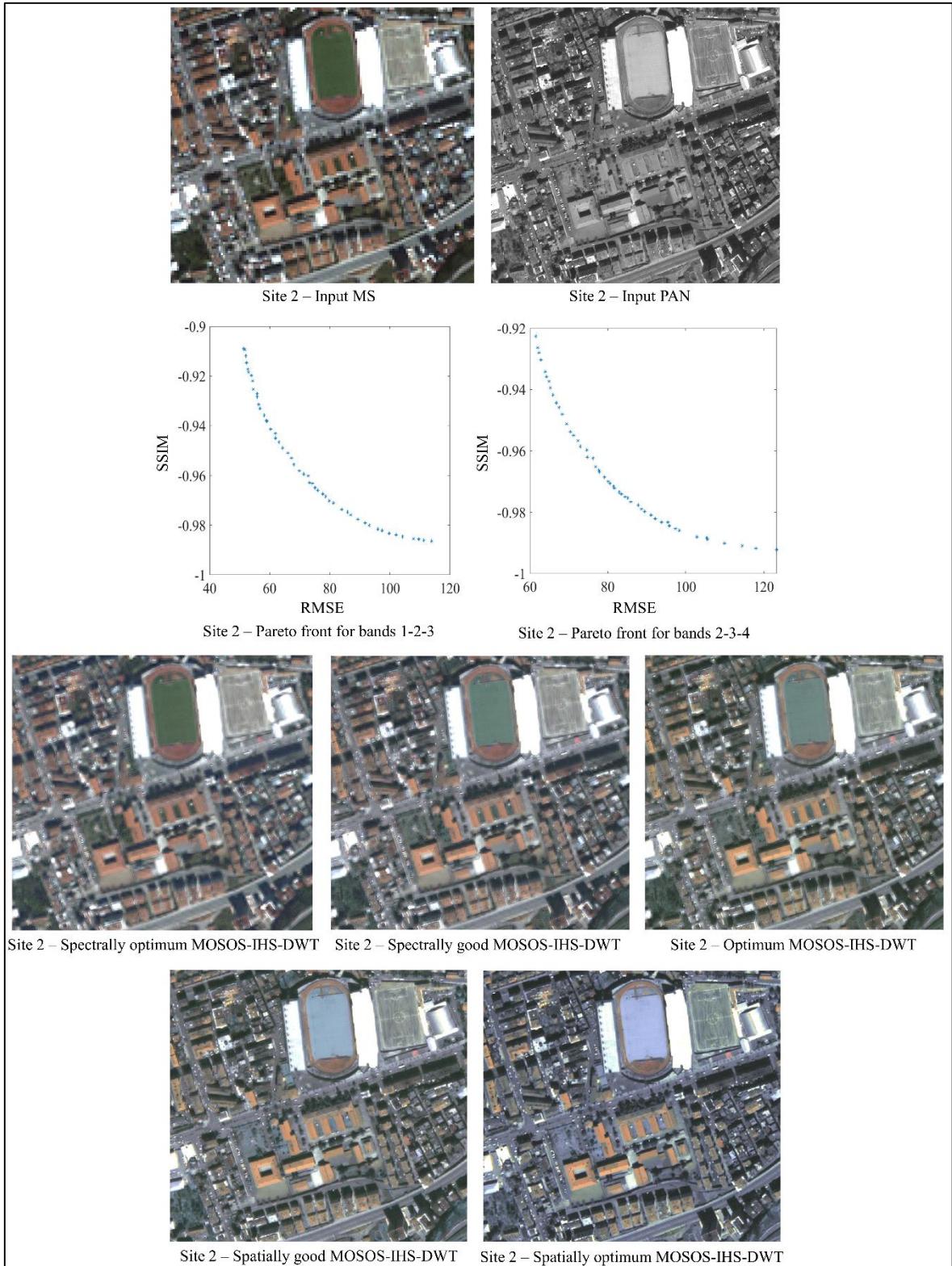


Figure 39. MOSOS-IHS-DWT results for the site 2

Figure 39 shows that, in the site 2, the global colour distortion increases from spectrally optimum MOSOS-IHS-DWT result towards spatially optimum MOSOS-IHS-DWT result.

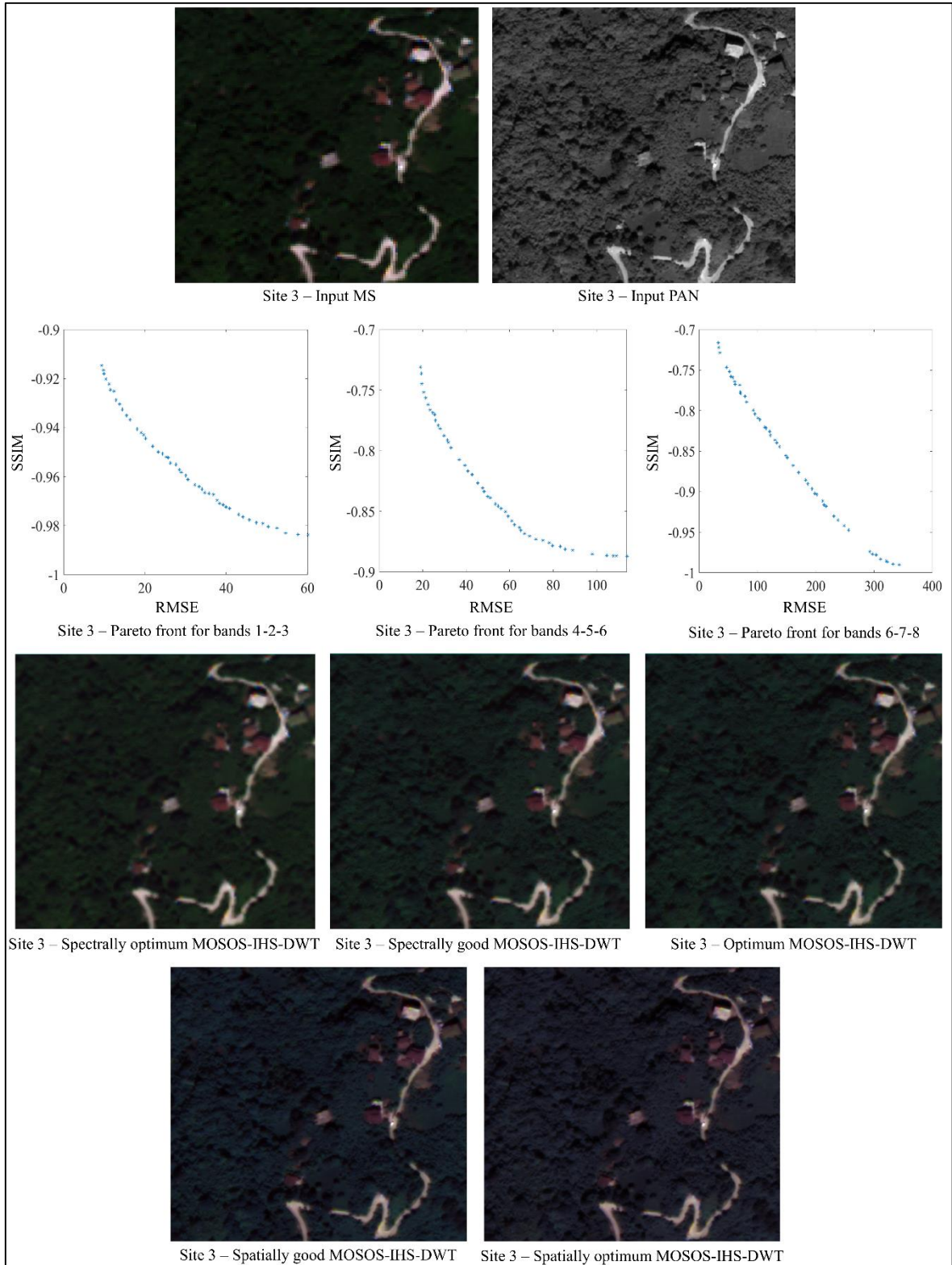


Figure 40. MOSOS-IHS-DWT results for the site 3

Figure 40 shows that, in the site 3, the global colour distortion increases from spectrally optimum MOSOS-IHS-DWT result towards spatially optimum MOSOS-IHS-DWT result.

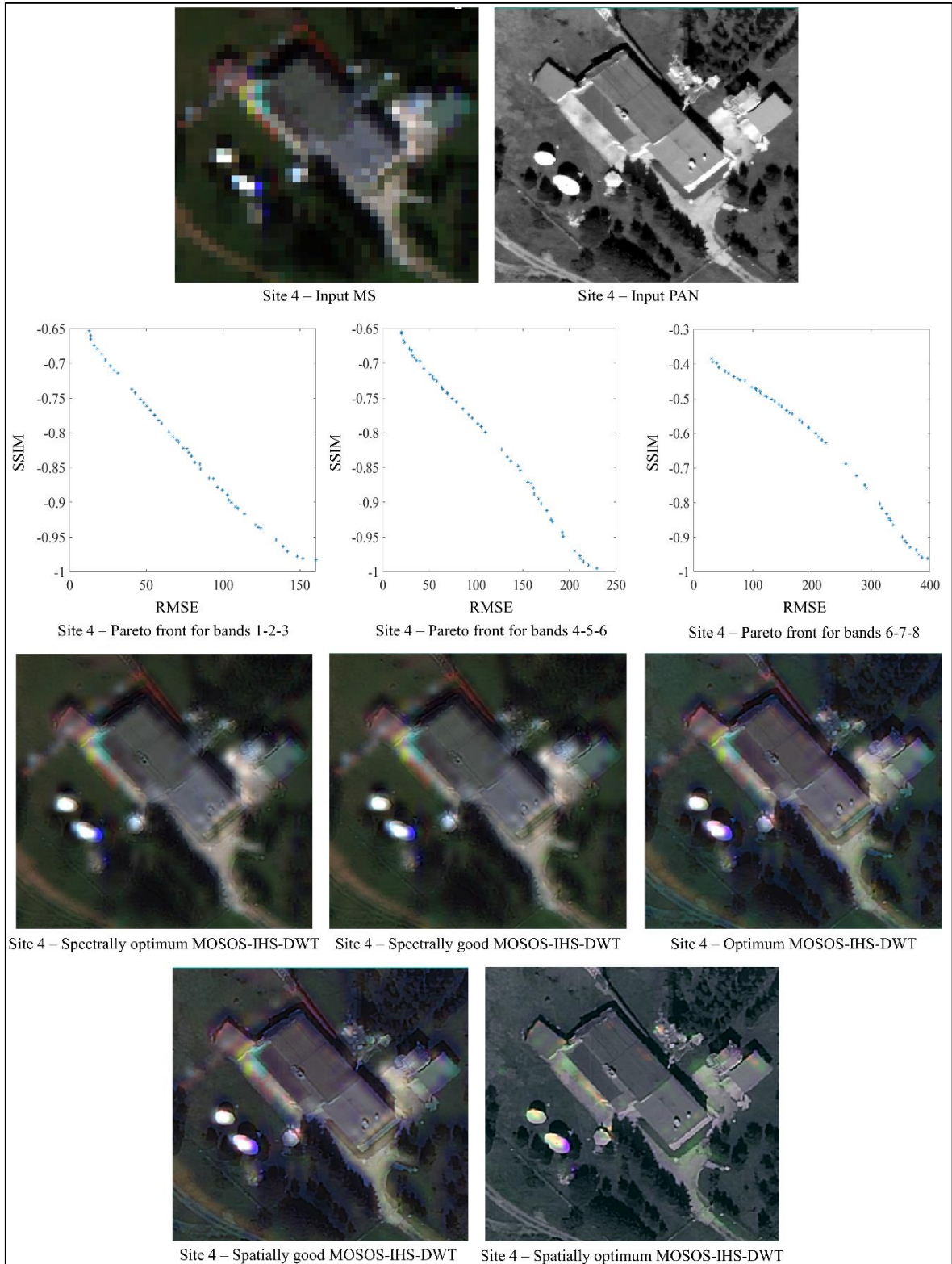


Figure 41. MOSOS-IHS-DWT results for the site 4

Figure 41 shows that, in the site 4, the global colour distortion increases from spectrally optimum MOSOS-IHS-DWT result towards spatially optimum MOSOS-IHS-DWT result.

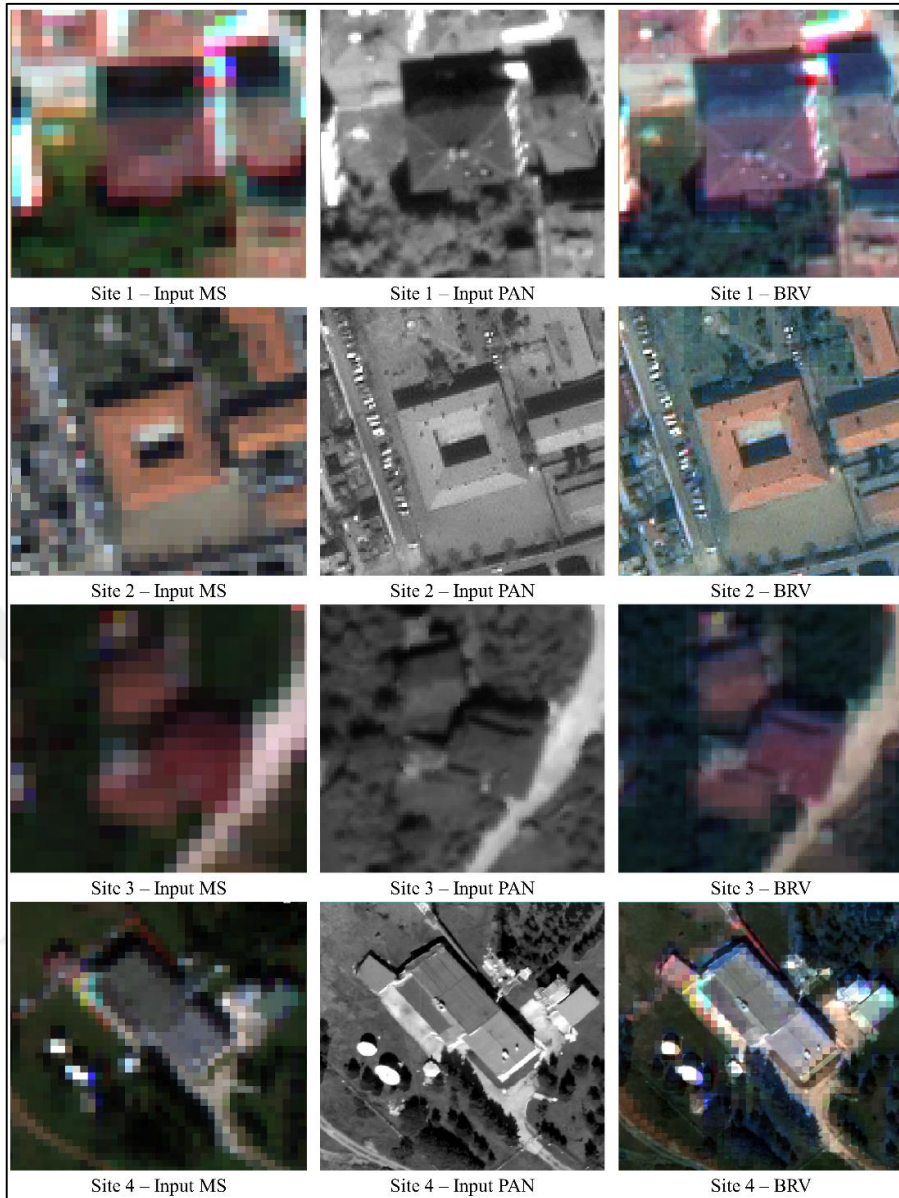


Figure 42. Zoomed-in BRV results for the test sites

Figure 42 shows that the BRV method achieved to transfer the spatial detail content of the input PAN images to some degree in all test sites. The figure also depicts that the BRV method could not manage to produce images of high spatial detail quality, causing some apparent mosaic effects in the sites 1, 3 and 4. The BRV method produced the sharpest image in the site 2. The BRV result of the site 3 looks almost like the input MS image in terms of spatial structure quality. In the site 4, pixel block effects are more obvious on the edges of the buildings and vegetation, whereas the vegetated areas seem to be clear from these effects, which can be seen in Figure 42.

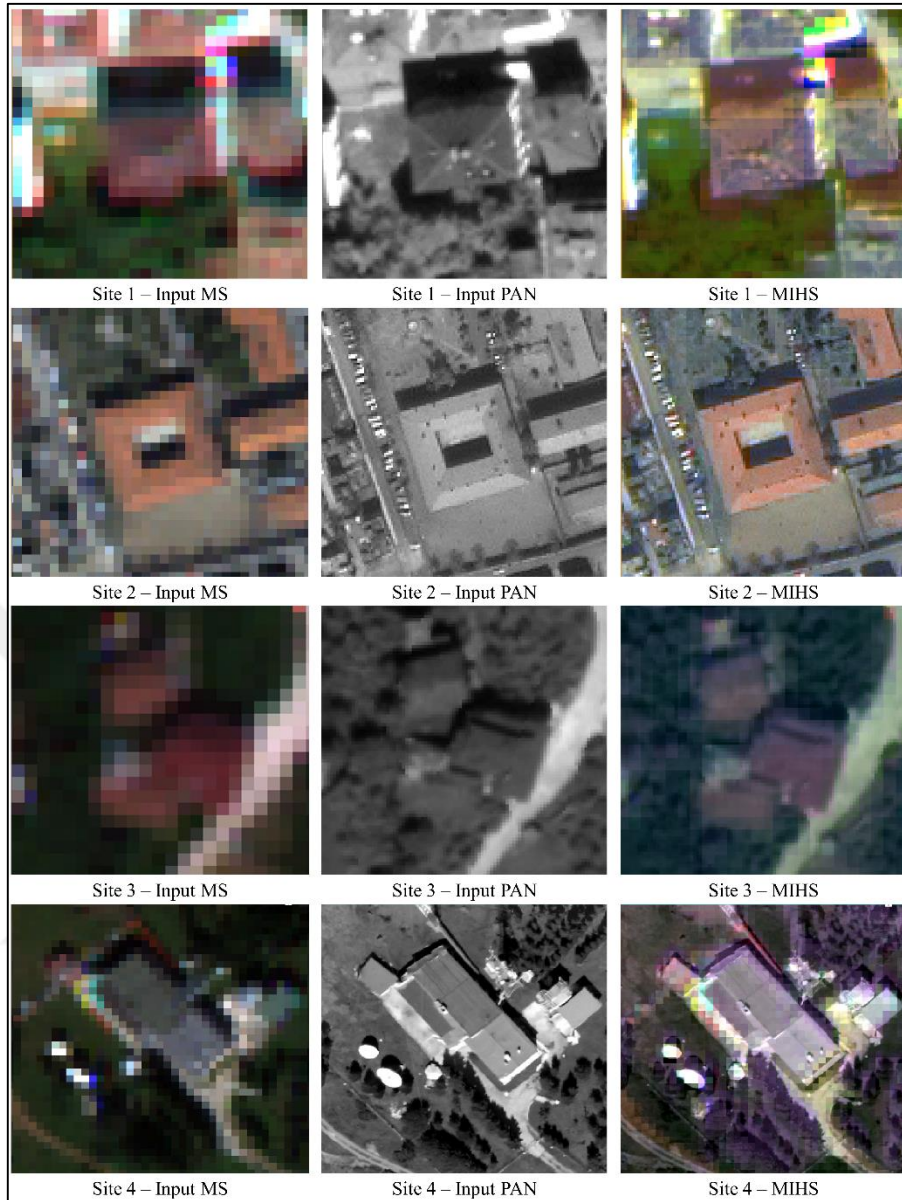


Figure 43. Zoomed-in MIHS results for the test sites

Figure 43 depicts that the MIHS method produced inconsistent spatial fidelity in the test sites. The MIHS method also returned some mosaic effects in the sites 1 and 3, whereas it achieved a high spatial structure quality in the site 2. The edges of the buildings and road look very sharp, almost like the input PAN image in the site 2. The pansharpened images produced by the MIHS method for the sites 1 and 3 seem like they are not the outcomes of a pansharpening process. It can also be seen in Figure 43 that the MIHS method did not only cause mosaic effects, but also caused smooth edge details in some parts of the vegetated areas.

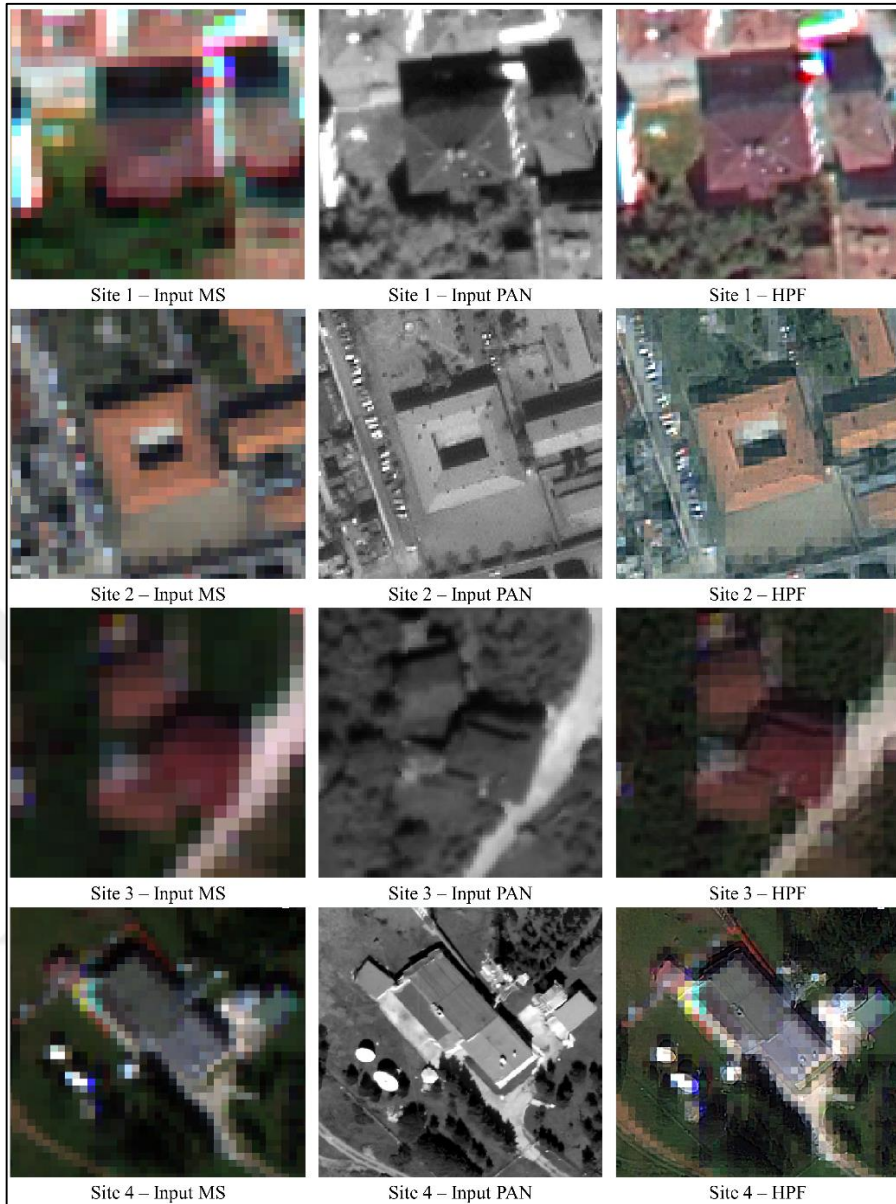


Figure 44. Zoomed-in HPF results for the test sites

As seen in Figure 44, the HPF method produced a crisp image only for the site 1. The HPF result of this site contains the majority of the spatial detail content of the input PAN data. The figure also demonstrates that the HPF method could not achieve to inject the spatial details of the input PAN images into the input MS images in the sites 2, 3 and 4. The HPF method resulted in the greatest amount of pixel artefacts in the sites 3 and 4. It is very hard to notice the edge details on the pansharpened image produced by the HPF method for these sites. Figure 44 shows that, despite the pixel artefacts, the edge details are observable on the pansharpened image produced for the site 2.

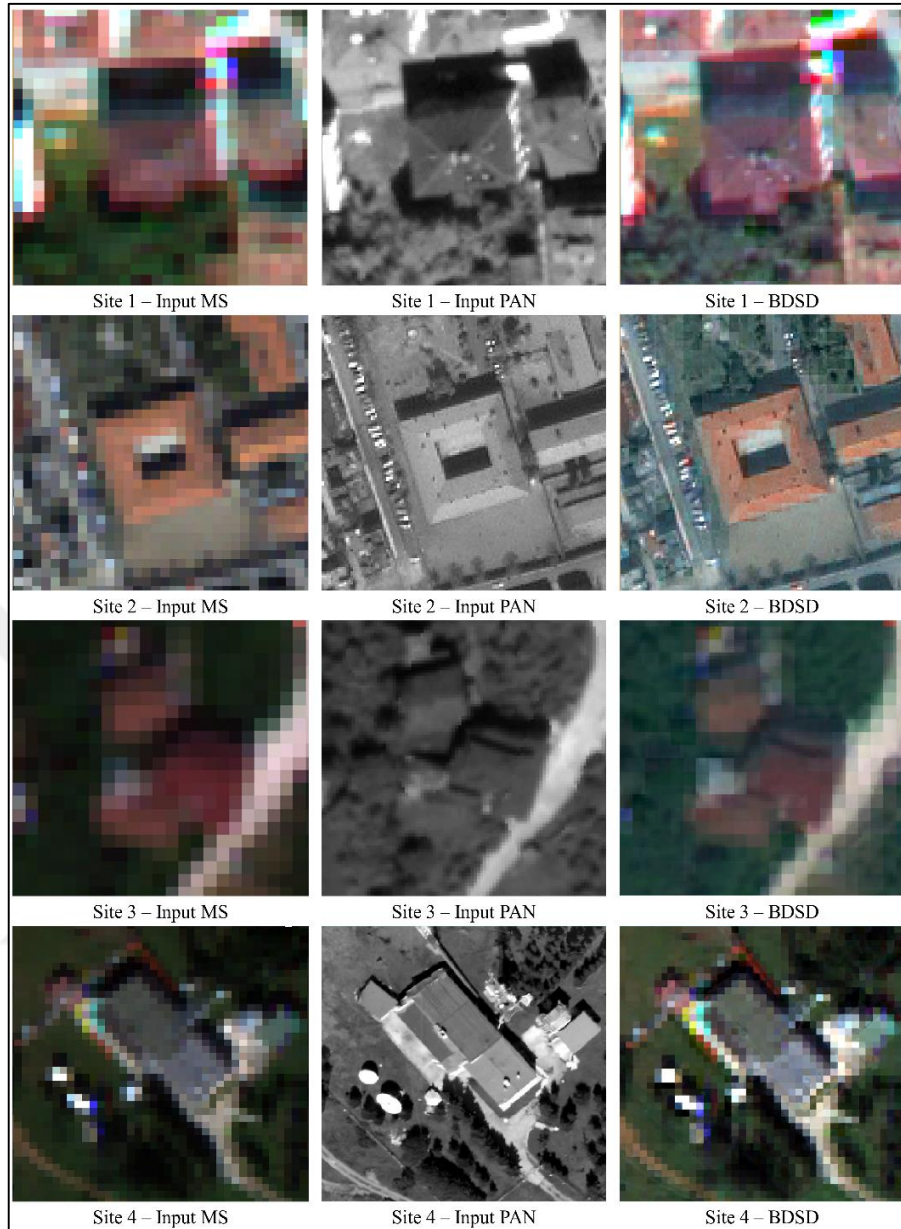


Figure 45. Zoomed-in BSD results for the test sites

Compared to the other sites, the BSD method produced sharper images for the sites 1 and 2, which can be seen in Figure 45. The pansharpened image produced by this method for the site 1 has still some mosaic effects. The BSD method returned images of very low spatial detail quality for the sites 3 and 4. As seen in Figure 45, the BSD results for these sites do not contain any spatial structure information from the input PAN data. On the other hand, a very small amount of pixel artefacts is observable on the pansharpened image produced by the BSD method for the site 2. These artefacts are mostly on the vegetated areas of this site.

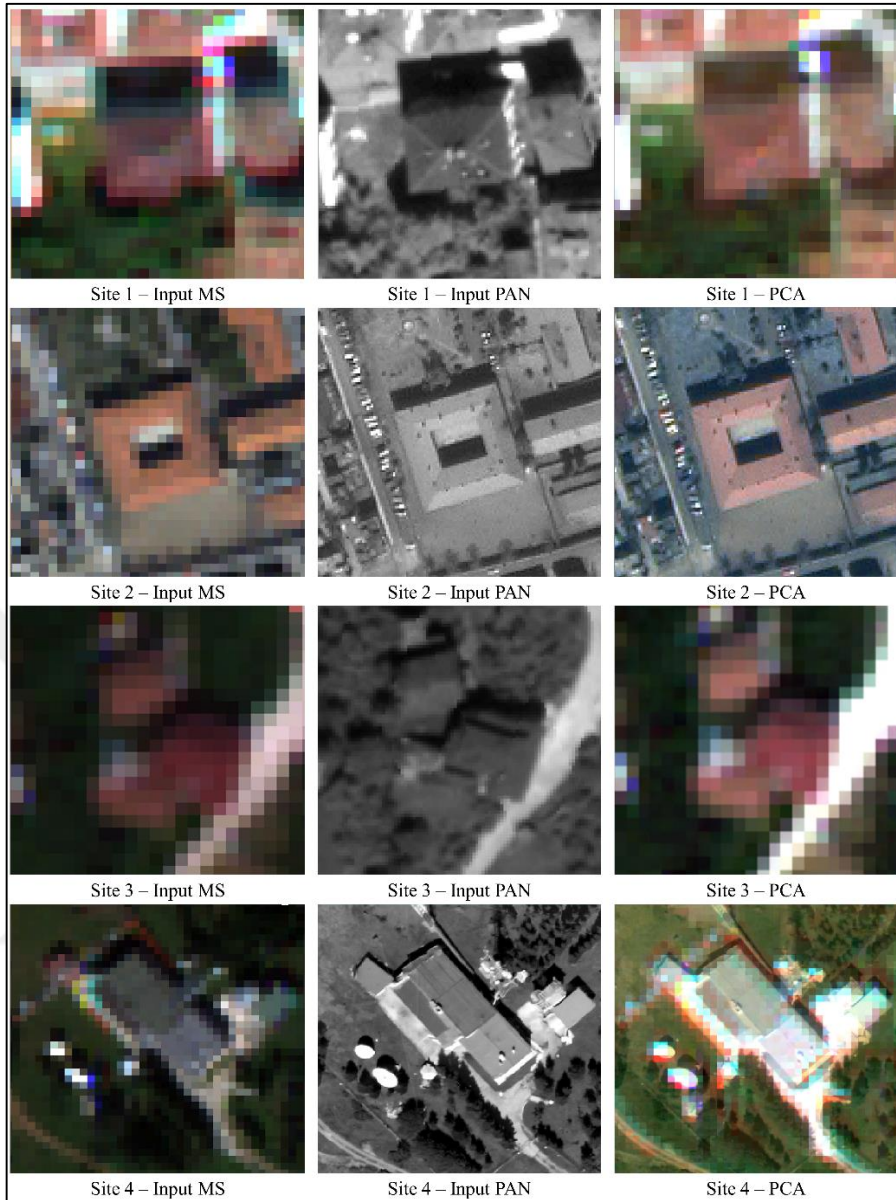


Figure 46. Zoomed-in PCA results for the test sites

Figure 46 shows that the PCA method produced an image of high spatial detail quality only in the site 2. Figure also depicts that the PCA method failed to transfer the spatial details of the input PAN image in the sites 1 and 3. As can be seen, the PCA results of these sites seem as if they are not products of a pansharpening process. On the other hand, the PCA method produced a very sharp image in the site 2. As seen in Figure 46, the PCA result of this site is very appropriate for human interpretation. Despite the fact that the edge details are apparent on the pansharpened image produced for the site 4, there are some mosaic effects on this image.

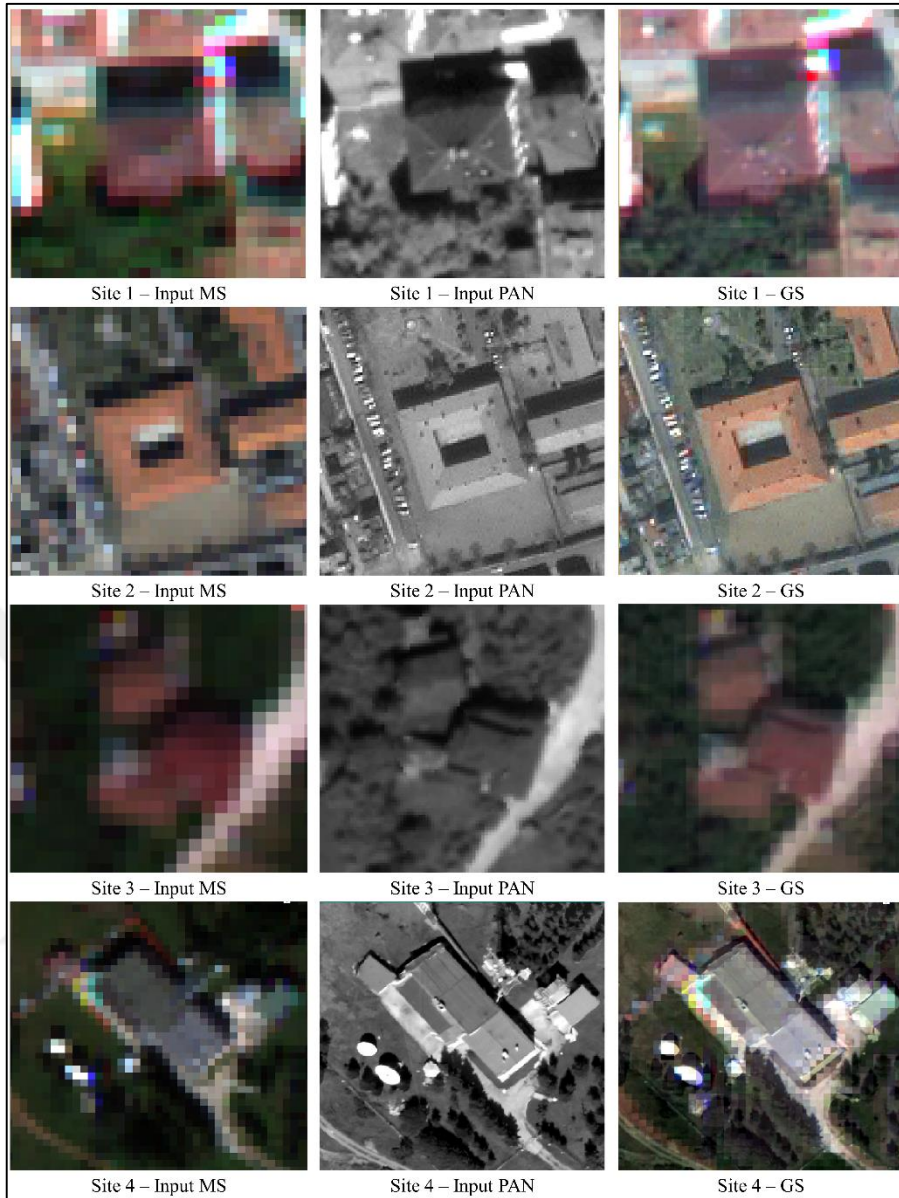


Figure 47. Zoomed-in GS results for the test sites

Figure 47 depicts that the GS method led to precarious spatial fidelity in the test sites. As seen in the figure, the GS method produced some pixel artefacts in the site 1. However, it did not implicitly deteriorate the spatial detail content of this site. The GS method produced a very sharp image for the site 2, which can be seen in Figure 47. The GS method resulted in some mosaic effects in the site 3. The most interesting result of the GS method is the one produced for the site 4. Because, the GS method produced an image whose spatial detail content is similar to the input PAN image. Despite this, there are still some mosaic effects on this image, which can be seen in Figure 47.

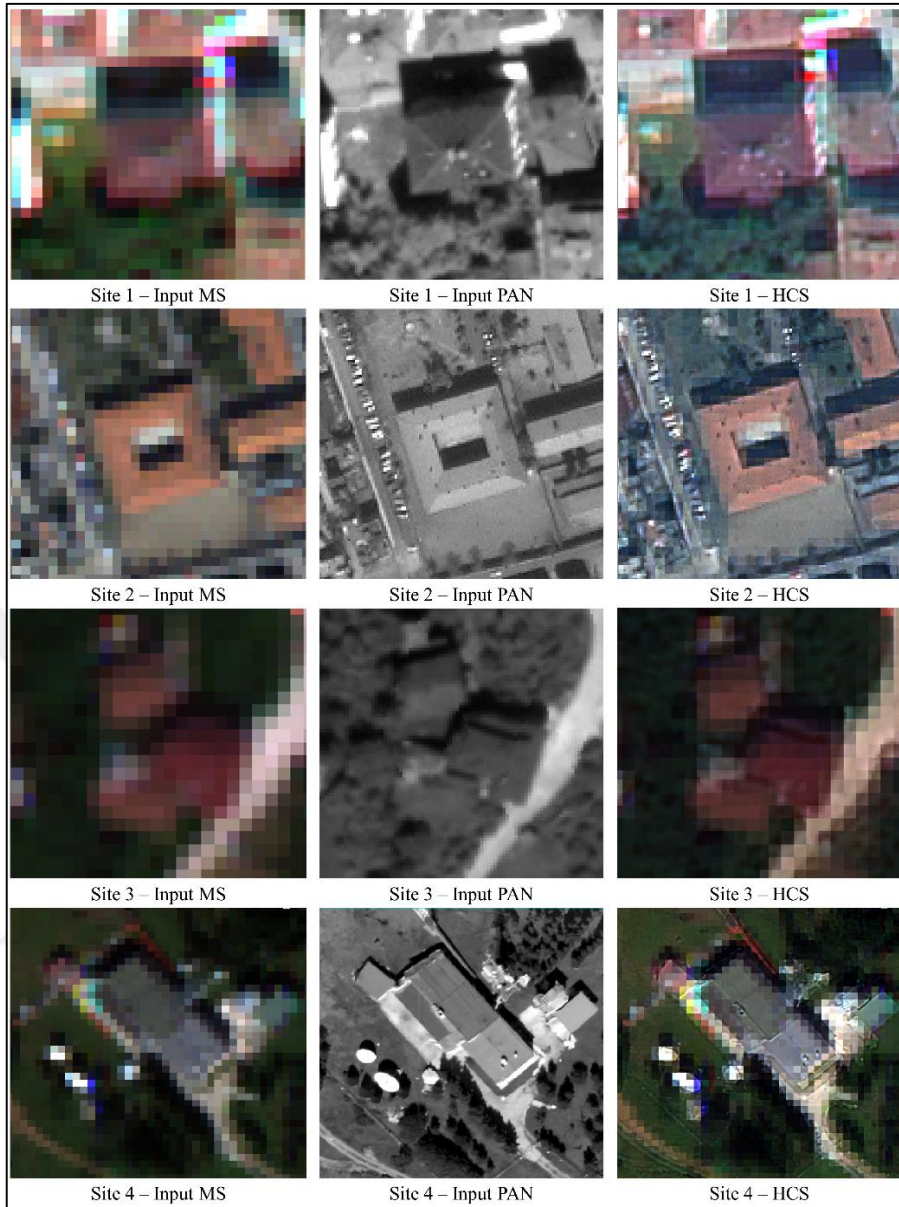


Figure 48. Zoomed-in HCS results for the test sites

As seen in Figure 48, the HCS method caused the deterioration of the spatial detail content to a certain degree in all test sites. Figure 48 depicts that, in the site 1, the HCS method achieved to transfer a very small amount of the spatial detail content of the input PAN image. The pansharpened image produced by the HCS method for the site 2 is the sharpest of all, which can be observed in Figure 48. On the other hand, the spatial details of the HCS result of the site 3 are barely observable. It can also be seen in Figure 48 that the HCS method distorted the spatial detail content of the site 4 to a large extent. To observe the edge information on the HCS result is almost impossible.

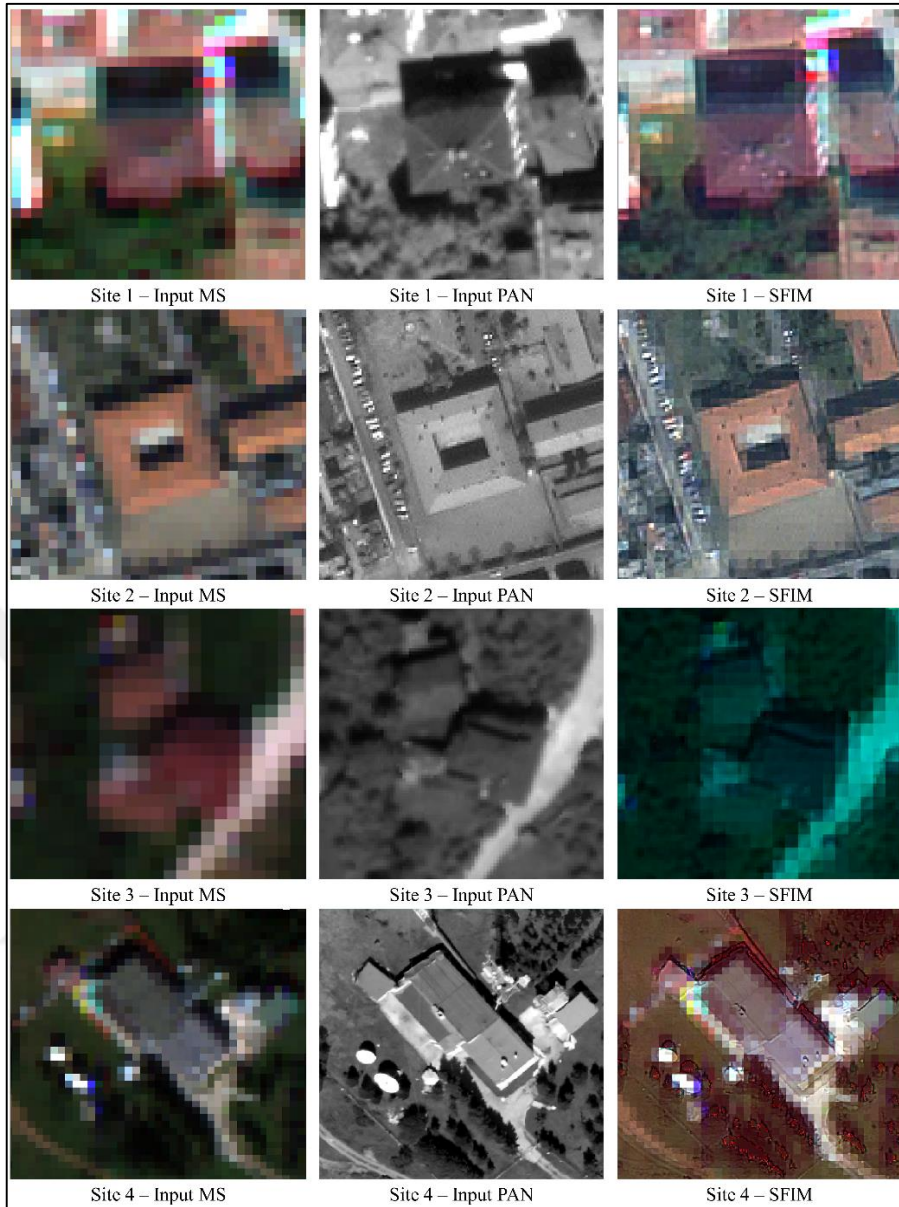


Figure 49. Zoomed-in SFIM results for the test sites

Figure 49 depicts that the SFIM method produced images of low spatial quality in all sites. As seen in the figure, the SFIM method returned a huge amount of mosaic effects in the site 1. Compared to that for the site 1, the pansharpened image produced by the SFIM method for the site 2 includes more spatial details. Despite the pixel artefacts, edge details are observable on the SFIM result of the site 2. As also seen in Figure 49, the SFIM result of the site 3 includes almost none of the spatial features of the input PAN data of this site. Despite the fact that some edge information is observable on the SFIM result of the site 4, a large amount of pixel artefacts exists in this image.

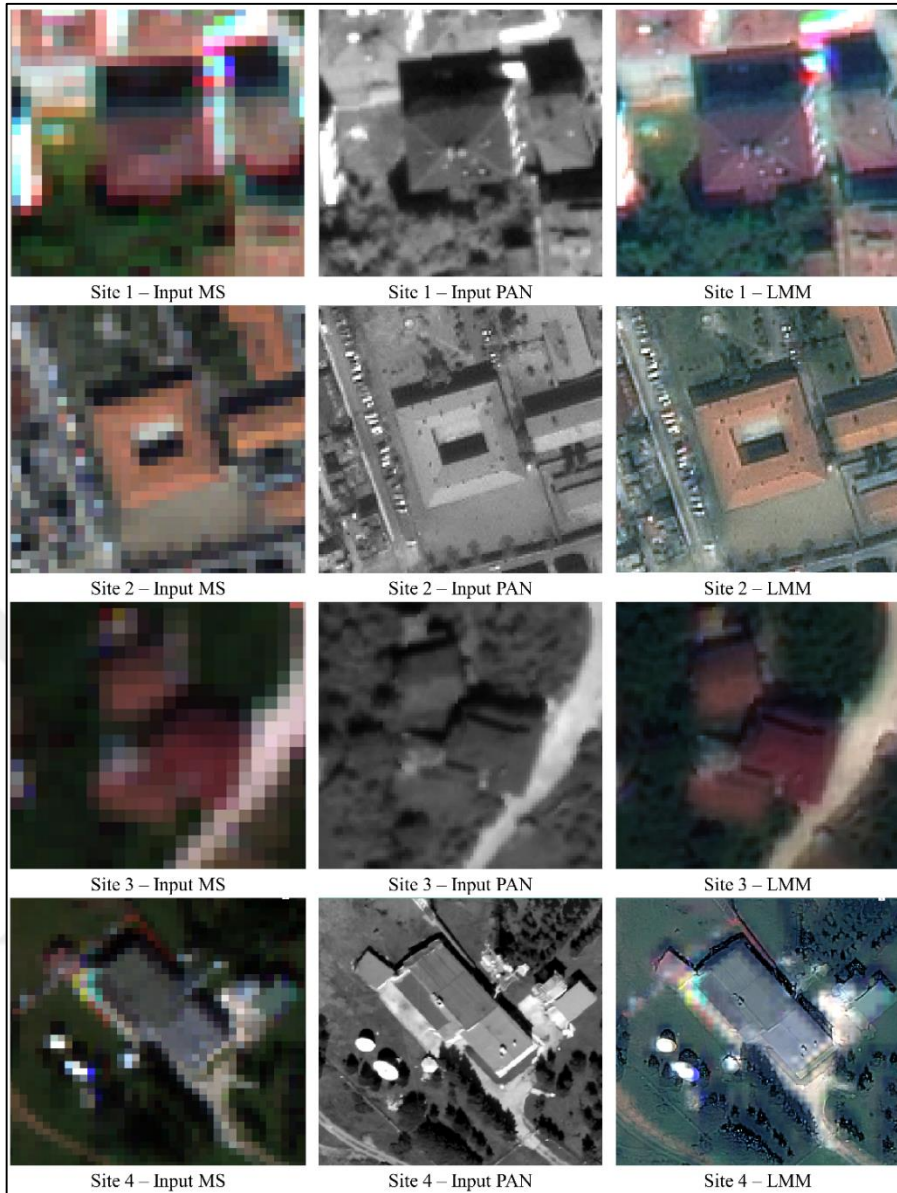


Figure 50. Zoomed-in LMM results for the test sites

As seen in Figure 50, the LMM method was moderately successful in transferring the spatial details in the test sites. The figure shows that the LMM method achieved to produce an image of high spatial detail quality in the sites 1, 2 and 3. The LMM method, on the other hand, caused a small amount of blurriness on the edges of the roads and buildings in the sites 1 and 3. Figure 50 also depicts that the LMM method achieved to transfer only a certain amount of the input PAN data into the input MS data in the site 4. The LMM method was also found to absorb the spatial detail content to some degree in this site, which can be observed in Figure 50.

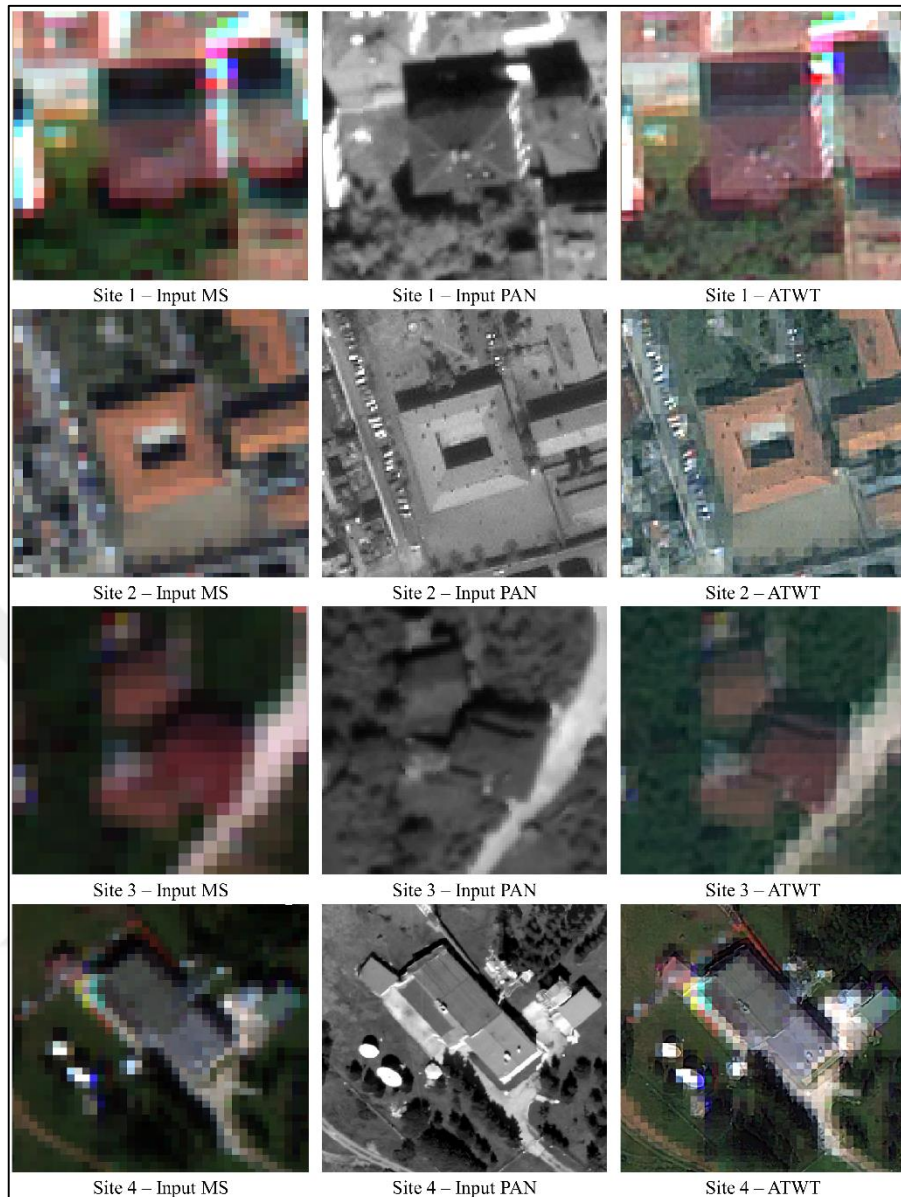


Figure 51. Zoomed-in ATWT results for the test sites

Figure 51 demonstrates that the ATWT method caused the deterioration of the spatial detail content in the test sites. As seen in Figure 51, the ATWT method returned mosaic effects in the site 1. It is almost impossible to notice the edge details in the ATWT result of the site 1. Although the ATWT result of the site 2 comprises mosaic effects, edge details are noticeable. On the other hand, the ATWT method failed to inject the spatial features of the input PAN data into the input MS image of the site 3. The ATWT method caused the absorbance of the spatial detail content in the site 4. Despite this, the edge details of the roads and buildings are barely noticeable.

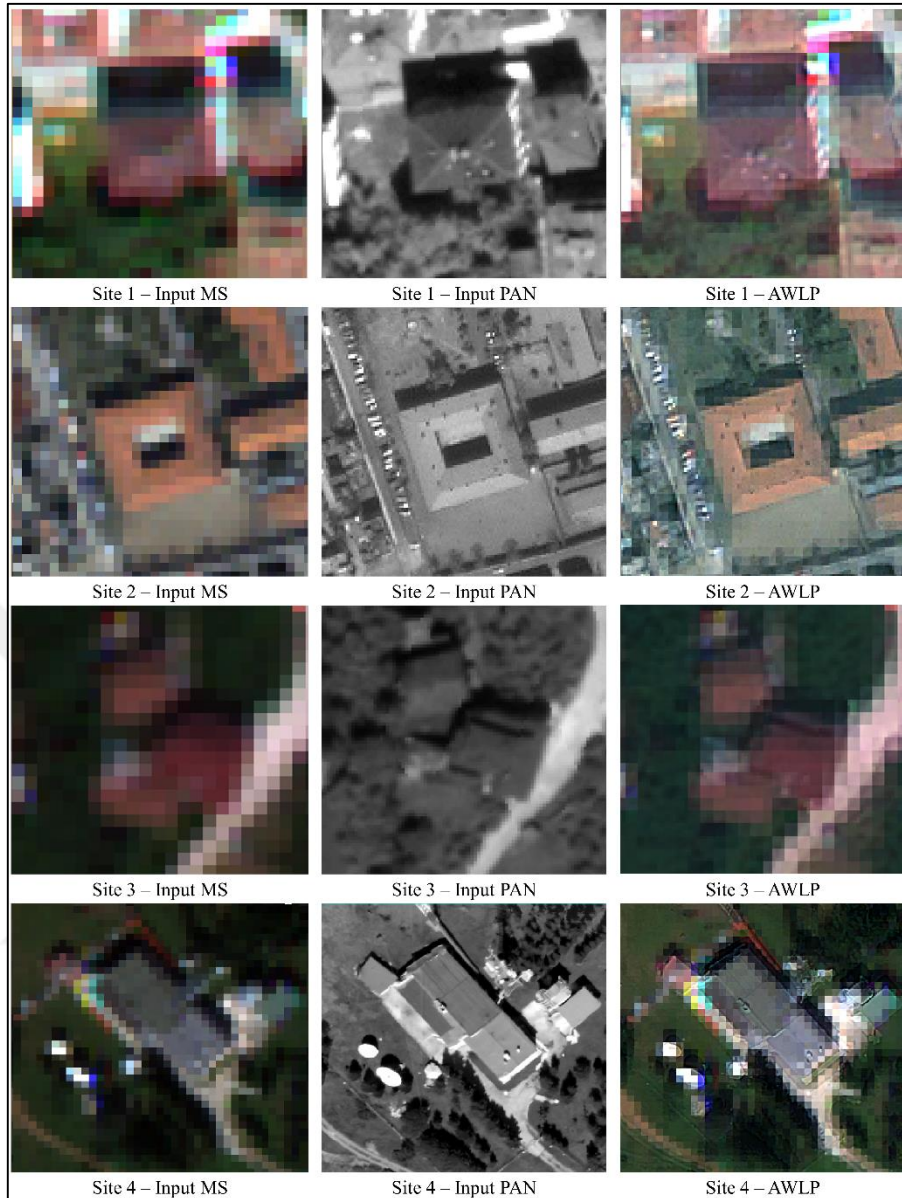


Figure 52. Zoomed-in AWLP results for the test sites

Figure 52 depicts that the AWLP method showed a very similar spatial detail injection performance to the ATWT method. As seen in Figure 52, the AWLP method tended to absorb the spatial features of the input PAN image in all test sites. The AWLP method returned the sharpest image in the site 2. The AWLP result of the site 3 contains a spatial detail content similar to the input MS image. It can also be inferred from Figure 52 that the AWLP method caused mosaic effects mostly on the edges of the buildings and roads. However, some sharp edge details are still observable on the AWLP result of the site 4, which can be seen in Figure 52.

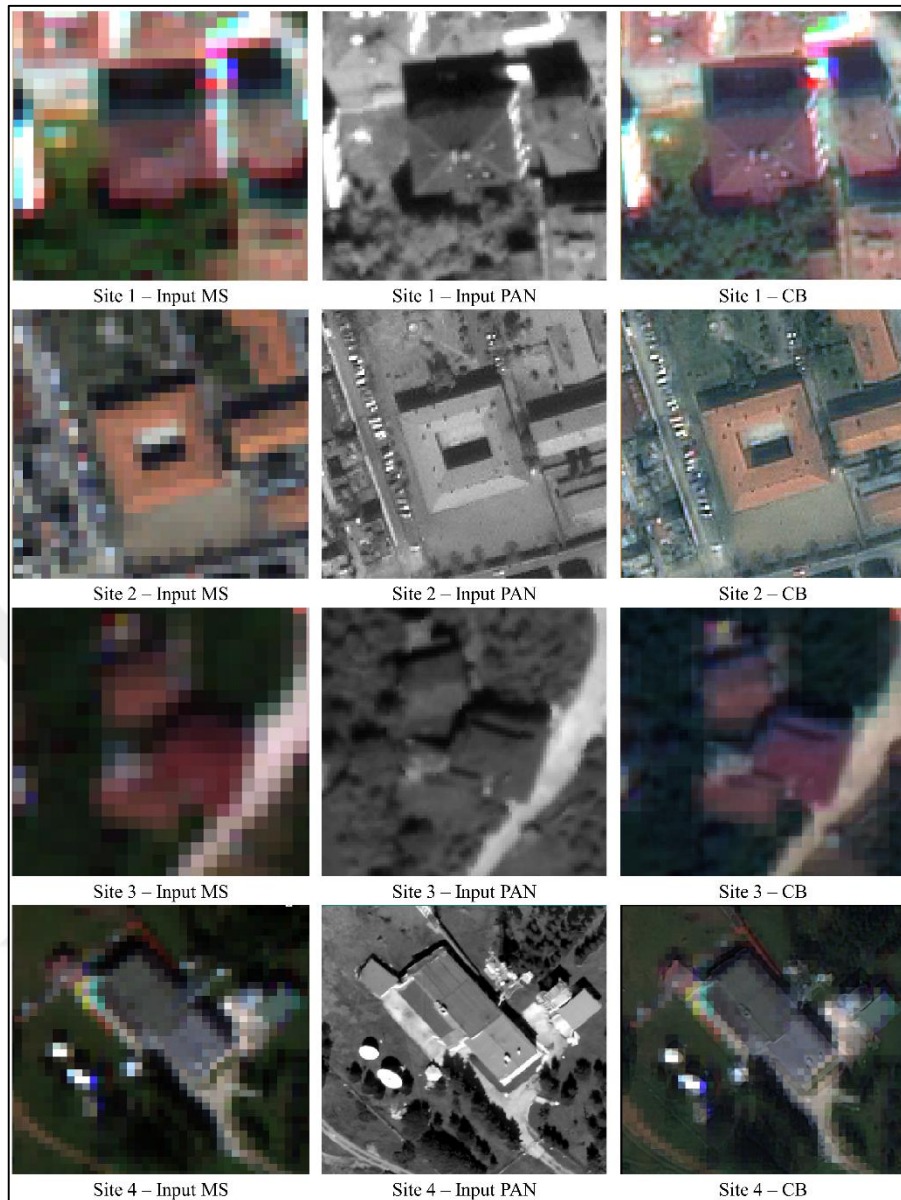


Figure 53. Zoomed-in CB results for the test sites

As seen in Figure 53, the CB method was partially successful in producing sharp images in the test sites. The figure demonstrates that the CB method produced spatially more consistent images in the sites 1 and 2. The CB method caused also a small amount of blurriness on the edges in these sites. Figure 53 also depicts that the CB method caused some mosaic effects in the sites 3 and 4. The CB result of the site 4 is spatially more consistent than that of the site 3, which can be observed in Figure 53. Examining the figure, it can be concluded that the CB method tends to keep the edge information, even if it produces images of mosaic effects.

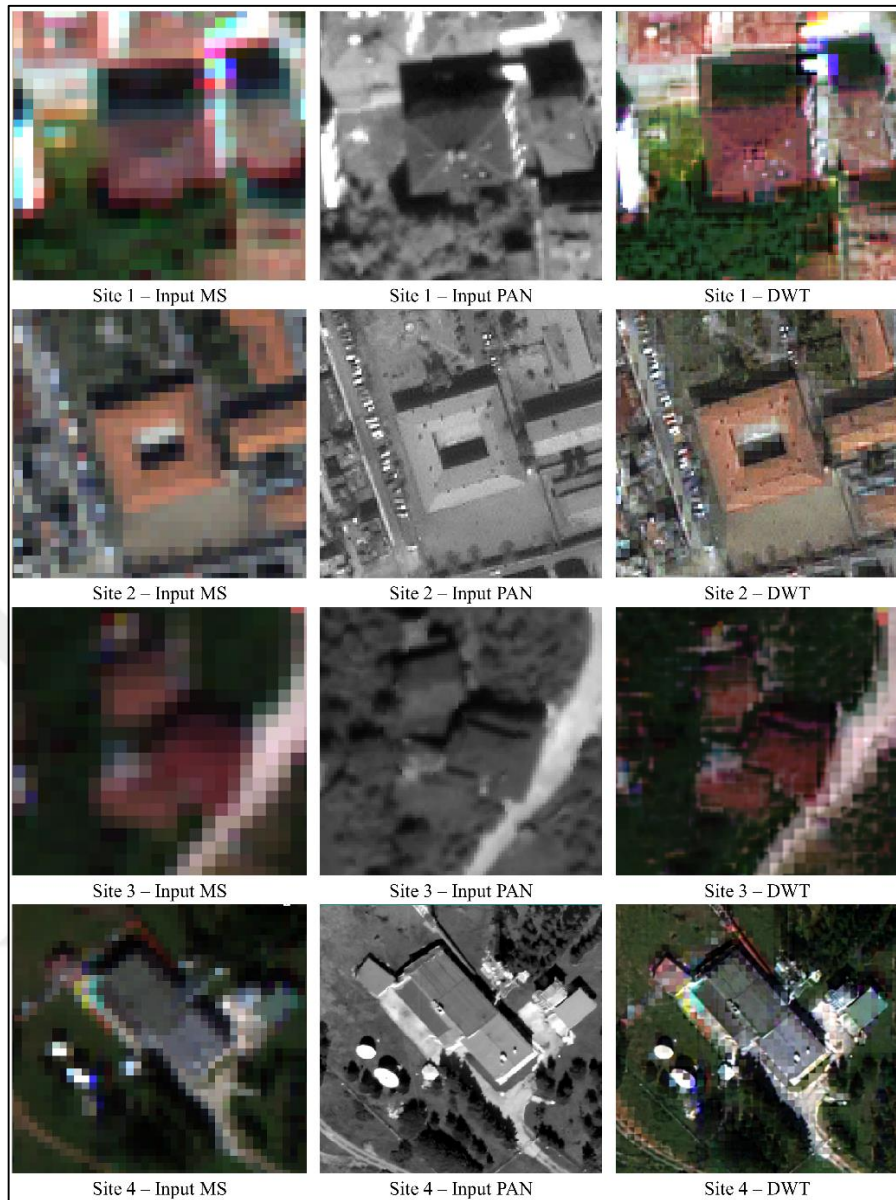


Figure 54. Zoomed-in DWT results for the test sites

Figure 54 demonstrates that the DWT method caused a considerable spatial deterioration in all test sites. The DWT method returned the greatest spatial distortion in the sites 1 and 3. The DWT method produced very messy images for these sites and it is almost impossible to obtain any spatial information from these images. Despite the pixel artefacts, the spatial details of the land cover features are still noticeable in the site 2 (see Figure 54). On the other hand, in the site 4, the DWT method resulted in an image of low spatial quality in the site 4. However, some edge details were still preserved in this site, as happened in the site 4.

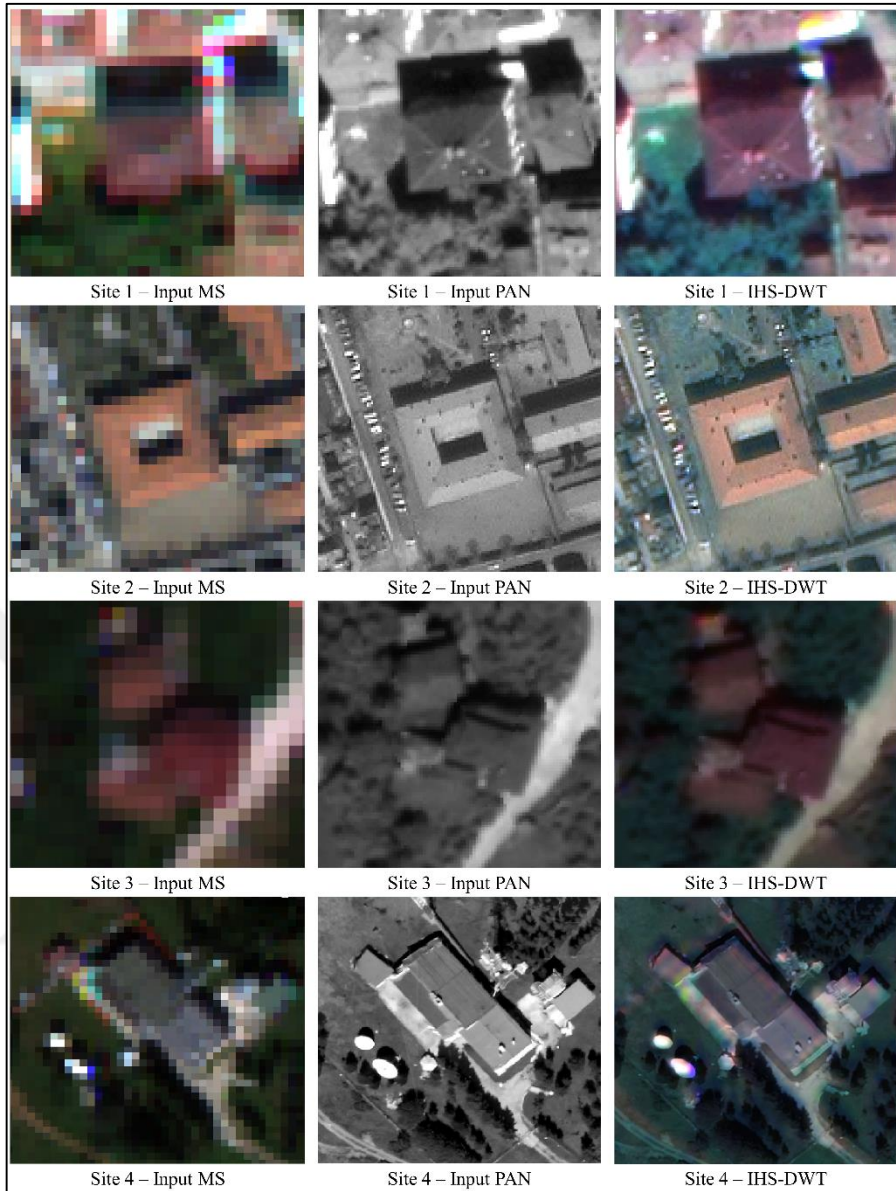


Figure 55. Zoomed-in IHS-DWT results for the test sites

Figure 55 shows that the IHS-DWT method succeeded in producing sharp images in all test sites. Figure 55 also shows that the IHS-DWT method returned a small blurriness on the edges of the buildings and roads in the sites 1 and 3. In addition, no pixel artefacts can be seen on the IHS-DWT results of these sites. Figure 55 also demonstrated that the IHS-DWT method generated a very sharp image in the site 2. As can be seen, no significant spatial detail difference can be observed between the IHS-DWT result and the input PAN image in this site. It should also be noted that the IHS-DWT method did not cause any mosaic effects in the site 4. As may be recalled, many other pansharpening methods caused pixel artefacts in this site.

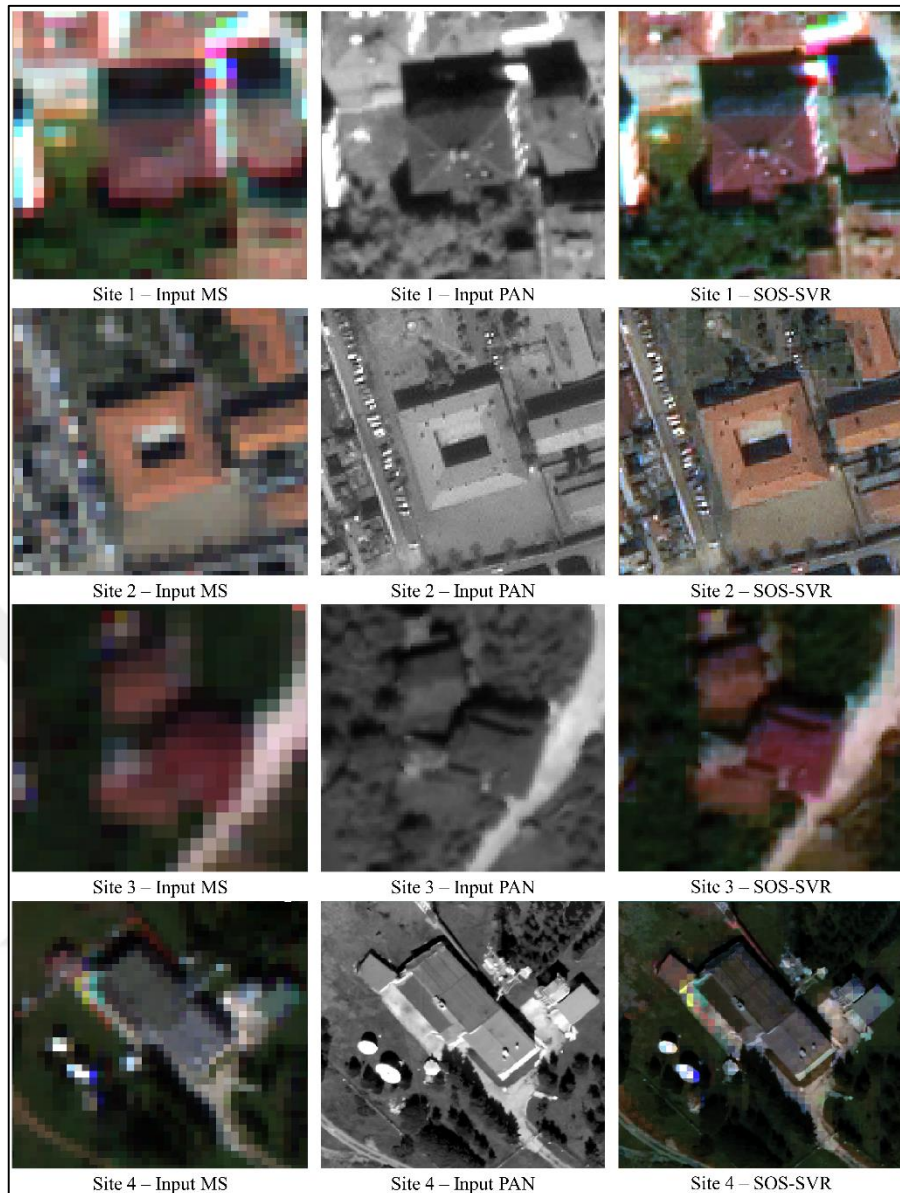


Figure 56. Zoomed-in SOS-SVR results for the test sites

Figure 56 depicts that the proposed SOS-SVR method presented a superb performance in producing sharp images. Despite this, the SOS-SVR method caused a very small amount of mosaic effects in the sites 1 and 2, as seen in Figure 56. The figure also shows that the SOS-SVR method produced a crisp image for the site 3, where the majority of the other pansharpening methods had a difficulty in ensuring the crispness. Another important conclusion drawn from Figure 56 that the SOS-SVR method led to captivating edge details in the site 4. Despite this, the SOS-SVR method caused a very small measure of pixel artefacts in this site.

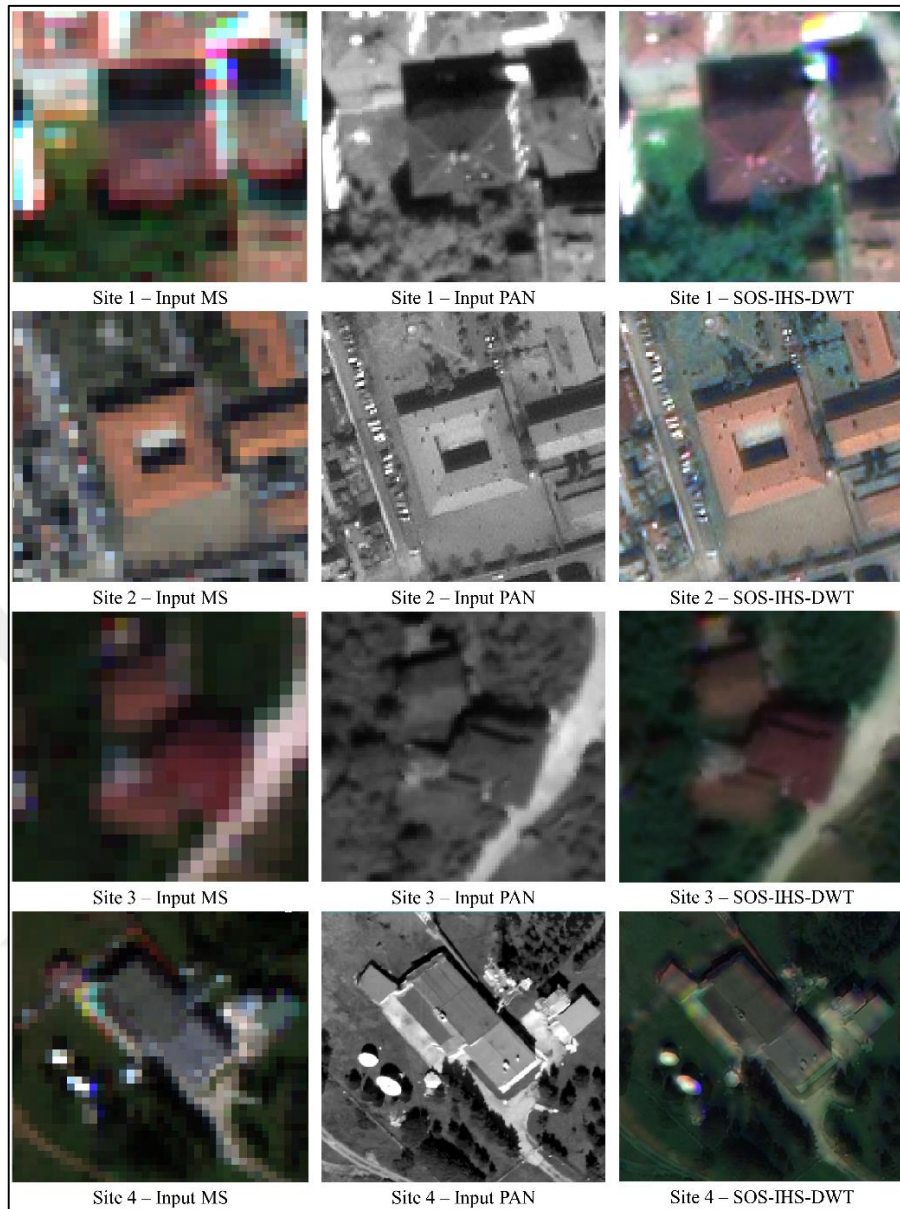


Figure 57. Zoomed-in SOS-IHS-DWT results for the test sites

Figure 57 depicts that the SOS-IHS-DWT method produced crisp images for all test sites. Although the SOS-IHS-DWT technique achieved a successful spatial detail transfer in the sites 1, 3 and 4, a small amount of blurring effects can be seen on the edges in these sites. However, these blurring effects do not have a negative effect on the noticeability of the spatial details in these sites. The SOS-IHS-DWT method produced the sharpest image for the site 2. As can be seen in Figure 57, the SOS-IHS-DWT result of the site 2 is as sharp as the PAN data of this site.

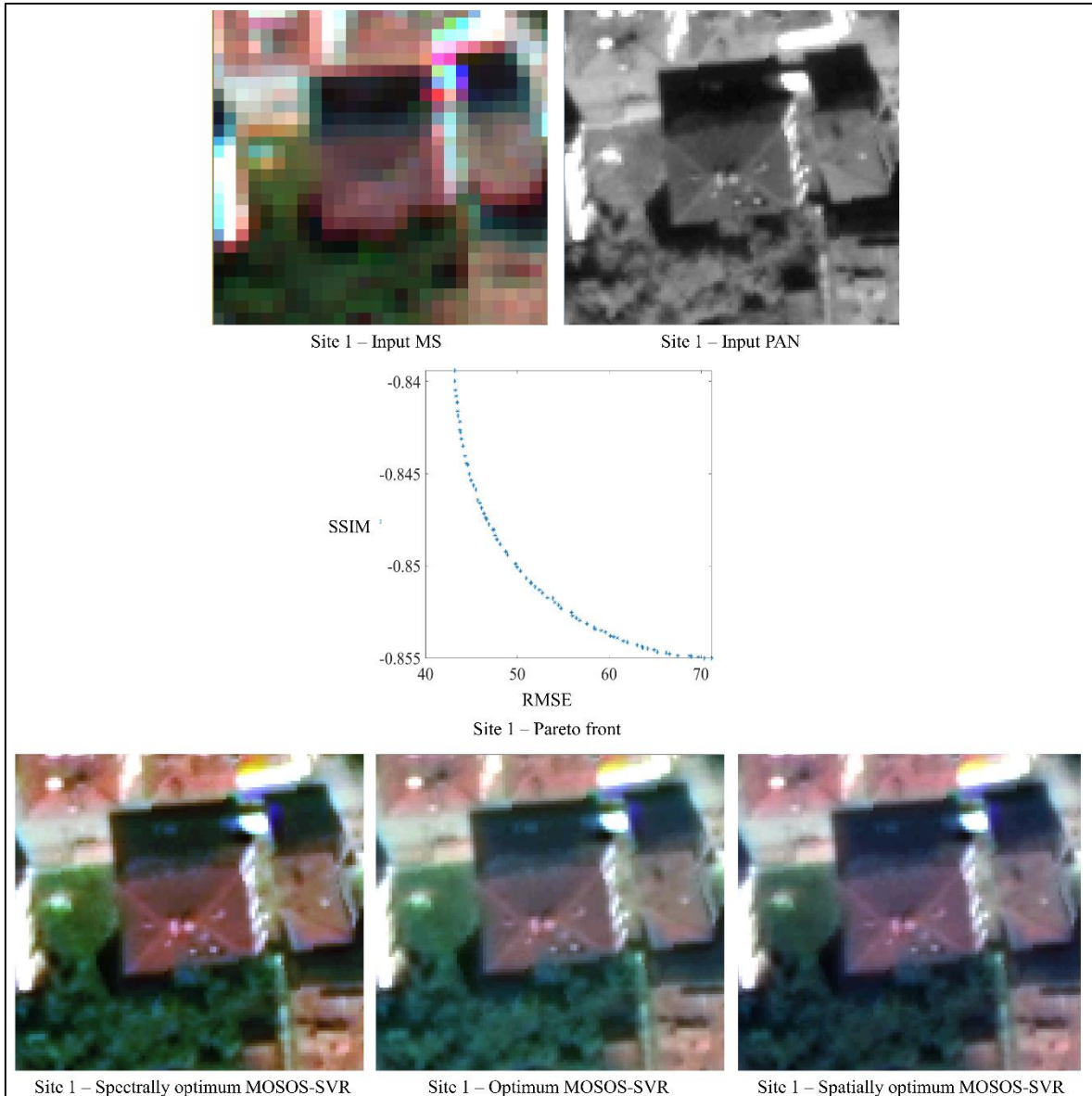


Figure 58. Zoomed-in MOSOS-SVR results for the site 1

The band weights estimated by the MOSOS-SVR method to spectrally and spatially optimize the pansharpening result were found to transfer the spatial structure of the site 1 with a very high success, which can be seen in Figure 58. In fact, it is hard to notice the spatial detail content difference between the spectrally and spatially optimum MOSOS-SVR results, as seen in Figure 58. On the other hand, the band weights obtained to ensure the best compromise between the colour and spatial structure quality achieved to produce a sharp image that is comparable to the spectrally and spatially optimum MOSOS-SVR results in terms of spatial detail quality.

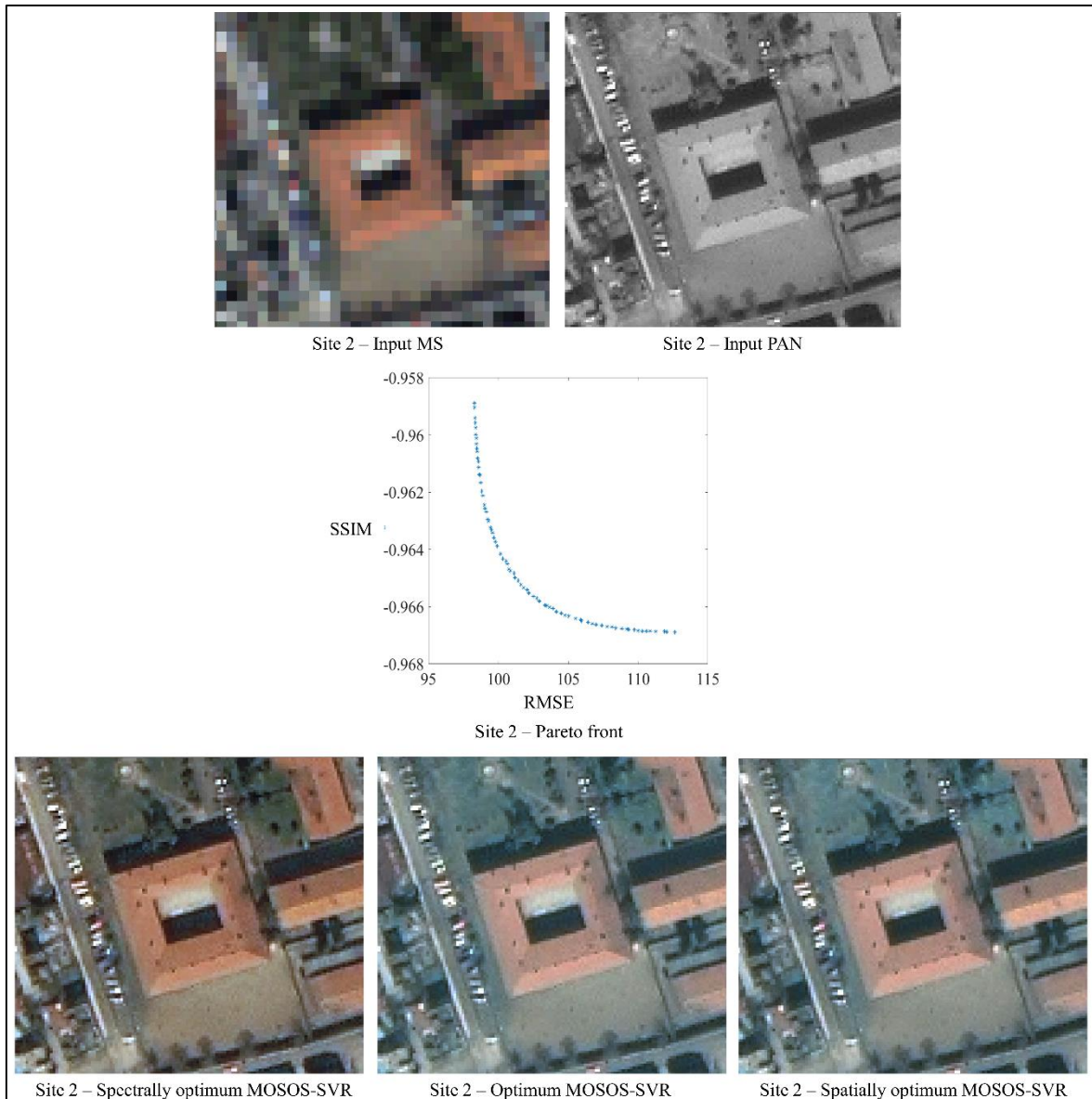


Figure 59. Zoomed-in MOSOS-SVR results for the site 2

As seen in Figure 59, the band weights obtained by the MOSOS-SVR method to optimize the spectral and spatial quality returned a very crisp image for the site 2. In fact, the spectrally and spatially optimum images produced from the MOSOS-SVR method contain a similar amount of edge information to the optimum MOSOS-SVR result of this site. As seen in Figure 59, it is very hard to visually observe the spatial detail differences among the spectrally optimum, spatially optimum and optimum MOSOS-SVR results of the site 2.

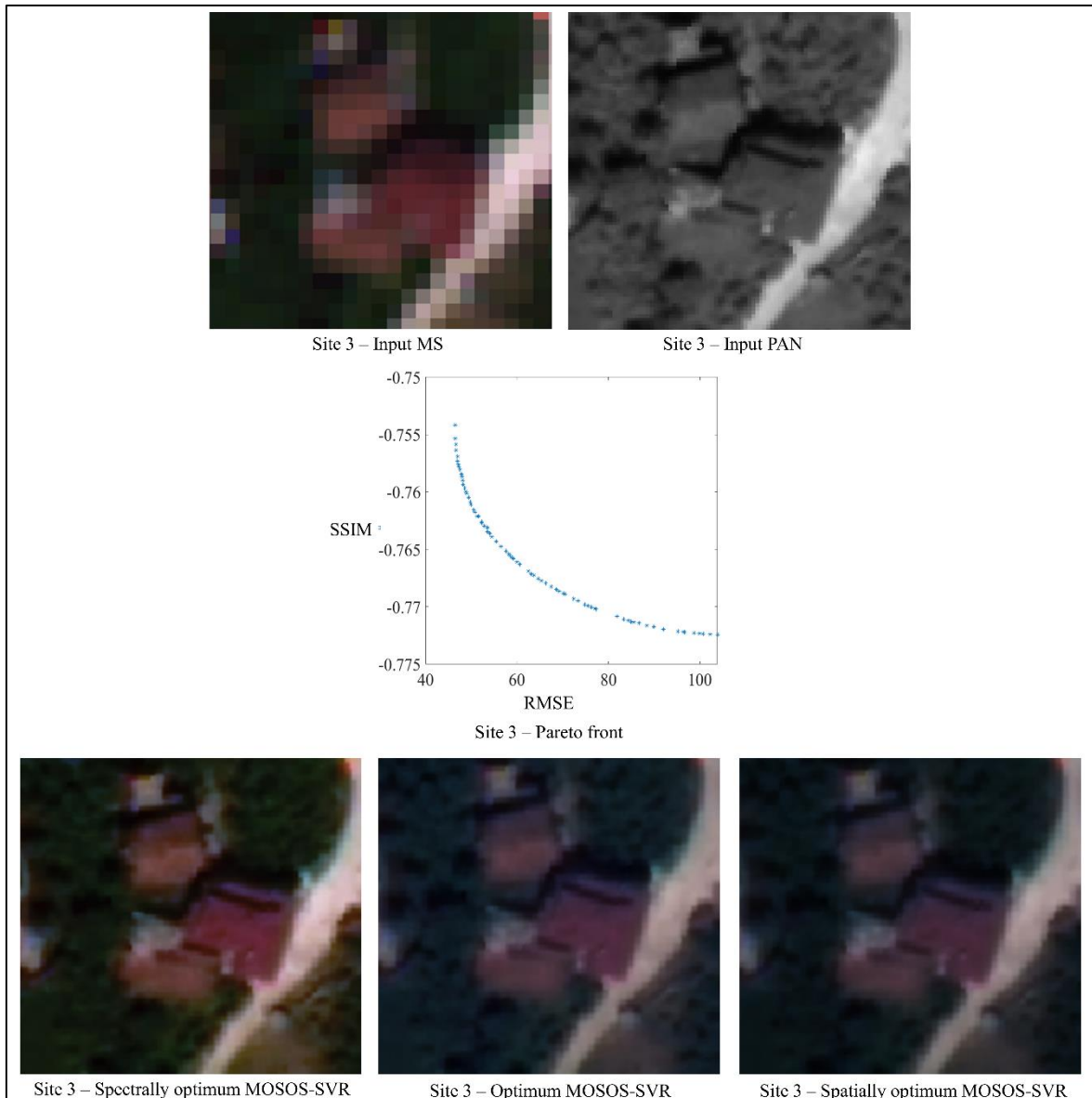


Figure 60. Zoomed-in MOSOS-SVR results for the site 3

Figure 60 depicts that the spectrally optimum MOSOS-SVR result contains the majority of the spatial details of the input PAN data of the site 3. The band weights obtained by the MOSOS-SVR method to achieve the optimum spatial quality and the optimum balance between the colour and spatial detail fidelity in the site 3 were found to generate images of very similar spatial detail content, which can be observed in Figure 60. Actually, all MOSOS-SVR results of the site 3 share almost the same spatial detail quality, as can be seen in Figure 60. Another important conclusion that can be drawn from Figure 60 is that the MOSOS-SVR results of the site 3 do not contain any mosaic effects. As may be remembered, many other methods led to mosaic effects in this site.

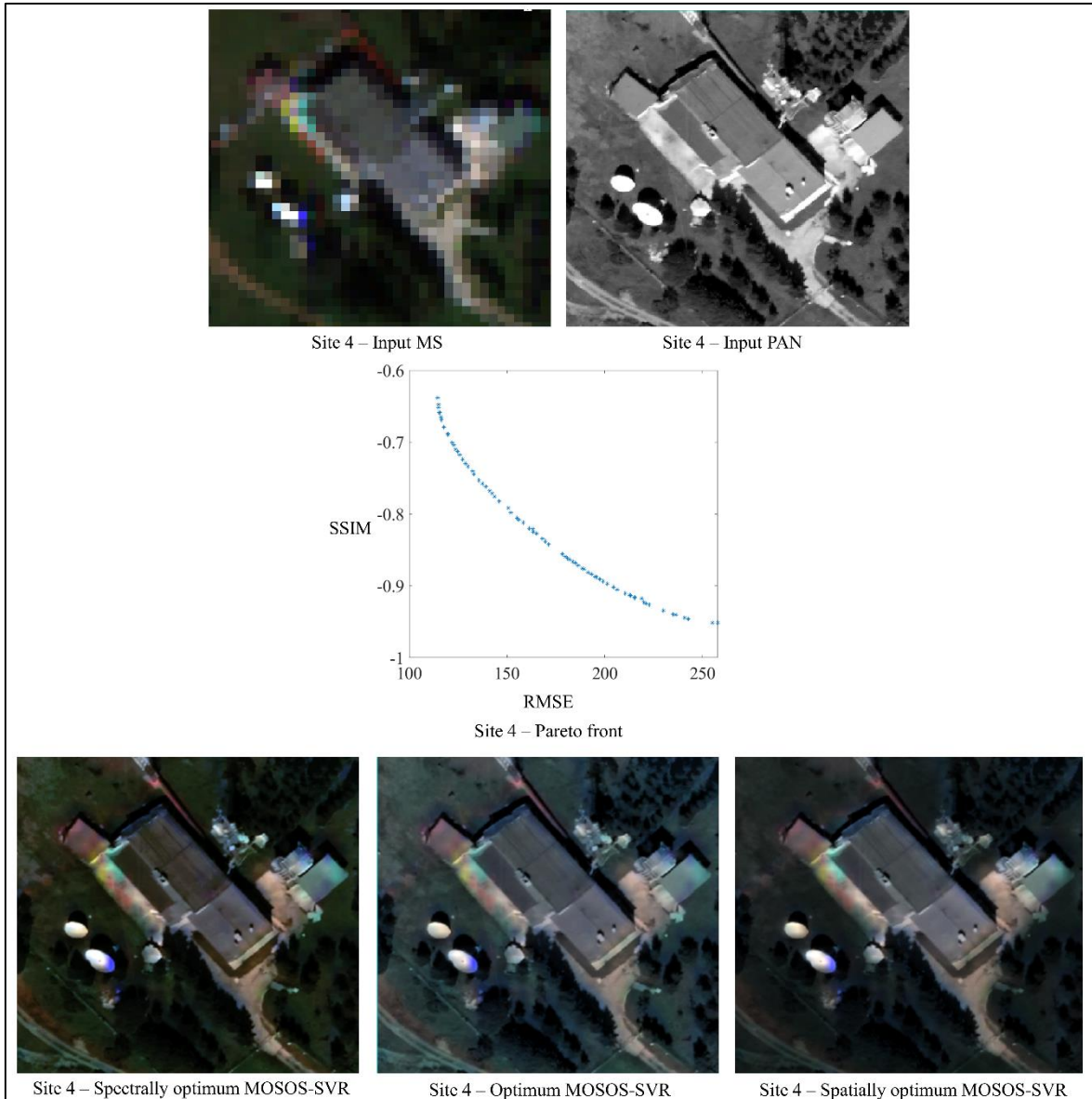


Figure 61. Zoomed-in MOSOS-SVR results for the site 4

Figure 61 shows that, in the site 4, the band weights estimated by the MOSOS-SVR method to produce the spectrally and spatially optimum pansharpener results were found to be very efficient in the accurate injection of the spatial details in this site. On the other hand, the optimum MOSOS-SVR result of the site 4 is almost as sharp as the spectrally and spatially optimum results of this site. Figure 61 also shows that the MOSOS-SVR method did not return any mosaic effects in any part of the scene. This, of course, shows the efficiency of the MOSOS-SVR technique in transferring the spatial details.

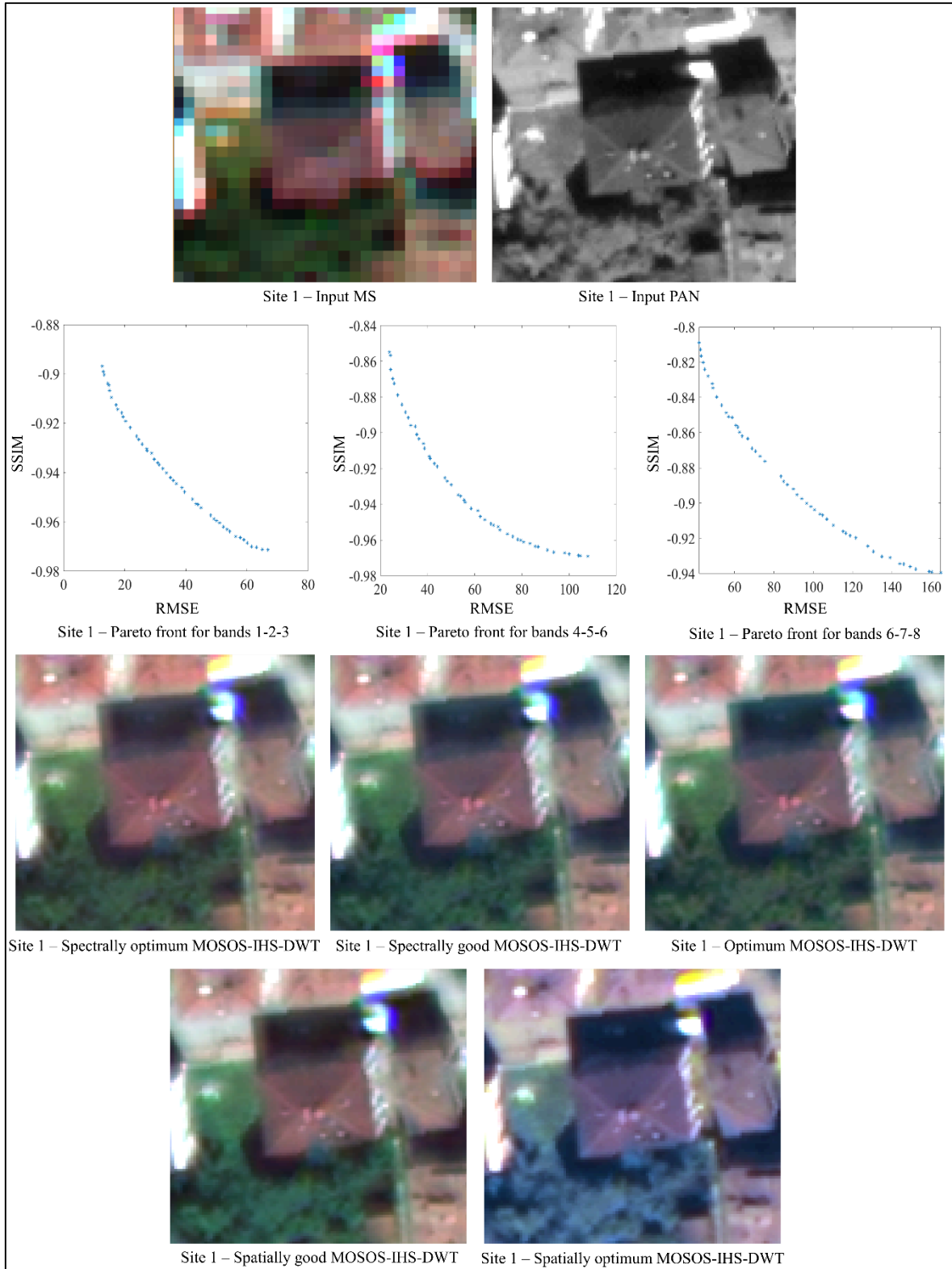


Figure 62. Zoomed-in MOSOS-IHS-DWT results for the site 1

As seen in Figure 62, in the site 1, the spatial distortion decreases from spectrally optimum MOSOS-IHS-DWT result towards spatially optimum MOSOS-IHS-DWT result.

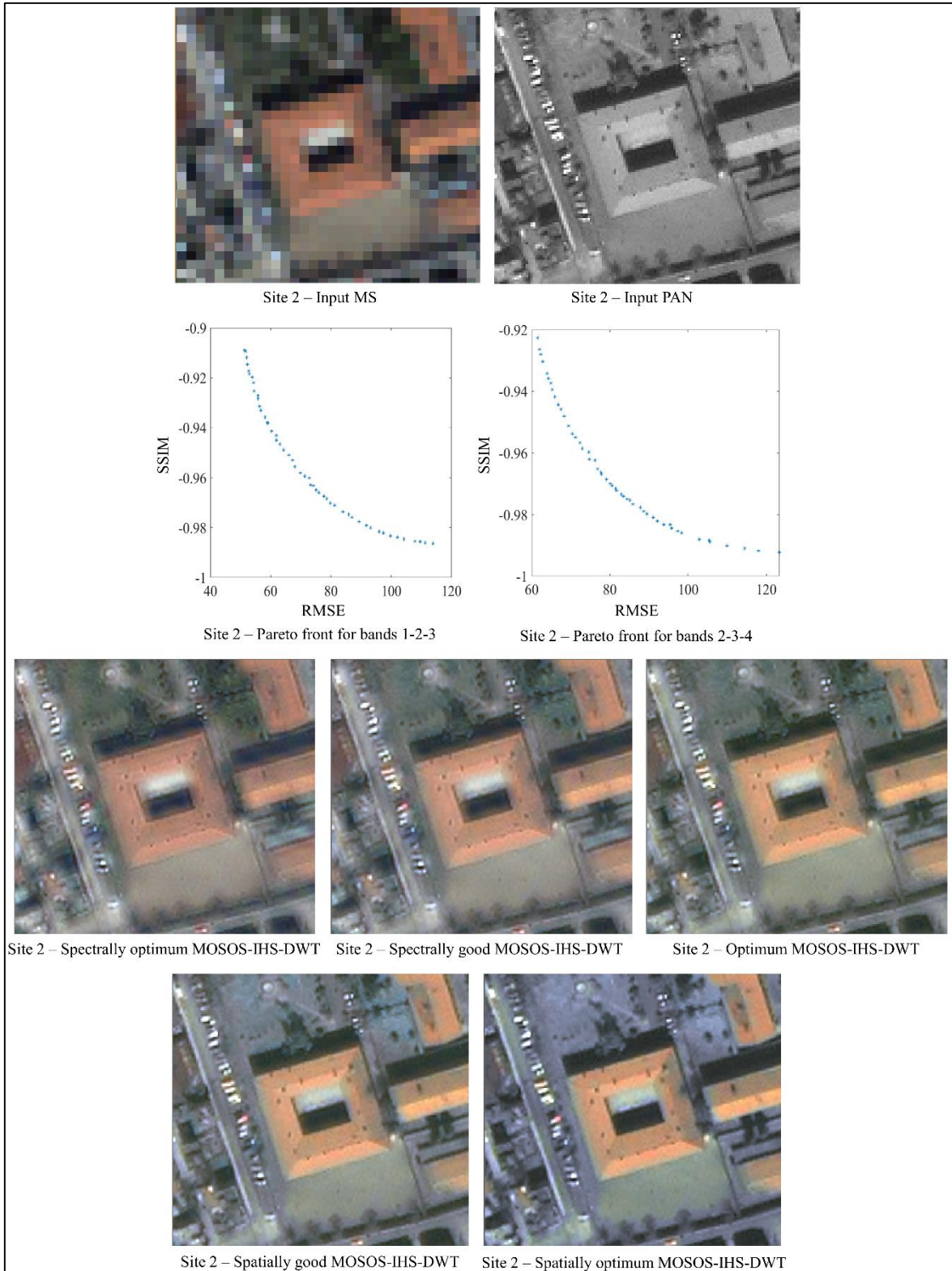


Figure 63. Zoomed-in MOSOS-IHS-DWT results for the site 2

Figure 63 depicts that, in the site 2, the spatial distortion decreases from spectrally optimum MOSOS-IHS-DWT result towards spatially optimum MOSOS-IHS-DWT result.

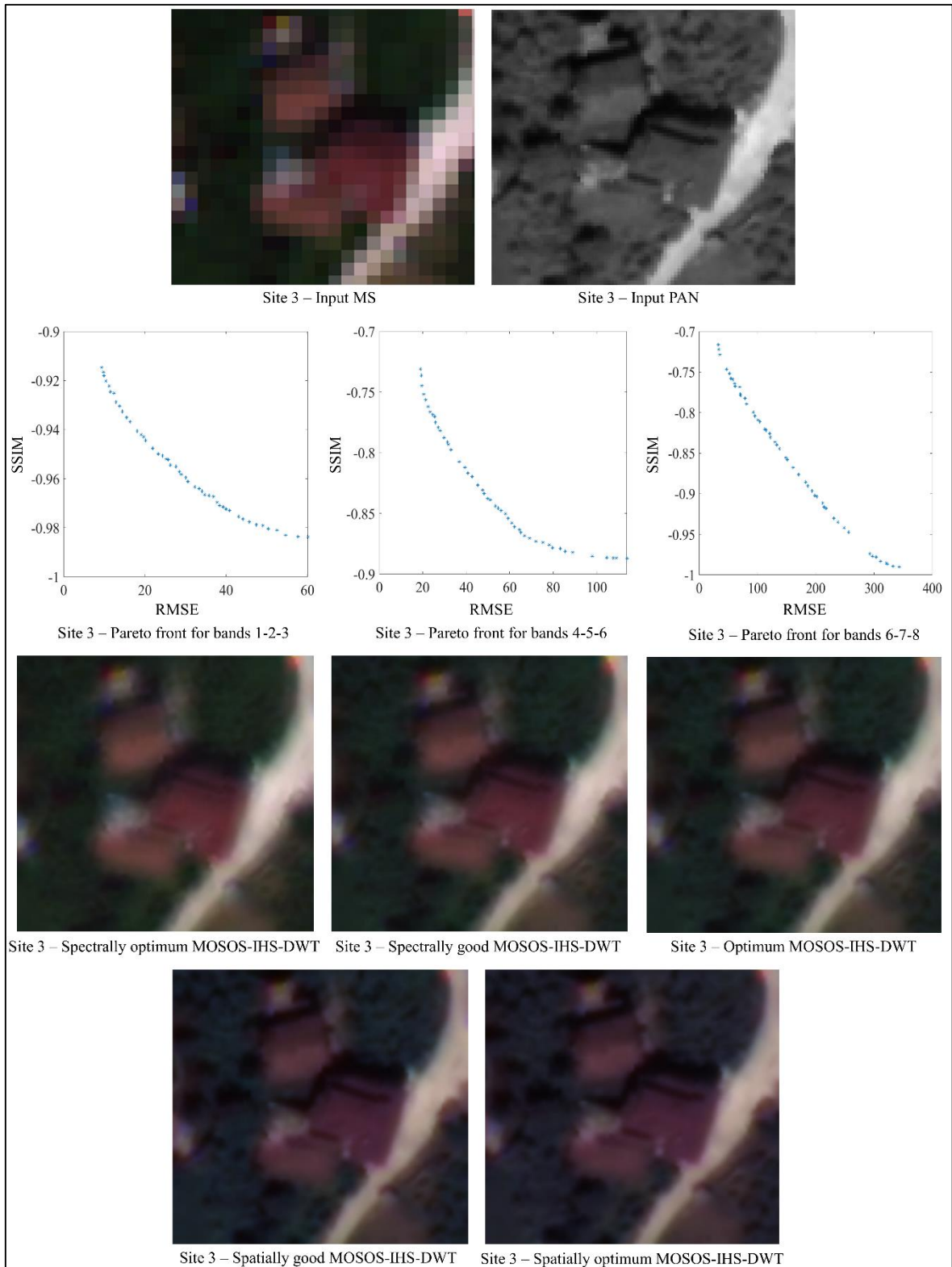


Figure 64. Zoomed-in MOSOS-IHS-DWT results for the site 3

As seen in Figure 64, in the site 3, the spatial distortion decreases from spectrally optimum MOSOS-IHS-DWT result towards spatially optimum MOSOS-IHS-DWT result.

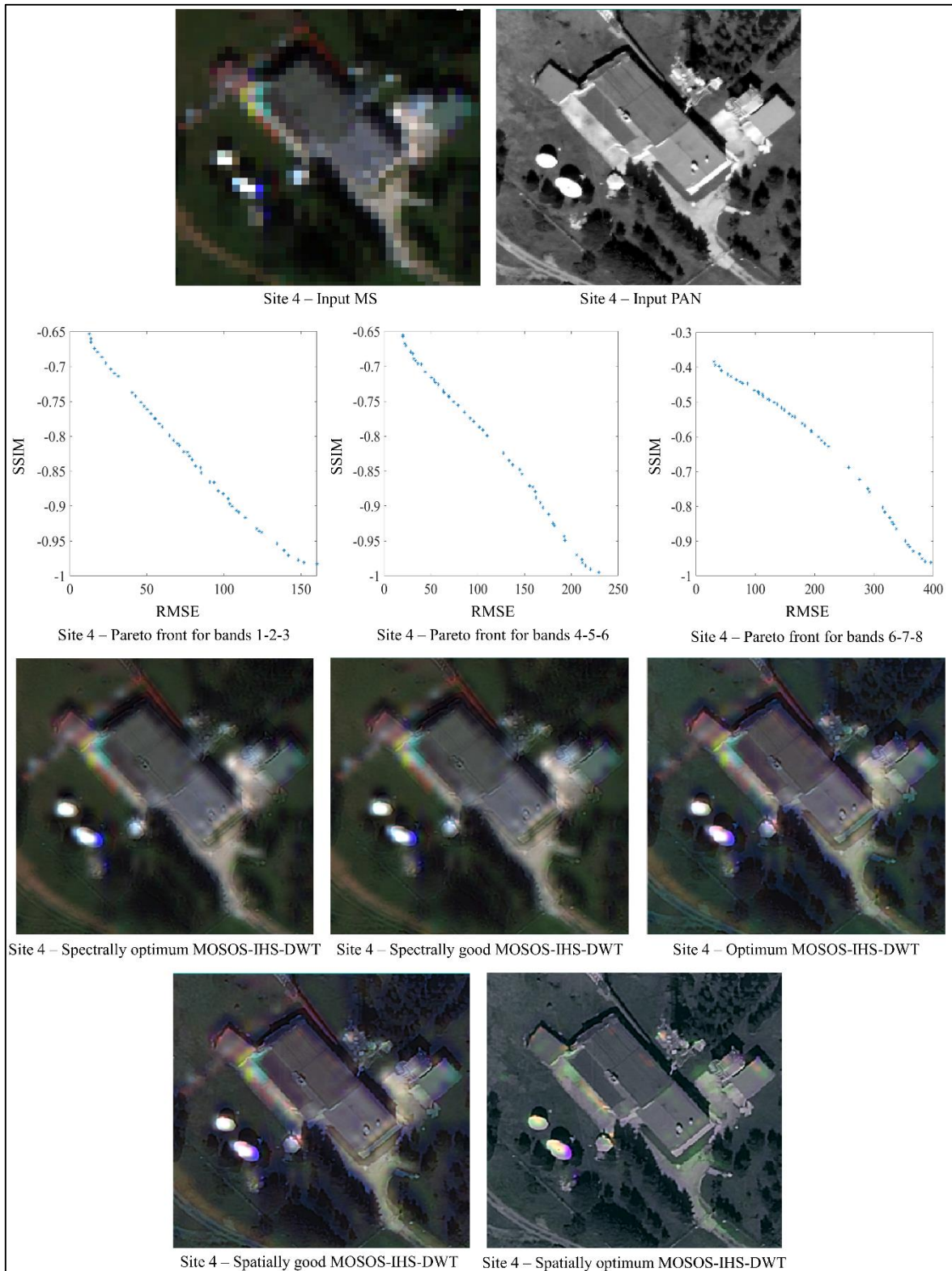


Figure 65. MOSOS-IHS-DWT results for the site 4

As seen in Figure 65, in the site 4, the spatial distortion decreases from spectrally optimum MOSOS-IHS-DWT result towards spatially optimum MOSOS-IHS-DWT result.

## 5.2. Quantitative Evaluation

Tables 9, 10, 11 and 12 show the spectral quality evaluation metric values computed for the sites 1, 2, 3 and 4, respectively. Note that the best value for each metric is shown bold in these tables.

Table 9. Spectral quality evaluation metric values for the site 1

Pansharpener Method	SR-SIM	ERGAS	SID	SAM	UIQI	SSIM	IW-SSIM	CC
<b>HPF</b>	<b>0.9919</b>	<b>1.0003</b>	<b>0.0010</b>	<b>1.0891</b>	<b>0.9680</b>	<b>0.9806</b>	<b>0.9936</b>	<b>0.9963</b>
MIHS	0.8900	9.8246	0.1178	13.6353	0.6262	0.7176	0.7238	0.7441
GS	0.8065	9.5045	0.1018	10.2345	0.2317	0.3427	0.3695	0.6581
HCS	0.8103	9.3812	0.0720	8.6933	0.2243	0.3385	0.3595	0.6569
SFIM	0.8130	9.2999	0.0725	8.7709	0.2286	0.3493	0.3643	0.6659
BRV	0.8002	9.4692	0.0737	8.6972	0.2349	0.3420	0.3684	0.6484
IHS-DWT	0.9087	6.3899	0.1125	12.0649	0.7482	0.7971	0.8174	0.8864
ATWT	0.8129	9.3687	0.0703	8.8053	0.2248	0.3454	0.3623	0.6637
AWLP	0.8130	9.3794	0.0689	8.7859	0.2260	0.3471	0.3625	0.6634
BDS	0.8086	9.9995	0.0825	10.0155	0.2028	0.3175	0.3419	0.6434
LMM	0.8132	9.0915	0.0702	8.5582	0.2317	0.3486	0.3651	0.6730
CB	0.9282	3.3670	0.0141	3.1762	0.7635	0.8132	0.8857	0.9057
PCA	0.9033	11.7245	0.2094	15.9249	0.7035	0.7607	0.7690	0.8998
DWT	0.9327	3.8534	0.0252	5.8673	0.7992	0.8617	0.9134	0.9599
SOS-SVR	0.9585	2.1931	0.0142	1.8779	0.8284	0.9088	0.9476	0.9702
SOS-IHS-DWT	0.9565	3.3929	0.0188	5.0937	0.8489	0.9068	0.9239	0.9512
<b>MOSOS-SVR-Spectrally Optimum</b>	0.9552	2.2207	0.0189	1.8233	0.8148	0.8979	0.9408	0.9670
<b>MOSOS-SVR-Optimum</b>	0.9500	2.6226	0.0028	1.5153	0.8631	0.8916	0.9408	0.9685
<b>MOSOS-SVR-Spatially Optimum</b>	0.9270	4.9971	0.0025	1.5194	0.8170	0.8608	0.8917	0.9548
<b>MOSOS-IHS-DWT-Spectrally Optimum</b>	0.9866	1.2376	0.0046	1.3947	0.9576	0.9746	0.9899	0.9943
<b>MOSOS-IHS-DWT-Spectrally Good</b>	0.9742	2.6442	0.0111	3.5532	0.9282	0.9534	0.9743	0.9896
<b>MOSOS-IHS-DWT-Optimum</b>	0.9501	4.7798	0.0284	6.9865	0.8768	0.9112	0.9353	0.9749
<b>MOSOS-IHS-DWT-Spatially Good</b>	0.9504	4.5303	0.0259	6.6446	0.8558	0.9020	0.9202	0.9542
<b>MOSOS-IHS-DWT-Spatially Optimum</b>	0.8649	11.7653	0.1519	16.1751	0.6204	0.7016	0.7213	0.7973

As seen in Table 9, the HPF result received the best values from all metrics in the site 1. The HPF result of the site 1 returned the SR-SIM, ERGAS, SID, SAM, UIQI, SSIM, IW-SSIM and CC values of 0.9919, 1.0003, 0.0010, 1.0891, 0.9680, 0.9806, 0.9936 and 0.9963, respectively. On the other hand, the spectrally optimum MOSOS-IHS-DWT result and a spectrally good MOSOS-IHS-DWT result achieved the second and third best metric values in the site 1, respectively. As also seen in Table 9, the SOS-SVR result, optimum MOSOS-SVR result, spectrally optimum MOSOS-SVR result, SOS-IHS-DWT result, optimum MOSOS-IHS-DWT result, spatially optimum MOSOS-SVR result and a spatially good

MOSOS-IHS-DWT result were found to keep the colour content of the site 1. On the other hand, the IHS-DWT, DWT, CB, LMM, PCA and MIHS results of the site 1 got promising metric values. The pansharpening results that received the worst metric values in the site 1 were produced by the SFIM, AWLP, ATWT, BRV, HCS, GS, BDSD methods. An important conclusion drawn from Table 9 is that the proposed SOS-SVR, MOSOS-IHS-DWT, MOSOS-SVR and SOS-IHS-DWT methods produced images that received better spectral quality metric values than those produced by the majority of the other methods used.

Table 10. Spectral quality evaluation metric values for the site 2

Pansharpening Method	SR-SIM	ERGAS	SID	SAM	UIQI	SSIM	IW-SSIM	CC
HPF	0.8185	11.0516	0.0479	7.0232	0.2087	0.1754	0.3042	0.5162
MIHS	0.8139	10.4122	0.0539	6.9119	0.2374	0.2074	0.3472	0.5358
GS	0.8155	10.4090	0.0532	6.8264	0.2404	0.2103	0.3487	0.5385
HCS	0.8177	11.3456	0.0491	6.9337	0.2056	0.1729	0.3048	0.5040
SFIM	0.8177	11.0360	0.0505	6.9974	0.2096	0.1764	0.3052	0.5165
BRV	0.8158	10.4929	0.0438	6.9525	0.2389	0.2085	0.3483	0.5375
IHS-DWT	0.9578	2.9794	0.0057	2.2971	0.8993	0.8921	0.9400	0.9598
ATWT	0.8190	11.1282	0.0376	7.0653	0.2084	0.1753	0.3045	0.5139
AWLP	0.8189	11.1354	0.0392	7.0198	0.2082	0.1753	0.3043	0.5137
BDSD	0.8204	11.0539	0.0468	7.2022	0.2409	0.2086	0.3442	0.5307
LMM	0.8167	10.7957	0.0506	6.7813	0.2145	0.1815	0.3101	0.5245
CB	0.8625	7.2336	0.0163	4.8857	0.5150	0.4656	0.6998	0.7910
PCA	0.9364	4.2880	0.0204	4.7104	0.8446	0.8357	0.8915	0.9274
DWT	0.9297	3.8814	0.0163	3.0747	0.8468	0.8321	0.9192	0.9460
SOS-SVR	0.9428	3.1962	<b>0.0032</b>	2.1018	0.8773	0.8658	0.9411	0.9614
SOS-IHS-DWT	0.9519	3.0696	0.0065	2.2707	0.8829	0.8755	0.9309	0.9652
MOSOS-SVR-Spectrally Optimum	0.9420	3.2739	0.0058	2.0489	0.8738	0.8617	0.9385	0.9600
MOSOS-SVR-Optimum	0.9457	3.7244	0.0056	1.8454	0.8812	0.8704	0.9380	0.9542
MOSOS-SVR-Spatially Optimum	0.9413	4.4719	0.0051	1.8576	0.8637	0.8540	0.9125	0.9385
<b>MOSOS-IHS-DWT-Spectrally Optimum</b>	<b>0.9741</b>	<b>2.0526</b>	0.0051	<b>1.6384</b>	<b>0.9503</b>	<b>0.9429</b>	<b>0.9818</b>	<b>0.9883</b>
MOSOS-IHS-DWT-Spectrally Good	0.9683	2.2675	<b>0.0032</b>	2.2530	0.9355	0.9301	0.9709	0.9830
MOSOS-IHS-DWT-Optimum	0.9605	2.7599	0.0037	3.4261	0.9189	0.9135	0.9556	0.9740
MOSOS-IHS-DWT-Spatially Good	0.9364	4.4837	0.0146	5.0735	0.8421	0.8345	0.8850	0.9248
MOSOS-IHS-DWT-Spatially Optimum	0.9224	5.7786	0.0288	6.6121	0.7986	0.7894	0.8409	0.8822

As seen in Table 10, the spectrally optimum MOSOS-IHS-DWT result obtained the best values from almost all metrics in the site 2. In this site, the spectrally optimum MOSOS-IHS-DWT result received the values of 0.9741, 2.0526, 1.6384, 0.9503, 0.9429, 0.9818 and 0.9883 from the SR-SIM, ERGAS, SAM, UIQI, SSIM, IW-SSIM and CC, respectively. The best SID value of 0.0032 was obtained by both the SOS-SVR result and a spectrally good MOSOS-IHS-DWT result in the site 2. Table 10 also demonstrates that a spectrally good

MOSOS-IHS-DWT result, optimum MOSOS-IHS-DWT result and IHS-DWT result got the best metric values after the spectrally optimum MOSOS-IHS-DWT result of the site 2. On the other hand, the SOS-SVR result, SOS-IHS-DWT result, optimum MOSOS-SVR result, spectrally optimum MOSOS-SVR result, spatially optimum MOSOS-SVR result, DWT result, PCA result, a spatially good MOSOS-IHS-DWT result, spatially optimum MOSOS-IHS-DWT result and CB result achieved to keep the colour balance after pansharpening to a certain degree. Table 10 depicts that the GS, BRV, BDS, MIHS, LMM, SFIM, ATWT, HPF, AWLP and HCS results received the worst spectral quality evaluation metric values in the site 2. As can be seen in Table 10, the proposed MOSOS-IHS-DWT, SOS-SVR, SOS-IHS-DWT and MOSOS-SVR methods managed to surpass many other methods in terms of colour quality preservation.

Table 11. Spectral quality evaluation metric values for the site 3

Pansharpening Method	SR-SIM	ERGAS	SID	SAM	UIQI	SSIM	IW-SSIM	CC
HPF	0.7158	11.9267	0.0683	9.1481	0.0416	0.1957	0.1512	0.1084
MIHS	0.6961	13.2543	0.0788	9.7033	0.0258	0.0840	0.0619	0.1099
GS	0.7035	12.3030	0.0653	8.8774	0.0349	0.1717	0.1305	0.1108
HCS	0.7137	11.9868	0.0696	9.1072	0.0399	0.1787	0.1437	0.1069
SFIM	0.7175	13.7126	0.0732	9.3100	0.0370	0.1800	0.1341	0.1056
BRV	0.6974	12.4482	0.0703	9.1418	0.0375	0.1438	0.1047	0.1128
IHS-DWT	0.8608	6.7303	0.1245	18.1254	0.6034	0.6347	0.6875	0.8818
ATWT	0.7154	11.9781	0.0674	9.1665	0.0406	0.1896	0.1492	0.1084
AWLP	0.7147	11.9529	0.0691	9.2338	0.0423	0.2062	0.1525	0.1079
BDS	0.7095	13.1970	0.0956	11.0091	0.0375	0.1512	0.1223	0.1049
LMM	0.7143	11.7176	0.0675	8.9184	0.0415	0.1845	0.1461	0.1104
CB	0.8974	5.4011	0.0225	4.8565	0.5332	0.5976	0.7729	0.7486
PCA	0.8717	9.7909	0.2283	21.3440	0.6425	0.6940	0.7050	0.8607
DWT	0.9492	2.8451	0.0076	2.8675	0.8470	0.8750	0.9342	0.9440
SOS-SVR	0.9542	2.0727	0.0037	1.9029	0.7347	0.8338	0.8829	0.9496
SOS-IHS-DWT	0.9544	2.0965	0.0066	3.0268	0.8101	0.8552	0.8915	0.9481
MOSOS-SVR-Spectrally Optimum	0.9551	2.0923	0.0035	1.9436	0.7399	0.8363	0.8909	0.9494
MOSOS-SVR-Optimum	0.9318	2.5079	0.0020	1.6887	0.7311	0.7675	0.8621	0.9394
MOSOS-SVR-Spatially Optimum	0.9103	6.0739	0.0020	1.6880	0.6617	0.7135	0.7833	0.9233
<b>MOSOS-IHS-DWT-Spectrally Optimum</b>	<b>0.9886</b>	<b>1.0199</b>	<b>0.0017</b>	<b>1.3712</b>	<b>0.9610</b>	<b>0.9722</b>	<b>0.9902</b>	<b>0.9931</b>
MOSOS-IHS-DWT-Spectrally Good	0.9676	3.3680	0.0050	3.9011	0.8639	0.8984	0.9206	0.9763
MOSOS-IHS-DWT-Optimum	0.9559	5.6700	0.0108	5.7095	0.8175	0.8564	0.8836	0.9683
MOSOS-IHS-DWT-Spatially Good	0.8785	11.1035	0.0743	13.2814	0.6334	0.6656	0.7071	0.9023
MOSOS-IHS-DWT-Spatially Optimum	0.7994	13.4534	0.2921	24.4165	0.4913	0.5198	0.5610	0.8179

Table 11 depicts that, in the site 3, the spectrally optimum MOSOS-IHS-DWT result achieved the best SR-SIM, ERGAS, SID, SAM, UIQI, SSIM, IW-SSIM and CC values of 0.9886, 1.0199, 0.0017, 1.3712, 0.9610, 0.9722, 0.9902 and 0.9931, respectively. A spectrally good MOSOS-IHS-DWT result, spectrally optimum MOSOS-SVR result, DWT result and SOS-SVR result were the other most successful ones in conserving the colour features of the site 3. Table 11 also demonstrates that the SOS-IHS-DWT result, optimum MOSOS-IHS-DWT result, optimum MOSOS-SVR result, spatially optimum MOSOS-SVR result, CB result, PCA result and IHS-DWT result got very good spectral quality evaluation metric values in the site 3. On the other hand, the HPF, LMM, AWLP, ATWT, GS, HCS, BRV, SFIM, BDS D and MIHS results got the worst spectral quality evaluation metric values in this site. As in the other sites, the proposed MOSOS-IHS-DWT, MOSOS-SVR, SOS-SVR and SOS-IHS-DWT methods outperformed the other methods in preserving the colour features of the site 3.

Table 12. Spectral quality evaluation metric values for the site 4

Pansharpening Method	SR-SIM	ERGAS	SID	SAM	UIQI	SSIM	IW-SSIM	CC
HPF	0.7991	4.9937	0.1182	12.8287	0.1021	0.0758	0.1123	0.3334
MIHS	0.7741	5.5993	0.1186	13.8443	0.0682	0.0372	0.0698	0.3012
GS	0.7939	5.2942	0.1094	13.0960	0.0697	0.0466	0.0736	0.2893
HCS	0.7986	4.9963	0.1195	12.8085	0.1028	0.0761	0.1136	0.3334
SFIM	0.7950	5.5478	0.2980	13.2268	0.0991	0.0723	0.1071	0.3232
BRV	0.4794	10.5184	0.0181	3.5041	0.0056	0.0086	0.0120	0.7514
IHS-DWT	0.8367	6.3548	0.0421	8.6439	0.4406	0.4392	0.5381	0.8635
ATWT	0.7993	5.0041	0.1130	12.8445	0.1014	0.0753	0.1116	0.3329
AWLP	0.7988	5.0024	0.1174	12.8381	0.1014	0.0754	0.1119	0.3329
BDS D	0.7967	5.5912	0.1463	14.8859	0.0934	0.0632	0.0948	0.3149
LMM	0.7948	5.0596	0.1093	12.7100	0.0940	0.0618	0.0966	0.3228
CB	0.9036	2.6608	0.0316	6.3817	0.7057	0.6901	0.8550	0.7852
PCA	0.9023	3.1557	0.0472	7.8773	0.6504	0.6499	0.7021	0.7183
DWT	0.9314	1.9001	0.0237	5.8086	0.7966	0.7770	0.9001	0.8980
SOS-SVR	0.9075	2.1714	0.0283	6.5665	0.7296	0.7142	0.8343	0.8422
SOS-IHS-DWT	0.9336	1.7101	0.0199	5.4756	0.8318	0.8190	0.8912	0.9174
MOSOS-SVR-Spectrally Optimum	0.8946	2.3317	0.0247	6.0317	0.6771	0.6559	0.7986	0.8036
MOSOS-SVR-Optimum	0.8691	3.3327	0.0178	3.2777	0.6451	0.6143	0.7839	0.7883
MOSOS-SVR-Spatially Optimum	0.7881	8.1464	0.0180	3.2746	0.2209	0.2238	0.3404	0.7309
<b>MOSOS-IHS-DWT-Spectrally Optimum</b>	<b>0.9854</b>	<b>0.8058</b>	<b>0.0045</b>	<b>2.5039</b>	<b>0.9666</b>	<b>0.9614</b>	<b>0.9880</b>	<b>0.9852</b>
MOSOS-IHS-DWT-Spectrally Good	0.9729	1.9888	0.0071	3.9347	0.9167	0.9107	0.9470	0.9846
MOSOS-IHS-DWT-Optimum	0.9116	3.8569	0.0178	6.0415	0.7190	0.7120	0.7110	0.9371
MOSOS-IHS-DWT-Spatially Good	0.8565	5.4268	0.0632	11.7053	0.5454	0.5481	0.6385	0.8939
MOSOS-IHS-DWT-Spatially Optimum	0.7340	7.8376	0.2972	22.9932	0.2167	0.2207	0.2733	0.6276

Table 12 shows that the spectrally optimum MOSOS-IHS-DWT result got the best values from all spectral quality evaluation metrics in the site 4. This was also the case in the site 3. In the site 4, the spectrally optimum MOSOS-IHS-DWT result achieved the best SR-SIM, ERGAS, SID, SAM, UIQI, SSIM, IW-SSIM and CC values of 0.9854, 0.8058, 0.0045, 2.5039, 0.9666, 0.9614, 0.9880 and 0.9852, correspondingly. Table 12 also shows that a spectrally good MOSOS-IHS-DWT result, SOS-IHS-DWT result, DWT result, optimum MOSOS-IHS-DWT result and SOS-SVR result achieved good spectral quality evaluation metric values. On the other hand, the spectrally optimum MOSOS-SVR result, optimum MOSOS-SVR result, CB result, PCA result, a spatially good MOSOS-IHS-DWT result, IHS-DWT result and spatially optimum MOSOS-SVR result achieved to keep the colour balance after pansharpening to a certain extent in the site 4. The worst spectral quality evaluation metric values were obtained by the results of the HPF, HCS, AWLP, ATWT, BRV, LMM, SFIM, GS, BSDS and MIHS methods in this site.

To measure the local colour quality in the pansharpened images, the CCs were calculated between the grey values corresponding to the user-defined polygons generated on the input MS bands and corresponding pansharpened bands. The polygons were drawn on the vegetated areas, building rooftops, water and roads in the site 1, whereas the polygons were generated on the vegetated areas, building rooftops and roads in the sites 2, 3 and 4. Figures 66, 67, 68 and 69 show the average CCs calculated from the user-defined polygons drawn for the sites 1, 2, 3 and 4, respectively.

As seen in Figure 66, proposed MOSOS-IHS-DWT, MOSOS-SVR, SOS-IHS-DWT and SOS-SVR methods dominated the others in keeping the local colour information of the MS data of the site 1. Figure 66 depicts that, in the site 1, the MOSOS-SVR, SOS-SVR, MOSOS-IHS-DWT, CB, SOS-IHS-DWT, HPF and IHS-DWT methods achieved to keep the colour of the vegetated areas with CCs greater than 0.7, whereas the AWLP, ATWT, SFIM, LMM, HCS, BRV, GS and BSDS techniques deteriorated the colours of the vegetated areas in the site 1. As also seen in Figure 66, the MOSOS-SVR, MOSOS-IHS-DWT, SOS-IHS-DWT, IHS-DWT and SOS-SVR methods preserved the colours of the building rooftops in the site 1, whereas the greatest amount of colour distortion on the building rooftops was caused by the BSDS, BRV, AWLP, GS, SFIM, ATWT, HCS and LMM methods. The MOSOS-SVR, MOSOS-IHS-DWT, SOS-IHS-DWT, IHS-DWT, SOS-SVR, HPF and CB methods retained the spectral features of the roads with CCs greater than 0.85. On the other hand, the SFIM, LMM, ATWT, AWLP, GS, HCS, BRV and BSDS

techniques were found to distort the colours of the roads in the site 1. The MOSOS-IHS-DWT, SOS-IHS-DWT, MOSOS-SVR, IHS-DWT, SOS-SVR, HPF, CB and MIHS conserved the spectral features of the water areas with CCs greater than 0.8, whereas the GS, HCS, ATWT, AWLP, SFIM, BRV, LMM and BSDS methods led to the greatest colour deterioration on the water areas in the site 1.

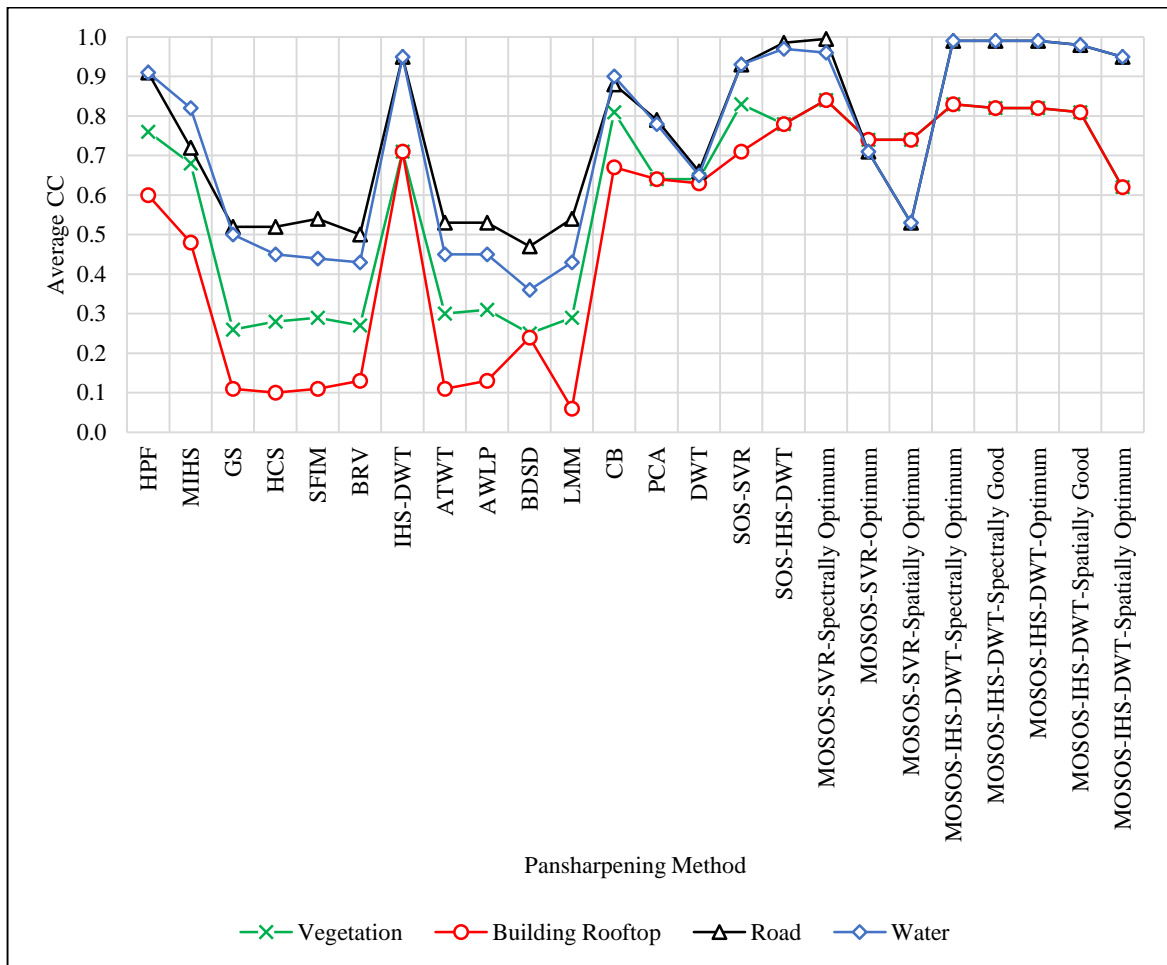


Figure 66. Average CCs computed from the user-defined polygons for the site 1

The proposed MOSOS-IHS-DWT, MOSOS-SVR, SOS-IHS-DWT, PCA, DWT and SOS-SVR methods showed a very good performance in preserving the local colour content of the land cover features of the site 2 (see Figure 66). As seen in the figure, in the site 2, the MOSOS-IHS-DWT, SOS-SVR, PCA, DWT and MOSOS-SVR methods preserved the spectral content of the vegetated areas with CCs greater than 0.76, whereas the SFIM, MIHS, AWLP, HCS, LMM, ATWT, IHS-DWT, HPF and BSDS methods were less successful in this regard. In the site 2, the colours of the building rooftops were kept by the MOSOS-IHS-

DWT, PCA, SOS-IHS-DWT, MOSOS-SVR, SOS-SV, IHS-DWT and DWT methods with CCs higher than 0.75. The BDS, GS, LMM, HPF, MIHS, SFIM, BRV, ATWT, AWLP and HCS methods led to the greatest colour deterioration on the building rooftops in the site 2. On the other hand, in the site 2, the SOS-IHS-DWT, MOSOS-SVR, IHS-DWT, PCA, DWT and MOSOS-IHS-DWT methods achieved to retain the colours of the roads with CCs greater than 0.7. The greatest colour distortions on the roads were caused by the CB, LMM, HPF, SFIM, ATWT, AWLP, MIHS, GS, HCS, BRV and BDS methods.

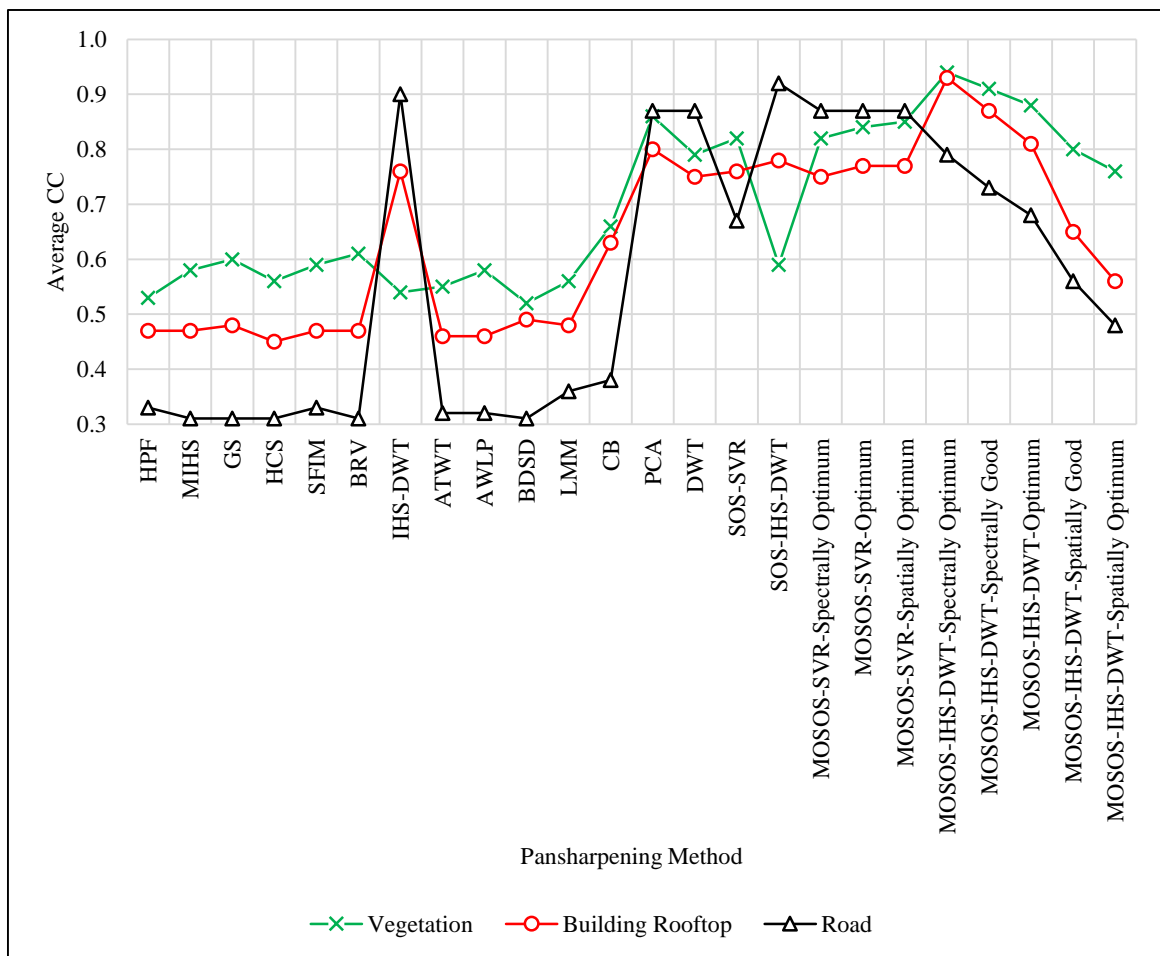


Figure 67. Average CCs computed from the user-defined polygons for the site 2

Figure 68 depicts that, in the site 3, the MOSOS-IHS-DWT, MOSOS-SVR, SOS-IHS-DWT, PCA, and DWT methods kept the colour of the vegetated areas with CCs greater than 0.75, whereas the CB, BDS, LMM, AWLP, HPF, HCS, ATWT, SFIM, GS, BRV and MIHS methods deteriorated the colours of the vegetated areas. As also seen in Figure 68, the SOS-SVR, MOSOS-IHS-DWT, MOSOS-SVR, CB and PCA methods achieved to retain

the colour information of the building rooftops in the site 3. The ATWT, AWLP, SFIM, HPF, HCS, LMM, BDSD, BRV, GS and MIHS techniques caused the greatest colour deterioration in the colours of the building rooftops in this site. Figure 68 also demonstrates that the SOS-SVR, SOS-IHS-DWT, MOSOS-IHS-DWT, IHS-DWT, DWT and CB methods kept the colour features of the roads in the site 3, whereas the MIHS, BRV, GS, BDSD, HCS, SFIM, HPF, ATWT, AWLP and LMM methods failed to keep the colours of the roads with CCs smaller than 0.

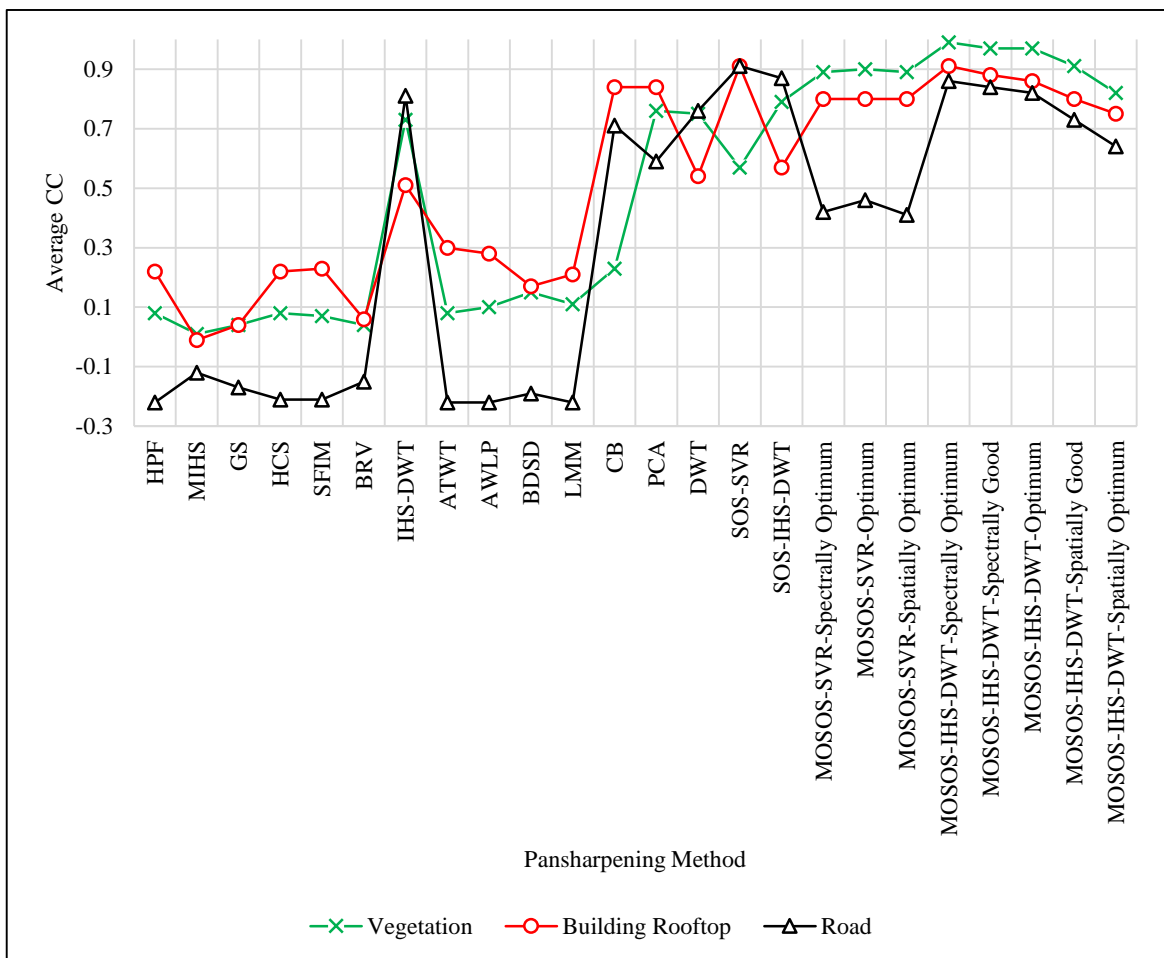


Figure 68. Average CCs computed from the user-defined polygons for the site 3

As depicted in Figure 69, in the site 4, the MOSOS-SVR, DWT and MOSOS-IHS-DWT kept the colour information of the vegetated areas with CCs greater than 0.7, whereas the SFIM, LMM, HPF, HCS, ATWT, AWLP, MIHS, GS and BDSD methods deteriorated the colours of the vegetated areas with CCs smaller than 0. As also seen in Figure 69, the MOSOS-IHS-DWT, SOS-SVR, PCA, MOSOS-SVR, DWT and CB methods were the most

successful ones in keeping the colours of the building rooftops in the site 4, whereas the BDS, HPF, HCS, ATWT, AWLP, LMM and SFIM methods distorted the colour features of the building rooftops. Figure 69 also shows that the MOSOS-IHS-DWT, DWT and MOSOS-SVR methods retained the colour content of the roads in the site 4, whereas the greatest amount of colour distortion on the roads was caused by the PCA, CB, BDS, HPF, ATWT, AWLP, HCS, SFIM, LMM, MIHS and GS methods.

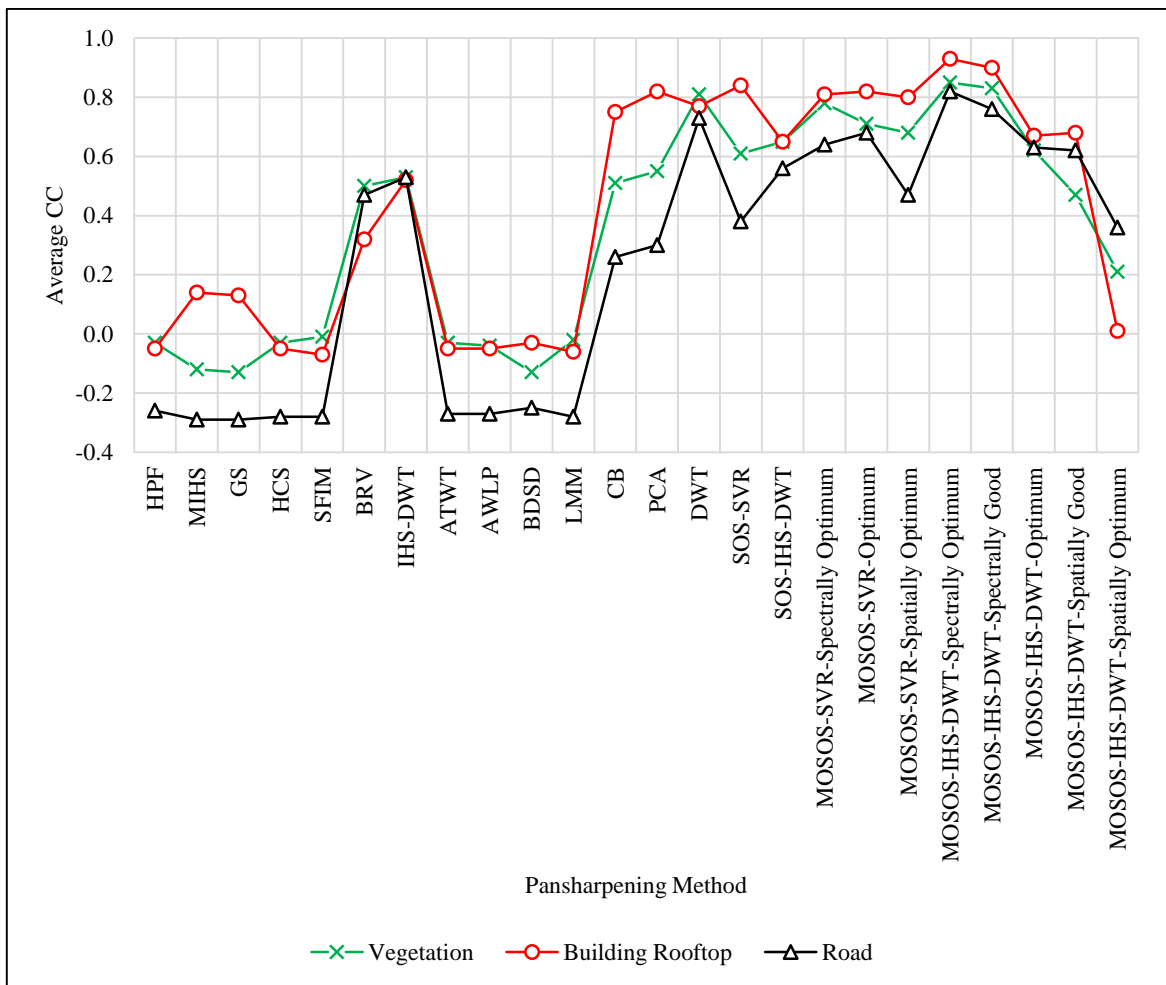


Figure 69. Average CCs computed from the user-defined polygons for the site 4

Tables 13, 14, 15 and 16 show the spatial quality evaluation metric values computed for the sites 1, 2, 3 and 4, respectively. The best value for each metric is shown bold in these tables.

Table 13. Spatial quality evaluation metric values for the site 1

Method	CC	SCC	SERGAS
HPF	0.76	0.93	14.47
MIHS	0.62	0.60	11.56
GS	0.76	0.70	10.73
HCS	0.75	0.64	11.70
SFIM	0.74	0.62	11.83
BRV	0.72	0.74	11.04
IHS-DWT	0.95	0.95	8.00
ATWT	0.75	0.67	11.81
AWLP	0.75	0.65	11.92
BDSB	0.72	0.56	12.55
LMM	0.75	0.90	11.53
CB	0.58	0.70	13.01
PCA	0.39	0.39	11.84
DWT	0.50	0.50	11.89
SOS-SVR	0.80	0.70	11.22
SOS-IHS-DWT	0.92	0.92	10.13
MOSOS-SVR-Spectrally Optimum	0.78	0.86	11.28
MOSOS-SVR-Optimum	0.81	0.95	10.56
MOSOS-SVR-Spatially Optimum	0.83	<b>0.96</b>	9.57
MOSOS-IHS-DWT-Spectrally Optimum	0.75	0.90	11.53
MOSOS-IHS-DWT-Spectrally Good	0.80	0.91	10.11
MOSOS-IHS-DWT-Optimum	0.82	0.92	9.35
MOSOS-IHS-DWT-Spatially Good	0.87	0.91	8.89
MOSOS-IHS-DWT-Spatially Optimum	<b>0.97</b>	0.95	<b>4.94</b>

As seen in Table 13, the proposed MOSOS-IHS-DWT, MOSOS-SVR, SOS-IHS-DWT and SOS-SVR methods outperformed the methods in producing crisp images in the site 1. Out of all results, the spatially optimum MOSOS-IHS-DWT result got the best CC and SERGAS values in the site 1. As also seen in Table 13, the best SCC value was obtained by the spatially optimum MOSOS-SVR result in this site. It can also be inferred from the metric values given in the table that the spatially optimum MOSOS-SVR and MOSOS-IHS-DWT results received better spatial quality evaluation metric values than the spectrally optimum results, which shows that integrating the MOSOS algorithm with the pansharpening methods enabled the optimization of the spatial fidelity in the site 1. Table 13 demonstrates that, in the site 1, the SOS-IHS-DWT and SOS-SVR methods were not as successful as the MOSOS-SVR and MOSOS-IHS-DWT methods in transferring the spatial details. On the other hand, even the spectrally optimum MOSOS-SVR and MOSOS-IHS-DWT results achieved better spatial quality evaluation metric values than the results of the GS, HPF, LMM, BRV, AWLP, MIHS, CB, BDSB, DWT and PCA methods in the site 1.

Table 14. Spatial quality evaluation metric values for the site 2

Method	CC	SCC	SERGAS
HPF	0.87	0.81	7.63
MIHS	0.92	0.96	6.12
GS	0.93	0.96	14.16
HCS	0.88	0.81	7.53
SFIM	0.87	0.80	7.63
BRV	0.91	0.95	6.62
IHS-DWT	0.94	0.94	5.29
ATWT	0.87	0.80	7.59
AWLP	0.90	0.80	7.63
BDSB	0.89	0.96	6.83
LMM	0.90	0.97	14.18
CB	0.53	0.61	13.01
PCA	0.94	0.76	5.11
DWT	0.85	0.83	7.74
SOS-SVR	0.94	0.95	6.22
SOS-IHS-DWT	0.94	0.93	5.91
MOSOS-SVR-Spectrally Optimum	0.93	0.98	6.07
MOSOS-SVR-Optimum	0.94	<b>0.99</b>	5.63
MOSOS-SVR-Spatially Optimum	0.94	<b>0.99</b>	5.93
MOSOS-IHS-DWT-Spectrally Optimum	0.86	0.93	7.62
MOSOS-IHS-DWT-Spectrally Good	0.91	0.95	6.51
MOSOS-IHS-DWT-Optimum	0.94	0.96	5.55
MOSOS-IHS-DWT-Spatially Good	<b>0.98</b>	0.97	3.62
MOSOS-IHS-DWT-Spatially Optimum	<b>0.98</b>	0.97	<b>3.17</b>

Table 14 depicts that, in the site 2, the MOSOS-IHS-DWT, MOSOS-SVR, SOS-IHS-DWT and SOS-SVR methods produced sharper images than the other methods used. As seen in the table, the spatially optimum MOSOS-IHS-DWT result and a spatially good MOSOS-IHS-DWT result achieved the best CC value of 0.98 in the site 2. On the other hand, the best SCC value of 0.99 was obtained by the optimum MOSOS-SVR result and spatially optimum MOSOS-SVR result; whereas the optimum SERGAS value of 3.17 was achieved by the spatially optimum MOSOS-IHS-DWT in the site 2. Table 14 also depicts that the proposed SOS-IHS-DWT and SOS-SVR methods produced images almost as crisp as the MOSOS-IHS-DWT and MOSOS-SVR methods. It can also be concluded from Table 14 that the PCA, BRV, BDSB, GS and LMM methods were partially successful in producing sharper images in the site 2, whereas the AWLP, ATWT, HPF, DWT, SFIM and CB methods produced images of the worst spatial fidelity in this site. In general, all pansharpening methods used managed to transfer the spatial detail content to a certain degree in the site 2.

Table 15. Spatial quality evaluation metric values for the site 3

Method	CC	SCC	SERGAS
HPF	0.72	0.64	17.19
MIHS	0.69	0.63	17.12
GS	0.75	0.70	16.87
HCS	0.72	0.58	17.17
SFIM	0.63	0.55	18.95
BRV	0.72	0.66	16.79
IHS-DWT	0.84	0.94	11.00
ATWT	0.73	0.63	17.18
AWLP	0.72	0.60	17.34
BDSB	0.68	0.50	17.95
LMM	0.74	0.92	16.93
CB	0.40	0.17	18.37
PCA	0.74	0.44	9.63
DWT	0.66	0.51	17.57
SOS-SVR	0.76	0.71	17.27
SOS-IHS-DWT	0.84	0.94	17.02
MOSOS-SVR-Spectrally Optimum	0.75	0.89	17.25
MOSOS-SVR-Optimum	0.81	<b>0.96</b>	16.39
MOSOS-SVR-Spatially Optimum	0.82	0.94	13.81
MOSOS-IHS-DWT-Spectrally Optimum	0.69	0.87	17.44
MOSOS-IHS-DWT-Spectrally Good	0.79	0.91	14.98
MOSOS-IHS-DWT-Optimum	0.81	0.92	13.60
MOSOS-IHS-DWT-Spatially Good	0.90	0.95	9.55
MOSOS-IHS-DWT-Spatially Optimum	<b>0.94</b>	<b>0.96</b>	<b>5.23</b>

As seen in Table 15, in the site 3, the proposed MOSOS-IHS-DWT, MOSOS-SVR and SOS-IHS-DWT methods achieved to produce images of a higher spatial structure quality, compared to the other methods used. The spatially optimum MOSOS-IHS-DWT result received the optimum CC and SERGAS values of 0.94 and 5.23, correspondingly. On the other hand, the optimum SCC value of 0.96 was obtained by both the optimum MOSOS-SVR result and spatially optimum MOSOS-IHS-DWT result in the site 3. Table 15 also shows that the SOS-SVR, IHS-DWT, LMM, GS, PCA and BRV methods presented comparable performances in producing sharp images in this site. The table also depicts that these images produced images of lower spatial fidelity, compared the MOSOS-IHS-DWT, MOSOS-SVR and SOS-IHS-DWT methods. On the other hand, the worst spatial quality evaluation metric values were obtained in the site 3 by the ATWT result, HPF result, MIHS result, HCS result, AWLP result, DWT result, BDSB result, SFIM result, CB result and spectrally optimum MOSOS-IHS-DWT result, which can be seen in Table 15.

Table 16. Spatial quality evaluation metric values for the site 4

Method	CC	SCC	SERGAS
HPF	0.54	0.64	30.19
MIHS	0.68	0.67	30.11
GS	0.74	0.67	29.43
HCS	0.53	0.53	30.35
SFIM	0.46	0.54	41.97
BRV	0.71	0.67	30.59
IHS-DWT	0.84	0.90	7.35
ATWT	0.54	0.64	30.19
AWLP	0.54	0.62	30.26
BDS	0.49	0.23	31.81
LMM	0.53	0.57	27.45
CB	0.42	0.12	30.79
PCA	0.83	0.62	30.50
DWT	0.63	0.63	30.53
SOS-SVR	0.85	0.86	6.34
SOS-IHS-DWT	0.77	0.88	30.20
MOSOS-SVR-Spectrally Optimum	0.78	0.85	30.08
MOSOS-SVR-Optimum	0.83	<b>0.95</b>	24.16
MOSOS-SVR-Spatially Optimum	0.90	<b>0.95</b>	4.33
MOSOS-IHS-DWT-Spectrally Optimum	0.55	0.85	31.08
MOSOS-IHS-DWT-Spectrally Good	0.55	0.88	24.69
MOSOS-IHS-DWT-Optimum	0.64	0.91	17.49
MOSOS-IHS-DWT-Spatially Good	0.76	0.93	10.05
MOSOS-IHS-DWT-Spatially Optimum	<b>0.92</b>	0.93	<b>2.42</b>

Table 16 shows that, in the site 4, the proposed MOSOS-IHS-DWT, MOSOS-SVR, SOS-SVR and SOS-IHS-DWT methods dominated the majority of the other methods used in sharpening the input images. In the site 4, the best CC and SERGAS values of 0.92 and 2.42 were achieved by the spatially optimum MOSOS-IHS-DWT result, respectively. On the other hand, the optimum SCC value of 0.95 was achieved by both the optimum MOSOS-SVR result and spatially optimum MOSOS-SVR result in the site 4. Table 16 shows that the spatially optimum MOSOS-SVR and MOSOS-IHS-DWT results better spatial fidelity evaluation metric values than the spectrally optimum MOSOS-SVR and MOSOS-IHS-DWT results, which shows that these methods succeeded in optimizing the spatial fidelity. This was also the case in the other test sites. As seen in Table 16, the GS result, MIHS result, PCA result, BRV result, HPF result and spectrally optimum MOSOS-IHS-DWT result offered a moderate spatial quality in the site 4, whereas the results of the LMM, DWT, AWLP, HCS, SFIM, BDS and CB methods had the lowest spatial detail quality, compared to the other methods used.

## 6. DISCUSSION

The BRV, which is one of the simplest pansharpening methods, computes each pansharpened band by dividing each input MS band by the input PAN image and dividing the result by the intensity image calculated as the sum of all MS bands. Normalizing the pansharpening result this way generally leads to an increase in the magnitudes of the pixel vectors, which was the main reason for the colour distortion in the test sites (see Tables 9, 10, 11 and 12). However, a direct multiplication with the PAN data was found to enable the spatial detail transfer into the input MS bands to a certain degree (see Tables 13, 14, 15 and 16).

The BRV method actually considers that each MS band contributes equally to the pansharpening result, which is not reasonable in most cases. Hence, the analysts came up with the idea to estimate an appropriate weight for each MS band to optimize the pansharpening result, which gave rise to the SVR pansharpening method. A number of approaches based on regression analysis were developed to estimate the optimum band weights within the SVR method (Munehika et al., 1993; Zhang et al., 1999). In the light of this, this thesis proposed to utilize the algorithm-specific parameter-free SOS metaheuristic algorithm to estimate a weight for each band to optimize the pansharpening result. The qualitative (see Figure 31) and quantitative (see Figures 65, 66, 67 and 68; and Tables 9, 10, 11 and 12) evaluations revealed that the proposed SOS-SVR method was found to be very successful in estimating the optimum band weights so as to conserve the colour content of the test sites. The main reason for this is that the SOS algorithm is very successful in searching for the best solutions in very large search spaces. The parasitism operator used by the SOS algorithm ensures the diversity in the parameter space and increases the exploration capability, whereas the mutualism and commensalism operators ensure the local search in the parameter space, increasing the exploitation capability without getting trapped in local optima. The SOS algorithm also offers a very good balance between the exploration and exploitation, which enabled the achievement of a good balance between the spectral and spatial structure quality of the SVR results. In general, integrating the SOS algorithm with the conventional SVR method can be said to have enabled the production of images of higher colour and spatial detail fidelity, compared to the other conventional pansharpening methods used.

A pansharpening procedure is considered successful if it achieves to preserve the colour features of the input MS data while producing crisp images. However, this is not always easy to achieve. In fact, the previously introduced pansharpening approaches focus much either on keeping the colour features or on transferring the spatial details properly. Hence, a certain amount of colour or spatial detail distortion is always expected, which was also stated by Yilmaz et al., (2019). Therefore, some new perspectives are needed to find the best balance between the spectral and spatial structure quality offered by the pansharpening methods. To this aim, this thesis proposed to utilize the MOSOS algorithm to find the best balance between the colour and spatial structure quality offered by the SVR method. The MOSOS algorithm considered the SVR as a two-objective scheme, where minimization of the colour distortion and spatial distortion are these objectives. The MOSOS-SVR method led to a Pareto front consisting of 75 different pansharpening results. It is worth noting that none of these solutions dominated each other, which means that all of them were of the same importance. In this case, the analyst may choose the result that is more appropriate for the application. Dealing with all 75 results were neither practical nor time-efficient. Hence, in this thesis, only three MOSOS-SVR results were focused for each test site: one with the best colour quality, one with the best spatial detail quality and one with the optimum colour and spatial detail quality. As seen in Figures 33, 34, 35 and 36, the colours of the spectrally optimum MOSOS-SVR results are very similar to those of the corresponding input images in the test sites. The spectral quality evaluation metric values given in Tables 9, 10, 11 and 12 comply with this inference. As also seen in Figures 33, 34, 35 and 36, the spatial detail content of the spatially optimum MOSOS-SVR results are pretty much identical with the corresponding input PAN images in the test sites, which was also justified by the spatial quality evaluation metric values given in Tables 13, 14, 15 and 16. Visual investigation of Figures 33, 34, 35 and 36 depicts that, for all test sites, the optimum MOSOS-SVR results offered a worse colour quality than the spectrally optimum result and a worse spatial detail quality than the spatially optimum result, which were also supported by quantitative evaluation results. This revealed the fact that utilizing the MOSOS algorithm within the SVR procedure enabled the production of a spectrally optimized result, a spatially optimized result and an optimum result where the spectral and spatial quality were balance. The question as to which of these pansharpening results should be used arises at this point. The answer depends totally on the purpose of the pansharpening. If a high colour quality is needed, then the spectrally optimum MOSOS-SVR result can be used, at the expense of a spatial detail

distortion to a certain degree. If a high spatial detail quality is needed, then the spatially optimum MOSOS-SVR result can be used, of course, at the cost of spectral distortion to a certain degree. If both the colour and spatial detail quality are important for the application, then the optimum MOSOS-SVR result would be a better choice.

The MIHS pansharpener method was developed to enhance the capability of the standard IHS method, which is able to process only three bands at a time. One major advantage of the IHS-based pansharpener techniques is that they tend to produce sharp images, causing spectral distortion on the pansharpener results. This was also the case in this study. As seen in Tables 9-16, the MIHS technique was found to be more successful in transferring the spatial structure than in keeping the colour features. As seen Figure 18, the MIHS method caused severe colour deterioration in the test sites. Since the MIHS technique assesses the spectral overlap between the input MS and PAN images and utilizes relative wavelengths to weighting the merge, it is expected to perform well with single-sensor input images. If the both input data are taken from different sensors, then the colour features of the pansharpener image are more likely to be distorted, which was the case in the site 4. Examination of the spectral quality evaluation metric values computed for the MIHS results revealed that the MIHS method showed its lowest colour conservation performance in the site 4.

The DWT is famous for its colour preservation performance. However, like many of the other MRA-based methods in the literature, it tends to distort the spatial characteristics of the PAN data. This is because the DWT is capable of extracting the spatial features only in horizontal, vertical and diagonal directions, which was also observed by Serifoglu Yilmaz et al., (2020). This, of course, causes significant distortions on the spatial features that lie in the other directions. This disadvantage is also shared by the ATWT and AWLP methods. Despite this disadvantage, the DWT method was very successful in retaining the colour content of the test sites. As seen in Tables 9, 10, 11, and 12, the DWT results returned better spectral quality evaluation metric values, compared to the results of many other pansharpener methods used, which was also justified by visual findings. As seen in Figures 29 and 53, the colours of the land cover features are similar to those of the corresponding input MS images in the test sites. Tables 13, 14, 15 and 16 show that the DWT results resulted in lower spatial quality evaluation metric values in the test sites, which was also in good agreement with DWT results given in Figure 53. The DWT method can be used for applications that require the preservation of the colour features. On the other hand, the

ATWT and AWLP methods were found to distort the spectral features and spatial structure content, which can also be seen in Tables 9-16. Despite the fact that the ATWT and AWLP methods seem to have preserved the colours of the land cover features in the site 4 (see Figures 26 and 27), the spectral quality evaluation metric values indicated the opposite. This shows that the visual findings may be misleading, which attaches importance on evaluating the pansharpening quality together with quantitative measures. A good advantage of the ATWT method is that it inserts zeros between filter coefficients in each decomposition level to avoid the shift-variance problem, which is a fact also approved by Gungor (2008) and Serifoglu Yilmaz et al., (2019). However, this procedure achieved to sharpen the images to only a certain degree. On the other hand, the main reason for the spectral and spatial distortions caused by the AWLP method was due to the histogram matching procedure conducted between the input PAN image and intensity component obtained from the IHS transform, which was also observed by Serifoglu Yilmaz et al., (2019). This procedure limited the capability of the AWLP method to relatively inject the spatial details to retain the inter-band relations after pansharpening.

The IHS-DWT method was developed to combine the colour preservation advantage of the DWT method and image sharpening advantage of the IHS method. The IHS-DWT method swaps the last approximation component achieved for the intensity component by its average with the last approximation component achieved for the histogram-matched PAN image, which was found to ensure the colour preservation while injecting the spatial details. It was also possible to increase the colour preservation capability of this method by using greater weights for the approximation component achieved from the intensity component, at the expense of colour distortion. Hence, to obtain the optimal spectral and spatial structure fidelity, equal weights were used in this thesis for the approximation components obtained from both the intensity components and histogram-matched PAN images in all test sites. As seen in Figures 30 and 54; and Tables 9-16, the IHS-DWT method presented a better colour preservation performance than the MIHS method and a better spatial detail injection performance than the DWT method. As also seen in these figures and tables, the IHS-DWT method was more successful in producing sharp images than in keeping the colour features. To tackle this issue and improve the colour preservation capability of this method, this thesis proposed to use the SOS algorithm to optimize the band weights used to compute the intensity components used by the IHS-DWT method in all test sites. As seen in Figures 32 and 56; and Tables 9-16, the proposed SOS-IHS-DWT method succeeded in minimizing the

colour distortion, while producing crisp images in all test sites. The SOS-IHS-DWT method did not only outperform the standard IHS-DWT procedure, but also the majority of the other methods used, in terms of colour and spatial structure fidelity. Another important conclusion drawn about the SOS-IHS-DWT method is that it presented a superb colour preservation and spatial detail injection transfer performance under challenging conditions. As may be remembered, the input data of the site 4 were taken from different sensors and the input PAN image of this site is ten times better than the input MS image. As depicted in Figures 32, 56, 65, 66, 67 and 68; and Tables 9-16, the SOS algorithm achieved to optimize the pansharpening result even under these challenging conditions, just like the SOS-SVR method. Defining the optimum ecosystem size for the SOS algorithm may be hard. However, experiments showed that the optimum pansharpening results were achieved even with relatively small ecosystem sizes. Another advantage of the SOS algorithm is that it is easy-to-implement and does not require complex calculations, which makes it usable for many analysts, even for inexperienced ones.

The performance of a pansharpening procedure is boosted if the contributions of the input images on the pansharpening result are identified accurately. In this way, the colour and spatial structure quality of the pansharpening results can be balanced. The IHS-DWT method was actually developed to achieve this. As mentioned before, this method tended to distort the colour features, while increasing the spatial detail content, which was why the SOS-IHS-DWT method was developed. To further improve the capability of the IHS-DWT method, this thesis proposed to use the MOSOS algorithm with the IHS-DWT method. The MOSOS-IHS-DWT method was not only used to estimate the optimum band weights for the input MS bands, but also to estimate the optimum weights for the approximation coefficients derived from the intensity component and histogram-matched PAN images. This enabled the generation of a 50-solution Pareto front that had a better variation in the solution space, compared to the MOSOS-SVR method. The proposed MOSOS-IHS-DWT method enables the analysts to produce pansharpening results that are of required spectral and spatial quality. The MOSOS-IHS-DWT method is also able to provide the optimum pansharpening result, where the spectral and spatial quality is balanced. In this thesis, out of fifty solutions, five MOSOS-IHS-DWT results were selected for each test site, which were the spectrally optimum result, a spectrally good result, spectrally and spatially optimum result, a spatially good result and the spatially optimum result. As seen in Figures 37, 38, 39 and 40, the colours of the spectrally optimum pansharpening results were very similar to those of the

corresponding input data, and the spatial detail content of the spatially optimum pansharpening results were very similar to those of the corresponding input PAN images. These figures also show that the colour quality decreases from the spectrally optimum results towards spatially optimum results, whereas the spatial detail quality increases from spectrally optimum results towards spatially optimum results, which was also justified by the spectral and spatial fidelity evaluation metric values given in Tables 9-16. This leads us to the fact that using the MOSOS algorithm with the IHS-DWT method enabled the production of pansharpened images of required spectral and spatial fidelity. As seen in Figures 61, 62, 63 and 64, the spectrally optimum MOSOS-IHS-DWT results may contain a huge amount of spatial distortion and spatially optimum MOSOS-IHS-DWT results may contain a considerable colour distortion, which may make it very hard for the analysts to use these images for further applications. In such cases, the analysts may use the optimum MOSOS-IHS-DWT results for their applications. It was, of course, possible to produce more optimized MOSOS-IHS-DWT results in this thesis. However, only five results were decided to present for the sake of the length. The same was also true for the results of the MOSOS-SVR method, where three optimized images were provided.

The PCA and GS methods, which are very similar to each other in the way they produce the pansharpened bands, were found to be partially successful in generating sharp images without distorting the colour characteristics of the input MS images, which can be observed in Figures 21, 22, 45 and 46. The PCA and GS are statistics-based methods, which means that their performances depend highly on the scene characteristics and statistical relationship between the input MS and PAN data, which was also stated by Serifoglu Yilmaz et al., (2020). As seen in Tables 12 and 16, colour preservation and spatial detail transfer performance of these methods decreased with input images of a large spatial resolution ratio.

The three criteria used by the CB method were found to keep the colour information to a certain degree. As seen in Tables 9, 10, 11 and 12, the CB method, in general, kept the colour characteristics of the test sites better than the PCA, HPF, LMM, ATWT, AWLP, BRV, GS, HCS, SFIM, MIHS and BDSF methods. Figures 28 and 52 show that the CB method had a difficulty in dealing with input images of a large spatial resolution difference (i.e. site 4). As seen in these figures, the CB results contain mosaic effects in many parts of the scene, deteriorating the spatial fidelity. The main reason for this was that the CB method performs within a processing window, whose size should be defined by the analyst. Inappropriate window sizes lead to spectral and spatial distortion, especially when there is a

significant spatial resolution difference between the input images. This thesis considered setting the window sizes to the closest odd number that was equal or greater than the spatial resolution ratio between both input data, as recommended by Gungor (2008). Larger window sizes were tried to further sharpen the results, however, larger window sizes significantly distorted the colour features.

As seen in Tables 9-16, the LMM technique cannot be considered successful in generating images of high colour and spatial fidelity in the test sites. This method employs processing windows to match the statistical characteristics of the MS bands to the corresponding pansharpened bands. This attributes importance on the window size. Since there is not a standard protocol to find the most appropriate window size for the LMM method, the analysts have to try different window sizes until the pansharpened image of optimum spectral and spatial quality is achieved. Hence, different window sizes were employed to optimize the pansharpening result. Experiments revealed that the optimum pansharpening results were achieved with window sizes that were set to the minimum odd number that was greater than the spatial resolution ratio between the input MS and PAN images. As seen in Tables 13, 14, 15 and 16, the LMM method is not able to produce images of a high spatial fidelity. Enlarged windows were used to minimize the spatial distortion by incorporating more grey values. However, this caused severe colour distortions in all test sites.

The SFIM method was found to have shown a very bad performance in the test sites. As seen in Figures 24 and 48; and Tables 9-16, the SFIM method did not manage to retain the colours of the land features and resulted in image of poor spatial detail content. The SFIM method makes use of the ratio between the input PAN image and its low-pass filtered version to modulate a low-resolution MS image. In this thesis, an averaging filter was used to calculate the smoothed images. Khan et al., (2007) recommended setting the size of the filter to the spatial resolution ratio between the input images. However, this approach was found to distort the colour features to a certain extent. Hence, greater window sizes were tried to improve the spectral quality of the pansharpening results. It was concluded that a  $7 \times 7$  filter provided the best colour quality in the sites 1, 2 and 3; whereas a  $13 \times 13$  filter was found to have achieved the best colour quality in the site 4. An important advantage of the SFIM method is that it uses the ratio between the input PAN image and its low-pass filtered version, which makes this method uncommitted from the colour diversity and contrast of the input PAN data, which is a fact also approved by Serifoglu Yilmaz et al., (2019). The

performance of the SFIM method can be enhanced by employing a more effective low-pass filter on the PAN image.

As seen in Tables 9, 10, 11 and 12, the HPF method presented a moderate performance in pansharpening the images of the test sites. The tables also show that the HPF technique performed best in the site 1. The performance of the HPF method relies on the size and content of the high-pass filter used to enhance the spatial details of the input PAN image. The used HPF procedure estimates the most appropriate size of the filter taking the spatial resolution ratio between the input images into consideration. A filter size of  $9 \times 9$  was offered by the used HPF procedure to achieve the optimum HPF results for all test sites. Despite this, windows with different sizes were tried to further optimize the pansharpening results in spectral and spatial manner. Larger filter sizes were found to produce crisper images, causing considerable colour distortions. Hence, the  $9 \times 9$  filter whose elements were -1, except for the centre element, which was set to 80, was decided to use for all test sites. The used HPF scheme conducted a linear histogram stretch between the pansharpened bands and MS bands, which was found to cause severe colour distortions, especially in the sites 3 and 4. Instead of using a linear contrast stretch, a histogram match between the pansharpened bands and corresponding input MS bands may be more reasonable to retain the colour content after pansharpening, which was also recommended by Yilmaz et al., (2020).

The HCS and BDSD methods were found to be unsuccessful in producing images of high spectral and spatial structure quality in the test sites, which can be seen in Figures 65, 66, 67 and 68; and Tables 9-16. As also seen in Figures 44 and 47, these methods returned pixel mosaic effects on the pansharpening results, especially in the sites 3 and 4. The HCS technique lost a significant amount of the colour and spatial detail information when transforming from native colour space to hyperspherical colour space in all test sites. The HCS method matches the mean and standard deviation of the square of the PAN data to those of the square of the intensity component, which was found to be the other reason for the colour and spatial structure distortions caused by this method. On the other hand, the BDSD method employs a linear-fitting scheme to produce the pansharpened bands, which emphasizes the accurate identification of the weights of the input images. This approach does not seem to work out well in the test sites, which was also observed by Serifoglu Yilmaz et al., (2019).

## 7. CONCLUSIONS

The success of pansharpening depends on the accurate specification of the contributions of the input data to the pansharpening result. These contributions are represented by weights in many cases. Inaccurate identification of these weights is likely to cause colour or spatial detail distortions on pansharpening results to a certain extent. The CS-based pansharpening techniques are among the most common pansharpening methods used in the literature. In spite of the fact that these methods offer a high performance in produce sharp images, they tend to deteriorate the colour content due to the way the intensity component is calculated from the input MS bands. Some approaches such as BRV and IHS consider that each MS band contributes equally to the intensity component. However, this is not reasonable in many real world scenarios and the contribution (i.e. weight) of each MS band should be accurately estimated to achieve a higher colour preservation performance. Hence, this thesis introduced to use the SOS algorithm, one of the most powerful metaheuristic optimization algorithms, to estimate the band weights used by the CS-based SVR pansharpening method; and a hybrid pansharpening approach consisting of the CS-based IHS and MRA-based DWT techniques to calculate the optimum intensity component, minimizing the colour deterioration. Since each pansharpening approach is expected to deteriorate either the spectral features or the spatial detail content to some degree, finding the optimum balance between the colour and spatial structure quality of the pansharpening results is very challenging. Hence, this thesis proposed to use the MOSOS algorithm with both the SVR and IHS-DWT methods to find the best balance between the colour and spatial structure fidelity offered by these methods. Actually, the MOSOS algorithm was not only used to find the best balance between the spectral and spatial fidelity, but also to enable the analysts to produce the spectrally best pansharpening result possible, the spatially best pansharpening result possible or any pansharpening results of required spectral and spatial quality.

The colour preservation and spatial detail transfer performances of the proposed SOS-SVR, MOSOS-SVR, SOS-IHS-DWT and MOSOS-IHS-DWT approaches were qualitatively and quantitatively compared against those of the popular pansharpening methods HPF, MIHS, GS, HCS, SFIM, BRV, IHS-DWT, ATWT, AWLP, BDSF, LMM, CB, PCA and DWT.

The qualitative evaluation of the pansharpening results revealed that the proposed SOS-SVR and SOS-IHS-DWT methods achieved to increase to colour fidelity with a very high success. Despite the fact that these methods were proposed to optimize the colour features, they presented a very good performance in producing sharp images, as can be observed in Figures 56 and 57. On the other hand, the colours in the spectrally optimum MOSOS-SVR and MOSOS-IHS-DWT results were found to be very similar to those in the corresponding input MS images (see Figures 34-41). Similarly, the spatial detail content of the spatially optimum MOSOS-SVR and MOSOS-IHS-DWT results were found to be very similar to those in the corresponding input PAN images (see Figures 58-65). As seen in Figures 34-41 and 58-65, the optimum MOSOS-SVR and MOSOS-IHS-DWT results have a lower spatial detail content compared to the spatially optimum results and a lower colour quality compared to the spectrally optimum results. In general, the proposed SOS-SVR, MOSOS-SVR, SOS-IHS-DWT and MOSOS-IHS-DWT methods produced images of superior colour and spatial structure fidelity, compared to the other techniques used in the content of this thesis.

Since qualitative evaluation of the pansharpening results is nominative and depends largely on both the analyst's perspective and the technical specifications of the monitor where the images are displayed, quantitative evaluation is required for a more robust performance assessment. In addition, it may be very hard to observe any subtle colour and spatial detail differences with the human eye (Serifoglu Yilmaz et al., 2019), which was another reason for the quantitative evaluation. Hence, in this thesis, the colour fidelity of each pansharpening result was evaluated with the quality metrics SR-SIM, ERGAS, SID, SAM, UIQI, SSIM, IW-SSIM and CC; whereas the spatial structure fidelity of each pansharpening result was evaluated with the quality metrics CC, SCC and SERGAS. The spectral quality evaluation metric values were determined between the MS bands and pansharpened bands, which were degraded to the size of the MS bands considering the protocol proposed by Wald et al., (1997). On the other hand, the spatial quality evaluation metric values were computed between the pansharpened bands and corresponding input PAN images. The calculated spectral and spatial fidelity evaluation metric values are given in Tables 9-16. Apart from the calculation of the quality metric values, the colour preservation abilities of all pansharpening approach was evaluated through the calculation of the CCs between the grey values corresponding to the user-defined polygons drawn on both the input MS bands and corresponding pansharpened bands. Calculated local CCs for

the land cover features are given in Figures 66, 67, 68 and 69. As seen in these figures, the proposed SOS-SVR, MOSOS-SVR, SOS-IHS-DWT and MOSOS-IHS-DWT methods were more successful in retaining the spectral information of the land cover features in the test sites, compared to the other methods used.

This thesis compared the performances of a total of 24 pansharpening methods through eight spectral quality evaluation metrics and three spatial quality evaluation metrics, which makes it harder to observe and comprehend the metric values given in Tables 9-16. Hence, to make it easier, each pansharpening result was given a score between 1 and 24 with respect to its spectral and spatial quality evaluation metric value. The better metric value, the greater score. A similar scoring protocol was also utilized by Gungor (2008), Yilmaz et al., (2019), Yilmaz and Gungor (2016a; 2016b), Serifoglu Yilmaz et al., (2019), Yilmaz et al., (2020) and Serifoglu Yilmaz et al., (2020). Tables 17, 18, 19 and 20 show the spectral quality scores for the sites 1, 2, 3 and 4, respectively. The spatial quality scores for the sites 1, 2, 3 and 4 are demonstrated in Tables 21, 22, 23 and 24, correspondingly.

Table 17. Spectral quality scores given for the site 1

Method	SR-SIM	ERGAS	SID	SAM	UIQI	SSIM	IW-SSIM	CC
HPF	24	24	24	24	24	24	24	24
MIHS	10	4	3	3	10	10	10	9
GS	2	5	5	5	6	4	8	4
HCS	4	7	9	11	2	2	2	3
SFIM	6	10	8	9	5	8	5	7
BRV	1	6	7	10	8	3	7	2
IHS-DWT	12	12	4	4	12	12	12	11
ATWT	5	9	10	7	3	5	3	6
AWLP	6	8	12	8	4	6	4	5
BDSB	3	3	6	6	1	1	1	1
LMM	8	11	11	12	6	7	6	8
CB	14	18	19	18	13	13	13	13
PCA	11	2	1	2	11	11	11	12
DWT	15	16	15	15	14	15	15	17
SOS-SVR	21	22	18	19	17	20	21	20
SOS-IHS-DWT	20	17	17	16	18	19	17	14
MOSOS-SVR-Spectrally Optimum	19	21	16	20	15	17	19	18
MOSOS-SVR-Optimum	16	20	22	22	20	16	19	19
MOSOS-SVR-Spatially Optimum	13	13	23	21	16	14	14	16
MOSOS-IHS-DWT-Spectrally Optimum	23	23	21	23	23	23	23	23
MOSOS-IHS-DWT-Spectrally Good	22	19	20	17	22	22	22	22
MOSOS-IHS-DWT-Optimum	17	14	13	13	21	21	18	21
MOSOS-IHS-DWT-Spatially Good	18	15	14	14	19	18	16	15
MOSOS-IHS-DWT-Spatially Optimum	9	1	2	1	9	9	9	10

Table 18. Spectral quality scores given for the sites 2

Method	SR-SIM	ERGAS	SID	SAM	UIQI	SSIM	IW-SSIM	CC
HPF	7	5	6	3	4	4	1	4
MIHS	1	9	1	8	7	7	8	8
GS	2	10	2	9	9	10	10	10
HCS	5	1	5	7	1	1	4	1
SFIM	5	6	4	5	5	5	5	5
BRV	3	8	8	6	8	8	9	9
IHS-DWT	21	21	18	17	21	21	20	18
ATWT	9	3	10	2	3	2	3	3
AWLP	8	2	9	4	2	2	2	2
BDS	10	4	7	1	10	9	7	7
LMM	4	7	3	10	6	6	6	6
CB	11	11	13	13	11	11	11	11
PCA	14	15	12	14	14	15	14	14
DWT	13	16	13	16	15	13	16	16
SOS-SVR	18	19	23	20	18	18	21	20
SOS-IHS-DWT	20	20	16	18	20	20	17	21
MOSOS-SVR-Spectrally Optimum	17	18	17	21	17	17	19	19
MOSOS-SVR-Optimum	19	17	19	23	19	19	18	17
MOSOS-SVR-Spatially Optimum	16	14	20	22	16	16	15	15
MOSOS-IHS-DWT-Spectrally Optimum	24	24	20	24	24	24	24	24
MOSOS-IHS-DWT-Spectrally Good	23	23	23	19	23	23	23	23
MOSOS-IHS-DWT-Optimum	22	22	22	15	22	22	22	22
MOSOS-IHS-DWT-Spatially Good	14	13	15	12	13	14	13	13
MOSOS-IHS-DWT-Spatially Optimum	12	12	11	11	12	12	12	12

Table 19. Spectral quality scores given for the sites 3

Method	SR-SIM	ERGAS	SID	SAM	UIQI	SSIM	IW-SSIM	CC
HPF	9	10	11	10	9	9	9	5
MIHS	1	3	5	6	1	1	1	7
GS	3	6	14	14	2	4	4	9
HCS	5	7	9	12	6	5	6	3
SFIM	10	1	7	7	3	6	5	2
BRV	2	5	8	11	4	2	2	10
IHS-DWT	12	14	3	3	13	13	12	14
ATWT	8	8	13	9	7	8	8	5
AWLP	7	9	10	8	10	10	10	4
BDS	4	4	4	5	4	3	3	1
LMM	6	11	12	13	8	7	7	8
CB	15	17	15	16	12	12	15	11
PCA	13	13	2	2	15	15	13	13
DWT	18	19	17	19	22	22	23	18
SOS-SVR	19	23	20	21	18	18	18	21
SOS-IHS-DWT	20	21	18	18	20	20	21	19
MOSOS-SVR-Spectrally Optimum	21	22	21	20	19	19	20	20
MOSOS-SVR-Optimum	17	20	22	22	17	17	17	17
MOSOS-SVR-Spatially Optimum	16	15	22	23	16	16	16	16
MOSOS-IHS-DWT-Spectrally Optimum	24	24	24	24	24	24	24	24
MOSOS-IHS-DWT-Spectrally Good	23	18	19	17	23	23	22	23
MOSOS-IHS-DWT-Optimum	22	16	16	15	21	21	19	22
MOSOS-IHS-DWT-Spatially Good	14	12	6	4	14	14	14	15
MOSOS-IHS-DWT-Spatially Optimum	11	2	1	1	11	11	11	12

Table 20. Spectral quality scores given for the sites 4

Method	SR-SIM	ERGAS	SID	SAM	UIQI	SSIM	IW-SSIM	CC
HPF	11	14	6	8	9	9	9	8
MIHS	3	5	5	3	2	2	2	2
GS	5	9	9	5	3	3	3	1
HCS	9	13	4	9	10	10	10	8
SFIM	7	7	1	4	6	6	6	5
BRV	1	1	19	21	1	1	1	13
IHS-DWT	13	4	13	12	13	13	13	18
ATWT	12	11	8	6	7	7	7	6
AWLP	10	12	7	7	7	8	8	6
BDSB	8	6	3	2	4	5	4	3
LMM	6	10	10	10	5	4	5	4
CB	18	18	14	15	18	18	20	14
PCA	17	17	12	13	16	16	15	11
DWT	21	22	17	18	21	21	22	20
SOS-SVR	19	20	15	14	20	20	19	17
SOS-IHS-DWT	22	23	18	19	22	22	21	21
MOSOS-SVR-Spectrally Optimum	16	19	16	17	17	17	18	16
MOSOS-SVR-Optimum	15	16	21	22	15	15	17	15
MOSOS-SVR-Spatially Optimum	4	2	20	23	12	12	12	12
MOSOS-IHS-DWT-Spectrally Optimum	24	24	24	24	24	24	24	24
MOSOS-IHS-DWT-Spectrally Good	23	21	23	20	23	23	23	23
MOSOS-IHS-DWT-Optimum	20	15	21	16	19	19	16	22
MOSOS-IHS-DWT-Spatially Good	14	8	11	11	14	14	14	19
MOSOS-IHS-DWT-Spatially Optimum	2	3	2	1	11	11	11	10

Table 21. Spatial quality scores given for the site 1

Method	CC	SCC	SERGAS
HPF	13	20	1
MIHS	4	4	10
GS	13	9	16
HCS	8	6	9
SFIM	7	5	7
BRV	5	12	15
IHS-DWT	23	21	23
ATWT	8	8	8
AWLP	8	7	4
BDSB	5	3	3
LMM	8	14	11
CB	3	9	2
PCA	1	1	6
DWT	2	2	5
SOS-SVR	16	9	14
SOS-IHS-DWT	22	18	18
MOSOS-SVR-Spectrally Optimum	15	13	13
MOSOS-SVR-Optimum	18	21	17
MOSOS-SVR-Spatially Optimum	20	24	20
MOSOS-IHS-DWT-Spectrally Optimum	8	14	11
MOSOS-IHS-DWT-Spectrally Good	16	16	19
MOSOS-IHS-DWT-Optimum	19	18	21
MOSOS-IHS-DWT-Spatially Good	21	16	22
MOSOS-IHS-DWT-Spatially Optimum	24	21	24

Table 22. Spatial quality scores given for the site 2

Method	CC	SCC	SERGAS
HPF	4	6	5
MIHS	13	15	15
GS	14	15	2
HCS	7	6	10
SFIM	4	3	5
BRV	11	12	12
IHS-DWT	16	11	21
ATWT	4	3	9
AWLP	9	3	5
BDS	8	15	11
LMM	9	19	1
CB	1	1	3
PCA	16	2	22
DWT	2	8	4
SOS-SVR	16	12	14
SOS-IHS-DWT	16	9	18
MOSOS-SVR-Spectrally Optimum	14	22	16
MOSOS-SVR-Optimum	16	23	19
MOSOS-SVR-Spatially Optimum	16	23	17
MOSOS-IHS-DWT-Spectrally Optimum	3	9	8
MOSOS-IHS-DWT-Spectrally Good	11	12	13
MOSOS-IHS-DWT-Optimum	16	15	20
MOSOS-IHS-DWT-Spatially Good	23	19	23
MOSOS-IHS-DWT-Spatially Optimum	23	19	24

Table 23. Spatial quality scores given for the site 3

Method	CC	SCC	SERGAS
HPF	7	10	9
MIHS	5	8	12
GS	14	12	15
HCS	7	6	11
SFIM	2	5	1
BRV	7	11	16
IHS-DWT	21	19	21
ATWT	11	8	10
AWLP	7	7	6
BDS	4	3	3
LMM	12	17	14
CB	1	1	2
PCA	12	2	22
DWT	3	4	4
SOS-SVR	16	13	7
SOS-IHS-DWT	21	19	13
MOSOS-SVR-Spectrally Optimum	14	15	8
MOSOS-SVR-Optimum	18	23	17
MOSOS-SVR-Spatially Optimum	20	19	19
MOSOS-IHS-DWT-Spectrally Optimum	5	14	5
MOSOS-IHS-DWT-Spectrally Good	17	16	18
MOSOS-IHS-DWT-Optimum	18	17	20
MOSOS-IHS-DWT-Spatially Good	23	22	23
MOSOS-IHS-DWT-Spatially Optimum	24	23	24

Table 24. Spatial quality scores given for the site 4

Method	CC	SCC	SERGAS
HPF	6	9	12
MIHS	13	11	13
GS	15	11	15
HCS	4	3	8
SFIM	2	4	1
BRV	14	11	5
IHS-DWT	21	19	21
ATWT	6	9	11
AWLP	6	6	9
BDS	3	2	2
LMM	4	5	16
CB	1	1	4
PCA	19	6	7
DWT	11	8	6
SOS-SVR	22	16	22
SOS-IHS-DWT	17	17	10
MOSOS-SVR-Spectrally Optimum	18	14	14
MOSOS-SVR-Optimum	19	23	18
MOSOS-SVR-Spatially Optimum	23	23	23
MOSOS-IHS-DWT-Spectrally Optimum	9	14	3
MOSOS-IHS-DWT-Spectrally Good	9	17	17
MOSOS-IHS-DWT-Optimum	12	20	19
MOSOS-IHS-DWT-Spatially Good	16	21	20
MOSOS-IHS-DWT-Spatially Optimum	24	21	24

The spectral and spatial quality scores of all pansharpening results achieved for all test sites were averaged to provide an overview for the colour preservation and spatial structure transfer performances of all pansharpening techniques used in this thesis, including the proposed ones. Figure 70 depicts the average colour and spatial fidelity scores obtained for each pansharpening methods.

As seen in Figure 70, the proposed SOS-SVR, MOSOS-SVR, SOS-IHS-DWT and MOSOS-IHS-DWT methods presented a very good colour conservation success in all test sites. The figure depicts that the spectrally optimum MOSOS-IHS-DWT result, a spectrally good MOSOS-IHS-DWT result, SOS-SVR result, SOS-IHS-DWT result, optimum MOSOS-IHS-DWT result, optimum MOSOS-SVR result and spectrally optimum MOSOS-SVR result provided the best colour fidelity in all test sites. Despite their superior colour qualities, the spectrally optimum MOSOS-IHS-DWT and MOSOS-SVR results may not be efficient for the applications that require a high spatial detail quality. For such cases, it would be more appropriate to use the optimum MOSOS-SVR result, optimum MOSOS-IHS-DWT result, SOS-SVR result or SOS-IHS-DWT result, which provided a higher colour fidelity compared to other conventional methods used. The LMM, AWLP, ATWT, BRV, GS, HCS,

SFIM, MIHS and BSDS methods caused the greatest amount of colour distortion in all test sites.

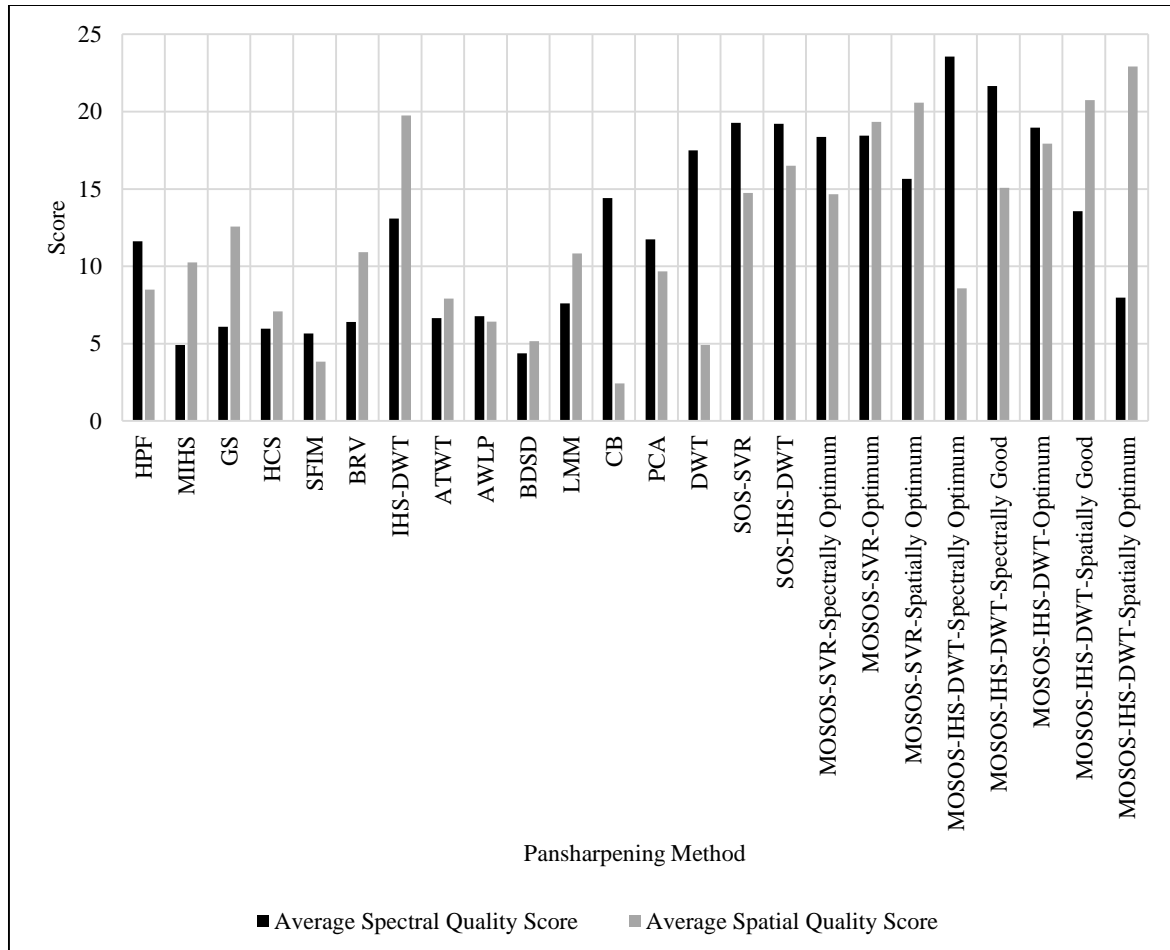


Figure 70. Average spectral and spatial quality scores calculated for all test sites

Figure 70 depicts that the SOS-SVR, MOSOS-SVR, SOS-IHS-DWT, MOSOS-IHS-DWT and IHS-DWT methods returned the sharpest images in all test sites. The figure demonstrates that the spatially optimum MOSOS-IHS-DWT result, a spatially good MOSOS-IHS-DWT result, spatially optimum MOSOS-SVR result, IHS-DWT result, optimum MOSOS-SVR result, optimum MOSOS-IHS-DWT result, SOS-IHS-DWT result, a spectrally good MOSOS-IHS-DWT result, SOS-SVR result and spectrally optimum MOSOS-SVR result provided the highest spatial fidelity in all test sites. Despite their superior spatial qualities, the spatially optimum MOSOS-IHS-DWT and MOSOS-SVR results may not be used in most occasions due to their colour distortions. For such cases, it would be more reasonable to use the optimum MOSOS-SVR and MOSOS-IHS-DWT

results, which returned a superior spatial detail quality compared to the other methods used. In general, the HPF, ATWT, HCS, AWLP, BDSD, DWT, SFIM and CB methods presented the lowest performance in producing sharp images in all test sites, which can also be seen in Figure 70.

The SOS algorithm was very effective in estimating the band weights that enabled the optimization of the pansharpening results. A good advantage of the SOS algorithm over many other metaheuristic algorithms is that it does not require any algorithm-specific parameters. This, of course, allows for avoiding any analyst-related errors. The SOS algorithm also offers a successful exploration and exploitation when exploring the parameter space, which was found to have enabled the estimation of the most appropriate band weights for the SVR and IHS-DWT methods, without getting trapped at local optima. Another important advantage of the SOS algorithm is that it does not need very large ecosystem sizes to find the optimum result. Thanks to its exploration and exploitation capability, it converges very fast, achieving the optimum result (i.e. band weights) in a short span of time.

The proposed SOS-SVR, MOSOS-SVR, SOS-IHS-DWT and MOSOS-IHS-DWT methods were found to present a very good colour preservation and spatial detail transfer success not only with single-sensor images, but also with multi-sensor images. These methods also achieved to deal with input images of a greater spatial resolution difference. Despite the fact that the SOS-SVR and SOS-IHS-DWT methods were specifically proposed to enhance the colour preservation performance of the SVR and IHS-DWT methods, they achieved a very good spatial detail quality in the test sites, which can also be seen in Figure 70. As seen in the figure, the SOS-SVR and SOS-IHS-DWT results outperformed the conventional pansharpening methods GS, BRV, LMM, MIHS, PCA, HPF, ATWT, HCS, AWLP, BDSD, DWT, SFIM and CB in terms of the preservation of the colour features in the test sites. On the other hand, the proposed MOSOS-IHS-DWT and MOSOS-SVR methods enabled the production of images of required colour or spatial detail quality, which makes these methods suitable for many remote sensing applications, where images of high spectral or spatial detail quality is needed. The main conclusion drawn from this thesis is that the metaheuristic algorithms can be effectively used to optimize the pansharpening results.

## 8. REFERENCES

- Aiazzi, B., Alparone, L., Baronti, S., Garzelli, A. and Selva, M., 2006. MTF-tailored multiscale fusion of high-resolution MS and Pan imagery, Photogrammetric Engineering & Remote Sensing, 72, 5, 591-596.
- Alam, M., N., Das, B. and Pant, V., 2015. A comparative study of metaheuristic optimization approaches for directional overcurrent relays coordination, Electric Power Systems Research, 128, 39-52.
- Almufti, S., M., 2019. Historical survey on metaheuristics algorithms, International Journal of Scientific World, 7, 1, 1-12.
- Alparone, L., Aiazzi, B., Baronti, S., Garzelli, A. and Nencini, F., 2006. Information-Theoretic Image Fusion Assessment without Reference, ESA-EUSC 2006: Image Information Mining for Security and Intelligence, Torrejon Air Base, Madrid, Spain.
- Alparone, L., Aiazzi, B., Baronti, S., Garzelli, A., Nencini, F. and Selva, M., 2008. Multispectral and panchromatic data fusion assessment without reference, Photogrammetric Engineering & Remote Sensing, 74, 2, 193-200.
- Alparone, L., Wald, L., Chanussot, J., Thomas, C., Gamba, P. and Bruce, L., M., 2007. Comparison of Pansharpening Algorithms: Outcome of the 2006 GRS-S Data-Fusion Contest, IEEE Transactions on Geoscience and Remote Sensing, 45, 10, 3012-3021.
- Amolins, K., Zhang, Y. and Dare, P., 2007. Wavelet based image fusion techniques—An introduction, review and comparison, ISPRS Journal of Photogrammetry and Remote Sensing, 62, 4, 249-263.
- Armenakis, C., Leduc, F., Cyr, I., Savapol, F. and Cavayas, F., 2003. A Comparative Analysis of Scanned Maps and Imagery for Mapping Applications, ISPRS Journal of Photogrammetry & Remote Sensing, 57, 5, 304-314.
- Atlas, M., 2008. Çok Amaçlı Programlama Çözüm Tekniklerinin Sınıflandırılması, Anadolu University Journal of Social Sciences, 8, 1.
- Azarang, A. and Ghassemian, H., 2017. An adaptive multispectral image fusion using particle swarm optimization, IEEE Iranian Conference on Electrical Engineering (ICEE), Tehran, Iran, 1708-1712.
- Barrero, O. and Perdomo, S., A., 2018. RGB and multispectral UAV image fusion for Gramineae weed detection in rice fields, Precision Agriculture, 19, 5, 809-822.
- Boussaïd, I., Lepagnot, J. and Siarry, P., 2013. A survey on optimization metaheuristics, Information Sciences, 237, 82-117.

- Broussard, R., P., Rogers, S., K., Oxley, M., E. and Tarr, G., L., 1999. Physiologically motivated image fusion for object detection using a pulse coupled neural network, IEEE Transactions on Neural Networks, 10, 3, 554-563.
- Burns, E., Lemons, S., Ruml, W. and Zhou, R., 2010. Best-first heuristic search for multicore machines, Journal of Artificial Intelligence Research, 39, 689-743.
- Cai, W., Xu, Y., Wu, Z., Liu, H., Qian, L. and Wei, Z., 2018. Pan-sharpening based on multilevel coupled deep network, IEEE International Geoscience and Remote Sensing Symposium (IGARSS), Valencia, Spain, 7046-7049.
- Cao, W., Li, B. and Zhang, Y., 2003. A Remote Sensing Image Fusion Method Based on PCA Transform and Wavelet Packet Transform, IEEE International Conference on Neural Networks and Signal Processing, Nanjing, China.
- Censor, Y., 1977. Pareto optimality in multiobjective problems, Applied Mathematics and Optimization, 4, 1, 41-59.
- Chavez, P., S., Sides, S., C. and Anderson, I., A., 1991. Comparison of three different methods to merge multiresolution and multispectral data: Landsat TM and SPOT panchromatic, Photogrammetric Engineering and Remote Sensing, 57, 3, 295-303.
- Chen, B., Huang, B. and Xu, B., 2017. Multi-source remotely sensed data fusion for improving land cover classification, ISPRS Journal of Photogrammetry and Remote Sensing, 124, 27-39.
- Chen, C., M., Hepner, G., F. and Forster, R., R., 2003. Fusion of hyperspectral and radar data using the IHS transformation to enhance urban surface features, ISPRS Journal of Photogrammetry and Remote Sensing, 58, 1-2, 19-30.
- Chen, L., Zhang, X. and Ma, H., 2018. Sparse representation over shared coefficients in multispectral pansharpening, Tsinghua Science and Technology, 23, 3, 315-322.
- Chen, Y. and Zhang, G., 2017. A pan-sharpening method based on evolutionary optimization and ihs transformation, Mathematical Problems in Engineering, 1-8.
- Chen, Y., Liu, C., Zhou, A. and Zhang, G., 2019. MIHS: A Multiobjective Pan-sharpening Method for Remote Sensing Images, IEEE Congress on Evolutionary Computation (CEC), Wellington, New Zealand, New Zealand, 1068-1073.
- Cheng, M., Y. and Lien, L., C., 2012. Hybrid artificial intelligence-based PBA for benchmark functions and facility layout design optimization, Journal of Computing in Civil Engineering, 26, 5, 612-624.
- Cheng, M., Y. and Prayogo, D., 2014. Symbiotic organisms search: a new metaheuristic optimization algorithm, Computers & Structures, 139, 98-112.

- Chibani, Y., 2006. Additive integration of SAR features into multispectral SPOT images by means of à trous wavelet decomposition, ISPRS Journal of Photogrammetry and Remote Sensing, 60, 5, 306-314.
- Das, B., Mukherjee, V. and Das, D., 2016. DG placement in radial distribution network by symbiotic organisms search algorithm for real power loss minimization, Applied Soft Computing, 49, 920-936.
- Das, S. and Bhattacharya, A., 2018. Symbiotic organisms search algorithm for short-term hydrothermal scheduling, Ain Shams Engineering Journal, 9, 4, 499-516.
- Das, S. and Suganthan, P., N., 2011. Differential evolution: A survey of the state-of-the-art, IEEE Transactions on Evolutionary Computation, 15, 1, 4-31.
- de Béthune, S., Muller, F. and Donnay, J., P., 1998. Fusion of multispectral and panchromatic images by local mean and variance matching filtering techniques, Fusion of Earth Data, 28-30.
- de Béthune, S., Muller, F. and Binard, M., 1997. Adaptive intensity matching filters: a new tool for multiresolution data fusion, Proceedings of the Multi-Sensor Systems and Data Fusion for Telecommunications, Remote Sensing and Radar, Lisbon, Portugal.
- Deb, K., 2001. Multi-objective optimization using evolutionary algorithms, vol. 16, John Wiley & Sons.
- Deb, K., Pratap, A., Agarwal, S. and Meyarivan, T., A., M., T., 2002. A fast and elitist multiobjective genetic algorithm: NSGA-II. IEEE Transactions on Evolutionary Computation, 6, 2, 182-197.
- Dechter, R. and Pearl, J., 1985. Generalized best-first search strategies and the optimality of A, Journal of the ACM, 32, 3, 505-536.
- Delleji, T., Kallel, A. and Ben Hamida, A., 2016. Iterative scheme for MS image pansharpening based on the combination of multi-resolution decompositions, International Journal of Remote Sensing, 37, 24, 6041-6075.
- Dian, R., Li, S., Guo, A. and Fang, L., 2018. Deep hyperspectral image sharpening, IEEE Transactions on Neural Networks and Learning Systems, 29, 5345-5355.
- Dorigo, M. and Di Caro, G., 1999. Ant colony optimization: a new meta-heuristic, In Proceedings of the IEEE Congress on Evolutionary Computation, vol. 2, 1470-1477.
- Dosoglu, M., K., Guvenc, U., Duman, S., Sonmez, Y. and Kahraman, H., T., 2018. Symbiotic organisms search optimization algorithm for economic/emission dispatch problem in power systems, Neural Computing and Applications, 29, 3, 721-737.
- Dou, W., Image Degradation for Quality Assessment of Pan-Sharpener Methods, 2018. Remote Sensing, 10, 1, 154.

- Du, K., L. and Swamy, M., N., S., 2016. Search and optimization by metaheuristics, *Techniques and Algorithms Inspired by Nature*, Birkhauser: Basel, Switzerland.
- Eckerstorfer, M., Bühler, Y., Frauenfelder, R. and Malnes, E., 2016. Remote sensing of snow avalanches: Recent advances, potential, and limitations, *Cold Regions Science and Technology*, 121, 126-140.
- Ehlers, M., 2005. Beyond Pan sharpening: Advances in Data Fusion for Very High Resolution Remote Sensing Data, *ISPRS Workshop 'High-Resolution Earth Imaging for Geospatial Information*, 17-20.
- Ehlers, M., Klonus, S., Johan Åstrand, P. and Rosso, P., 2010. Multi-sensor image fusion for pansharpening in remote sensing, *International Journal of Image and Data Fusion*, 1, 1, 25-45.
- El-Samie, F., E., A., Hadhoud, M., M. and El-Khamy, S. E., 2012. *Image super-resolution and applications*, CRC press.
- Evans, G., 1984. An Overview of techniques for solving multiobjective mathematical programs, *Management Science*, 30, 11, 1268-1282.
- Fei, R., Zhang, J., Liu, J., Du, F., Chang, P. and Hu, J., 2019. Convolutional sparse representation of injected details for pansharpening, *IEEE Geoscience and Remote Sensing Letters*, 16, 10, 1595-1599.
- Garzelli, A. and Nencini, F., 2006. PAN-sharpening of very high resolution multispectral images using genetic algorithms, *International Journal of Remote Sensing*, 27, 15, 3273-3292.
- Garzelli, A., Nencini, F. and Capobianco, L., 2008. Optimal MMSE pan sharpening of very high resolution multispectral images, *IEEE Transactions on Geoscience and Remote Sensing*, 46, 1, 228-236.
- Gascho, D., Flach, P., M., Schaerli, S., Thali, M., J. and Kottner, S., 2018. Application of 3D image fusion for radiological identification of decedents, *Journal of Forensic Radiology and Imaging*, 13, 12-16.
- Gavrilas, M., 2010. Heuristic and metaheuristic optimization techniques with application to power systems, *Proceedings of the 12th WSEAS International Conference on Mathematical Methods and Computational Techniques in Electrical Engineering*.
- Ghahremani, M., Liu, Y., Yuen, P. and Behera, A., 2019. Remote sensing image fusion via compressive sensing, *ISPRS Journal of Photogrammetry and Remote Sensing*, 152, 34-48.
- Ghassemian, H., 2016. A review of remote sensing image fusion methods, *Information Fusion*, 32, 75-89.

- Glover, F., 1989. Tabu search—part I, ORSA Journal on Computing, 1, 3, 190-206.
- Gogineni, R. and Chaturvedi, A., 2018. Sparsity inspired pan-sharpening technique using multi-scale learned dictionary, ISPRS Journal of Photogrammetry and Remote Sensing, 146, 360-372.
- Goldfeld, S., M., Quandt, R., E. and Trotter, H., F., 1966. Maximization by quadratic hill-climbing, Econometrica: Journal of the Econometric Society, 541-551.
- Gong, M., Zhou, Z. and Ma, J., 2011. Change detection in synthetic aperture radar images based on image fusion and fuzzy clustering, IEEE Transactions on Image Processing, 21, 4, 2141-2151.
- Gonzales, R., C. and Woods, R., E., 2003. Digital Image Processing, 2nd Edition, Pearson Education (Singapore), Pte. Ltd., Indian Branch, Delhi, India.
- González-Audicana, M., Saleta, J., L., Catalán, R., G. and García, R., 2004. Fusion of multispectral and panchromatic images using improved IHS and PCA mergers based on wavelet decomposition, IEEE Transactions on Geoscience and Remote Sensing, 42, 6, 1291-1299.
- Gonzalo, C. and Lillo-Saavedra, M., 2008. A directed search algorithm for setting the spectral-spatial quality trade-off of fused images by the wavelet à trous method, Canadian Journal of Remote Sensing, 34, 4, 367-375.
- Gonzalo-Martín, C. and Lillo-Saavedra, M., 2011. Balancing the Spatial and Spectral Quality of Satellite Fused Images through a Search Algorithm, In: Search Algorithms and Applications, 156, 307, 953-978.
- Gungor, O., 2008. Multi Sensor Multi Resolution Image Fusion, PhD thesis, Dept. of Civil Engineering, Purdue University, USA.
- Hallada, W., A. and Cox, S., 1983. Image sharpening for mixed spatial and spectral resolution satellite systems, Proc. 17th International Symposium on Remote Sensing of Environment, Ann Arbor, MI, 1023-1032.
- Holland, J., H., 1975. Adaptation in Natural and Artificial Systems, University of Michigan Press, Ann Arbor, MI, USA.
- Huang, W., Xiao, L., Wei, Z., Liu, H. and Tang, S., 2015. A new pan-sharpening method with deep neural networks, IEEE Geoscience and Remote Sensing Letters, 12, 5, 1037-1041.
- Hwang, C., R., 1988. Simulated annealing: Theory and applications, Acta Applicandae Mathematicae, 12, 1, 108-111.
- Imani, M., 2018. Band dependent spatial details injection based on collaborative representation for pansharpening, IEEE Journal of Selected Topics in Applied Earth Observations and Remote Sensing, 11, 12, 4994-5004.

- Jaszkiewicz, A. and Branke, J., 2008. Interactive multiobjective evolutionary algorithms, In: *Multiobjective optimization*, Springer, Berlin, 179-193.
- Jin, Y., Olhofer, M. and Sendhoff, B., 2001. Dynamic weighted aggregation for evolutionary multiobjective optimization: why does it work and how? *Proceedings of the 3rd Annual Conference on Genetic and Evolutionary Computation*, Morgan Kaufmann Publishers Inc., 1042-1049.
- Kanal, L. and Kumar, V. 2012. *Search in artificial intelligence*, Springer Science & Business Media.
- Kang, X., Li, S. and Benediktsson, J., A., 2013. Feature extraction of hyperspectral images with image fusion and recursive filtering, *IEEE Transactions on Geoscience and Remote Sensing*, 52, 6, 3742-3752.
- Karaboga, D., 2010. Artificial bee colony algorithm. *Scholarpedia*, 5, 3, 6915.
- Kennedy, J. and Eberhart, R., 1995. Particle swarm optimization, *Proceedings of the IEEE International Conference on Neural Networks*, Piscataway, NJ: IEEE Press, 1942-1948.
- Khademi, G. and Ghassemian, H., 2017. A multi-objective component-substitution-based pansharpening, *IEEE 3rd International Conference on Pattern Recognition and Image Analysis (IPRIA)*, Shahrekord, Iran, 248-252.
- Khan, M., M., Chanussot, J., Montanvert, A. and Condat, L., 2007. Pan-sharpening using induction. *IEEE International Geoscience and Remote Sensing Symposium*, Barcelona, Spain, 314-317.
- Kim, Y., Lee, C., Han, D., Kim, Y. and Kim, Y., 2010. Improved additive-wavelet image fusion, *IEEE Geoscience and Remote Sensing Letters*, 8, 2, 263-267.
- Kirkpatrick, S., Gelatt, C., D. and Vecchi, M., P., 1983. Optimization by simulated annealing, *Science* 220, 4598, 671-680.
- Klockgether, J. and Schwefel, H., P., 1970. Two-phase nozzle and hollow core jet experiments. In *Proceedings of 11th Symposium on Engineering Aspects of Magnetohydrodynamics*, Pasadena, CA: California Institute of Technology, 141-148.
- Klonus, S., 2008. Comparison of pansharpening algorithms for combining radar and multispectral data, *The International Archives of the Photogrammetry, Remote Sensing and Spatial Information Sciences*, 37, B6b, 189-194.
- Kooy, H., M., Van Herk, M., Barnes, P., D., Alexander III, E., Dunbar, S., F., Tarbell, N., J., Mulkern, R., V., Holupka, E., J. and Loeffler, J., S., 1994. Image fusion for stereotactic radiotherapy and radiosurgery treatment planning, *International Journal of Radiation Oncology\* Biology\* Physics*, 28, 5, 1229-1234.

- Kundur, D. and Hatzinakos, D., 2004. Toward robust logo watermarking using multiresolution image fusion principles, IEEE Transactions on Multimedia, 6, 1, 185-198.
- Laben, C., A. and Brower, B., V., 2000. Process for enhancing the spatial resolution of multispectral imagery using pan-sharpening, U.S. Patent No: 6,011,875.
- Li, S., Kwok, J., T. and Wang, Y., 2002. Using the discrete wavelet frame transform to merge Landsat TM and SPOT panchromatic images, Information Fusion, 3, 1, 17-23.
- Lieberman, E. R., 1991. Soivet Multi-objective mathematical programming methods: an overview, Management Science, 37, 9, 1147-1165.
- Lillo-Saavedra, M., Gonzalo, C., Arquero, A. and Martinez, E., 2005. Fusion of multispectral and panchromatic satellite sensor imagery based on tailored filtering in the Fourier domain, International Journal of Remote Sensing, 26, 6, 1263-1268.
- Ling, Y., Ehlers, M., Usery, E., L. and Madden, M., 2007. FFT-enhanced IHS transform method for fusing high-resolution satellite images, ISPRS Journal of Photogrammetry and Remote Sensing, 61, 6, 381-392.
- Liu, J., G., 2000. Smoothing filter-based intensity modulation: A spectral preserve image fusion technique for improving spatial details, International Journal of Remote Sensing, 21, 18, 3461-3472.
- Lotfi, V., Yoon, Y., S. and Zions, S., 1997. Aspiration-based search algorithm (ABSALG) for multiple objective linear programming problems: theory and comparative tests, Management Science, 43, 8, 1047-1059.
- Lu, L., Zhang, X., Xu, X. and Shang, D., 2017. Multispectral image fusion for illumination-invariant palmprint recognition, PloS One, 12, 5.
- Marler, R., T. and Arora, J., S., 2010. The weighted sum method for multi-objective optimization: new insights, Structural and Multidisciplinary Optimization, 41, 6, 853-862.
- Masi, G., Cozzolino, D., Verdoliva, L. and Scarpa, G., 2016. Pansharpening by convolutional neural networks, Remote Sensing, 8, 7, 594.
- Maurer, T., 2013. How to pan-sharpen images using the Gram-Schmidt pan-sharpen method—A recipe, The International Archives of the Photogrammetry, Remote Sensing and Spatial Information Sciences, XL-1/W1, 239-244.
- Maignan, D., Knust, S., Frayret, J., M., Pesant, G. and Gaud, N., 2015. A review and taxonomy of interactive optimization methods in operations research, ACM Transactions on Interactive Intelligent Systems, 5, 3, 17.

- Mezura-Montes, E. and Coello, C., A., C., 2005. A simple multimembered evolution strategy to solve constrained optimization problems, IEEE Transactions on Evolutionary Computation, 9, 1, 1-17.
- Michaels, J., E. and Michaels, T., E., 2007. Guided wave signal processing and image fusion for in situ damage localization in plates, Wave Motion, 44, 6, 482-492.
- Mirjalili, S. and Dong, J., S., 2020. Multi-Objective Optimization using Artificial Intelligence Techniques, Springer International Publishing.
- Mirjalili, S., 2019. Evolutionary algorithms and neural networks, Studies in Computational Intelligence.
- Mirjalili, S., Faris, H. and Aljarah, I., 2020. Evolutionary Machine Learning Techniques.
- Munehika, C., K., Warnick, J., S., Salvaggio, C. and Schott, J., R., 1993. Resolution enhancement of multispectral image data to improve classification accuracy, Photogrammetric Engineering and Remote Sensing, 59, 1, 67-72.
- Niazi, S., M., N., Zade, M., M. and Zadeh, F., S., 2016. A Novel IHS-GA Fusion Method Based on Enhancement Vegetated Area, Journal of Geomatics Science and Technology, 6, 1, 235-248.
- Nunez, J., Otazu, X., Fors, O., Prades, A., Pala, V. and Arbiol, R., 1999. Multiresolution-based image fusion with additive wavelet decomposition, IEEE Transactions on Geoscience and Remote Sensing, 37, 3, 1204-1211.
- Otazu, X., González-Audicana, M., Fors, O. and Núñez, J., 2005. Introduction of sensor spectral response into image fusion methods. Application to wavelet-based methods, IEEE Transactions on Geoscience and Remote Sensing, 43, 10, 2376-2385.
- Padwick, C., Deskevich, M., Pacifici, F. and Smallwood, S., 2010. WorldView-2 pan-sharpening, In Proceedings of the ASPRS 2010 Annual Conference, San Diego, CA, USA.
- Palsson, F., Sveinsson, J., R. and Ulfarsson, M., O., 2017. Multispectral and hyperspectral image fusion using a 3-d-convolutional neural network, IEEE Geoscience and Remote Sensing Letters, 14, 5, 639-643.
- Pham, D., T., Ghanbarzadeh, A., Koc, E., Otri, S., Rahim, S. and Zaidi, M., 2006. The Bees algorithm, a novel tool for complex optimisation problems. Proceedings of the 2nd international virtual conference on intelligent production machines and systems, Elsevier: Oxford, 454-9.
- Piella, G., 2009. Image fusion for enhanced visualization: A variational approach, International Journal of Computer Vision, 83, 1, 1-11.
- Pohl, C. and van Genderen, J., 2016. Remote sensing image fusion: A practical guide, Crc Press.

- Pradhan, P., 2005. Multiresolution Based, Multisensor, Multispectral Image Fusion, Ph.D. Dissertation, Mississippi State University.
- Prayogo, D., Cheng, M., Y. and Prayogo, H., 2017. A novel implementation of nature-inspired optimization for civil engineering: a comparative study of symbiotic organisms search, Civil Engineering Dimension, 19, 1, 36-43.
- Raskar, R., Ilie, A. and Yu, J., 2005. Image fusion for context enhancement and video surrealism, In ACM SIGGRAPH 2005 Courses, 4-es.
- Rathore, N., S., Singh, V., P. and Phuc, B., D., H., 2019. A modified controller design based on symbiotic organisms search optimization for desalination system, Journal of Water Supply: Research and Technology—AQUA, 68, 5, 337-345.
- Resende, M., G. and Ribeiro, C., C., 2003. Greedy randomized adaptive search procedures, In: Handbook of metaheuristics, Springer, Boston, 219-249.
- Ruzika, S. and Wiecek, M., M., 2005. Approximation methods in multiobjective programming. Journal of Optimization Theory and Applications, 126, 3, 473-501.
- Schowengerdt, R., A., 1980. Reconstruction of multispatial, multispectral image data using spatial frequency content, Photogrammetric Engineering and Remote Sensing, 46, 10, 1325-1334.
- Serifoglu Yilmaz, C., Yilmaz, V. and Güngör, O., 2020. On the use of the SOS metaheuristic algorithm in hybrid image fusion methods to achieve optimum spectral fidelity, International Journal of Remote Sensing, 41, 10, 3993-4021.
- Serifoglu Yilmaz, C., Yilmaz, V., Gungor, O. and Shan, J., 2019. Metaheuristic pansharpening based on symbiotic organisms search optimization, ISPRS Journal of Photogrammetry and Remote Sensing, 158, 167-187.
- Seshadri, A., 2006. A fast elitist multiobjective genetic algorithm: NSGA-II ToolBox, Technical report.
- Shahdoosti, H., R. and Ghassemian, H., 2016. Combining the spectral PCA and spatial PCA fusion methods by an optimal filter, Information Fusion, 27, 150-160.
- Siddiqui, Y., 2003. The modified IHS method for fusing satellite imagery, ASPRS 2003 Annual Conference Proceedings, Anchorage, Alaska.
- Singh, S., Gyaourova, A., Bebis, G. and Pavlidis, I., 2004. Infrared and visible image fusion for face recognition. In Biometric Technology for Human Identification, vol. 5404, 585-596.
- Singh, S., P., Prakash, T. and Singh, V., P., 2020. Coordinated tuning of controller-parameters using symbiotic organisms search algorithm for frequency regulation of multi-area wind integrated power system, International Journal of Engineering Science and Technology, 23, 1, 240-252.

- Song, H., Liu, Q., Wang, G., Hang, R. and Huang, B., 2018. Spatiotemporal satellite image fusion using deep convolutional neural networks, IEEE Journal of Selected Topics in Applied Earth Observations and Remote Sensing, 11, 3, 821-829.
- Starck, J., L. and Murtagh, F., 1994. Image restoration with noise suppression using the wavelet transform, Astronomy and Astrophysics, 288, 342-348.
- Strait, M., Rahmani, S. and Markurjev, D., 2008. Evaluation of Pan-Sharpener Methods, UCLA Department of Mathematics.
- Talbi, E., G., 2009. Metaheuristics: from design to implementation, John Wiley & Sons.
- Tran, D., H., Cheng, M., Y. and Prayogo, D., 2016. A novel Multiple Objective Symbiotic Organisms Search (MOSOS) for time–cost–labor utilization tradeoff problem, Knowledge-Based Systems, 94, 132-145.
- URL-1, NASA Ames National Full-Scale Aerodynamics Complex (NFAC). <http://www.nasa.gov/centers/ames/multimedia/images/2005/nfac.html>. Accessed 2020-03-24, accessed on 15 May 2020.
- Verhoeven, G., Nowak, M. and Nowak, R., 2016. Pixel-level image fusion for archaeological interpretative mapping, 8th International Congress on Archaeology, Computer Graphics, Cultural Heritage and Innovation (ARQUEOLÓGICA 2.0), 404-407.
- Vicinanza, M., R., Restaino, R., Vivone, G., Dalla Mura, M. and Chanussot, J., 2014. A pansharpening method based on the sparse representation of injected details, IEEE Geoscience and Remote Sensing Letters, 12, 1, 180-184.
- Vivone, G., Restaino, R., Dalla Mura, M., Licciardi, G. and Chanussot, J., 2014a. Contrast and error-based fusion schemes for multispectral image pansharpening, IEEE Geoscience and Remote Sensing Letters, 11, 5, 930-934.
- Vivone, G., Simões, M., Dalla Mura, M., Restaino, R., Bioucas-Dias, J., M., Licciardi, G. A. and Chanussot, J., 2014b. Pansharpening based on semiblind deconvolution, IEEE Transactions on Geoscience and Remote Sensing, 53, 4, 1997-2010.
- Wald, L., 2000. Quality of high resolution synthesized images: Is there a simple criterion? 3<sup>rd</sup> Conference 'Fusion of Earth data: merging point measurements, raster maps and remotely sensed images', Sophia Antipolis, France, 99-105.
- Wald, L., Ranchin, T. and Mangolini, M., 1997. Fusion of satellite images of different spatial resolutions: Assessing the quality of resulting images, Photogrammetric Engineering & Remote Sensing, 63, 691-699.
- Wang, W., Jiao, L. and Yang, S., 2014. Fusion of multispectral and panchromatic images via sparse representation and local autoregressive model, Information Fusion, 20, 73-87.

- Wang, X., Bai, S., Li, Z., Song, R. and Tao, J., 2019. The PAN and MS image pansharpening algorithm based on adaptive neural network and sparse representation in the NSST domain, IEEE Access, 7, 52508-52521.
- Wang, Z. and Bovik, A., C., 2002. A universal image quality index, IEEE Signal Processing Letters, 9, 3, 81-84.
- Wang, Z. and Li, Q., 2011. nformation content weighting for perceptual image quality assessment, IEEE Transactions on Image Processing, 20, 5, 1185-1198.
- Wang, Z., Bovik, A., C., Sheikh, H., R. and Simoncelli, E., P., 2004. Image quality assessment: from error visibility to structural similarity, IEEE Transactions on Image Processing, 13, 4, 600-612.
- Wei, Y., Yuan, Q., Shen, H. and Zhang, L., 2017. Boosting the accuracy of multispectral image pansharpening by learning a deep residual network, IEEE Geoscience and Remote Sensing Letters, 14, 10, 1795-1799.
- Witharana, C., LaRue, M., A. and Lynch, H., J., 2016. Benchmarking of data fusion algorithms in support of earth observation based Antarctic wildlife monitoring, ISPRS Journal of Photogrammetry and Remote Sensing, 113, 124-143.
- Wolpert, D., H. and Macready, W., G., 1997. No free lunch theorems for optimization. IEEE Transactions on Evolutionary Computation, 1, 1, 67-82.
- Wu, B., Fu, Q., Sun, L. and Wang, X., 2015. Enhanced hyperspherical color space fusion technique preserving spectral and spatial content, Journal of Applied Remote Sensing, 9, 1, 097291.
- Xiao, Y., Fang, F., Zhang, Q., Zhou, A. and Zhang, G., 2015. Parameter selection for variational pan-sharpening by using evolutionary algorithm, Remote Sensing Letters, 6, 6, 458-467.
- Xing, Y., Wang, M., Yang, S. and Jiao, L., 2018. Pan-sharpening via deep metric learning, ISPRS Journal of Photogrammetry and Remote Sensing, 145, 165-183.
- Xiong, G., Zhang, J., Yuan, X., Shi, D. and He, Y., 2018. Application of symbiotic organisms search algorithm for parameter extraction of solar cell models, Applied Sciences, 8, 11, 2155.
- Yang, R. H., Pan, Q. and Cheng, Y., M., 2006. A New Method of Image Fusion Based on M-Band Wavelet Transform. Proceedings of the 5th International Conference on Machine Learning and Cybernetics, Dalian, 13-16.
- Yang, X., S. and Deb, S., 2009. Cuckoo search via Lévy flights, IEEE World congress on nature & biologically inspired computing (NaBIC), 210-214.
- Yang, X., S., 2011. Metaheuristic optimization, Scholarpedia, 6, 8, 11472.

- Yang, X., S., 2010b. Firefly algorithm, Levy flights and global optimization. In: Research and development in intelligent systems XXVI, 209-218, Springer, London.
- Yang, X., S., 2010a. Nature-inspired metaheuristic algorithms, Luniver press.
- Yang, X., S., 2014. Nature-inspired optimization algorithms, Elsevier.
- Yao, X. and Liu, Y., 1996. Fast evolutionary programming, Evolutionary Programming, 3, 451-460.
- Yilmaz, V. and Gungor, O., 2016b. Determining the optimum image fusion method for better interpretation of the surface of the Earth, Norsk Geografisk Tidsskrift-Norwegian Journal of Geography, 70, 2, 69-81.
- Yilmaz, V. and Gungor, O., 2016a. Fusion of very high-resolution UAV images with criteria-based image fusion algorithm, Arabian Journal of Geosciences, 9, 1.
- Yilmaz, V., 2012. Görüntü Kaynaştırma Yöntemlerinde Performans Analizi, Yüksek Lisans Tezi (Master Thesis), Fen Bilimleri Enstitüsü, Karadeniz Teknik Üniversitesi.
- Yilmaz, V., Serifoglu Yilmaz, C. and Gungor, O., 2019. Genetic algorithm-based synthetic variable ratio image fusion, Geocarto International, 1-18.
- Yilmaz, V., Serifoglu Yilmaz, C., Güngör, O. and Shan, J., 2020. A genetic algorithm solution to the Gram-Schmidt image fusion, International Journal of Remote Sensing, 41, 4, 1458-1485.
- Yin, H., 2019. PAN-Guided Cross-Resolution Projection for Local Adaptive Sparse Representation-Based Pansharpening, IEEE Transactions on Geoscience and Remote Sensing, 57, 7, 4938-4950.
- Yin, H., 2015. Sparse representation based pansharpening with details injection model, Signal Processing, 113, 218-227.
- Yuret, D. and De La Maza, M., 1993. Dynamic hill climbing: overcoming the limitations of optimization techniques, In: The second Turkish Symposium on Artificial Intelligence and Neural Networks, Citeseer, 208-212.
- Zeng, Y., Huang, W., Liu, M., Zhang, H. and Zou, B., 2010. Fusion of satellite images in urban area: Assessing the quality of resulting images, 18<sup>th</sup> IEEE International Conference on Geoinformatics, Beijing, China, 1-4.
- Zhang, L. and Li, H., 2012. SR-SIM: A fast and high performance IQA index based on spectral residual, 19<sup>th</sup> IEEE International Conference on Image Processing, Orlando, FL, USA, 1473-1476.
- Zhang, Y., 1999. A new merging method and its spectral and spatial effects, International Journal of Remote Sensing, 20, 10, 2003-2014.

- Zhang, Z. and Blum, R., S., 1997. Region-based image fusion scheme for concealed weapon detection, In Proceedings of the 31st annual conference on information sciences and systems, 168-173.
- Zhou, J., Civco, D., L. and Silander, J., A., 1998. A wavelet transform method to merge Landsat TM and SPOT panchromatic data, International Journal of Remote Sensing, 19, 743-757.



## CURRICULUM VITAE

Çiğdem ŞERİFOĞLU YILMAZ was born in Istanbul, Turkey in 1990. She graduated from the Ankara Ayrancı High School in 2008. She received her B.Sc. degree from the Department of Geomatics Engineering, Karadeniz Technical University in 2014. She graduated from this department with the highest grade point average. She also received her M.Sc. degree from the same department in 2016. She has been working at the Department of Geomatics Engineering of the Karadeniz Technical University as a research assistant since 2015. Her main research topics include point cloud processing, metaheuristic optimization, image interpolation and image fusion. She completed a certain part of her PhD studies at the Wrocław University of Environmental and Life Sciences, Poland in 2017. She studied English in the United Kingdom in 2012. Some of her current journal papers are as follows:

- Serifoglu Yilmaz, C., Yilmaz, V. and Güngör, O., On the use of the SOS metaheuristic algorithm in hybrid image fusion methods to achieve optimum spectral fidelity, *International Journal of Remote Sensing*, 41, 10 (2020) 3993-4021.
- Yilmaz, V., Serifoglu Yilmaz, C., Güngör, O. and Shan, J., A genetic algorithm solution to the Gram-Schmidt image fusion, *International Journal of Remote Sensing*, 41, 4 (2020) 1458-1485.
- Serifoglu Yilmaz, C., Yilmaz, V., Gungor, O. and Shan, J., Metaheuristic pansharpening based on symbiotic organisms search optimization, *ISPRS Journal of Photogrammetry and Remote Sensing*, 158 (2019) 167-187.
- Yilmaz, V., Serifoglu Yilmaz, C. and Gungor, O., Genetic algorithm-based synthetic variable ratio image fusion, *Geocarto International*, (2019) 1-18.
- Yilmaz, V., Konakoglu, B., Serifoglu, C., Gungor, O. and Gökalp, E., Image classification-based ground filtering of point clouds extracted from UAV-based aerial photos, *Geocarto International*, 33, 3 (2018) 310-320.
- Serifoglu Yilmaz, C. and Gungor, O., Comparison of the performances of ground filtering algorithms and DTM generation from a UAV-based point cloud, *Geocarto International*, 33, 5 (2018) 522-537.

- Serifoglu Yilmaz, C., Yilmaz, V. and Güngör, O., Investigating the performances of commercial and non-commercial software for ground filtering of UAV-based point clouds, *International Journal of Remote Sensing*, 39, 15-16 (2018) 5016-5042.

